UNIVERSITÀ
DEGLI STUDI
DI PADOVA

Sede Amministrativa: Università degli Studi di Padova

Dipartimento di GEOSCIENZE

SCUOLA DI DOTTORATO DI RICERCA IN SCIENZE DELLA TERRA

CICLO: XXII

ANATECTIC MELTING IN A METAPELITIC SYSTEM: A FLUID AND MELT INCLUSION STUDY

Direttore della Scuola : Prof. Gilberto Artioli

Supervisore : Prof. Bernardo Cesare

Co-supervisore: Prof. Robert J. Bodnar

Co-supervisore: Dr. Emma Salvioli Mariani

Dottorando : Silvio Ferrero

We shall not cease from exploration,
And the end of all our exploring
Will be to arrive where we started
And know the place for the first time.
(Little Gidding, T. S. Eliot)

To many petrologists a volatile component is exactly like a Maxwell daemon;
it does just what one may wish it to do
(The evolution of the igneous rocks, N.L. Bowen, 1928)

Abstract

In this thesis, a melt and fluid inclusion study was performed to investigate both anatectic melt and fluid phase during anatexis of metapelitic rocks, by studying samples from two different geological settings, the khondalites of the Kerala Khondalite Belt, India, and the granulitic enclaves from El Hoyazo, Neogene Volcanic Province, Spain.

In khondalites (garnet-sillimanite-cordierite granulite/gneiss), melt inclusions (MI), interpreted as containing anatectic melt, were found for the first time in peritectic minerals from classic regionally metamorphosed metapelitic migmatites, partially melted at T~900°C and 6-8 kbar. A detailed study was carried out to characterize the petrographic features of MI, their chemical composition and the structures of the crystallized phases within the inclusions, by microscope observation, FESEM imaging in BSE mode, X-ray elemental mapping, EMP and Micro-Raman analyses. Peritectic garnets contain irregular clusters of hundreds of MI, from totally crystallized (*nanogranites*) to totally glassy, often negative-crystal in shape. Nanogranites are 5-25 μm across and contain a cryptocrystalline aggregate of Bt+Kfs+Pl+Qtz±Ap, along with trapped phases (apatite, zircon, rutile, Zn-bearing spinel and rarely ilmenite) that are likely to have favoured the entrapment of the anatectic melt during the host growth. The grain size of crystals in nanogranite is variable, from few tens of nanometer to several microns. Partially crystallized inclusions contain a differentiated melt that occupies 60 to 20% of the inclusion area, along with Qtz, Kfs and Bt. Glassy inclusions are usually smaller (2.5–17.5 μm) than nanogranites and represent about 15% of the total amount of MI in the clusters. They contain an amorphous phase, along with the same trapped phases found in nanogranites. EMP analysis of the glass provides an ultrapotassic and rhyolitic composition, with K_2O >> Na_2O. The EMP totals suggest a H_2O content (calculated by difference to 100%) <3 wt%. The occurrence of preserved glassy MI is an unprecedented finding, and since the mean diameter (8 μm) of glassy inclusions is smaller than those of nanogranites (13 μm), we propose that this difference in size was influential to the crystallization of melt droplets, so that most of the smaller inclusions remained glassy because of inhibited nucleation. Nanogranites were homogenized using a heating stage at controlled atmosphere, and then analyzed, to obtain a consistent set of compositional data on their bulk composition. EMP analyses on homogenized inclusions show a compositional homogeneity of the melt from all the nanogranites, with strong similarity to those of preserved glassy inclusions. Melt composition is Na-poor, and plots very far from the “minimum melt” of the

haplogranitic system in the Q-Ab-Or diagram, commonly accepted as the composition of the anatectic melt produced by partial melting of metapelites. The retrieved composition, although uncommon for anatectic melts, is reported for natural rhyolites and for experimental products, and accounts for partial melting conditions with T in excess of 850°C, in agreement with the inferred PT conditions of partial melting for these rocks. Moreover, it testifies that assuming a minimum melt composition as representative of the anatectic melt is not correct in the present case study and should not be considered a general rule. The consistency of the compositional data and the careful microstructural investigation of the samples, coupled with the use of the correct techniques of MI homogenization, microchemical analyses and data correction, support for the interpretation of these data as representative of the phase trapped in MI, and the conclusion that MI in garnet from khondalites contain droplets of anatectic melt. This novel result represents therefore an important contribution to the knowledge of anatectic melt in natural rocks.

In the second part of the research the granulitic enclaves of El Hoyazo are studied. These partially melted metapelites, ripped off from the basement when anatexis was still an on-going process, contain abundant rhyolitic glass both as layers and pockets, and as glassy inclusions in almost all the minerals of the assemblage. Unlike regionally, slowly cooled rocks, in this case the anatectic conditions were frozen by the rapid ascent of the samples in a uprising magma. MI-bearing garnet is the first peritectic phase produced by partial melting at ~700°C and 5-7 kbar, and contains abundant FI with no visible evidence of post-entrapment modifications, trapped in conditions of fluid-melt immiscibility. A FI study was performed on garnets from Spl-Crd and Bt-Grt-Sil enclaves by microscope investigation, microthermometric studies, Micro-Raman analyses, mass balance calculation and TEM investigation. In Spl-Crd enclaves FI are two-phase (L+V), spherical to tubular, and often contain graphite as trapped phase. Trapped fluid is a mixture of H_2O+CO_2+N_2±H_2S±CH_4, with water up to 95 mol%, while in Bt-Grt-Sil enclaves FI in garnet are one phase, and contain a CO_2+N_2 mixtures. In both samples FI have densities that are not consistent with the inferred trapping conditions, and suggest that despite of their primary-looking features, FI re-equilibrated during uprising. TEM investigation on Bt-Grt-Sil samples showed partially healed cracks at sub-μm scale, possible escape pathways for the leakage of fluids out of the inclusions. In Spl-Crd enclaves microchemical data acquired on MI and biotite inclusions, that occur in the same cluster along with FI, demonstrate that a water-rich leucogranitic melt was trapped along with a H_2O-rich, COH phase at conditions

consistent with the inferred garnet growth (c. 700°C). In garnet from Bt-Grt-Sil enclaves, the almost complete decrepitation and fluid leakage suffered by the studied FI did not allow to estimate the original composition of fluids hosted in garnet. Based on the H_2O content of coexisting melt inclusions, however, the fluid is inferred to have been more CO_2-rich than the fluid in the Spl-Crd enclaves. This work adds further compositional constraints to the characterization of anatexis of metapelites in the lower crust: in fact, although final results clearly show that enclaves lost part of the original components, the composition of fluid trapped in garnet from Spl-Crd enclaves is probably very close to the original, and is consistent with the composition of the coexisting melt.

Research on melt and fluid inclusions in peritectic minerals represents a new approach to the problem of partial melting in natural rocks, and the present study demonstrated that reliable petrological and geochemical information on anatexis can be collected from nano- to micron-scale objects. The dataset reported in this study widens the horizons in crustal petrology, because for the first time the crustal melt composition can be analyzed rather than assumed. Moreover, MI study in migmatites is likely to have large potentials of development, as confirmed by recent findings of anatectic melt trapped in inclusions in peritectic minerals from various migmatite terrains. As regard the fluid coexistent with anatectic melt, the exceptional occurrence of MI and FI in garnets from El Hoyazo enclaves allowed the identification and characterization of a H_2O-rich fluid present during the first step of anatexis of these metapelites.

Riassunto

Nel presente lavoro di tesi sono riportati i risultati dello studio di inclusioni fluide e di fuso silicatico effettuato sulle khondaliti della Kerala Khondalite Belt, India, e sugli inclusi granulitici di El Hoyazo, Neogene Volcanic Province, Spagna meridionale, con il fine di caratterizzare l`anatessi di rocce metapelitiche.

Nelle khondaliti (gneiss granulitici a granato-sillimanite-cordierite), inclusioni di fuso silicatico (*inclusioni vetrose*, o MI), interpretate come contenenti fuso anatettico, sono state rinvenute per la prima volta in fasi peritettiche di classiche migmatiti metapelitiche, caratterizzate da metamorfismo regionale con fusione parziale a T~900°C e 6-8 kbar. Le caratteristiche petrografiche delle MI, la loro composizione chimica e il loro fabric interno, dovuto alla presenza di fasi cristallizzate, sono state caratterizzate attraverso l`uso del microscopio ottico e di quello elettronico a scansione con emissione di campo (FESEM), l`acquisizione di mappe elementari ai raggi X e le analisi alla microsonda elettronica (EMP) e in spettroscopia Micro-Raman.

I granati peritettici contengono aggregati irregolari costituiti da centinaia di MI, le quali vanno da totalmente cristallizzate (*nanograniti*) a vetrose, spesso con forme a cristallo negativo. I nanograniti presentano dimensioni tra 5 e 25 μm, e contengono un aggregato criptocristallino di Bt+Kfs+Pl+Qtz±Ap, oltre a fasi accessorie (apatite, zircone, rutilo, spinello e occasionalmente ilmenite) che molto probabilmente hanno favorito l`intrappolamento di porzioni di fuso durante la crescita del granato e la conseguente formazione di inclusioni. La grana delle fasi cristalline nei nanograniti è variabile, da pochi nanometri fino ad alcuni micron. Le inclusioni parzialmente cristallizzate contengono un fuso differenziato, che può occupare il 20-60% dell`area dell`inclusione, coesistente con quarzo, K-feldspato e biotite. Le inclusioni vetrose hanno solitamente dimensioni inferiori, 2.5–17.5 μm, a quelle dei nanograniti e costituiscono circa il 15 % delle inclusioni di ogni ammasso. Al loro interno è presente una fase vetrosa, solitamente coesistente con le stesse fasi accidentali riconosciute nei nanograniti. Dati microchimici sul vetro mostrano una composizione riolitica ultrapotassica, con K_2O >> Na_2O. Il contenuto di acqua stimato dalla differenza da 100 wt% dei totali delle analisi EMP è inferiore a 3 wt%. La presenza di inclusioni vetrose preservate in questo contesto è una scoperta senza precedenti. Il diametro medio delle inclusioni vetrose (8 μm) è inferiore a quello dei nanograniti (13 μm), e si propone che tale differenza di dimensioni abbia influito sulla cristallizzazione delle porzioni di fuso intrappolato, inibendo la nucleazione delle fasi cristalline nella maggior parte delle inclusioni più piccole.

I nanograniti sono stati rifusi attraverso l`uso di un tavolino riscaldante ad atmosfera controllata, e successivamente analizzati al fine di ottenere dati sulle loro composizioni totali. Le analisi in microsonda elettronica mostrano in tutte le inclusioni rifuse una composizione molto simile a quella delle inclusioni vetrose preservate. Avendo un chimismo povero in Na, nel diagramma Q-Ab-Or per il sistema aplogranitico questo fuso si trova molto lontano dalla composizione del “minimum melt”, comunemente accettata come rappresentativa di un fuso anatettico prodotto dalla fusione parziale di metapeliti. Tale composizione, sebbene non sia comune, è segnalata in letteratura per magmi riolitici e per prodotti sperimentali, e suggerisce che la fusione parziale di sia avvenuta a temperature superiori a 850°C, in accordo con le condizioni di anatessi proposte per queste rocce. Questi dati mostrano che assumere una composizione da “minimum melt” come rappresentativa non sia corretto nel presente caso di studio, e che non dovrebbe essere considerata quindi una regola generale. La coerenza dei dati microchimici ottenuti e l`attento studio microstrutturale dei campioni, unito all’uso delle opportune tecniche di rifusione, di microanalisi e di correzione dei dati, supportano l`interpretazione delle composizioni ottenute come rappresentative della fase intrappolata nelle inclusioni, e la conclusione che le MI nei granati delle khondaliti contengano porzioni di fuso anatettico. Questo risultato originale costituisce quindi un importante contributo alla conoscenza di fusi anatettici in rocce naturali.

Nella seconda parte del progetto di ricerca sono stati studiati gli inclusi granulitici di El Hoyazo. Queste metapeliti, parzialmente fuse, sono state rimosse dalla bassa crosta mentre l`anatessi stava avendo luogo, e contengono abbondante vetro riolitico in livelli e sacche, oltre che in inclusioni vetrose in quasi tutti i minerali della paragenesi. Diversamente dalle rocce sottoposte a metamorfismo regionale e raffreddate lentamente, in questo caso i caratteri microstrutturali dovuti alla fusione parziale sono stati “congelati” dalla rapida risalita dei campioni in un magma in eruzione. Il granato che contiene inclusioni vetrose è stato la prima fase solida prodotta dalla fusione parziale a ~700°C e 5-7 kbar, e, oltre alle MI, contiene numerose inclusioni fluide (FI) intrappolate in condizioni di immiscibilità fuso-fluido e che non presentano evidenze di modificazioni successive alla loro formazione. Lo studio delle FI nei granati degli inclusi a Spl-Crd e a Bt-Grt-Sil è stato condotto attraverso la loro caratterizzazione petrografica, studi microtermometrici, analisi in spettroscopia Micro-Raman, calcoli di bilanci di massa e studi al microscopio elettronico a trasmissione (TEM). Negli inclusi a Spl-Crd le FI sono bifasiche (L+V), da sferiche a tubulari, e spesso contengono grafite come fase intrappolata. Il fluido contenuto nelle inclusioni è una miscela di $H_2O+CO_2+N_2\pm H_2S\pm CH_4$, con abbondante H_2O, fino a 95 mol%. Negli inclusi a Bt-Grt-

Sil, le inclusioni fluide nel granato sono monofasiche e contengono una miscela gassosa a CO_2+N_2. In entrambi i campioni le inclusioni fluide presentano densità in disaccordo con le proposte condizioni di intrappolamento, e suggeriscono che, nonostante il loro aspetto primario preservato, esse si siano riequilibrate durante la risalita. Lo studio al TEM dei granati negli inclusi a Bt-Grt-Sil ha mostrato, alla scala sub micrometrica, la presenza di fratture parzialmente rinsaldate, interpretabili come possibili vie di fuoriuscita di componenti dalle inclusioni fluide. Negli inclusi a Spl-Crd, i dati raccolti sulle biotiti e le inclusioni vetrose, entrambi coesistenti con le inclusioni fluide, dimostrano che un fuso leucogranitico e una fase COH, entrambi ricchi in acqua, sono stati intrappolati a condizioni di temperatura in accordo con quelle proposte per la formazione del granato (c. 700°C). Negli inclusi a Bt-Grt-Sil, invece, la quasi totale decrepitazione delle inclusioni fluide e la conseguente perdita di componenti non hanno permesso la caratterizzazione della composizione originale del fluido intrappolato nel granato. Tuttavia, sulla base dei contenuti in acqua delle inclusioni vetrose coesistenti, si ipotizza che il fluido fosse in origine più ricco in CO_2 di quello presente negli inclusi a Spl-Crd. Il presente studio fornisce ulteriori dati sulla caratterizzazione della fusione parziale di metapeliti nella bassa crosta. Infatti, sebbene i risultati mostrino che gli inclusi hanno perso parte dei componenti originali, la composizione del fluido negli inclusi a Spl-Crd molto probabilmente è simile a quella primaria, in accordo con la composizione del fuso coesistente

Lo studio di inclusioni fluide e di fuso silicatico in minerali peritettici rappresenta un nuovo tipo di approccio al problema della fusione parziale in rocce naturali, e questa tesi dimostra che è possibile ottenere risultati validi e rappresentativi, sia dal punto di vista petrologico che geochimico, attraverso lo studio di campioni come i nanograniti, con dimensioni micrometriche o inferiori. Il set di dati ottenuto in questo studio amplia gli orizzonti dello studio petrologico della crosta, in quanto per la prima volta la composizione dei fusi crostali può essere analizzata invece che ipotizzata. Lo studio delle MI nelle migmatiti rappresenta inoltre un campo di studio con grandi potenziali di sviluppo, come è stato recentemente confermato dall`individuazione di ulteriori esempi di nanograniti intrappolati in minerali peritettici di differenti basamenti migmatitici. Per quanto riguarda il fluido coesistente col fuso anatettico, l`eccezionale presenza di MI e FI nei granati di El Hoyazo ha permesso l`identificazione e la caratterizzazione del fluido ricco in acqua che era presente in queste metapeliti all`inizio dell`anatessi.

Contents

Chapter 1
Characterizing the anatectic melt in the metapelitic system

1.1) Introduction

The term “anatexis” (from greek roots, ανα- and τηκειν, *“to melt down again”*), or partial melting, is referred to the process through which a sedimentary, igneous or metamorphic rock undergoes melting. The result of partial melting is a two-phase, solid + melt, system formed by a remnant (called *residuum;* Sawyer, 2008) and a melt (Clemens, 1990, 2006; Vielzeuf et al., 1990). The less dense and less viscous melt can be easily separated from the solid residue under deformation and for differential buoyancy effects (Brown, 2007). This process causes the geochemical differentiation of the continental crust (Brown and Rushmer, 2006) when the segregation process reaches a length scale comparable with the crustal thickness, with the emplacement of granitoid magmas in the upper crust (e.g. late orogenic granites emplaced in the Alpine orogenic belt). The comprehension of the partial melting, and related processes, e.g. mechanisms of melt segregation and emplacement in the upper crust, is a fundamental step to understand how the crust behaves on deformation and evolves in the geological time (Brown and Rushmer, 2006). Both the rheology of the crust and its geodynamical behavior are strongly influenced by the presence of melt in different geological settings, because the presence of weaker melt-rich layers deeply affects the partitioning and the accommodation of strain during the tectonic evolution of orogenic belts and plateaus (e.g., Vanderhaeghe, 2001). Partial melting generates *migmatites*, characterized by the coexistence of the residuum of the partial melting (called *melanosome*) and crystallized melt (called *leucosome*). Melt extraction may be highly variable extent reached by the, from none (in this case migmatites are called *diatexite*) to important (*metatexite*) (Sawyer, 2008). Granulites are often associated to migmatites and represent in this case the residuum of rocks that have undergone a complete melt extraction at particularly high T (e.g. Fyfe, 1973; Sawyer, 1996; Brown, 2007). The present work is focused on the characterization of partial melting in a metapelitic system. Metapelites and metagraywackes, common in the middle crust, are very fertile (melt-producing) lithologies, and are responsible for the production of S-type granitoid magmas (White and Chapell, 1983) with calc-alkaline and peraluminous characters, typically found in collisional settings (see Pitcher, 1993).

1.2) Classic approaches to the characterization of the anatectic melt

A quantitative study of the natural melting in migmatite leucosomes has a fundamental obstacle in the unconstrained composition of the melt. Although the leucosome composition is quite simple and mainly consists of quartz, K-feldspar and plagioclase, modifications of the rock microstructures and phase assemblage of migmatites commonly occur during the retrograde path, and make a difficult task the identification and the estimation of the melt composition based on the crystallized products. Generally, the most common processes that may change the original leucosomes chemistry are cumulus phenomena, fractional crystallization, and presence of xenocrysts (Sawyer, 1996, 2008; Marchildon and Brown, 2001), while often the microstructures that witness the presence of melt are wiped out by the extensive recrystallization that commonly occurs in high grade rocks during their retrograde path. For the reasons listed above, the experimental approach became in the last decades a well established tool to investigate the partial melting of metapelitic protoliths (e.g., Thompson 1982; Vielzeuf & Holloway 1988; Carrington & Harley 1995; Gardien et al. 1995; Stevens et al. 1997; Patino Douce & Harris 1998). This approach is based on the heating at controlled P-T-X conditions of both natural and synthetic samples, commonly characterized by a simplified composition chosen as representative of the rocks that form the medium-deep crust. The aim of the experimental studies is reproducing the typical reactions that commonly occur in metapelites and metagraywackes during partial melting, mainly the dehydration melting of muscovite and biotite, both abundant in these rocks, and characterizing the reaction products. Experimental results showed that the melt produced by partial melting of these rocks has always a peraluminous and granitic composition similar to those produced by melting in the haplogranite system Q-Or-Ab (Tuttle and Bowen, 1958). Although these experiments refer to subaluminous and metaluminous melts, this similarity allowed to describe in a more precise way the anatectic melt composition and its evolution at supersolidus conditions as well as the behavior of the coexisting fluid, based on the large amount of available experimental data (see Johannes and Holtz, 1996 and references therein). This approach, although extremely important and powerful, suffers from two main problems: (1) since the starting material has a relatively simple composition, it may not be a valid analogue for the crust; (2) the used time scale is necessarily much shorter than the geologic time scale, and the size of experimental charges extremely small and these makes doubtful whether the equilibrium conditions were attained during the experimental runs.

Melt compositions retrieved by the experimental approach, along with the advent of new internally consistent thermodynamic databases (Holland and Powell, 1998) allowed the applicability of the petrogenetic modeling to migmatites (e.g. White, 2008). This approach permits to predict the behavior of anatectic rocks with changing P-T-X conditions, and to estimate the amount of melt produced by partial melting, also in rocks that underwent complete melt extraction (e.g. granulites).

The presence of H_2O in metasedimentary rocks is fundamental to understand the partial melting of this system, i.e. *fluid-present* versus *fluid-absent* (dehydration) melting. Since metapelites and metasedimentary granulites often contain graphite (see Cesare et al., 2005 and references therein), a complex fluid in the COH system, rather than pure H_2O, is expected to be present during anatexis, as product of the interaction between graphite and the H_2O released by devolatilization reactions, e.g. breakdown of phyllosilicatic minerals, on the prograde path of the rock (e.g. Cesare and Maineri, 1999; Pattison, 2006). The presence of graphite constrains the coexistent fluid phase on the graphite saturation curve of the COH diagram (Connolly and Cesare, 1993; Cesare, 1995) and therefore lowers the water activity. This lead to a shift of the solidus curves toward higher temperatures, as also showed by experimental studies on granitic melts (Johannes and Holtz, 1996). Since no systematic studies (field-based, theoretical or experimental) have been published on the melting of graphitic protoliths, the study of the COH phase in these rocks would allow the characterization of volatiles that may play an important role in the petrogenetic processes that involves partial melting of metasedimentary rocks.

1.3) Melt and fluid inclusion study in migmatites: a new approach

A novel small-scale approach to the geochemical characterization of anatectic melts was recently made possible by the detailed study of partially melted metapelitic enclaves in the Neogene Volcanic Province (NVP) in southern Spain. These enclaves represent a unique case in which magma eruption rapidly brought these “migmatites-in-progress” to the surface, freezing the residual melanosomes and allowing the preservation of many of the features they had at depth. This occurrence permits to verify many of the current ideas on the mechanisms of partial melting derived by the petrological characterization of classic migmatites, where the slow cooling have reset many of the features that formed on anatexis.

In these samples a melt (Acosta-Vigil et al., 2007,2010; Cesare et al., 2007) is preserved as an amorphous phase (glass) in intergranular layers, in microfractures

(white arrows, Fig.1) and in melt inclusions (MI; red arrows, Fig.2) in several host minerals, in particular garnet. Microstructural and compositional characterization (Acosta-Vigil et al., 2007, Cesare et al., 2007), along with trace element studies (Acosta-Vigil et al., 2010), support the hypothesis that glass within MI is the anatectic melt produced during peritectic reactions at $T > 700$ °C, preserved by rapid cooling.

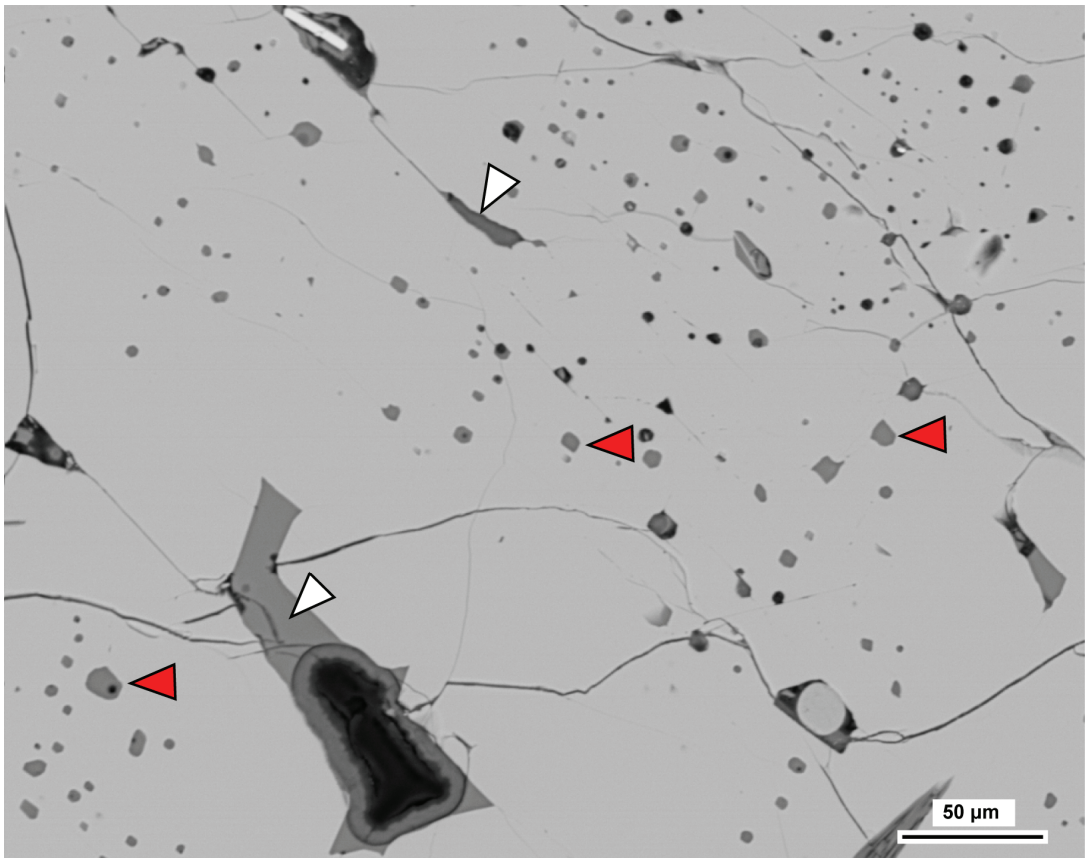

Figure 1: *melt enclosed in peritectic garnet from NVP enclaves, BSE image (courtesy of A. Acosta-Vigil).*

Although these enclaves represent a peculiar case, they suggest that (former) melt inclusions might be present also in more classic high-temperature settings where they must have undergone crystallization (or devetrification) to some extent because of the slow cooling (Cesare, 2008). When looking for melt inclusions in regional migmatites, the target host minerals should be the peritectic phases (i.e. garnet, orthopyroxene, and spinel) that grow during the melting reaction and have, therefore, the potential to trap droplets of melt.

In literature the occurrence of MI in regionally metamorphosed and melted migmatites and granulites has been reported only in few case studies: 1) small (≤10 µm across) silicate inclusions were found in quartz and plagioclase from migmatitic

leucosomes in high grade terrains by Tomilenko and Chupin (1983) (see also Touret and Olsen, 1985); these inclusions are reported to contain an unknown silicate phase along with crystals and often a shrinkage bubble. Since they occur in phases crystallized from the leucosome, they are likely to contain an evolved anatectic melt, already differentiated via crystal fractionation and therefore not anymore representative of the melt produced by partial melting; 2) crystallized MI in garnet were briefly reported by Hartel et al., (1990) in felsic migmatites from the western central Sulawesi, Indonesia. Devitrified MI are 2-10 μm across, with dodecahedral shape and a roughly granitic composition, from microchemical data obtained by using a defocalized analytical beam and subtracting the estimated host contribution. These inclusions were inferred to represent the melt produced by biotite dehydration melting.

The possibility of finding workable MI of anatectic melt in classic high grade rocks received a first confirmation by the reported occurrence of melt inclusions in peritectic garnets from the granulite-migmatites terrain of the Proterozoic Kerala Khondalite Belt (KKB, India) (Cesare, 2008; Cesare et al., 2009; present study), extensively investigated and considered as representatives of a regional anatectic crustal terrain. These rocks underwent ultra-high temperature metamorphism and partial melting during the Pan-African orogeny, with the development of migmatites characterized by Qtz-feldspars leucosomes and Grt-Crd-Sil-Bt-bearing melanosomes (*khondalites*). Further findings of anatectic melt as MI in peritectic minerals have been reported more recently in an increasing number of migmatites from different settings, e.g. low-pressure migmatites (i.e., Ronda migmatites; Cesare et al., 2009b) and ultrahigh-pressure migmatites (i.e., Ulten Zone; Braga and Massonne, 2008).

The MI study is a long lasting and widely accepted technique in the study of magmatic rocks, both volcanic and plutonic (Bodnar and Student, 2006). The first detailed discussion on MI in a rigorous geological and petrological context was published by Sorby (1858), who observed both glassy and crystallized MI and drew illustrative sketches of inclusions in plutonic environments (Fig.2) some of those strongly resemble crystallized MI in migmatites. Over the past few decades, the study of MI has matured and has become a fundamental tool to investigate the composition and evolution of melts (Bodnar and Student, 2006 and references therein), their volatile content (Lowenstern, 1995; 2003) and the composition of the coexistent vapour in volcanic systems. With the finding of MI in high-grade metamorphic rocks, the partial melting may be now characterized by using the technique of the MI study, and this represent a revolutionary approach to the investigation of natural high-grade rocks.

As discussed in section 1.2, a COH fluid phase is common in a graphite-bearing protolith during partial melting. Fluid inclusions (FI) containing CO_2-rich fluid with variable amounts of CH_4, N_2, H_2 are commonly reported in high grade rocks, while H_2O may be locally present along with CO_2 (Touret, 2009 and references therein). This is consistent with the low solubility of CO_2 with respect to H_2O in silicate melts, demonstrated by experimental studies (Holloway, 1976; Tamic et al., 2001). However, in available FI studies the genetic relationships between partial melting and trapped fluids are not clearly demonstrated on microstructural basis (e.g. by the occurrence of MI in the same mineral, see Roedder, 1984), but very often it is inferred.

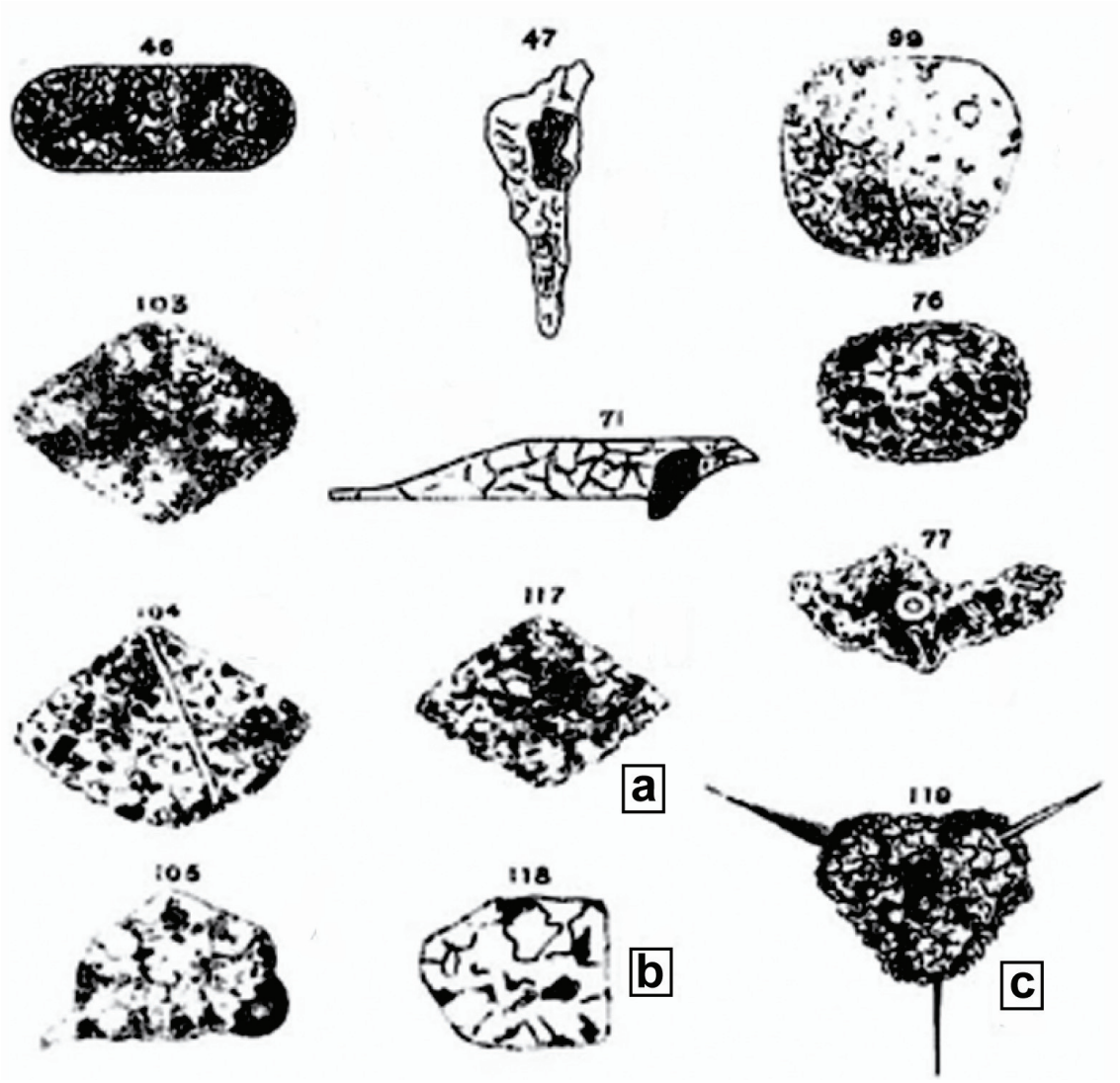

Figure 2: *Sketches of crystallized melt inclusions from Sorby (1858). The number above each drawing refers to the figure number in the original publication. Sorby did not report any scale and the magnification of the inclusions in linear dimensions is reported for MI of interest in parentheses, along with the estimated real size. a) MI in quartz from the granite at St. Austell, UK (X1000, ~200 µm); b) MI in quartz from a coarse-grained granite near Cape Cornwall, UK (X800, ~175 µm); c) MI in quartz from the granite at St. Austell, UK, with radiating fractures (X600, ~300 µm). Modified after Bodnar and Student, (2006).*

In the case of the El Hoyazo enclaves, MI coexist with FI, both considered primary based on their microstructural features (Roedder, 1984). This occurrence is reported in different minerals such as cordierite and plagioclase (Cesare et al., 2007) and garnet (present work). In cordierite and plagioclase FI contain a COH fluid phase that has been interpreted as trapped along with anatectic melt in conditions of fluid-melt immiscibility.

Moreover, the limited effect of cooling on samples allows the study of FI that in classic high-grade rocks are likely to be destroyed or changed by re-crystallization (and deformation, where occurred) during the retrograde PT evolution. The presence of constraints on the FI coexistence with anatectic melt suggest that the characterization of these FI will give valuable data on the composition of the fluid phase present during the partial melting of a metapelitic protolith.

1.4) Aim of the study

The present study investigates the melt-fluid relationships during anatexis of metapelitic protoliths, by performing a melt and fluid inclusion study on samples from two different geological settings. The presence of anatectic melt during the entrapment of the studied inclusions has been verified by a detailed petrographic study of the inclusion-bearing samples.

The occurrence of crystallized MI in peritectic garnets from garnet-cordierite-sillimanite granulites (khondalites) from KKB, southern India, is the first finding of MI in classic metapelitic migmatites. A detailed study was carried out on MI petrographic features, on the composition of the crystallized phases within the inclusions and on their internal structures, to verify 1) that they were trapped during the host growth at partial melting conditions, i.e. they are primary MI, and 2) that they did not undergo chemical changes due to the slow cooling. Re-heating experiments were then performed on selected samples, to retrieve as best as possible the composition of the homogenized glass, assumed to represent the anatectic melt originally trapped.

The occurrence of FI along with MI within the partially melted metapelitic enclaves from El Hoyazo, southern Spain, allowed the characterization of the fluid present in these rocks during partial melting. A detailed microstructural study at μm- and sub μm-scale was performed on FI and of their host mineral to verify their primary features and possible modifications occurred after entrapment. The fluid phase was characterized by using microthermometric means combined with Raman analyses and a mass balance calculation approach, to constrain both the density and the fluid composition. Biotite

crystals and MI, trapped along with FI, were also characterized by the microchemical point of view, integrating the existent compositional datasets with new data.

Because the two case studies considered in this thesis have fairly similar PT conditions of formation and bulk composition, they allow to compare anatectic melts produced by the partial melting of metapelitic enclaves as they occurred at depth, frozen by the almost instantaneous cooling, with anatectic melts in more classic migmatites, that experienced a slow cooling typical of high-grade metamorphic rocks.

Chapter 2

Primary Melt and Fluid Inclusions in Migmatites from the Kerala Khondalite Belt

2.1) Introduction

The present chapter discusses the occurrence of MI in garnet from the migmatites of the Kerala Khondalite Belt (KKB), Southern India and also the FI that occur in the same rocks. The occurrence of inclusions of melt in peritectic minerals is reported for granulitic enclaves from the Neogene Volcanic Province, in southern Spain (Cesare, 2008a and references therein; Acosta-Vigil et al., 2010). There, the trapped melt is rhyolitic and peraluminous (Acosta-Vigil et al., 2007) and is interpreted as the melt produced by partial melting of metapelitic rocks. The Spanish enclaves represent a world unique case study; however they support the idea that peritectic minerals may trap droplets of anatectic melt during their growth also in “common”, slowly cooled migmatitic terrains, as discussed by Cesare (2008a,2009a).

In the present work classic techniques such as petrographic, microchemical, microthermometric studies were used to characterize the host rocks, while MI characterization was done, because of their small size, by using Laser and electron-beam microanalytical techniques and by performing re-heating experiments. The obtained dataset of compositional and microstructural information, integrated with data from previously published paper (Cesare et al., 2009a) and communications (Ferrero et al., 2009a,b), is reported and discussed to support the conclusion that khondalites represent the first reported case where preserved portions of anatectic melt trapped in MI are found, as proposed by Cesare et al. (2009a).

2.2) Geological setting of the Kerala Khondalite Belt

The KKB, also called “Trivandrum Block” (renamed after Geological Survey of India, 1995), belongs to the Precambrian high grade granulite terrain of southern India (Chacko et al., 1987; Santosh et al., 1996) that exposes a deep crustal section of partially melted metasedimentary rocks. This terrain is divided in four main blocks (Fig.1a), Nilgiri Block, Madras Block, Madurai Block and Trivandrum Block (Harris et al, 1994), by late proterozoic shear zones (Drury, 1984). The first two blocks are orthogneiss-dominated terrains, with a granulitic metamorphism at around 2.5 Ga (Peucat et al., 1989). The

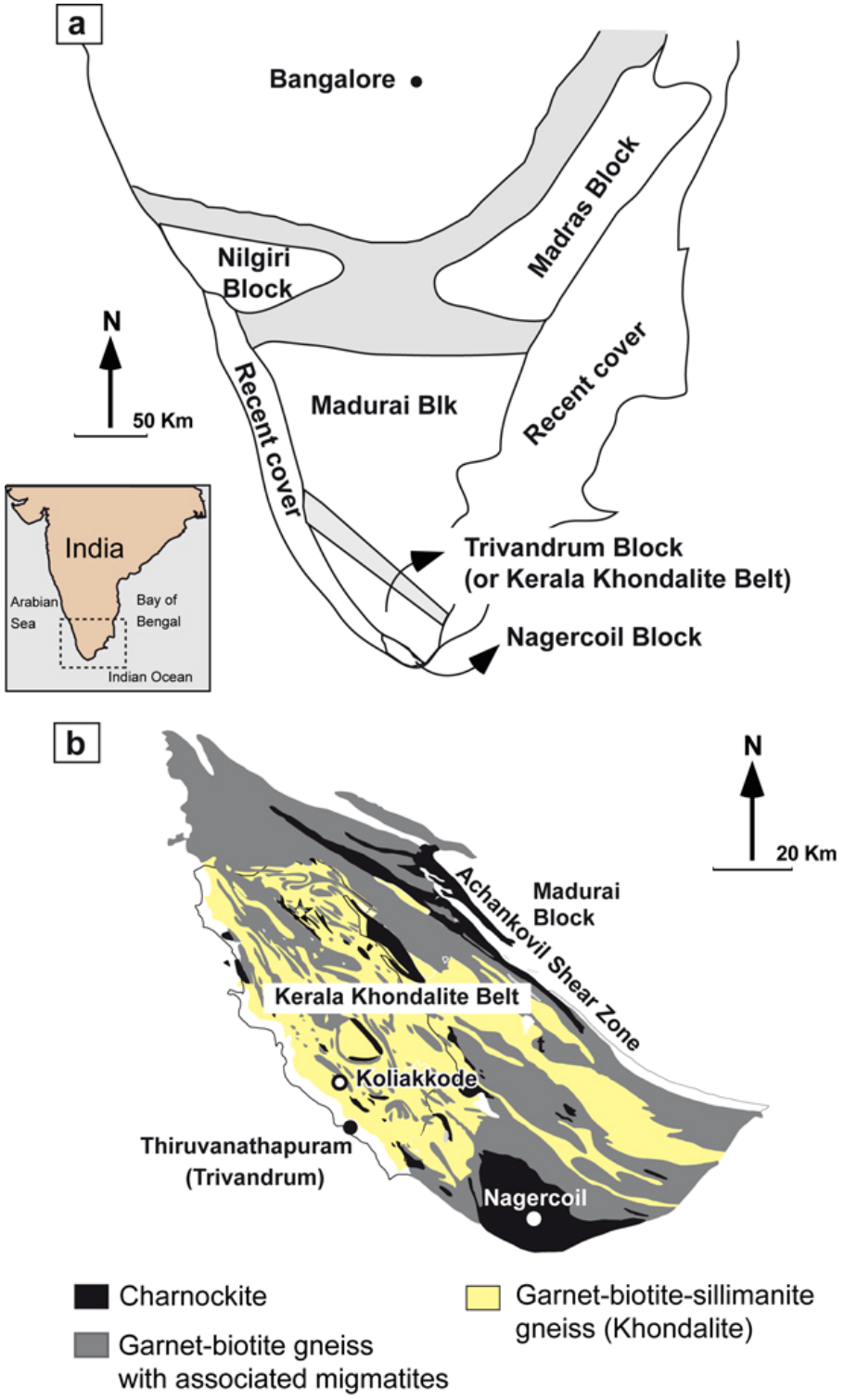

Figure 1: *a) Geologic outline of southern India, with reported the four main blocks (redrawn after Bindu, 1997); b) Detailed sketch of the Kerala Khondalite Belt with main lithologies (redrawn after Shabeer et al, 2005).*

Madurai and Trivandrum Blocks are metasedimentary terrains, characterized by high-grade metamorphism during the Pan-African orogeny (600-540 Ma), that led to the amalgamation of the Gondwana supercontinent. Both blocks are believed to have been part of the Mozambique Belt, along with Madagascar and Sri Lanka (Collins and Wandley, 2002).

The Trivandrum Block is the southernmost unit and is divided from the Madurai Block by the Achankovil shear zone (ACSZ). It comprises ACSZ, the KKB *s.s* and the small Nagercoil Block, that bounds the KKB toward south (Fig.1b). The ACSZ consists of a metasedimentary sequence of cordierite-bearing metapelites, calc-silicate rocks and marbles, bounded by two NW-SE trending strike slip shear zones, while the Nagercoil block is formed by massive charnockites of igneous origin (Santosh, 1996). The KKB has strongly supracrustal features and consists of garnet and orthopyroxene-bearing charnockites, migmatized garnet-biotite-graphite bearing gneisses (leptynites) and the most widespread garnet-sillimanite-graphite gneisses (khondalites), along with minor amounts of charnockites, mafic granulites, calc-silicate rocks and cordierite gneisses. The metapelitic rocks often show migmatization phenomena (Chacko et al, 1992; Braun et al., 1996; Shabeer et al., 2004). Khondalites and leptynites, both of sedimentary origin, mainly occur in the central part, whereas charnockites are more abundant going toward the northern and southern margins of KKB (Shabeer, 2004). The Nagercoil Block is mainly formed by massive charnockites, with less abundant metapelitic rocks (Shabeer, 2004 and references therein).

Several studies on the PT conditions of migmatization of the KKB rocks have been published, but their metamorphic history still needs to be better defined. Until the early nineties of the last century, the proposed PT peak conditions for charnockites and khondalites were moderate temperature and pressure, 600-750°C and 4-5 kbar (Srintakappa et al., 1985; Chacko et al., 1987; Hansen et al., 1987). More recent studies found out evidence of an ultra high temperature (UHT) metamorphism, with evidence of a fluid-absent dehydration melting of biotite (Braun et al., 1996, Cenki et al., 2002), at temperatures in excess of 900°C, obtained from integrated ternary feldspar composition (Braun et al., 1996). Temperatures >900°C were confirmed by Chacko et al. (1996), Harley and Santosh (1995), Satish Kumar et al. (1996) and Nandakumar and Harley (2000) on different lithologies (charnockites, cordierite gneisses, calc-silicate rocks), mainly along the KKB boundaries with the Madurai Block, while in the central part reported

peak T are lower, ~850°C. Evidence of UHT metamorphism in the central area is reported by Shabeer et al. (2002) and by Tadokoro et al. (2008), with peak conditions respectively around 900°C±30°C and 900-1000°C. Regarding the pressure at which partial melting took place, many different values have been proposed, from 5 kbar (Nandakumar and Harley, 2000) to 12 kbar for the central eastern part of the KKB (Tadokoro et al., 2008). The most accepted P range is 6-8 kbar (Cenki et al., 2002). Referring to the post peak trajectory, Nandakumar and Harley (2000), proposed a retrograde trajectory first characterized by a cooling with limited decompression, followed by the near-isothermal decompression, from 8-6.5 kbar to 5.5-3 kbar at ~800°C, recognized by several authors (Santosh, 1986; Chacko et al., 1987).

Reported ages for UHT metamorphism and partial melting in the KKB are 590-550 Ma by U-Pb monazite dating (Cenki et al. 2004) and 530 Ma by SHRIMP U-Pb zircon dating (Shabeer et al. 2005), while cooling below c. 400-500 °C took place at 490-470 Ma (Rb-Sr dating of biotite, Cenki et al. 2004). These rocks are therefore characterized by very slow cooling rates of <10 °C/m.y.

Metamorphic conditions of studied samples

The studied samples are from the central-western part of the KKB. Nandakumar and Harley (2000) and Braun et al. (1996) suggest a peak T of 830-900ºC for this region, based on core composition of garnet and cordierite and integrated ternary feldspar composition, while pressure is less constrained (4.5-6 kbar). Such values are agreement with those from Chacko et al. (1996) proposed for the central part of the terrain, although no evidence of the highest proposed values (970ºC) were retrieved. Preliminary data on restites from Koliakkode quarry (from where the study samples were collected), based on thermodynamic modelling of a pseudosection calculated in the NCKFMASHTO system, give 820ºC and 5 kbar (L. Tajcmanova, pers.comm) as equilibration conditions for the Grt-Crd-Sil-Bt-Spl-Ilm assemblage, with good correspondence with Nandakumar and Harley (2000) and Braun et al. (1996). The presence of inclusions of rutile in garnet, however, suggests that this phase may have crystallized at higher pressure values than those calculated. Tadokoro et al. (2008) suggests UHT and HP (10 kbar) peak conditions: since our samples were collected about 20 km far westward from the end of the studied traverse, the high P value proposed by Tadokoro et al. (2008) may not apply to the present case. Bindu (1997) investigated samples from a locality also called Koliakkode, close to our sample quarry, but focusing on the post anatexis, decompressional history.

2.3) Samples and methods

2.3.1) Characterization of host rock and melt inclusions

Approximately 50 thin sections and doubly polished thick sections were used to characterize the host rocks, MI and FI in the khondalites from Koliakkode quarry. Sample preparation and petrographic study were carried out at Department of Geosciences, University of Padova – Italy. MI-bearing samples were prepared via a physico-chemical process of polishing, based on colloidal silica (SITON).

The composition of minerals of interest in the host rocks (tables 1-5) was determined by using an EMP (Electron MicroProbe) Cameca SX50 of C.N.R.-I.G.G. (Consiglio Nazionale delle Ricerche-Istituto di Geoscienze e Georisorse), at the Department of Geosciences, University of Padova-Italy. Measurements were performed using 20 kV accelerating voltage, 20 nA beam current and 2 μm as probe diameter on garnet, spinel and cordierite and in raster mode (window 8x5 μm) on feldspar, plagioclase and biotite. Profiles on garnet were acquired at the Department of Geosciences, Virginia Tech, Blacksburg-Virginia (USA) with an electron microprobe Cameca SX50, using 15 kV accelerating voltage, 20 nA beam current and 5 μm as probe diameter.

The characterization of the phase assemblage and microstructures in MI has been carried out on about 100 MI, by using different techniques besides optical investigation. Crystallized minerals and chemistry of the components were investigated by SE (Secondary Electrons) and BSE (Back-scattered Secondary Electrons) imaging, semi-quantitative EDS (Energy Dispersive X-ray Spectroscopy) analyses and X-ray mapping. Data were collected with two different FEG (Field Emission Gun) electron microscopes:

1) a Jeol JSM-6500F thermal FESEM (Field Emission Scanning Electron Microscope), available at the High Temperature/High Pressure Laboratory, I.N.G.V. (Istituto Nazionale Geofisica e Vulcanologia), Rome;

2) a FEI Quanta 600 FEG, equipped with a Bruker EDX with a Silicon Drifted Detector, available at the Nanoscale Characterization and Fabrication Laboratory, I.C.T.A.S. (Institute for Critical Technology and Applied Science), Virginia Tech, USA.

BSE images were normally acquired at 10kV accelerating voltage, except for few cases in which accelerating voltage was raised to 20kV. X-ray maps of Si, Al, Na, K, Ca, Ti, Fe, Mg, Cl, P, Zn were acquired at 20kV accelerating voltage and at variable magnifications, in the range 5000-6000X, depending on the MI size, with resolution 500X375 pixel.

EMP analyses on minerals and glasses within MI were performed where possible, e.g. in the largest phases, using a Jeol JXA 8200 Superprobe of the High Temperature/High Pressure Laboratory, I.N.G.V., Rome, and a Cameca SX50 of C.N.R.-I.G.G., Padova. Analytical parameters (accelerating voltage, probe current, probe diameter and counting times) were changed depending on the used instrument and object size. The key factor is represented by the tiny size of the MI, close to the limits of the analytical resolutions. Analytical parameters were therefore set to obtain a good compromise between the needs to have a small beam excitation volume, to avoid host mineral contributions to the collected signal, and the need to use an accelerating voltage high enough to collect a statistically representative counting for each analyzed element.

Biotite (table 6) and glass (table 7) compositions within inclusions were determined at the INGV-Rome, using 15 kV accelerating voltage, 8 nA beam current and probe diameter 0.5μm.

For glass compositions reported in table 8, variable analytical parameters were used. Analyses (1) and (6,7) were collected at the I.N.G.V.- Rome, using 15 kV accelerating voltage, 8 nA beam current and 0.5 μm probe diameter for point (1), and 15 kV accelerating voltage, 3.5 nA beam current and 0.5 μm probe diameter for point (6) and (7); in both cases Na, Si, K, Ca and Al were analyzed as first elements, with counting times of 10 s on peak and 5 on background and a ZAF data correction. Analyses (2) to (5) were collected at C.N.R.-I.G.G.- Padova, using 20 kV accelerating voltage, 7 nA beam current; Na, Si, K and Ca were analyzed as first elements to eliminate the influence of alkali loss on the counting statistics on the two most abundant elements (Si, Al), using counting times 8 s on peak, 4 s on background for Na, and 10 s on peak and 5 on background for other elements, applying a PAP data correction.

The Na migration out of the beam excitation volume during EMP analyses on silicate glasses is a well known and studied phenomenon (Morgan and London, 2005 and references therein). This “loss” results in a overestimation of relatively immobile major elements such as Si, Al, K. The entity of Na migration depends on current density (expressed in nA/μm^2 and determined by the analytical conditions), and on the glass composition (mainly its H_2O content): if Na migration is expected based on these parameters, therefore a correction factor needs to be estimated to recalculate the collected data. Analyses recalculation consists of increasing the Na_2O content of the determined correction factor (expressed in % of loss), and decreasing SiO_2 and Al_2O_3 contents of the

calculated Na_2O increase. For data collected at C.N.R.-I.G.G.- Padova, Na_2O correction factor was estimated at the same analytical conditions of the reported glass analyses (table 8). The estimation was done by comparing Na_2O values from two different analyses performed, in the same point, on a rhyolitic glass standard (studied by Morgan and London, 2005) with similar composition to those expected in studied samples, and the Na decrease was verified to be 30% relative. Glass analyses were corrected as previously explained by adopting a conservative value of 40% relative as Na correction factor. For data collected at I.N.G.V.- Rome, the analytical conditions adopted for glass analyses in table 8 did not produce any Na migration in the rhyolitic glass standard previously described, therefore no recalculation was applied to the data.

The microthermometric (MT) study and Raman analyses were performed at the Department of Geosciences, Virginia Tech –USA. 44 fluid inclusions, recognized as primary and belonging to the same Fluid Inclusion Assemblage (FIA, Goldstein and Reynolds, 2003) were analyzed at the Fluid Inclusion Lab using a Linkam THMSG 600°C programmable heating/cooling stage, mounted on Olympus BX60 microscope. The accuracy of measurements is ±0.1°C in the range -100/+31°C. Stage calibration was done using synthetic CO_2-H_2O synthetic FI standards (Sterner and Bodnar, 1984).

Raman analyses were carried out at the Vibrational Spectroscopy Laboratory, using a Jobin Yvon Horiba HR 800 LabRAM Raman microprobe equipped with an Ancor electronically cooled charge-coupled device (CCD) detector. The excitation source is a 514.57 nm Ar-ion laser operated in confocal mode with the slit width set to 150 μm and confocal aperture set to 400 μm. The microprobe is coupled with an Olympus BX 41 petrographic microscope. The irradiation power measured on the samples was 3-4 mW. For quantitative measurements, spectra were acquired at 80X of magnification between 1000 cm^{-1} and 4200 cm^{-1}, integrating 5 cycles of 10-20 sec for each measure and using a grating of 600 g/mm. Spectral resolution was about 1.5 cm^{-1}. Qualitative Raman analyses were conducted on about 50 FI, while in 20 of them gas species proportions were also characterized.

2.3.2) Re-heating experiments and characterization of homogenized inclusions

A few tens of chips of garnet with MI clusters were separated from double-polished thick sections, selected among those previously studied.

Re-homogenization experiments were performed at the Earth Science Department-University of Parma-Italy. About 40 samples were analyzed at the Fluid Inclusion Laboratory using a LINKAM TS1500 high temperature stage, in an inert atmosphere of He to prevent sample oxidation. A T correction factor was applied, after have determined a calibration curve by using different standards of $K_2Cr_2O_7$, Ag and Au with melting T respectively of 398°C, 962°C and 1064°C. The accuracy of measurements is ±15°.

The elaboration of an appropriate heating ramp to reach MI homogenization was not straightforward. In magmatic rocks MI are commonly heated with a constant heating rate until melting, as widely reported in literature (Bodnar and Student, 2006 and references therein). In the present case such approach produced a pervasive oxidation of the host garnet at T>800°C, despite the use of a controlled atmosphere, not allowing any longer the visual control of the MI behavior on heating. Oxidation effects were also correlated with the amount of cracks in the sample and its thickness, being more pervasive in thin samples with several cracks. Another effect of rapid heating was a widespread microfracturing that interested in many cases every MI in the cluster, favoring internal modifications of the inclusion bulk composition. Several experiments have been therefore performed to define which samples preparation and which heating ramp would allow to avoid, or limit, both oxidation and microfracturating. The best results were obtained on 200 μm-thick chips relatively poor of cracks and with a heating ramp (E. Salvioli-Mariani, pers.comm) characterized by a rate of 50°C/min up to 500°C, followed by a 2 hours stop at that temperature. Afterwards, a heating rate of 40°C/min was applied until the MI, under continuous observation during the last portion of ramp, showed modifications of the internal crystal boundaries, interpreted as the beginning of melting. The sample was then kept at melting T for 15-30 min to allow a complete homogenization, and then quenched in liquid nitrogen to avoid as much as possible glass crystallization. This procedure brought to a complete homogenization of nanogranite inclusions at temperature of c. 1050°C (after correction). Higher experimental temperatures have resulted in extensive melt-host interactions with microfracturing and formation of peritectic phases. Homogenized MI were selected by microscope investigation, and brought to the surface through a hand-polishing process, using abrasive sheets coated of Al-oxide and Si-carbide with variable grain-size.

The microstructural characterization of homogenized MI was carried out on about 80 MI by using SE and BSE imaging and semi-quantitative EDS analyses. Data were collected using a Jeol JSM-6500F thermal FESEM, at I.N.G.V., Rome. BSE images were acquired

at 10kV accelerating voltage. Compositional data were then obtained by EMP, using a Jeol JXA 8200 Superprobe available at I.N.G.V., Rome. Analytical parameters were set as previously reported for crystallized phases in nanogranites and preserved glassy inclusions (section 2.3.1) at 15 kV accelerating voltage, 3.5 nA beam current and 0.5 μm probe diameter. Chosen analytical conditions allowed us to collect data using a very small excitation volume, 2 μm across, and localized very close to the surface, with maximum depth estimated 2 μm. Since the adopted analytical conditions did not produce any Na migration in the rhyolitic glass standard (see section 2.3.1) no recalculation was applied to the reported data which are considered of good quality also in terms of Na values.

2.4) Khondalites from Koliakkode quarry

The samples characterized in the present work were collected in the quarry of Koliakkode, about 15 km northward from the city of Trivandrum (coordinates N8 38' 24" E76 53' 30.5"). Rocks on the quarry front have a typical stromatic-diatexitic appearance (Fig.2a), and underwent an intensive deformation with segregation of melt to form layers and small veins of leucosome. Khondalites are coarse to medium grained, characterized by a purple to dark melanosome (labelled as “m”, Fig.2a) and a greenish leucosome (labelled as “l”, Fig.1c). On the fresh-cut surface, porphyroblasts of violet cordierite and red garnet are visible in the melanocratic portion, along with acicular sillimanite and biotite (Fig.2b). The leucosome mainly consists of light greenish K-feldspar, quartz and plagioclase in variable amounts.

2.4.1) Petrography of the samples

Under the microscope, the melanocratic portion of the rock consists of garnet porphyroblasts, ≤2 cm across, large cordierite grains, coarse-grained sillimanite, biotite, ilmenite, green spinel, small amounts of feldspar. The leucosome consists of quartz and massive feldspar porphyroblasts, up to 5 mm, characterized by a complex pattern of different perthitic exsolutions. Locally clear plagioclase is abundant. Melt inclusions always occur in garnet crystallized in the melanosomes.

Two different types of melanosome may be distinguished:

1. Biotite-poor melanosomes (Fig.3a): most of the studied samples are mainly formed by this melanosome type, in which MI-bearing garnets are surrounded by large aggregates of cordierite grains, ≤1 cm across, and show a strongly restitic

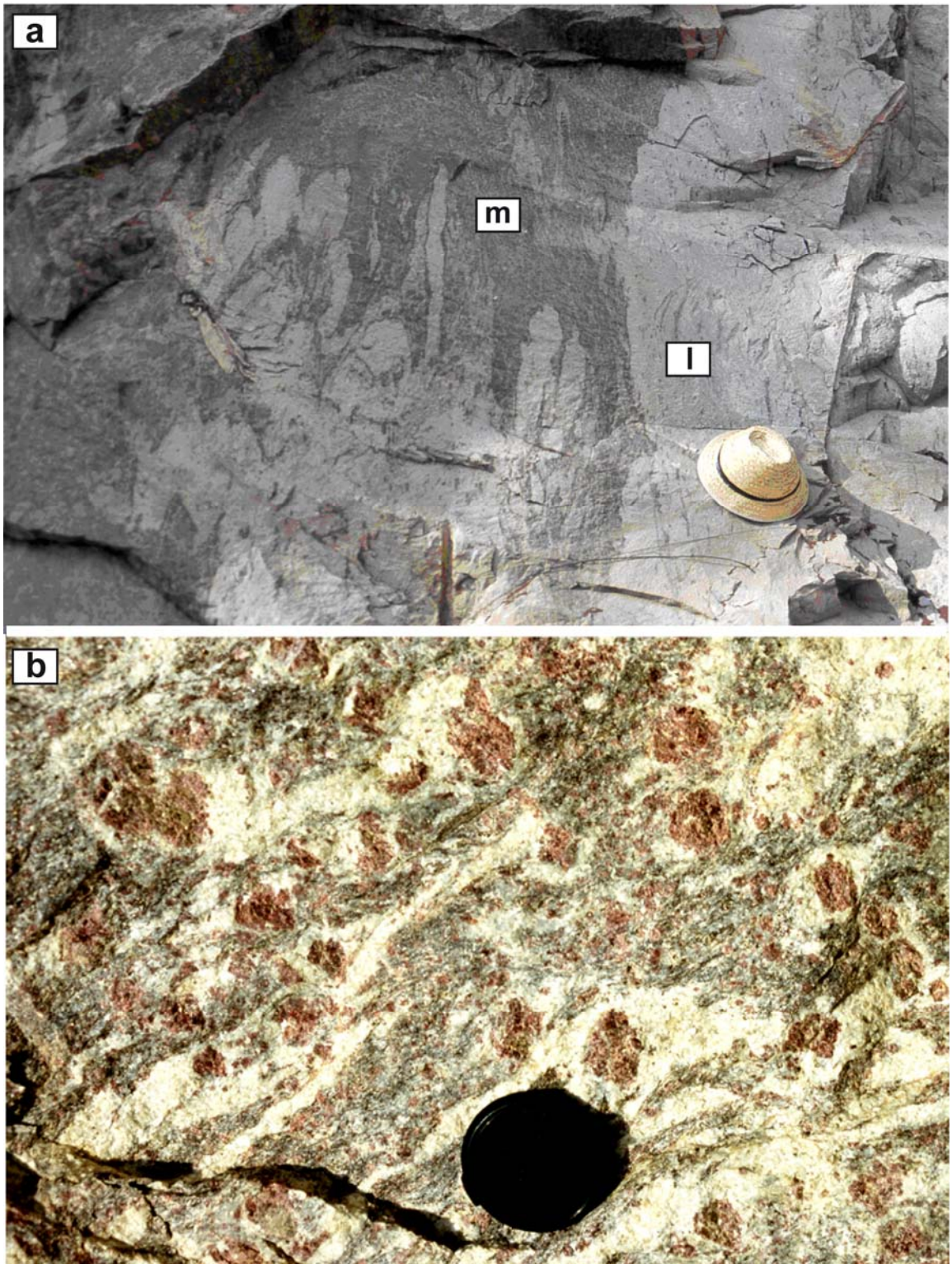

Figure 2: *a) khondalites outcropping at Koliakkode quarry; m= melanosome, l= leucosome; b) close-up of Khondalite outcrop, lens cap=6 cm.*

composition. This melanosome is always coexistent with leucosome at thin section scale;

2. Biotite-rich melanosomes (Fig.3b): MI-bearing garnets in few cases occur in a melanosome with a less restitic character (i.e. abundant biotite) and with no evidence of crystallized melt except for MI.

Bt-rich melanosome, Bt-poor melanosome and leucosome may occur in the same sample at thin section scale, in variable modal percentages (mineral abbreviation after Kretz, 1983). The occurrence of Bt-rich and Bt-poor (or free) restitic domains could reflect a non homogeneous protolith, with a more or less refractory assemblage, even at thin section scale (see also section 2.4.2). The Bt-rich melanosome shows a spaced foliation, due to isoorientation of coarse-grained sillimanite and biotite, while the Bt-poor melanosome is not internally foliated, but defines a mineralogical banding through interfingering with leucosomic domains.

Garnet commonly occur in the khondalites from Koliakkode quarry as subhedral to anhedral porphyroblasts, ≤2 cm across, in places slightly elongated along the foliation, with extremely abundant inclusions such as fibrolitic and prismatic sillimanite (the latter normally enclosed near the rim), biotite (≤0.5 mm), ilmenite (≤1 mm), plagioclase and round crystals of quartz (Fig.3c). Fibrolite and biotite are usually oriented, defining a relict schistosity, sub parallel to the rock foliation. In the studied samples however, MI-bearing garnets are remarkably different in appearance: in fact, they contain almost exclusively MI (Fig.3d), while the “normal” mineral inclusions such as biotite or ilmenite are scarce or absent (Fig.3a,c). Garnet porphyroblasts in the melanosome are usually irregular, with more or less pronounced embayments, and rich of microfractures (Fig 2a,b). In the leucosomes, garnet forms subhedral porphyroblasts, ≤5mm across, normally free of inclusions.

Cordierite may crystallize in mm-sized xenomorphic crystals, up to 3 mm depending on the sample. Large cordierite crystals show peculiar irregular polysynthetic and sector twinning, and contain in places round quartz and rare idiomorphic biotite. In Bt-rich melanosomes, cordierite forms anhedral grains interlocked with biotite, sillimanite, ilmenite and green spinel. In Bt-poor melanosomes, domains of granoblastic cordierite surround completely garnets (Fig.3a,4a), in association with green spinel, ilmenite and sillimanite. In both melanosome types cordierite overgrows garnet porphyroblasts, but it is more

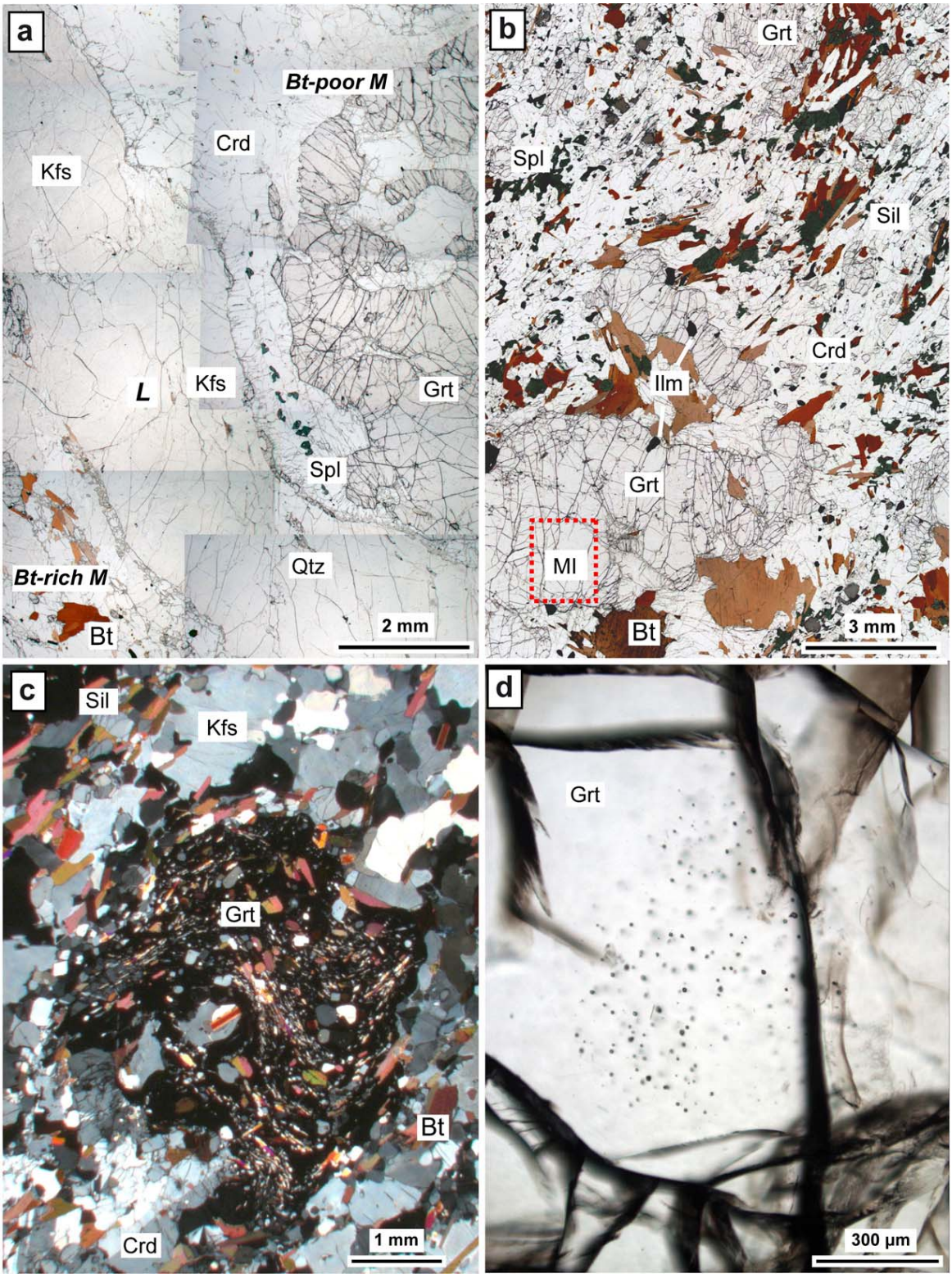

Figure 3: *MI-bearing samples photomicrographs. a) sample where Bt-poor, Bt-rich melanosome and leucosome occur together at thin section scale. b) MI-bearing sample exclusively formed by Bt-rich melanosome; c) common occurrence of inclusion-rich garnet in khondalites from Koliakkode quarry, at crossed polars; d) detail of a MI cluster in garnet.*

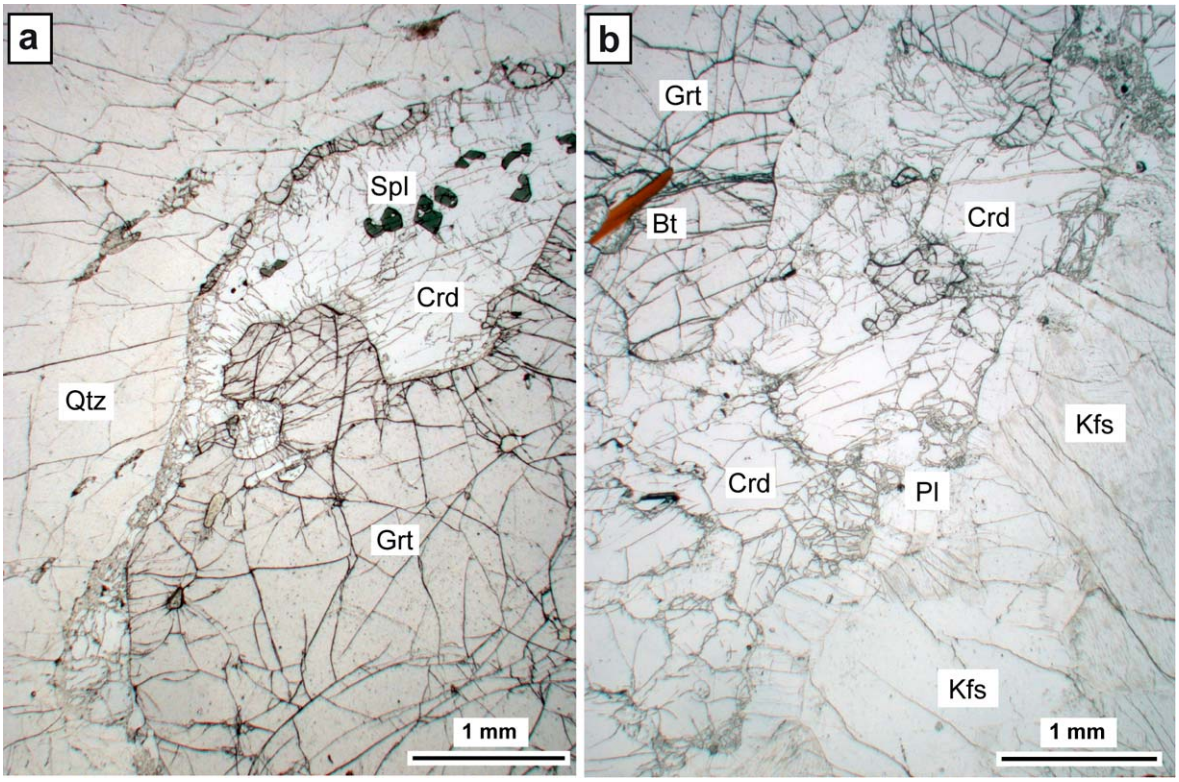

Figure 4: *MI-bearing samples photomicrographs. a) Bt-poor melanosome, showing garnet embayments with Crd and Spl; b) Bt-poor melanosome, Crd overgrowth on peritectic garnet and Crd alteration (pinitization) where in contact with leucosome.*

abundant in the Bt-poor type. When in touch with leucosomes, cordierite-bearing domains develop alteration products (pinite) along cracks and crystal phase boundaries (Fig.4b). In places cordierite crystallizes in garnet embayments, along with green spinel, ilmenite, small amounts of sillimanite, feldspar and quartz (Fig.4a). Locally, cordierite may form symplectic structures with quartz at garnet boundaries (Fig.5a) or with K-feldspar and plagioclase where in contact with leucosome.

Sillimanite mainly occurs in Bt-rich melanosomes, as prismatic, coarse grained crystals (up to several mm in length, Fig.3b), weakly oriented to define a foliation, that in places anastomoses around garnet porphyroblasts. Prismatic sillimanite may also occur as inclusion at the rim of garnet. In places largest idiomorphic crystals of sillimanite contain primary fluid inclusions, tubular to spherical in shape, along with graphite flakes (≤100 μm) and rare biotite (see section 2.7 for FI study). Sillimanite is in textural equilibrium with cordierite, and tends to overgrow both garnet and rarely also biotite, while a small rim of

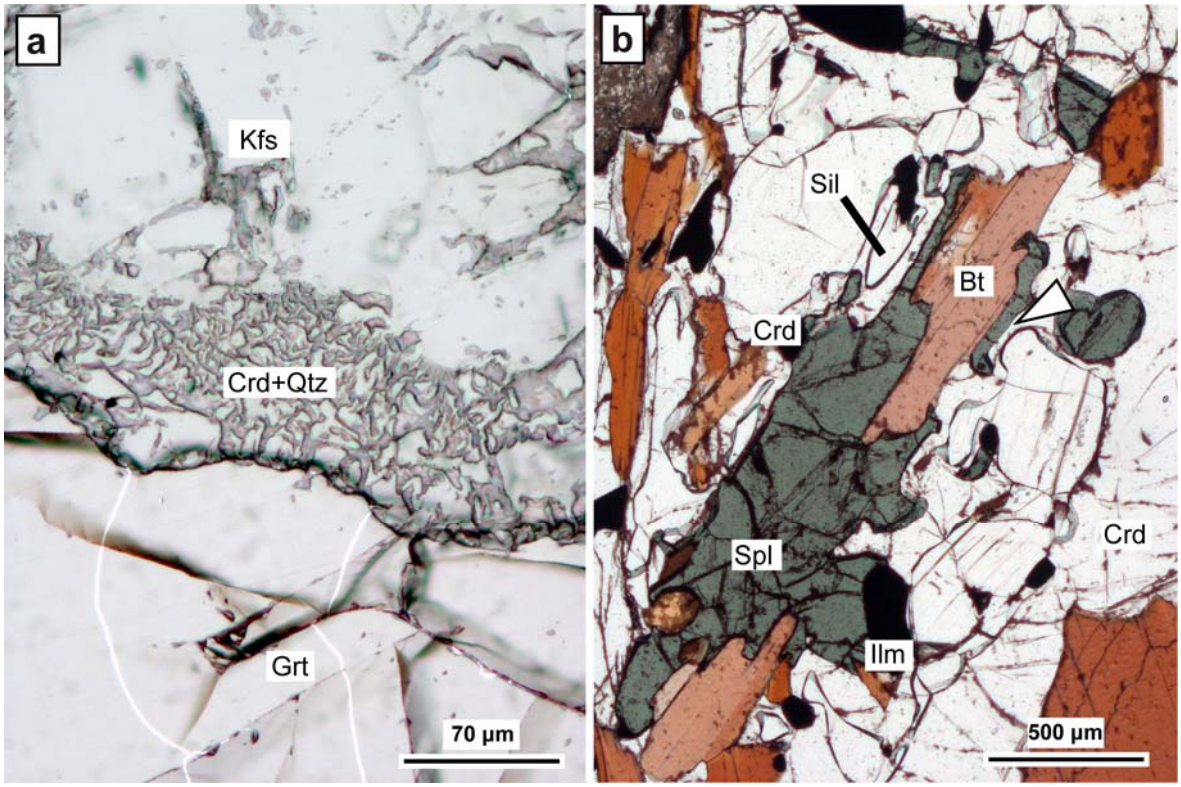

Figure 5: *a) Qtz-Crd symplectic intergrowths, plane polarized light; b) green spinel overgrowth on biotite, plane polarized light. White arrow: interstitial cordierite.*

cordierite grows between sillimanite and green spinel. In Bt-poor melanosomes, sillimanite is scarce and mainly present as partially consumed grains in garnet embayments, along with cordierite and green spinel and often K-feldspar. Fibrolitic sillimanite often occurs as unoriented crystals in MI clusters, ≤20 µm across. Although fibrolitic sillimanite was a reactant in the melting reaction, probably it was stable during and afterward the anatectic event, with a general coarsening of the crystals, from fibrolite needles in garnet, where they occur along with MI, to coarse-grained prismatic sillimanite in the surrounding matrix.

Biotite has a variable occurrence, which defines the two melanosome types. In Bt-rich melanosomes it occurs both in garnet, as partially resorbed inclusions, and in the matrix, as abundant coarse to fine-grained crystals (Fig.3b). In places biotite forms bent flakes, up to 2 mm in size, with embayments filled with cordierite. In the matrix, biotite is abundant and weakly oriented, locally overgrown by green spinel and ilmenite (Fig.5b). In Bt-poor melanosomes, biotite locally crystallizes in small subhedral grains interstitial with respect to cordierite, or occurs as partially resorbed inclusion both in garnet (Fig.4a) and cordierite.

Rarely, subhedral biotite is present in leucosomes. Biotite may crystallize replacing garnet if this phase is in contact with leucosome, probably due to a melt-consuming back-reaction.

Green spinel crystallizes in subhedral to euhedral crystals in Bt-rich melanosome, overgrowing biotite in close association with ilmenite (Fig.3b). In the Bt-poor melanosome, it forms a reaction product of the garnet along with cordierite, ilmenite, and sillimanite (Fig.4a). Spinel is not in equilibrium with sillimanite, and it reacts producing cordierite. Rarely spinel is observed enclosed in garnet.

Ilmenite is present as small crystals in all the studied samples, and occurs in association with green spinel in Bt-rich melanosome, in interstitial position with granoblastic cordierite in Bt-poor melanosomes, and as inclusion in garnet (mainly close to garnet boundaries, Fig.3b) in all studied samples. Locally, abundant ilmenite also surrounds peritectic garnet.

Leucosomes occurs both as large domains and as mm-scale veinlets that inject Bt-poor melanosome at the scale of the thin section. They consist of quartz, perthitic K-feldspar and plagioclase, small amounts of ilmenite and rare flakes of biotite (Fig.3a). Their relative modal proportions vary from quartz-rich domains with few K-feldspars grains, mainly crystallized at the border with melanosome, to both perthitic K-feldspar and plagioclase rich domains with only minor quartz, depending on the sample.

Quartz forms large crystals in leucosome, and may occur in garnet inside MI clusters, in variable size, from few to tens of μm, in the former case being very similar to MI at first sight. In leucosome It may also crystallize as interstitial phase in Kfs-rich domains, or develop symplectic intergrowths with cordierite if it grows at the boundary between Pl-rich leucosome and Bt-poor melanosome.

In Bt-poor melanosome perthitic K-feldspar only occurs as anhedral grains in embayments, along with cordierite, green spinel and interstitial quartz, while it is totally absent in Bt-rich melanosome. In the leucosome, it forms large grains with a complex pattern of perthitic systems (Fig.6). A first order of perthites, ≤ 20 μm across, is often present with spacing of a few tens of μm. In thick (~150 μm) section this system of perthites may show two different orientations, that form an angle of about 30 degrees (Fig.6b).

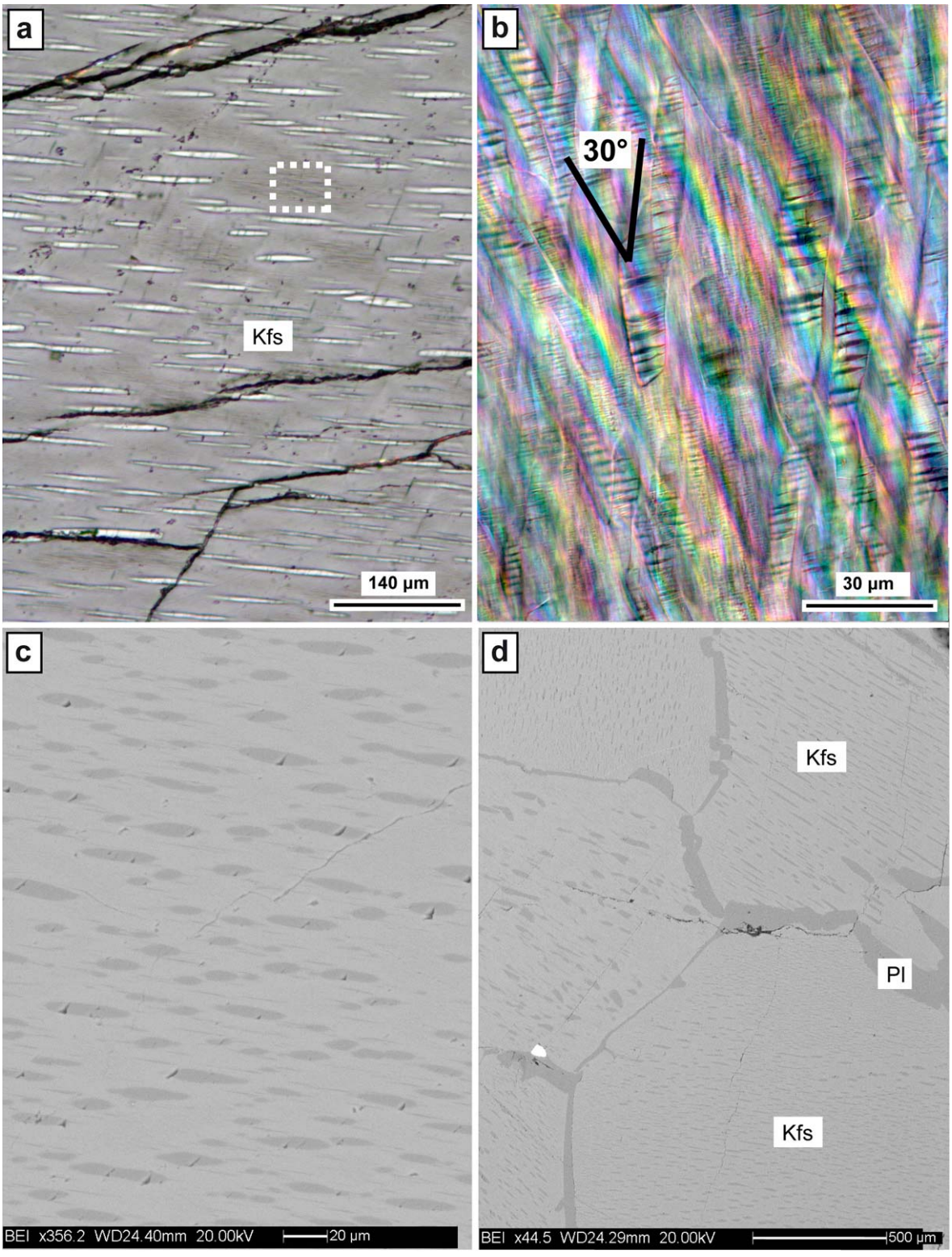

Figure 6: *Perthitic alkali feldspar. a) typical occurrence of alkali feldspar, in light color the 1st order perthites at plane-polarized light. Dashed box: 2nd. order perthites; b) close up of a thick perthitic alkali feldspar at crossed polars; c) SEM image of the 2nd. order perthites; d) SEM image of the alkali feldspar-rich leucosome.*

A second order of perthites, is characterized by thin lamellae (<5 μm across), fine-spaced (*white box*, Fig.6a,c) with elongation parallel to the first system of perthites. Locally the first order of perthites contains further exsolutions, at high angle with respect to the elongation, with spacing ≤ 5 μm (Fig.6b). Normally the first perthite system is better developed in the inner part of the crystal, while close to the boundaries and around mineral inclusions only the second system is present (Fig.6d).

Plagioclase forms allotriomorphic (Fig.4b) to interstitial grains (Fig.6d), with characteristic polysynthetic twinning and no visible exsolutions. It may be very abundant in some leucosomes, whereas it is rare in Bt-poor melanocratic portions, interlocked with granoblastic cordierite. Rarely plagioclase occurs as inclusion in garnet, and it is totally absent in Bt-rich melanosome.

Apatite, rutile, zircon and monazite occur both in leucosome and melanosome. Graphite and sulphides, mainly pyrite and locally chalcopyrite, are present in the Bt-rich melanosome.

One of the main problems in petrographic study of migmatites and granulites is inferring the former presence of a melt phase, i.e. that the rock was partially melted. The microstructural criteria for the recognition of former presence of melt have been reviewed by Vernon (2004) and include crystal faces developed in minerals that grows in contact with melt (e.g. plagioclase, K-feldspar, cordierite, garnet) and highly cuspate-lobate grains with low dihedral angle, interpreted as having nucleated and infilled pores that formerly contained melt (Marchildon and Brown, 2002). Such microstructures, termed *pseudomorphs after melt* (Holness and Clemens, 1999) or *melt pseudomorphs* (Clemens and Holness, 2000; Brown, 2001; Walte et al., 2005), were investigated more recently by Holness and Sawyer (2008) which used the term *pseudomorphs of melt-filled pores*, also adopted in this work. Pseudomorph of melt-filled pores are commonly recognized in Koliakkode quarry samples at the contact between garnet and leucosome, and consists of crystallized quartz (Fig.7a) or plagioclase (Fig.7b).

2.4.2) Metamorphic reactions and microstructural crystal phase evolution

A detailed petrographic study on melt-producing and melt-consuming metamorphic reactions in khondalites was carried out by Shabeer (2004), and many of the described reactions can be also inferred for the studied samples. Based on mineral inclusions

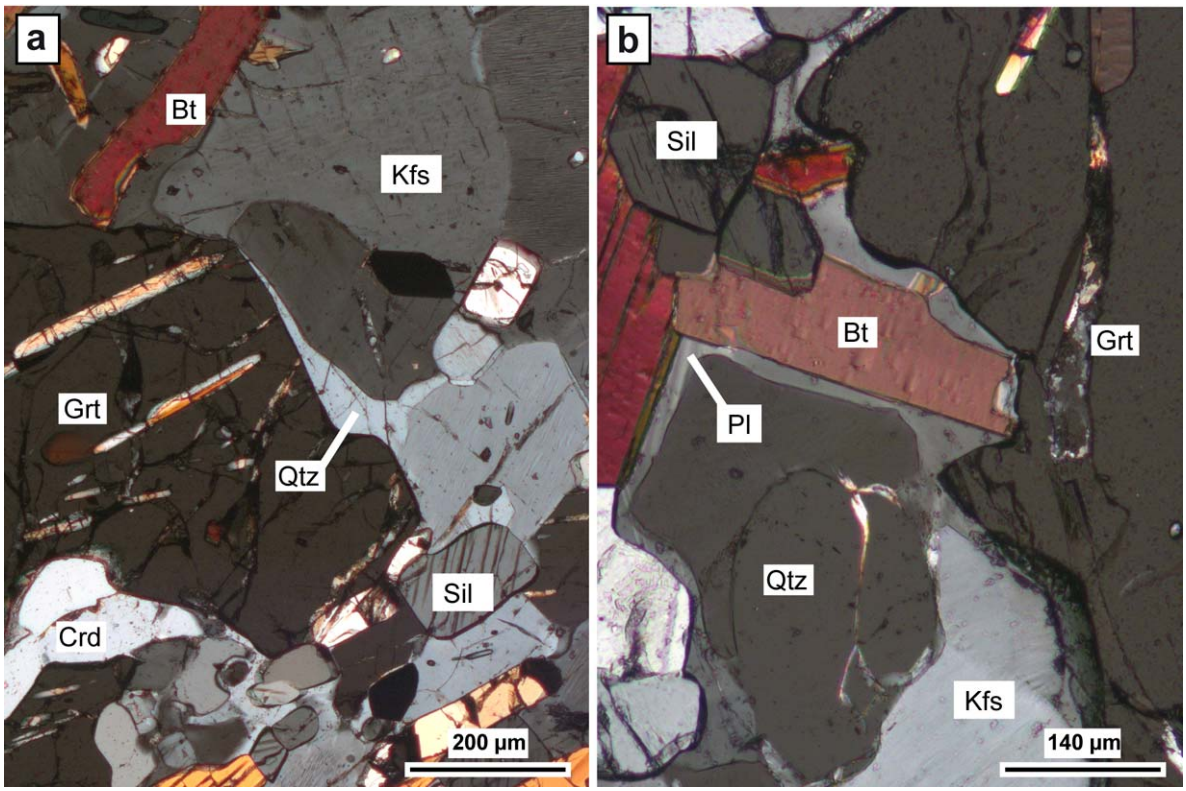

Figure 7: *Pseudomorphs of melt-filled pores. a) quartz crystallized in a pore at crossed polars; b) plagioclase crystallized from a melt film in between Qtz and Bt at crossed polars.*

assemblage and microstructures two main melting reactions have been identified. In Bt-poor melanosomes, the onset of the anatectic event starts with a typical biotite dehydration melting reaction (e.g. Thompson, 2001),

Bt+Sil+Qtz±Pl=Grt+Melt1±Ilm (2)

testified by the presence of partially resorbed biotite, fibrolite and rarely quartz as inclusion in peritectic garnet (Fig.3b,c).In the studied rocks, melt produced by reaction (2) is enclosed in peritectic garnets as MI (see below).

The second melt producing reaction involves garnet, biotite and sillimanite as reactants, according to the reaction

Bt+Grt+Sil±Pl=Spl+Crd+Ilm+Melt2 (3)

The products of this reaction occur in garnet embayments, along with relict sillimanite. Embayments may also contain leucosome, formed by K-feldspar and quartz. The latter phase may crystallize in pseudomorphs of melt-filled pores. This reaction is likely to have produced a limited amount of melt with respect to the dehydration melting of biotite, based on the limited development of garnet embayments, the small amount of crystallized melt in embayments and the scarcity of biotite in the samples in which this reaction is reported.

After this reaction, on the retrograde path of the rock, cordierite continued to grow, forming symplectic intergrowths with quartz on garnet (Fig.5a), probably according to reaction

Grt+Melt=Crd+Qtz. (4)

In the Bt-rich melanosome, the only supersolidus reaction is represented by the reaction (2) according to the occurrence of (rare) resorbed biotite, fibrolite and μm-size quartz included in garnet and the only melt now present is enclosed as MI in the garnet, while leucosome is totally absent. This suggests that melt has been (almost) totally drained from the rock. It is also possible that the amount of melt produced by reaction (3) was extremely low, differently than in Bt-poor melanosome-bearing samples, because of the different protolith composition. Differences in partial melting PT conditions are not expected between the two types of melanosome, since they are intimately interfingered also at hand specimen scale.

Other reactions identified in this melanosome type are (a) green spinel overgrowth on biotite (Fig.5b), locally with production of ilmenite, and (b) cordierite crystallization as reaction product of sillimanite and green spinel (white arrow,Fig.5b). Both reactions are likely to have occurred along the retrograde path.

2.4.3) Mineral chemistry

The composition of garnet, cordierite, biotite, green spinel, alkali feldspar and plagioclase has been measured by EMP analyses. Results are reported in tables 1 to 5. The analyses of MI in garnet are reported and discussed in section 2.5.

Garnet is an almandine-rich solid solution, with small to negligible amounts of spessartine and grossular components (table 1).

	Bt-rich melanosome				Bt-poor melanosome				
	MI-brg	MI-brg	MI-free	MI-free	MI-brg	MI-brg	MI-free	MI-free	MI-free
Na_2O	0.00	0.03	0.00	0.04	0.03	0.01	0.01	0.00	0.00
MgO	7.85	8.23	7.13	7.22	8.03	8.69	7.40	7.13	6.69
Al_2O_3	22.21	22.21	21.94	22.29	21.85	21.96	22.11	21.94	22.28
SiO_2	37.78	38.30	37.72	38.04	38.19	38.71	37.96	37.72	38.02
K_2O	0.00	0.01	0.03	0.00	0.01	0.00	0.00	0.03	0.00
CaO	0.90	0.77	0.77	0.82	0.89	0.84	0.78	0.77	0.75
TiO_2	0.06	0.03	0.04	0.05	0.07	0.06	0.04	0.04	0.08
Cr_2O_3	0.03	0.00	0.01	0.06	0.04	0.00	0.03	0.01	0.01
MnO	0.60	0.51	0.53	0.65	0.49	0.52	0.32	0.53	0.30
FeO	31.28	30.74	31.95	31.55	30.81	30.29	32.03	31.95	33.47
Total	100.71	100.85	100.13	100.73	100.40	101.10	100.67	100.13	101.58
Si	2.939	2.962	2.960	2.959	2.970	2.978	2.957	2.960	2.952
Ti	0.003	0.002	0.002	0.003	0.004	0.003	0.003	0.002	0.004
Al	2.036	2.024	2.029	2.043	2.003	1.991	2.030	2.029	2.038
Cr	0.002	0.000	0.001	0.004	0.002	0.000	0.002	0.001	0.001
Fe^{2+}	2.034	1.988	2.096	2.053	2.004	1.949	2.087	2.096	2.173
Mn	0.040	0.033	0.035	0.043	0.032	0.034	0.021	0.035	0.020
Mg	0.910	0.949	0.834	0.838	0.931	0.997	0.860	0.834	0.775
Ca	0.075	0.064	0.065	0.068	0.074	0.069	0.065	0.065	0.062
Na	0.000	0.004	0.000	0.005	0.005	0.002	0.001	0.000	0.000
K	0.000	0.001	0.003	0.000	0.001	0.000	0.000	0.003	0.000
X_{Mg}	0.31	0.32	0.28	0.29	0.32	0.34	0.29	0.29	0.26
Sps	0.01	0.01	0.01	0.01	0.01	0.01	0.01	0.01	0.01
Pyp	0.30	0.32	0.28	0.28	0.31	0.33	0.30	0.28	0.26
Alm	0.64	0.63	0.67	0.67	0.64	0.62	0.67	0.68	0.70
Grs	0.02	0.02	0.02	0.02	0.02	0.01	0.02	0.03	0.02

Table 1: *Representative microprobe analyses of peritectic garnets. All Fe considered as Fe^{2+}. MI-brg: MI-bearing garnets; MI-free: garnets free of MI.*

Generally in Bt-rich melanosome X_{Mg} values are higher in MI-bearing than in MI-free garnets: the first garnet type has average composition $Alm_{64}Pyr_{31}Grs_1Sps_2$, and X_{Mg}=0.31-0.33, while the second type has average composition $Alm_{66}Pyr_{28}Grs_1Sps_2$ and X_{Mg}=0.28-

0.31. In Bt-poor melanosome garnets show a wider range of compositions, $Alm_{70-62}Pyr_{25-33}Grs_{1-2.5}Sps_{0.5-1}$, with X_{Mg} in the range 0.25-0.34 without a clear correlation with the presence of MI. Lower X_{Mg} values (0.25) characterize small (<1mm) resorbed garnets that occur in cordierite-rich domains, suggesting that their composition was particularly affected by Fe-Mg exchange phenomena because of their small size.

In larger MI-bearing garnet porphyroblasts, possible compositional variations between MI-rich and MI-free zones in garnet were investigated acquiring EMP profiles across clusters (Fig.8). These garnets occur in a Bt-poor melanosome and are overgrown by cordierite. Each analytical profile was acquired across one single MI cluster, with ending points as close as possible to the garnet boundary with cordierite. Profiles from a representative sample are reported in Fig.8. The analyzed MI-bearing garnet has average composition $Alm_{70}Pyp_{26}Grs_2Sps_1$ in the central part (where MI are hosted), with X_{Mg}=0.28.

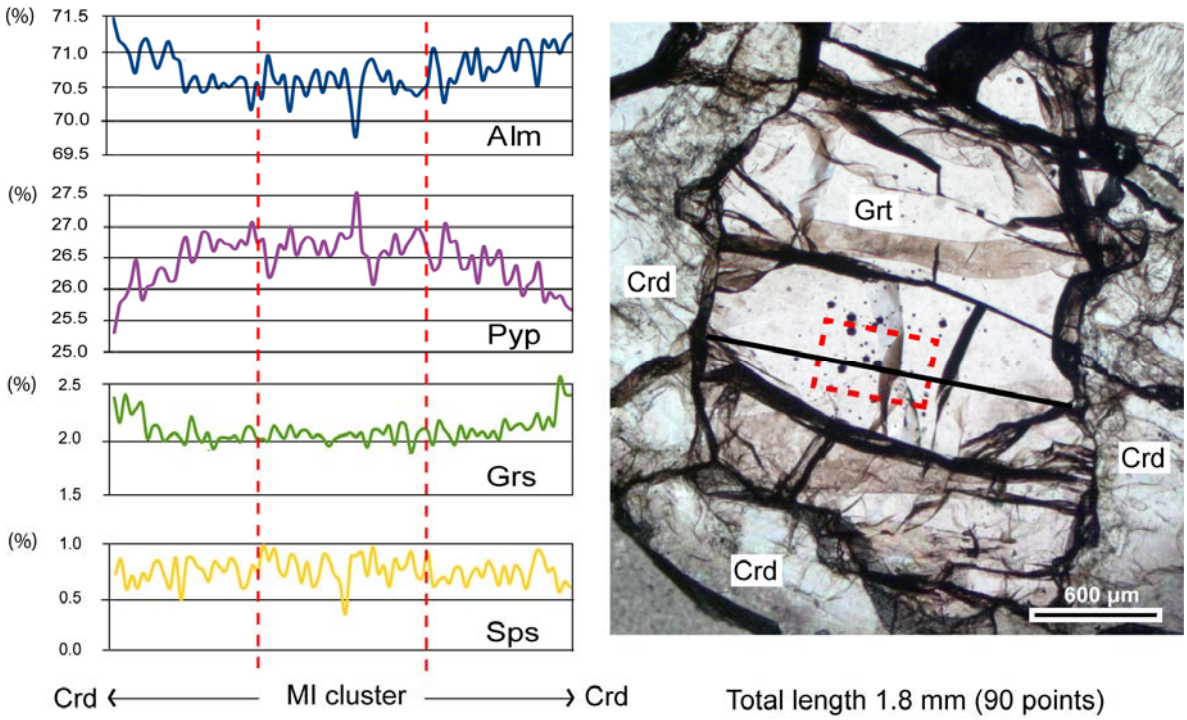

Figure 8: *garnet end-members variation across a MI cluster, calculated from EMP analytical profiles of MI-bearing garnet. Red dashed box and lines: cluster limits; black line: trace of chemical profile.*

The profile of pyrope component is almost flat in the central part, with a plateau around 26.5-27% mol%, while at both ends values have a slight decrease to 25.5 mol% Pyp, close

to the boundaries with cordierite. Almandine component defines an opposite trend, with central plateau at 70.5-71 mol% Alm, but with ends bent upward to reach 71.5 mol% Alm. A similar shape is shown by the profile of grossular component, with central plateau at 2 mol% Grs and both ends at 2.5 mol% Grs. No variations are visible in spessartine component profile. Lateral variations of Alm, Pyp and Grs do not correlate with presence of MI clusters, in fact they start always at least 300 μm far from the cluster edge toward the crystal boundaries. Therefore, garnet is internally homogeneous, and Fe-Mg exchange on the retrograde metamorphic path had a small effect only at garnet rim when in touch with cordierite.

Cordierite is generally Mg-rich, with some variations in the two different melanosome types, depending on microstructural position (table 2). In Bt-rich melanosome cordierite both in contact with garnet and in the matrix has X_{Mg}=0.70-0.72, while if product of reaction between sillimanite and green spinel it shows higher X_{Mg} of c. 0.75. In Bt-poor melanosome cordierite in the matrix has generally lower X_{Mg}, 0.65-0.68, while in garnet embayments cordierite shows X_{Mg} =0.74-0.76.

Biotite composition varies depending on the melanosome type and also on its microstructural position, and Tio_2 and X_{Mg} show in general a negative correlation (Fig.9) (see also Guidotti, 1984; Cesare, 2008), although few exceptions were found (table 3). In both melanosome types partially resorbed biotite grains show the highest X_{Mg} values (0.69-0.73) with highly variable TiO_2 content, 3.8-5.9 wt% (dashed oval, Fig.9): they are probably relicts of the melting reaction, and occur in peritectic garnet or interstitial in Crd-rich domains. Similar X_{Mg} values, 0.71-0.72, and lower TiO_2, 2.4-3.2 (average 2.8) wt% are shown by biotite produced by back-reaction between garnet and melt (*Bt2*, Fig.9). In the matrix of Bt-rich melanosome biotite has higher X_{Mg} (0.61-0.66) than in Bt-poor melanosome, where biotite has lower X_{Mg} (0.55-0.61) while the TiO_2 content variation is less straightforward but generally lower (3.7-5.2, average 4.6 wt%) in the first type than in the second (4.3-5.6, average 5.3 wt%). Biotite flakes dispersed in the melt (*Bt in melt*, Fig.9) have the lowest average X_{Mg} (0.55) and the highest TiO_2 content, 5.1-6.0 (average 5.4) wt%.

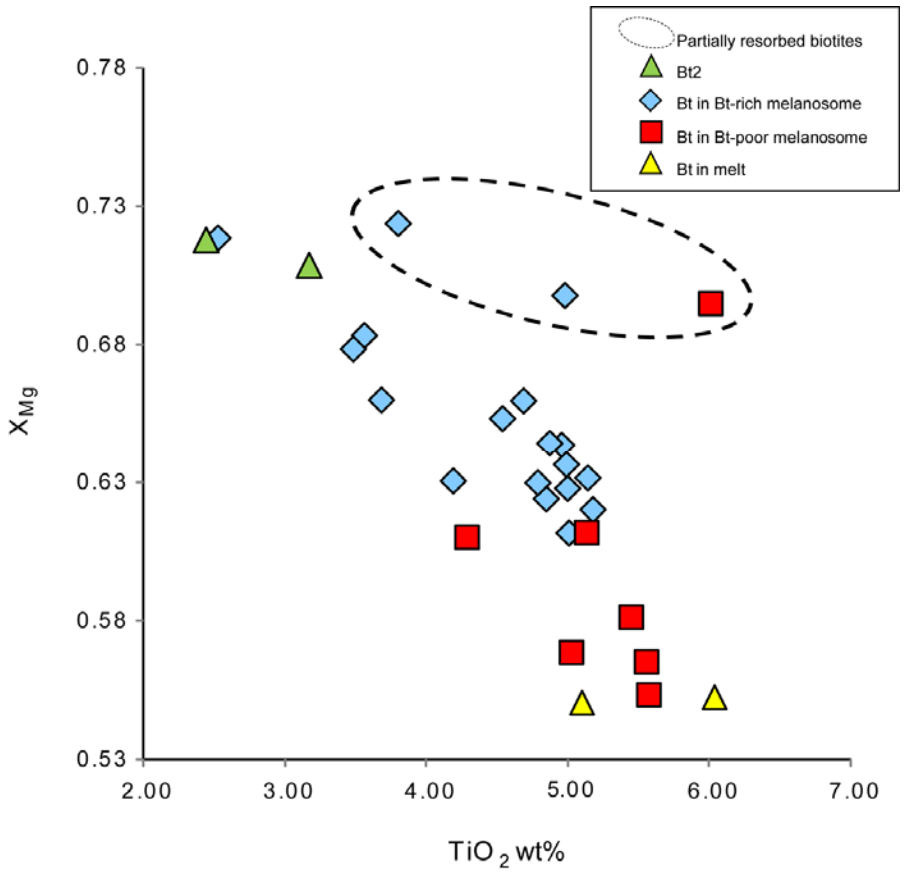

Figure 9: *X_{Mg} values and Ti contents in the analyzed biotites, classified according to their microstructural position (see text for details).*

Green spinel shows variable X_{Mg}, depending on microstructural position (table 4). In Bt-rich melanosome, green spinel overgrows biotite and has low X_{Mg}, 0.21-0.23, and low ZnO content (~1 wt %). In Bt-poor melanosome spinel forms grains with X_{Mg} =0.23-0.25 when it occurs in Crd-rich domains. Here, ZnO content has a wide range, 3.9-6.1 wt%, locally with high concentrations, probably related to local variation in the zinc content of the protolith. In garnet embayments, where green spinel represents a peritectic phase from melting reaction (3), X_{Mg} is higher (0.27-0.28) with ZnO=3.3-3.7 wt%. Also Cr_2O_3 content varies depending on the microstructural position: in Bt-rich melanosome green spinel that overgrows biotite has Cr_2O_3=0.41-0.62, while in garnet embayments it shows very low Cr_2O_3 content (0.02 – 0.10).

	Bt-rich melanosome				Bt-poor melanosome			
	Crd mtx	Crd mtx	Crd mtx	Crd $_{Sil+Spl}$	Crd mtx	Crd mtx	Crd mtx	Crd$_{emb}$
Na_2O	0.02	0.10	0.00	0.11	0.17	0.13	0.01	0.06
MgO	9.40	9.29	9.55	10.14	8.91	8.66	8.90	9.82
Al_2O_3	33.39	34.32	33.54	33.85	33.12	32.90	33.39	33.41
SiO_2	48.66	49.60	48.85	49.00	48.55	48.01	48.38	49.24
K_2O	0.00	0.00	0.01	0.00	0.00	0.03	0.01	0.00
CaO	0.03	0.02	0.02	0.02	0.01	0.01	0.02	0.04
TiO_2	0.01	0.00	0.00	0.01	0.01	0.00	0.00	0.00
Cr_2O_3	0.00	0.00	0.00	0.02	0.01	0.00	0.00	0.02
MnO	0.05	0.05	0.02	0.03	0.03	0.01	0.03	0.04
FeO	6.95	7.06	6.72	6.05	7.34	8.18	7.93	6.21
Total	98.51	100.44	98.71	99.22	98.14	97.92	98.67	98.85
Si	4.969	4.966	4.971	4.949	4.985	4.964	4.955	4.992
Ti	0.001	0.000	0.000	0.000	0.001	0.000	0.000	0.000
Al	4.019	4.050	4.022	4.030	4.008	4.009	4.030	3.992
Cr	0.000	0.000	0.000	0.002	0.001	0.000	0.000	0.002
Fe^{2+}	0.593	0.591	0.571	0.511	0.630	0.707	0.679	0.527
Mn	0.004	0.004	0.001	0.003	0.003	0.001	0.002	0.004
Mg	1.431	1.386	1.449	1.527	1.364	1.334	1.359	1.485
Ca	0.003	0.002	0.003	0.002	0.001	0.001	0.002	0.004
Na	0.003	0.019	0.000	0.022	0.034	0.026	0.002	0.013
K	0.000	0.000	0.002	0.000	0.000	0.003	0.002	0.000
Total	11.023	11.019	11.019	11.046	11.026	11.046	11.032	11.017
X_{Mg}	0.71	0.70	0.72	0.75	0.68	0.65	0.67	0.74

Table 2: *Representative microprobe analyses of cordierite. All Fe considered as Fe^{2+}. Crd mtx: cordierite in the matrix; Crd $_{Sil+spl}$: cordierite produced by reaction among spinel and sillimanite; Crd$_{emb}$: cordierite in garnet embayments*

	Bt-rich melanosome					Bt-poor melanosome								
Position	Bt incl	Bt mtx	Bt mtx	Bt mtx	Bt mtx	Bt incl	Bt mtx	Bt mtx	Bt mtx	Bt mtx	Bt2	Bt2	Bt in melt	Bt in melt
Na_2O	0.42	0.14	0.08	0.24	0.15	0.44	0.00	0.00	0.05	0.09	0.17	0.00	0.00	0.00
MgO	16.84	13.45	13.74	15.83	13.75	14.78	13.50	11.99	11.69	13.52	16.51	16.62	11.76	11.68
Al_2O_3	15.86	15.91	15.78	16.12	15.97	15.73	14.96	15.01	15.30	15.27	15.40	15.50	14.89	15.10
SiO_2	37.80	36.77	36.82	37.17	36.74	37.07	37.27	37.41	36.37	37.15	38.00	38.16	36.70	36.68
K_2O	9.47	9.56	9.61	9.29	9.51	9.37	9.49	9.55	9.49	9.54	9.37	10.03	9.59	9.54
CaO	0.00	0.00	0.00	0.01	0.02	0.02	0.01	0.00	0.00	0.00	0.02	0.03	0.00	0.00
TiO_2	3.80	5.01	5.18	3.56	4.19	5.94	5.13	5.03	5.57	4.29	3.18	2.44	5.10	6.04
Cr_2O_3	0.03	0.05	0.08	0.05	0.07	0.09	0.03	0.07	0.19	0.10	0.08	0.02	0.08	0.15
MnO	0.00	0.00	0.00	0.01	0.02	0.00	0.04	0.00	0.04	0.00	0.00	0.00	0.00	0.00
FeO	11.46	15.21	15.00	13.08	14.36	11.48	15.25	16.21	16.81	15.39	12.10	11.64	17.11	16.87
Total	95.68	96.11	96.29	95.37	94.78	94.92	95.69	95.26	95.50	95.35	94.82	94.43	95.24	96.07
Si	5.525	5.456	5.449	5.489	5.504	5.472	5.551	5.617	5.480	5.557	5.611	5.659	5.551	5.492
Ti	0.418	0.559	0.576	0.396	0.472	0.659	0.575	0.568	0.632	0.482	0.353	0.273	0.581	0.680
Al	2.732	2.782	2.752	2.806	2.820	2.736	2.626	2.657	2.718	2.693	2.680	2.709	2.655	2.664
Cr	0.003	0.006	0.009	0.006	0.009	0.010	0.004	0.008	0.022	0.012	0.009	0.002	0.010	0.017
Fe^{2+}	1.401	1.888	1.857	1.615	1.799	1.418	1.900	2.035	2.118	1.926	1.494	1.444	2.164	2.112
Mn	0.000	0.000	0.000	0.001	0.002	0.000	0.005	0.000	0.005	0.000	0.000	0.000	0.000	0.000
Mg	3.669	2.974	3.031	3.485	3.070	3.251	2.997	2.684	2.625	3.015	3.635	3.674	2.651	2.608
Ca	0.000	0.000	0.000	0.002	0.003	0.003	0.002	0.000	0.000	0.000	0.003	0.004	0.000	0.000
Na	0.118	0.040	0.023	0.068	0.043	0.127	0.000	0.000	0.013	0.025	0.050	0.000	0.000	0.000
K	1.766	1.810	1.813	1.750	1.817	1.765	1.802	1.829	1.824	1.821	1.766	1.897	1.850	1.823
Total	15.632	15.516	15.512	15.619	15.539	15.441	15.461	15.397	15.437	15.531	15.600	15.662	15.461	15.398
A site	1.884	1.851	1.837	1.820	1.863	1.895	1.804	1.829	1.837	1.846	1.818	1.901	1.850	1.823
X_{Mg}	0.72	0.61	0.62	0.68	0.63	0.70	0.61	0.57	0.55	0.61	0.71	0.72	0.55	0.55

Table 3: *Representative microprobe analyses of biotite. All Fe considered as Fe^{2+}. Bt incl: biotite inclusions in garnet; Bt mtx: biotite in the matrix; Bt2: biotite produced by back-reaction of Grt+melt; Bt in melt: biotite dispersed in the leucosome*

	Bt-rich melanosome			Bt-poor melanosome					
	Spl on Bt	Spl on Bt	Spl on Bt	Spl-Crd	Spl-Crd	Spl-Crd	Spl_{emb}	Spl_{emb}	Spl_{emb}
MgO	5.17	5.32	5.54	5.72	5.14	5.06	6.35	6.29	6.40
Al_2O_3	60.12	60.29	60.70	60.64	59.95	59.02	59.98	60.30	60.20
SiO_2	0.11	0.13	0.12	0.16	0.13	0.16	0.15	0.10	0.72
TiO_2	0.03	0.02	0.01	0.02	0.02	0.06	0.04	0.04	0.07
Cr_2O_3	0.62	0.48	0.41	0.04	0.07	0.07	0.05	0.11	0.11
MnO	0.08	0.07	0.05	0.05	0.09	0.01	0.02	0.08	0.05
FeO	33.98	33.54	32.98	29.81	30.65	29.61	30.14	30.24	29.74
ZnO	1.03	0.85	0.83	3.90	4.34	6.07	3.27	3.52	3.67
Total	101.15	100.69	100.64	100.34	100.40	100.07	100.00	100.69	100.95
Si	0.003	0.004	0.003	0.004	0.004	0.004	0.004	0.003	0.020
Ti	0.001	0.000	0.000	0.000	0.000	0.001	0.001	0.001	0.001
Al	1.965	1.972	1.980	1.986	1.977	1.965	1.970	1.970	1.954
Cr	0.014	0.010	0.009	0.001	0.002	0.001	0.001	0.002	0.002
Fe^{2+}	0.788	0.779	0.763	0.693	0.717	0.699	0.702	0.701	0.685
Mn	0.002	0.002	0.001	0.001	0.002	0.000	0.001	0.002	0.001
Mg	0.214	0.220	0.229	0.237	0.215	0.213	0.264	0.260	0.263
Zn	0.021	0.017	0.017	0.080	0.090	0.127	0.067	0.072	0.075
Total	3.007	3.005	3.002	3.002	3.006	3.011	3.010	3.010	3.001
X_{Mg}	0.21	0.22	0.23	0.25	0.23	0.23	0.27	0.27	0.28

Table 4: *Representative microprobe analyses of spinel. All Fe considered as Fe^{2+}. Spl on Bt: spinel overgrown on biotite; Spl-Crd: spinel in cordierite-rich domains; Spl_{emb}: spinel in garnet embayments.*

In the exsolved alkali feldspar, only the first order perthites are wide enough to be analyzed by EMP, and have an albite-rich composition ($Ab_{73}An_{26}Or_1$, table 5). Second order perthites are too small (<5 μm) to obtain a valid analysis of the single lamellae, therefore compositional information have been obtained by acquiring analytical profiles in raster mode in the gap between two first order perthites, with trajectory perpendicular to their elongation; collected analyses do not represent the whole alkali-feldspar composition, but exclusively the composition of the portion of exsolved K-feldspar with fine-spaced, second order perthite system. Average analyses show an orthoclase-rich composition, with $Ab_{20}An_2Or_{78}$. Analytical profiles on feldspar show a variation in Na_2O content

						Bt-poor melanosome					Leucosome					
	Kfs	Kfs	Kfs	Kfs	1st Perth	Pl incl	Pl mel	Pl mel	Pl mel	Pl mel	Pl leuco	Pl leuco	Pl leuco	Pl leuco	Pl leuco	Pl leuco
Na_2O	2,23	1,55	2,01	2,58	8,46	8,40	8,09	8,75	8,69	8,69	8,56	8,81	8,60	7,23	7,66	7,16
MgO	0,02	0,01	0,03	0,01	0,00	0,00	0,00	0,00	0,00	0,01	0,10	0,00	0,00	0,00	0,00	0,00
Al_2O_3	19,65	19,61	19,38	19,07	24,55	24,40	23,83	24,10	24,16	24,10	24,93	24,11	23,96	24,21	24,79	25,00
SiO_2	64,06	63,34	63,53	63,79	60,45	61,38	62,18	62,23	62,25	61,75	60,70	62,39	62,95	61,33	60,56	58,85
K_2O	12,94	13,72	13,13	12,31	0,09	0,17	1,25	0,30	0,49	0,28	0,16	0,37	0,46	1,27	0,73	1,11
CaO	0,72	0,97	0,47	0,26	5,47	5,40	4,85	4,72	4,89	4,78	5,80	4,59	5,13	5,63	6,37	6,32
MnO	0,01	0,01	0,00	0,00	0,00	0,02	0,01	0,00	0,04	0,00	0,00	0,00	0,00	0,01	0,00	0,00
FeO	0,02	0,02	0,04	0,01	0,00	0,13	0,02	0,02	0,03	0,00	0,16	0,02	0,09	0,01	0,05	0,01
Total	99,71	99,30	98,68	98,04	99,01	100,04	100,26	100,20	100,63	99,64	100,58	100,34	101,33	99,72	100,23	98,46
Si	2,942	2,933	2,949	2,968	2,711	2,725	2,757	2,752	2,746	2,746	2,689	2,755	2,757	2,736	2,695	2,670
Al	1,063	1,070	1,060	1,046	1,297	1,277	1,245	1,256	1,256	1,263	1,302	1,255	1,237	1,273	1,300	1,337
Fe^{2+}	0,001	0,001	0,002	0,000	0,000	0,005	0,001	0,001	0,001	0,000	0,006	0,001	0,003	0,001	0,002	0,001
Mn	0,000	0,000	0,000	0,000	0,000	0,001	0,000	0,000	0,002	0,000	0,000	0,000	0,000	0,000	0,000	0,000
Mg	0,001	0,000	0,002	0,001	0,000	0,000	0,000	0,000	0,000	0,001	0,007	0,000	0,000	0,000	0,000	0,000
Ca	0,035	0,048	0,024	0,013	0,263	0,257	0,230	0,224	0,231	0,228	0,275	0,217	0,241	0,269	0,304	0,307
Na	0,198	0,140	0,181	0,233	0,736	0,723	0,695	0,750	0,743	0,750	0,736	0,755	0,731	0,625	0,661	0,630
K	0,758	0,810	0,777	0,730	0,005	0,010	0,071	0,017	0,028	0,016	0,009	0,021	0,026	0,073	0,041	0,064
Total	5,002	5,005	4,998	4,991	5,011	5,001	5,002	5,001	5,009	5,004	5,029	5,005	5,000	4,977	5,005	5,009
Ab	20	14	18	24	73	73	70	76	74	75	72	76	73	65	66	63
An	4	5	2	1	26	26	23	23	23	23	27	22	24	28	30	31
Or	76	81	79	75	1	1	7	2	3	2	1	2	3	7	4	6

Table 5: *Representative microprobe analyses of K-feldspar, 1st order perthites and plagioclase. All Fe considered as Fe^{2+}.1st Perth: first order perthites; Pl incl: plagioclase as mineral inclusion in garnet; Pl mel: plagioclase crystallized in the melanosome; Pl leuco: plagioclase crystallized in the leucosome*

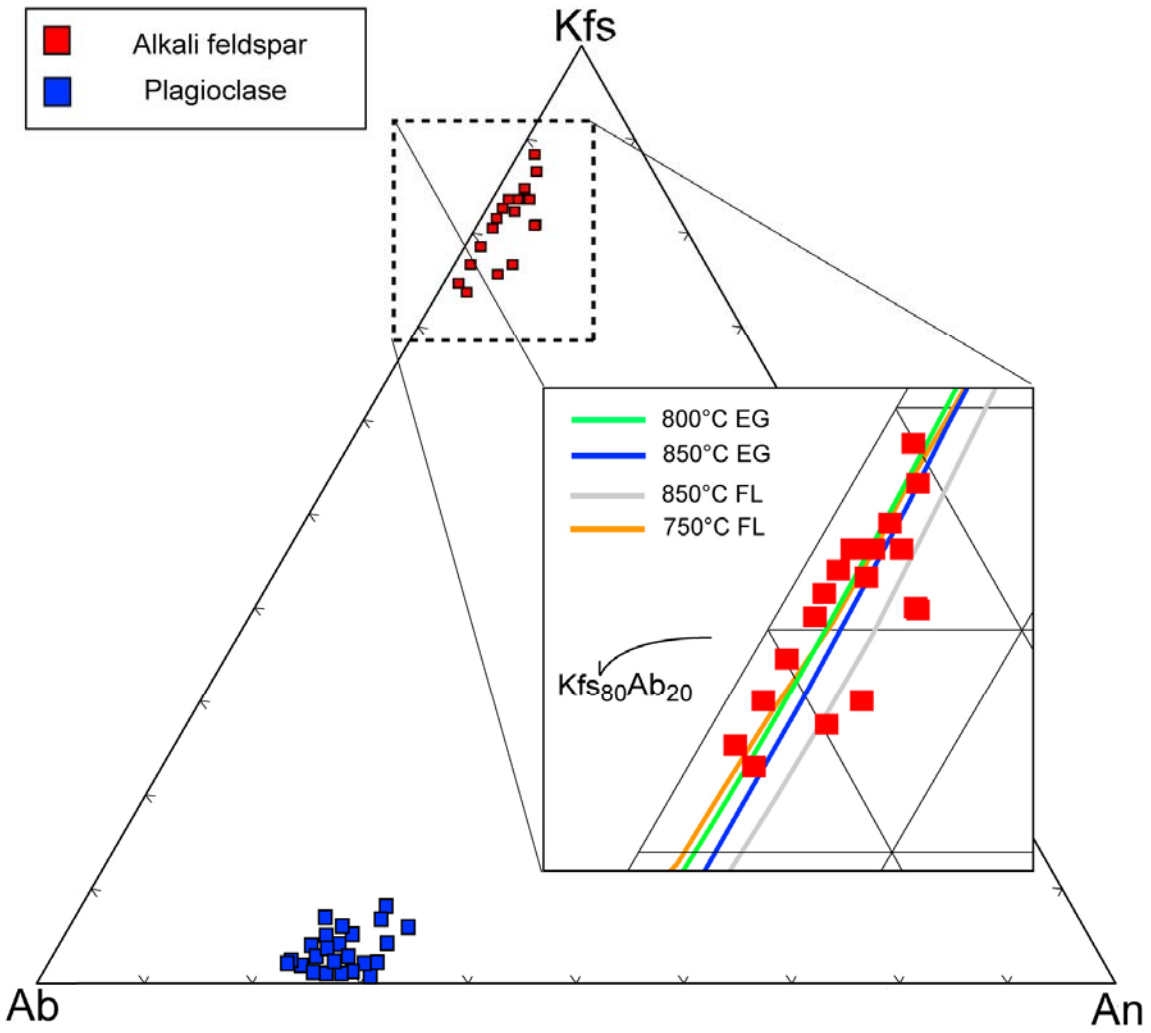

Figure 10. *Kfs-Ab-An ternary diagram for feldspars, with partial Kfs composition (only exsolved Kfs with 2nd order perthites) and Pl composition. The enlarged field illustrates the Kfs compositions along with the traces of the solvi after Fuhrman and Lindsley (1988, abbreviated FL), and Elkins and Grove (1990, abbreviated EG), as calculated at 6 kbar using SolvCalc 2.0 (Shaoxiong Wen, 1996).*

(up to 1 wt%), while CaO is always <1 wt%. Analyses collected on first order perthites and average analyses on the surrounding feldspar are reported in table 5.

Plagioclase in leucosomes from different samples has variable composition, from oligoclase, $Ab_{76}An_{22}Or_2$ to andesine, $Ab_{63}An_{31}Or_6$ (table 5; Fig.10). In Bt-poor melanosome, where plagioclase occurs interlocked with granoblastic cordierite, it has average composition $Ab_{73}An_{24}Or_3$, similar to residual plagioclase in garnet, $Ab_{73}An_{26}Or_1$.

In the Ab-An-Or ternary diagram (Fig.10), alkali feldspar compositions collected from different samples are scattered (as can be appreciated from data in table 5). A limited number of datapoints plot within the miscibility gap for ternary feldspars at 800°C (as defined by Elkins and Grove, 1990) or at 750°C (as defined by Furhman and Lindsley, 1988). These datapoints suggest then that unmixing of alkali-rich feldspar started at T> 800°C, even if most other compositions suggest that reequilibration procedeed at lower temperatures. Few analyses plot within the miscibility gap at 850°C (Furhman and Lindsley, 1988), and could suggest higher minimum crystallization T. However, these datapoints may also be meaningless, due to contamination by exsolved oligoclase lamellae. Estimated minimum T of crystallization agrees with T commonly reported for rocks in the central part of the KKB, 800-850°C (Shabeer et al., 2004; Cesare et al., 2008). It must be also considered that these compositions represent the alkali feldspar portion depleted of the plagioclase component after the exsolutions of the 1st order perthites, and not the total crystals composition.

2.5) Melt inclusions microstructures

MI occur in peritectic garnet as clusters, ≤1 cm across, formed by hundreds of inclusions (Fig.3d,11a) with spacing in the order of 50-100 μm. Only in few cases MI are isolated. Clusters do not have a preferred microstructural position, but they never touch garnet boundaries. MI have a variable size in the range 3-25 μm, with some exceptional MI up to 40 μm in diameter. Tiny mineral inclusions (25 μm, size range comparable with largest MI) may be present along with MI in cluster: they are mainly unoriented fibrolite (Fig.11f, h), round quartz, rare graphite and accessory minerals (apatite, zircon, rutile, titanite).

Occurrence of inclusions in clusters suggests a primary origin, i.e. entrapment by garnet during its growth (Roedder, 1984). Under the optical microscope inclusions appear brownish to transparent, depending on the degree of crystallization (see Fig.11, and details below). Brownish inclusions (Fig.11b,d,i,m) consist of a polycrystalline aggregate of birefringent minerals, better distinguishable at crossed polars (Fig.11c,e,g), and are hereafter named “crystallized MI”. Transparent MI represent a small fraction (≈ 15%) of the total content of a cluster, are smaller (2.5-17.5 μm) than the crystallized ones (Fig. 11f,g,l) and contain a homogeneous phase, isotropic at crossed polars (Fig.11g), always coexistent with an accessory mineral. The shape of MI is commonly isometric, although

crystallized MI may have more or less developed “tails” (Fig.11i) filled of birefringent crystals.

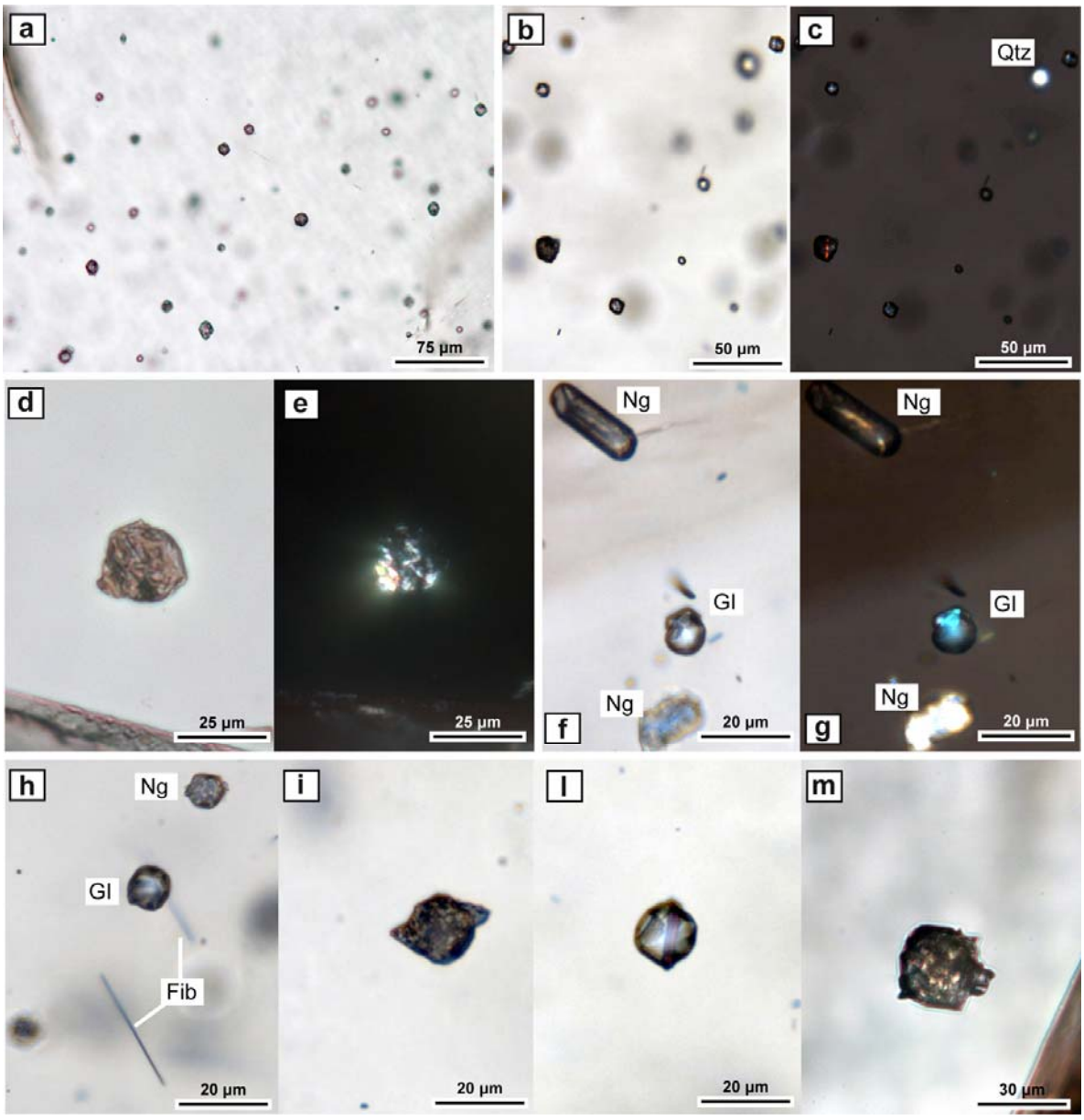

Figure 11: *MI photomicrographs. Ng: nanogranite; Gl: glassy inclusion a) cluster of negative-crystal shaped nanogranites and glassy inclusions; b) and c) cluster detail at plane-polarized light and crossed polars, respectively; d) and e) close view of a nanogranite, at plane-polarized light and crossed polars, respectively; f) and g) close view of a glassy inclusion and two nanogranites (one tubular), at plane-polarized light and crossed polars, respectively; h) glassy inclusion coexistent with a nanogranite and fibrolite needles (Fib); i) partially decrepitated nanogranite with symmetrical microfractures; l) glassy inclusion with a large acicular trapped mineral phase (Rt?); m) partially decrepitated nanogranite, with asymmetrical microfractures.*

In very few cases crystallized MI are tubular (Fig.11f). As regards fluid inclusions, only one primary FI has been detected in MI-bearing garnet, while trails of secondary FI are more common: no further study has been conducted on these FI because they are not related to the conditions of formation of the garnet.

BSE imaging and X-ray mapping show that crystallized MI contain biotite, K-feldspar, plagioclase and quartz (Fig.12, see also Supplementary Material 1), along with accessory minerals such as apatite, zircon, rutile, Zn-bearing spinel and rarely ilmenite, interpreted mainly as solid inclusions (Fig.2f and 3c,e,f in Sup.Mat.1). In places apatite is likely to be a daughter mineral crystallized from the melt, because of the small size and the irregular shape. In few cases Fe-oxides microfractures occur in largest MI (Fig.12a). The internal texture of crystallized MI is variable also within the same inclusion (Fig.12a): mineral phases may occur as idiomorphic to allotriomorphic grains, with a wide variability in grain size, from tens of nanometers up to 10μm.

Inclusions show a variable shape, from a perfect faceted negative-crystal to irregular, as a result of the interplay among crystallizing phases and host re-crystallization along the cooling path. Many inclusions show round cavities, ≤ 1 μm across (*white arrows*, Fig.12a,b,f and 2b in Sup.Mat.1), interpreted as a primary porosity, since the round shape of the cavities allows us to exclude that these are holes left by crystals removed or dissolved during sample preparation. Locally cuspate-lobate microstructures (Holness and Sawyer, 2008) are present, e.g. the thin (c. 50 nm) film of a dark material (Qtz?) visible in Fig.12b (*white box*). They are similar to the pseudomorphs of melt-filled pores, described in section 2.4.2. The tails recognized at optical investigation are microfractures that probably developed on cooling, now filled by crystal phases, i.e. biotite and quartz (*black arrow*, Fig.12f and 3a in Sup.Mat.1).

In SE and BSE images biotite is distinguishable because of the basal cleavage (Fig.12d) and the irregular surface (mostly visible in Fig.12b), due to the polishing process, more effective than on the host mineral because of the strong difference in hardness.

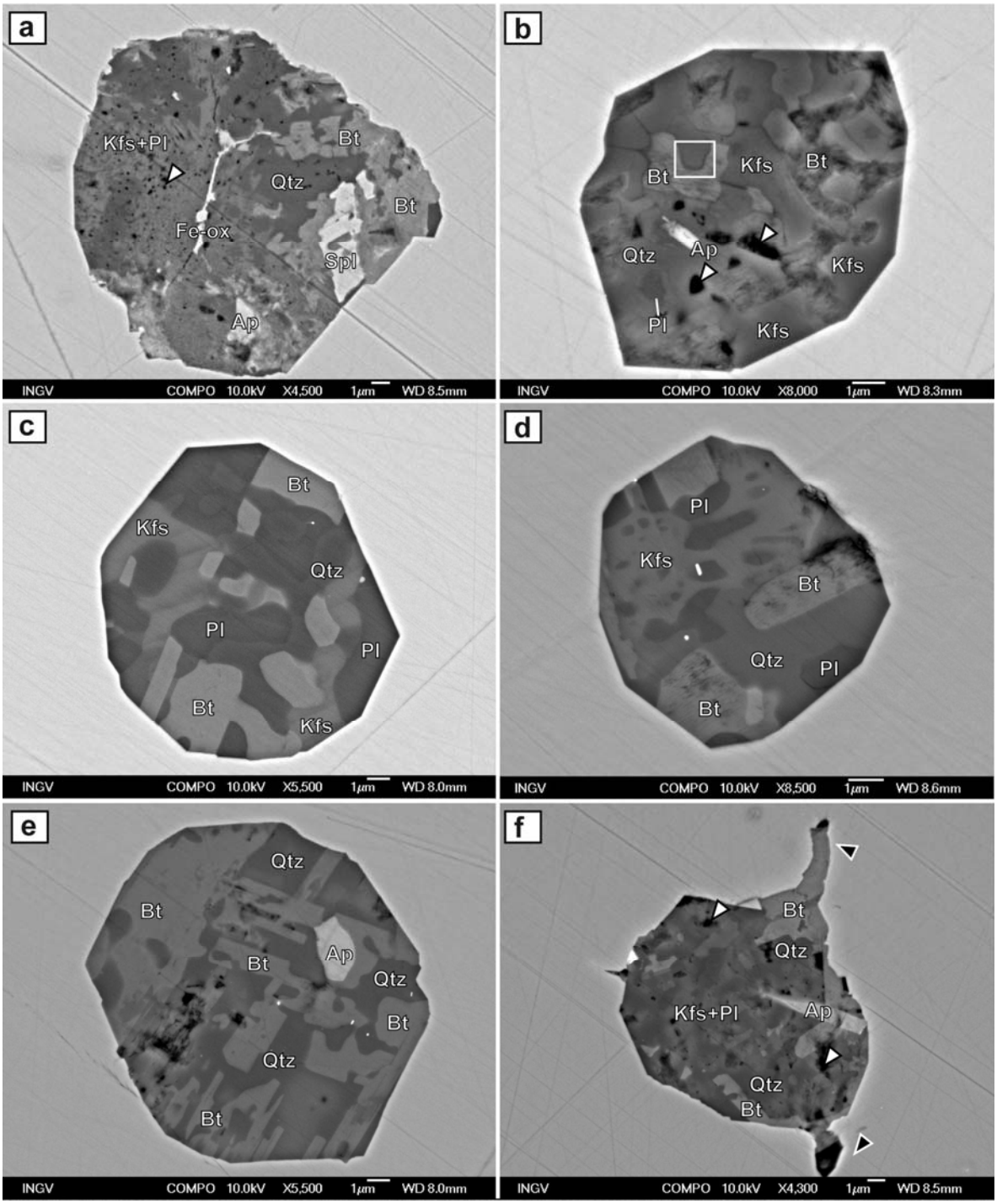

Figure 12: *BSE images of nanogranites. Black arrows: decrepitation microfractures; white arrows: primary nanoporosity; white box: cuspate microstructure resembling a pseudomorph of melt-filled pores (elemental maps on MI in fig.12c,e are reported in Fig.1,2 in sup.Mat.2).*

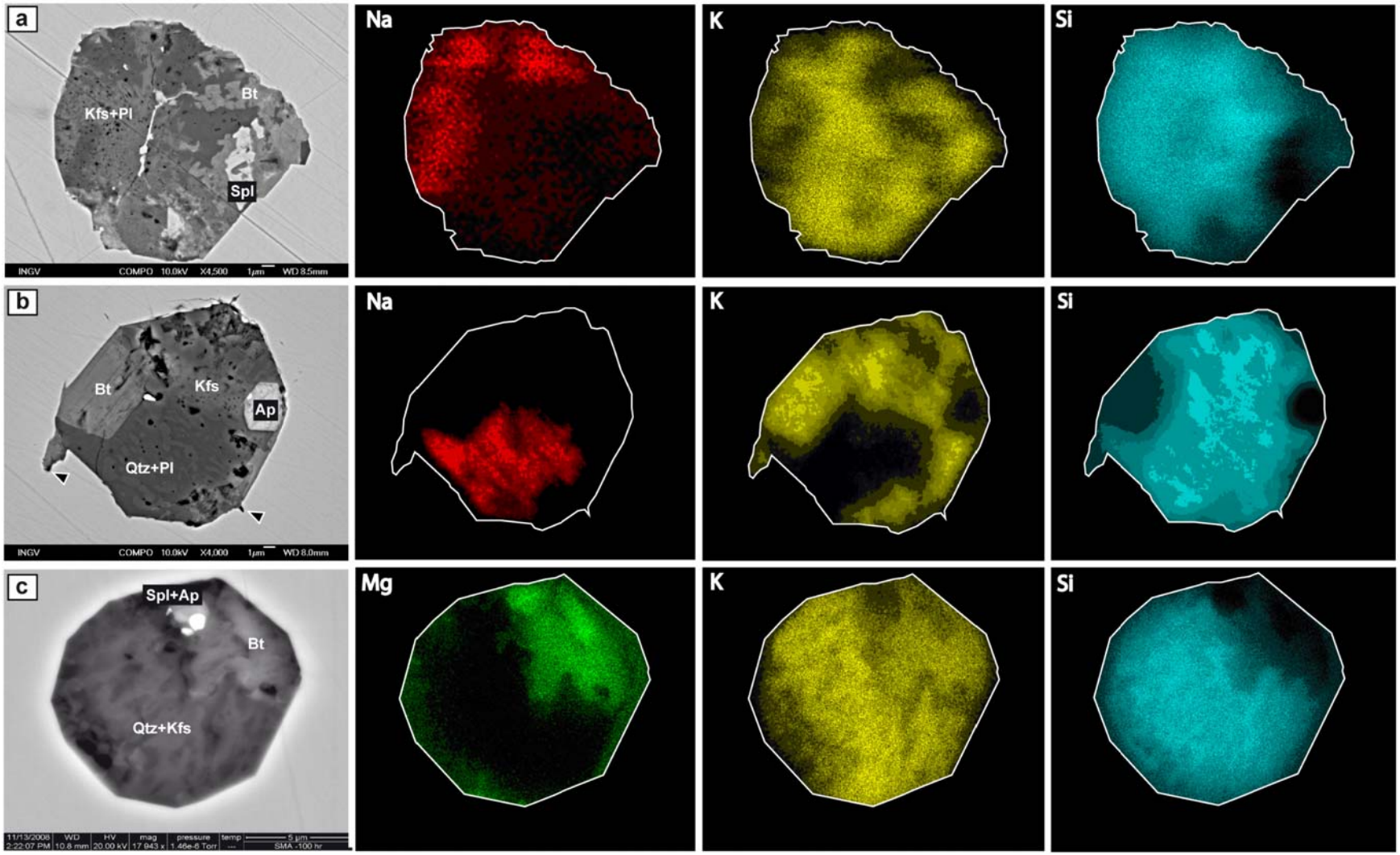

Figure 13: *BSE images (a, b) and SE image (c) of three nanogranites with relative X-ray maps on nanogranites.*

	MI225_1	MI226_2	MI229
Na_2O	0.17	0.10	0.07
MgO	16.93	15.16	17.19
Al_2O_3	22.55	21.01	22.65
SiO_2	38.47	39.41	39.15
K_2O	10.09	10.34	10.98
CaO	0.00	0.04	0.02
TiO_2	0.05	0.00	0.31
MnO	0.00	0.00	0.00
FeO	9.25	9.10	7.16
Cl	0.51	0.72	0.22
Total	98.02	95.88	97.75
Si	5.395	5.648	5.462
Ti	0.005	0.000	0.033
Al	3.727	3.548	3.724
Fe^{2+}	1.085	1.091	0.835
Mn	0.000	0.000	0.000
Mg	3.539	3.239	3.575
Ca	0.000	0.006	0.003
Na	0.046	0.028	0.019
K	1.805	1.890	1.954
Cl	0.121	0.175	0.052
Total	15.723	15.625	15.656
A site	1.851	1.924	1.976
X_{Mg}	0.77	0.75	0.81

Table 6: *EMP analyses of biotite in nanogranites. All Fe considered as Fe^{2+}. Analytical conditions are reported in section in section 3.3.*

Microstructures suggest that biotite crystallizes as first phase, nucleating preferentially on the MI walls and forming subhedral to euhedral grains, ≤10μm across. Biotite composition (table 6) is Mg-rich (X_{Mg}= 0.75-0.81), with low TiO_2 content (≤0.31 wt%), the latter in agreement with the very low Ti contents of melt produced by metasedimentary protolith (Patiño-Douce and Harris, 1998). Kfs, Pl and Qtz show different mutual relationships, suggesting different crystallization sequences in different inclusions. K-feldspar occurs as euhedral to anhedral crystals, ≤10μm across, and may form with plagioclase a very fine grained (≥100 nm) aggregate (Fig.13a and related maps). K-feldspar may also crystallize in micrographic structures with large quartz crystals (Fig.13c and related maps). Based on X-ray maps of elements listed in section 2.3.1(see also Sup.Mat.2), plagioclase forms subhedral to round crystals, ≤5 μm across, and has an albite-rich composition. In places plagioclase forms granophyric structures with quartz, where elongated Pl grains are

oriented (Fig.13b and related maps). Quartz may also occur as inclusion in large grains of K-feldspar or as interstitial phase (Fig.13a). In places anhedral apatite and subhedral spinel form aggregates (Fig.13c).

According to the mineral assemblage and X-ray elemental maps, analyzed MI have a granitic bulk composition, with K higher than Na, low Ca (in fact apatite is the only Ca-bearing phase), and low Fe (Mg-rich biotite as only detected mafic mineral).

Because of this kind of compositional inference is highly qualitative, the crystallized MI have been re-melted and homogenized to characterize the bulk composition. Procedures and results of this approach and are discussed in detail in sections 2.3.2 and 2.6.

Both mineral assemblage and crystallization structures, e.g. graphic intergrowths, are typical of a magmatic intrusive rock and the grain size of the crystals is 10^{-2} to 10^{1} μm: based on these considerations, these crystallized inclusions have been then named *nanogranites* (Cesare et al., 2009).

A sub-type of MI consists of partially crystallized inclusions, that can be recognized only at FEG electron microscope investigation (see fig.3,4 in Sup.Mat.2). These consist of biotite, K-feldspar, quartz, an unknown phase (≤60 area%), and apatite, spinel and rare rutile as mineral accessories (Fig.14 and 2a in Sup. Mat.1). Also in this case MI shape is variable from well developed negative-crystal to irregular. Biotite, K-feldspar and quartz present same features as in crystallized inclusions, but no plagioclase has been detected. EMP analyses on the unknown phase provided a silica-rich granitic composition, with similar K_2O and Na_2O contents (3.5 wt%), CaO=2.3 wt% and FeO≈1 wt% (table 7). ASI (Alumina Saturation Index) values are quite consistent, in the range 0.74-0.83. Since this composition is not compatible with any rock-forming mineral, the interstitial unknown phase has been interpreted as the melt residue left from partial crystallization. Often melt microstructures have cuspate-lobate geometries (*red arrow*, Fig.14c) resembling the shape of the pseudomorphs of melt-filled pores, but in the present case melt is still present, preserved as glass. Locally residual melt presents a porosity (Fig.14b,d and 3f in Sup.Mat.1).

The elemental distribution within partially crystallized inclusions shows that Na, Ca and Cl have the same distribution, with the highest concentration in the residual melt (Fig.15 and Fig.3,4 in sup.Mat.2). This is different from crystallized inclusions, where Na, Ca and Cl have the highest concentrations respectively in plagioclase, apatite and biotite. Such a partitioning is

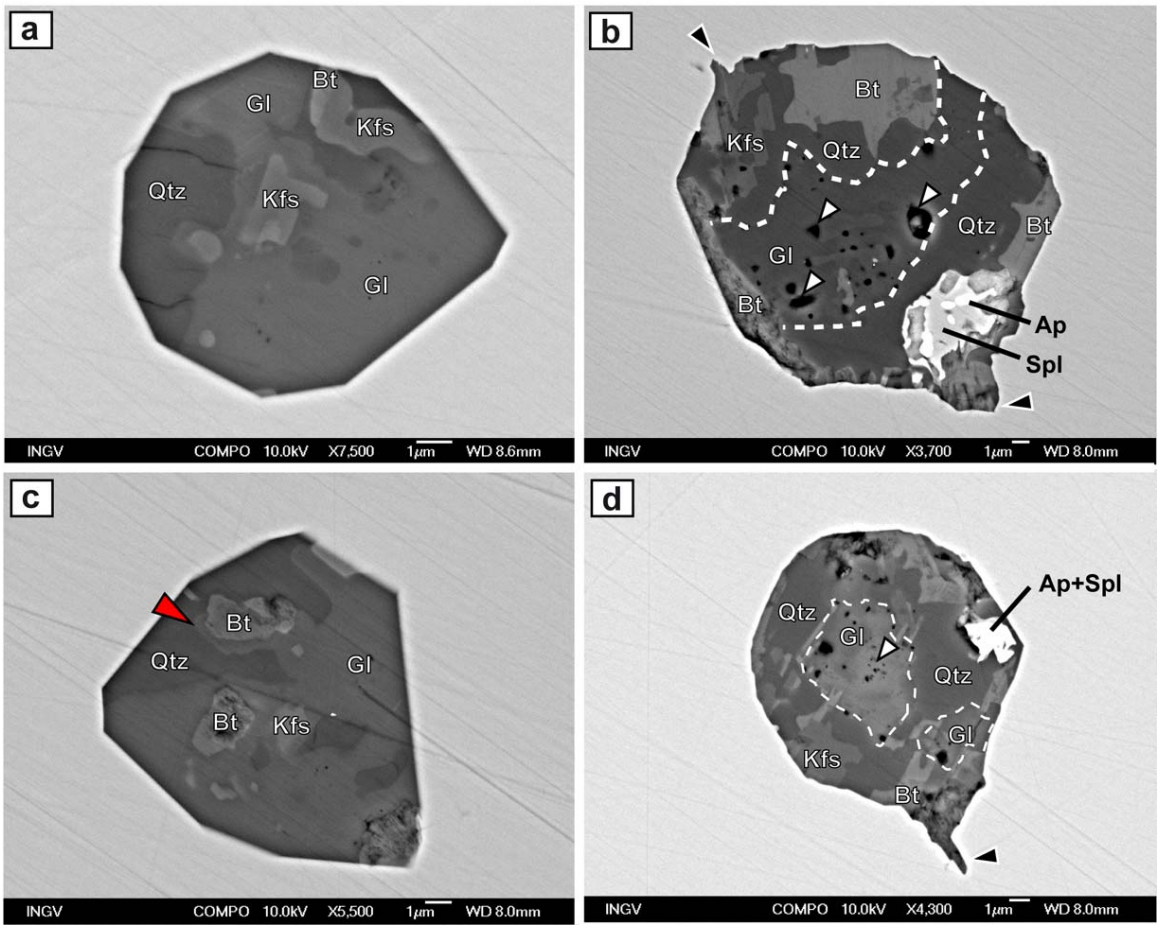

Figure 14: *BSE images of partially crystallized MI. Black arrows: decrepitation microfractures; red arrow: cuspate microstructure resembling a pseudomorph of melt-filled pores. Dashed white lines: glass boundaries.*

	MI245_1	MI245_1b	255	255b
SiO_2	72.49	69.78	71.25	72.67
TiO_2	0.04	0.00	0.01	0.00
Al_2O_3	12.89	13.42	13.53	11.47
FeO	0.98	0.96	1.10	1.17
MgO	0.02	0.02	0.02	0.05
CaO	2.52	2.12	2.48	2.21
Na_2O	5.40	4.10	5.85	4.78
K_2O	3.69	5.12	2.74	2.74
P_2O_5	0.08	0.08	0.13	0.19
Total	99.03	96.30	98.83	96.14
ASI	0.74	0.83	0.79	0.77
Norm Qz	24	23	23	31
Norm Ab	46	35	50	40
Norm Or	22	30	16	16
Norm An	0	3	3	2

Table 7: *EMP analyses of glass in partially crystallized MI. All Fe considered as Fe^{2+}. Analytical conditions and Na migration correction are reported in section 3.3.*

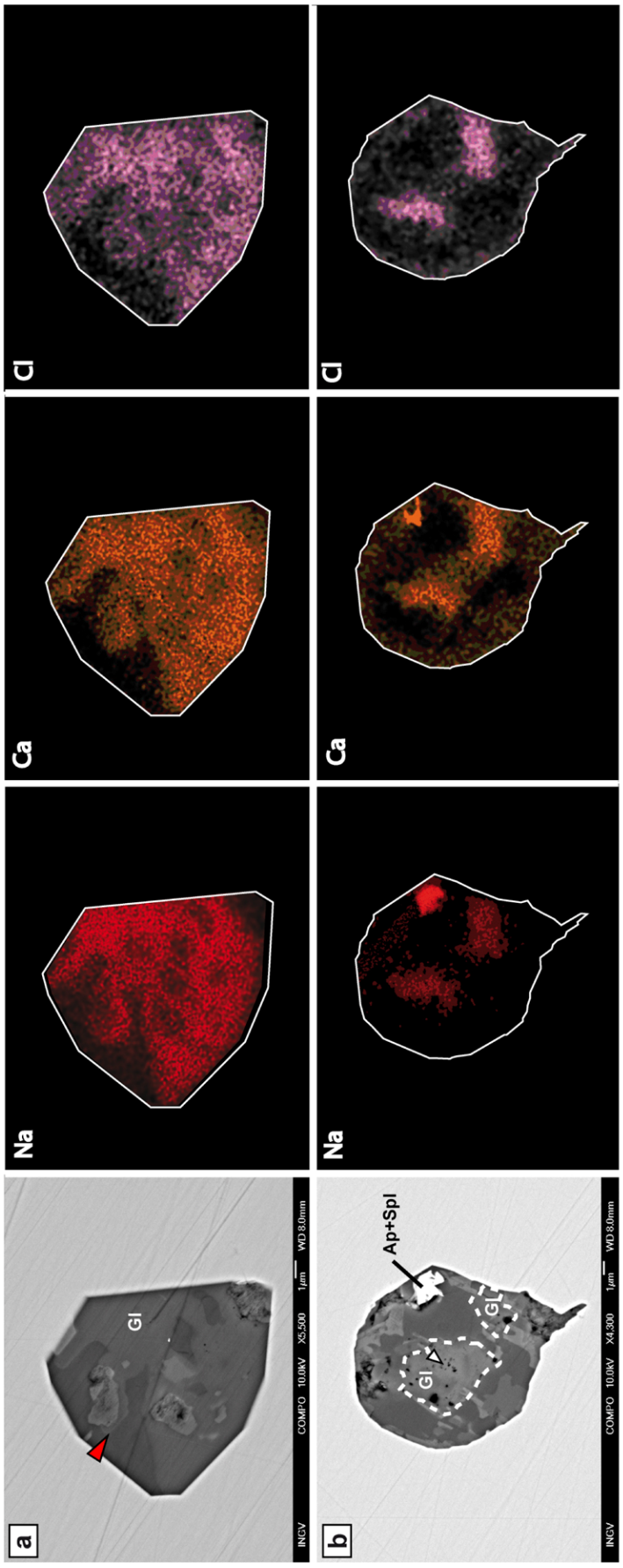

Figure 15: *BSE images and X-ray maps on partially crystallized MI. Red arrow: cuspate microstructure resembling a pseudomorph of melt-filled pores.*

consistent with the crystallization of a granitic melt, that formed biotite, K-feldspar and quartz. The high-Na zone visible on the right hand side of the inclusion in Fig.15b (see also Fig. is an artifact, caused by a Zn-rich spinel clearly visible in BSE image: in fact the emission line Kα of Na and Lα of Zn in the EDS spectra are partially superimposed.

Homogeneous inclusions consist of a unknown phase that in BSE images commonly occurs with euhedral accessory minerals such as rutile, apatite, zircon and titanite. They have a perfect crystal shape, common to all the detected homogeneous inclusions (Fig.16). In few cases (Fig.16c) the garnet-inclusion boundary may present a stepped shape, that resembles the aspect of growing crystal faces (white arrow). Raman spectrum (Fig.17) on the phase hosted in these inclusions displays a prominent broad band centered around 450 cm^{-1}, and less pronounced bands, at around 590, 790 and 1140 cm^{-1}. These bands are characteristic of silica-rich glasses, as shown by the spectrum, reported in Fig.17 for comparison, of the same anhydrous haplogranitic glass used as standard for EMP analyses. According to Raman data, and given the lack of crystallized mineral phases, these inclusions are interpreted as containing preserved primary melt, “frozen” despite the slow rock exhumation. The non-crystalline nature of these inclusions is indirectly attested also by their composition: EMP analyses of the glass (table 8) indicate a persilicic composition, very high in K_2O (>7 wt%) and low in Na_2O (<1 wt% even after correction for Na loss) and CaO, with 1–2 wt% FeO and ASI values in the range 1.15-1.40. These MI are hereafter named “*glassy inclusions*”.

A study of the inclusion diameter was performed on about 300 MI in different clusters to obtain a statistically representative estimation of the size variation between nanogranites and glassy inclusions: the resultant histograms, reported in Fig.18, clearly show that glassy and nanogranite inclusions have different size distributions, with mean values at 8.2 and 12.9 μm, respectively. The implications of this difference in size will be discussed in section 2.8.

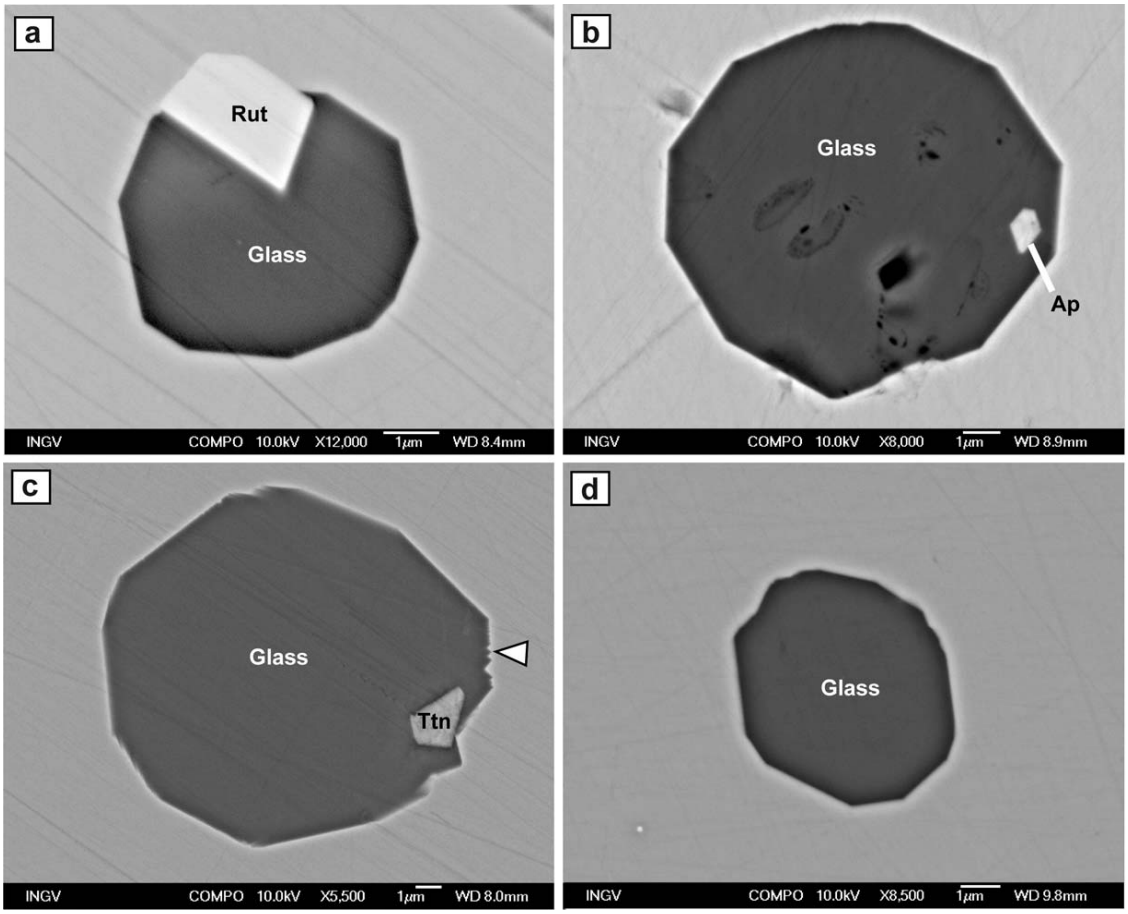

Figure 16: *BSE images of glassy MI. White arrow: stepped faces.*

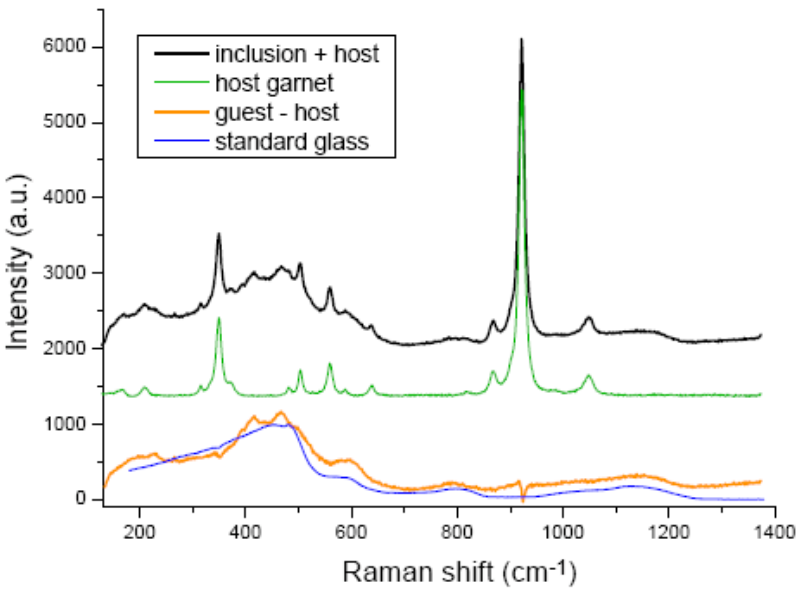

Figure 17: *Stack of Raman spectra of a glassy inclusion from Khondalites (black), the host garnet (green), and the glassy inclusion after subtraction of the contribution of the garnet (orange). The latter is comparable with the Raman signal of the synthetic anhydrous haplogranitic standard glass (blue) studied by Morgan and London, (2005).* ***a.u.*** *=arbitrary units. From Cesare et al. (2009)*

	1	2	3	4	5	6	7
	246	mi08a3	mi08a4	mi94a9	mi94a7	8_1	8_3
SiO_2	77.27	72.20	73.26	74.95	74.31	77.91	77.98
TiO_2	0.00	0.07	0.02	0.49	0.04	0.13	0.00
Al_2O_3	11.96	13.14	12.62	11.40	11.77	11.90	11.84
FeO	0.91	2.65	1.47	1.50	2.43	0.97	1.15
MnO	0.00	0.07	0.04	0.00	0.00	0.00	0.11
MgO	0.02	0.70	0.58	0.05	0.35	0.02	0.00
CaO	0.03	0.03	0.33	0.04	0.05	0.00	0.06
Na_2O	1.02	0.34	0.30	0.41	0.39	0.98	0.91
K_2O	7.56	7.93	8.49	7.13	7.80	7.27	7.96
P_2O_5	n.a.	n.a.	n.a.	n.a.	n.a.	0.12	0.19
Total	98.76	97.13	97.11	95.96	97.13	99.34	100.25
ASI	1.21	1.43	1.23	1.35	1.28	1.26	1.16
Norm Cor	2	4	2	3	3	3	2
Norm Qz	42	37	36	44	40	46	46
Norm Ab	9	3	3	3	3	7	9
Norm Or	45	47	50	42	46	47	45

Table 8: *EMP analyses of glassy inclusions. Analytical conditions and Na migration correction factors for each analyses are reported in section 2.3.1.*

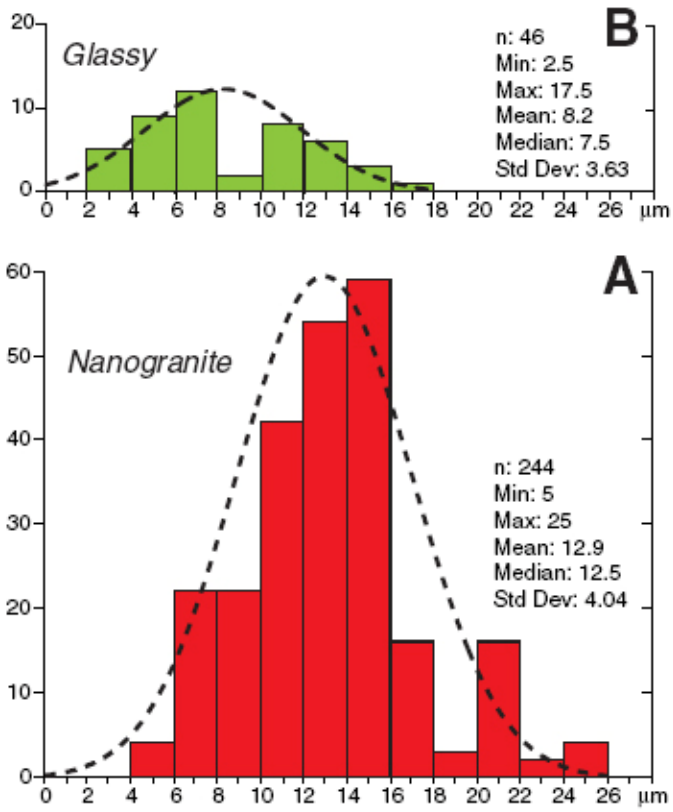

Figure 18: *a) Histogram and Gaussian curve of the diameter (µm) of nanogranite inclusions measured in two clusters in one garnet. B) Histogram and Gaussian curve of the diameter of glassy inclusions in the same clusters (from Cesare et al., 2009).*

2.6) Re-homogenization experiments on nanogranites and melt inclusions composition

As reported in the previous section, collected data on nanogranites are sufficient to roughly define their bulk composition, but uncertainties on the phase identification, mainly due to their small size, and the large variability in microstructure and grain size do not allow a reliable estimate of nanogranite modal composition based on image analyses. The occurrence of glassy inclusions allowed us to collect only a limited microchemical dataset, because of their rarity and their small size, often below the analytical limits. Heating experiments on MI-bearing samples have been therefore performed, in the attempt to re-homogenize the melt crystallized as nanogranites.

The approach is the same as that routinely adopted in the petrological studies of inclusions from plutonic rocks and in mafic-ultramafic xenoliths: inclusions are heated until their crystalline assemblage is completely melted and the vapour bubble commonly visible disappears (Lowenstern, 1995, Bodnar and Student, 2006). However, this is the first time such an approach has been attempted in high-grade metamorphic rocks. The obtained "newly-glassy" inclusions have been then characterized by means of electron-beam microanalytical techniques, with the aim of obtaining a representative dataset of the bulk compositions of the melt originally trapped within garnet.

2.6.1 Microstructural features of the MI in re-heated samples

Under optical investigation in plane-polarized light, MI clusters generally show a number of transparent MI higher (~50% of the total) than the same sample before the heating run (~15%), suggesting that at least a part of the nanogranite inclusions in the cluster melted. The "newly-glassy" inclusions, named hereafter "homogenized inclusions" or simply MI, contain a transparent glass (Fig.19), isotropic at crossed polars (Fig.19f). Homogenized inclusions contain one or more small bubbles, ≤2μm in size (Fig.19b,c,d). The occurrence of a bubbles indicates that melt + vapor homogenization was not reached, as commonly observed instead during microthermometric studies on MI in magmatic rocks (Bodnar and Student, 2006). Therefore the term "homogenized inclusions" in the present work only refers to the fate of the crystalline assemblage on melting.

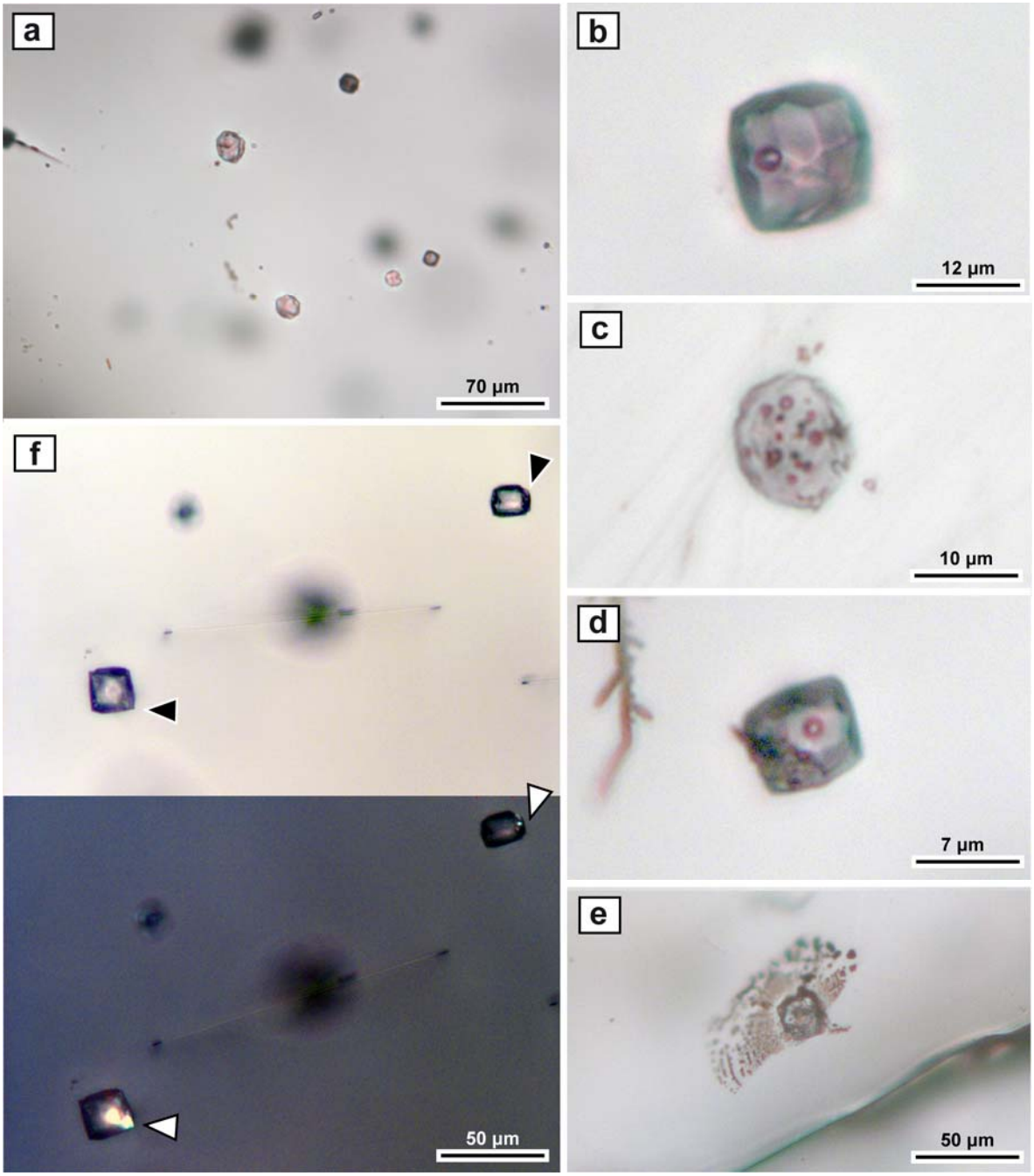

Figure 19: *optical features of homogenized inclusions features: a) common occurrence, plane polarized light; b) well developed negative crystal shape;, plane polarized light; c) occurrence of multiple bubbles, plane-polarized light d) well-developed negative crystal shape, plane-polarized light; e) decrepitation halo, plane-polarized light; f) plane-polarized (left) and crossed polars (right) images of homogenized inclusions with different solid inclusions of variable size. Arrows: solid inclusions.*

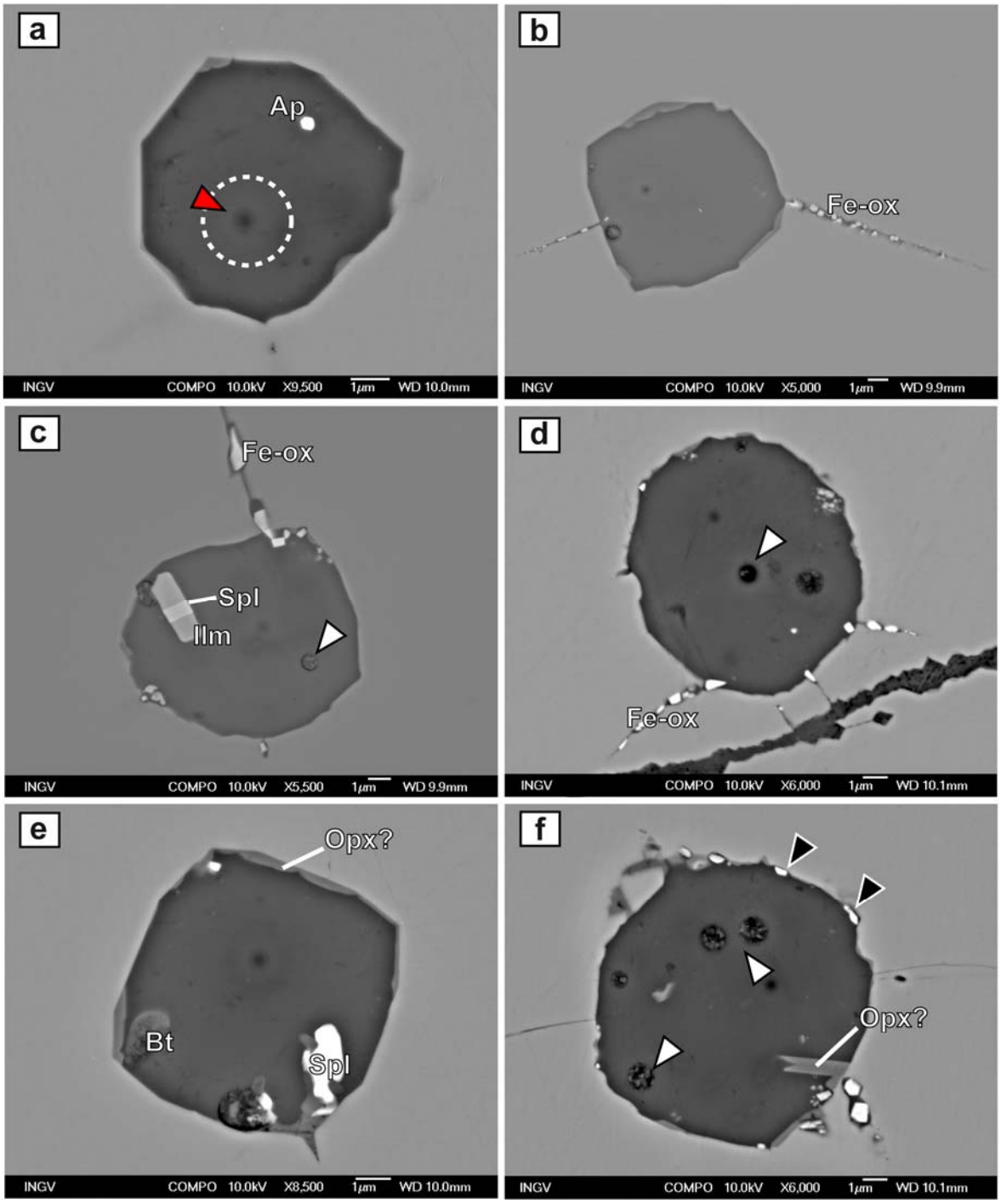

Figure 20: *BSE images of homogenized inclusions. Red arrow: pit left on the sample by the EMP beam; white dashed circle: diameter of the estimated excitation volume produced by the beam in the sample; white arrows: porosity; black arrows: embayments with Fe-oxides.*

At crossed polars one single birefringent crystal phase, usually euhedral in shape, is visible in many inclusions (Fig.19f) and it is likely to be considered as a solid inclusion as

commonly detected both in nanogranites and preserved glassy inclusions. This is also supported by the size of these solid inclusions, that may occupy a variable portion of the total volume (fig.19f). The shape of homogenized inclusions is commonly isometric, often with well developed faceted negative crystal, locally visible in plane-polarized light (Fig. 19a). In places they present a single fracture, symmetrically developed across the MI and partially healed (Fig.19e). Smaller microfractures may occur on MI walls and extend for few microns, often containing dark material. Some inclusions contain glass along with two or more anhedral birefringent crystals, interpreted as relicts of the original polycrystalline aggregate of nanogranites that underwent an incomplete melting. Preserved nanogranites still present are generally larger in size than homogenized inclusions, and are darker than in not reheated samples. They commonly show microfracturation.

While all the transparent inclusions identified under optical microscope observation contain a more or less important amount of glass, BSE investigation showed that only few of them reached a significant degree of melting or a total homogenization of the crystalline assemblage to melt. Investigated MI have a variable shape (Fig.20), from a well developed negative crystal to irregular, and locally with a nanoporosity (white arrow, Fig.20d, f). Solid inclusions that commonly occur along with glass were identified via EDS analyses as rutile, Zn-bearing spinel, apatite and ilmenite (Fig.20a,c,e). In places MI walls show limited embayments (black arrows, Fig.20f), in which a Fe oxide may crystallize in euhedral crystals of variable size, up to 1 μm across. These solids are interpreted as products of garnet-melt interaction. The same phase commonly occurs in cracks developed at MI walls, where crystals may reach ~2μm in size (Fig.20b,f). Partially melted nanogranites, at BSE investigation, show the occurrence of biotite relicts, <1 μm in size (Fig.20e). Most of the investigated inclusions also contain an unknown new phase, not present in nanogranite assemblage, that may form anhedral crystals along the MI boundaries, with size ~0.5 μm, or euhedral crystals, ~2 μm in size, perpendicular to the inclusion walls (Fig. 20f). EDS data showed that this phase contains SiO_2=56 wt%, Al_2O_3 = 9, MgO ~20 wt% and FeO ~12 wt%, resembling the composition of a high T orthopyroxene (e.g. Sato, 2004).

	Glassy inclusions		Homogenized inclusions												
	246	8_1	12_1	12_8	10_7	9_1	9_2	7_5	7_6	6_1	6_3	4_5	4_11	average	std dev
SiO_2	77.56	77.91	70.87	74.11	69.24	77.02	76.28	75.84	76.81	75.92	72.93	72.08	72.42	73.96	2.63
TiO_2	0.00	0.13	0.00	0.27	0.18	0.00	0.10	0.02	0.11	0.20	0.11	0.18	0.00	0.08	0.08
Al_2O_3	12.25	11.90	14.45	13.86	14.90	12.62	11.11	11.93	11.32	11.71	14.12	12.99	13.41	13.31	1.28
FeO	0.91	0.97	3.18	2.94	4.13	2.73	3.12	2.70	2.16	2.38	2.47	3.14	4.39	3.03	0.83
MnO	0.00	0.00	0.06	0.07	0.07	0.01	0.08	0.00	0.06	0.00	0.00	0.00	0.06	0.03	0.03
MgO	0.02	0.02	0.72	0.42	0.90	0.67	0.40	0.43	0.62	0.99	0.91	0.66	0.45	0.76	0.31
CaO	0.03	0.00	0.48	0.70	0.88	0.55	0.54	0.11	0.33	0.57	0.54	0.51	0.63	0.60	0.27
Na_2O	0.73	0.98	1.41	1.02	1.24	0.51	0.70	0.80	1.30	1.07	1.24	1.48	1.38	1.14	0.41
K_2O	7.56	7.27	8.19	7.04	6.24	6.66	6.36	7.14	6.24	5.83	7.60	6.23	6.43	6.76	0.81
P_2O_5	0.00	0.12	0.04	0.10	0.00	0.02	0.02	0.17	0.00	0.00	0.00	0.02	0.02	0.09	0.18
Cl	0.00	0.06	0.36	0.21	0.34	0.08	0.14	0.09	0.18	0.20	0.37	0.44	0.33	0.25	0.12
total	99.05	99.34	99.76	100.74	98.12	100.86	98.85	99.23	99.12	98.88	100.29	97.73	99.53	99.13	1.22
H2O by diff	0.95	0.66	0.24	-0.74	1.88	-0.86	1.16	0.77	0.88	1.12	-0.29	2.27	0.47	0.87	1.22
ASI	1.30	1.26	1.20	1.31	1.43	1.39	1.23	1.29	1.19	1.29	1.26	1.29	1.29	1.30	0.10
Norm Cor	3	2	2	4	4	4	2	3	2	3	3	3	3	3	1
Norm Qz	44	44	31	42	40	50	50	46	47	50	37	42	41	42	5
Norm Ab	6	8	14	10	13	5	7	7	12	11	12	15	14	11	4
Norm Or	45	43	56	48	47	45	43	47	41	40	51	44	45	47	5
Norm An	0	0	2	3	4	3	3	0	2	3	3	2	3	2	1
Q/(Q+Or)	0.49	0.50	0.35	0.47	0.46	0.53	0.54	0.49	0.53	0.55	0.42	0.49	0.47	0.47	
Q/ (Q+Ab)	0.88	0.84	0.69	0.81	0.75	0.91	0.88	0.86	0.79	0.83	0.75	0.74	0.74	0.79	

Table 9: *representative EMP analyses of homogenized inclusions and preserved glassy inclusion, reported for comparison. All Fe considered as* Fe^{2+}.

2.6.2 Chemistry of the homogenized glass

EMP analyses were performed on 70 homogenized inclusions identified by optical investigation. Since these inclusions showed different degrees of homogenization, BSE images were acquired for each inclusion to verify its degree of melting and the homogeneity of the volume excited by the EMP electron-beam during the analyses. Based on the collected microstructural information, about 40 analyses have been therefore considered as representative of the glass produced by the (almost) complete re-homogenization of nanogranites.

Representative analyses of homogenized inclusions are reported in table 9, and the complete dataset is presented in the Supplementary Material 2. All the selected homogenized inclusions contain a peraluminous and rhyolitic melt. The average composition has SiO_2=73 wt%, K_2O = 6.7 wt %, and Na_2O ~1 wt%, while CaO content is low, <1 wt%. TiO_2 content, <0.1 wt%, is low and consistent with commonly reported values for anatectic melts (Patiño-Douce and Harris, 1998). FeO content, averaging 3 wt%, shows a wide variation in reported analyses, up to almost 30% relative. ASI values are in the range 1.11-1.54, with average 1.30. The melt composition is similar to that of preserved glassy inclusions in not re-heated samples, as both contain a rhyolitic melt. However, small differences in major elements are visible in table 9, where analyses of preserved glassy inclusions are reported for comparison. The most important variation is the FeO content, lower in preserved glass, ~1 wt%, when compared with homogenized inclusions, 3 wt%. Also the SiO_2 content is slightly different, higher in the first type than in the latter (77 wt% versus 73 wt%). The alkali contents are also different, with higher Na_2O and lower K_2O in homogenized inclusions. The condition $K_2O >> Na_2O$ is anyway still valid.

The analyses of homogenized inclusions show some variations in major elements. The widest variation, in relative percentages, involves the FeO content: as already observed, FeO is generally higher in homogenized inclusions than in preserved glassy inclusions. This suggests that a possible influence of the Fe-rich host garnet on the MI composition should be evaluated, both in terms of possible host melting and of elemental exchange during the experimental runs.

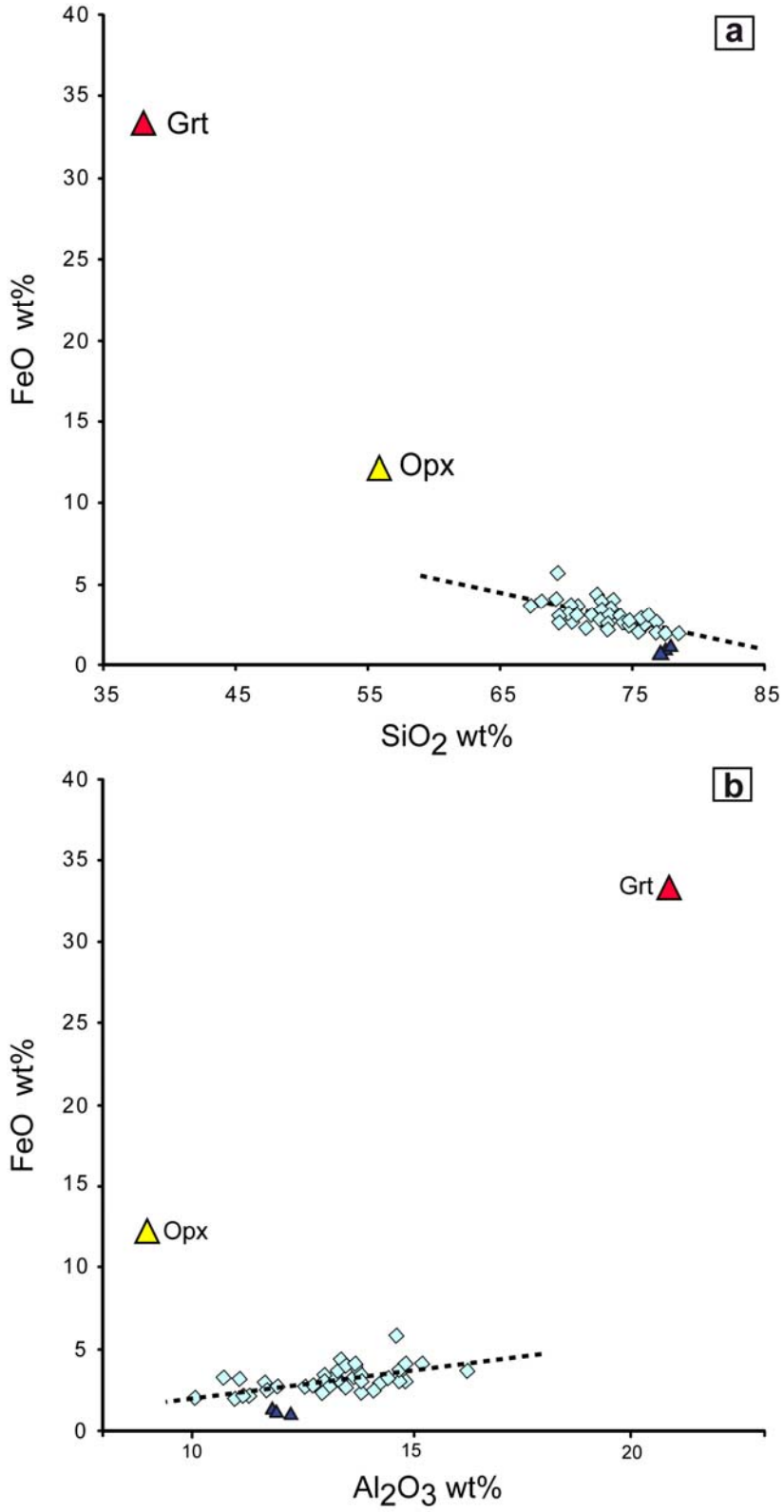

***Figure 21**: Binary compositional plots for homogenized inclusions (light blue squares). Blue triangle: preserved glassy inclusion. a) SiO_2 – FeO diagram; b) Al_2O_3 – FeO diagram.*

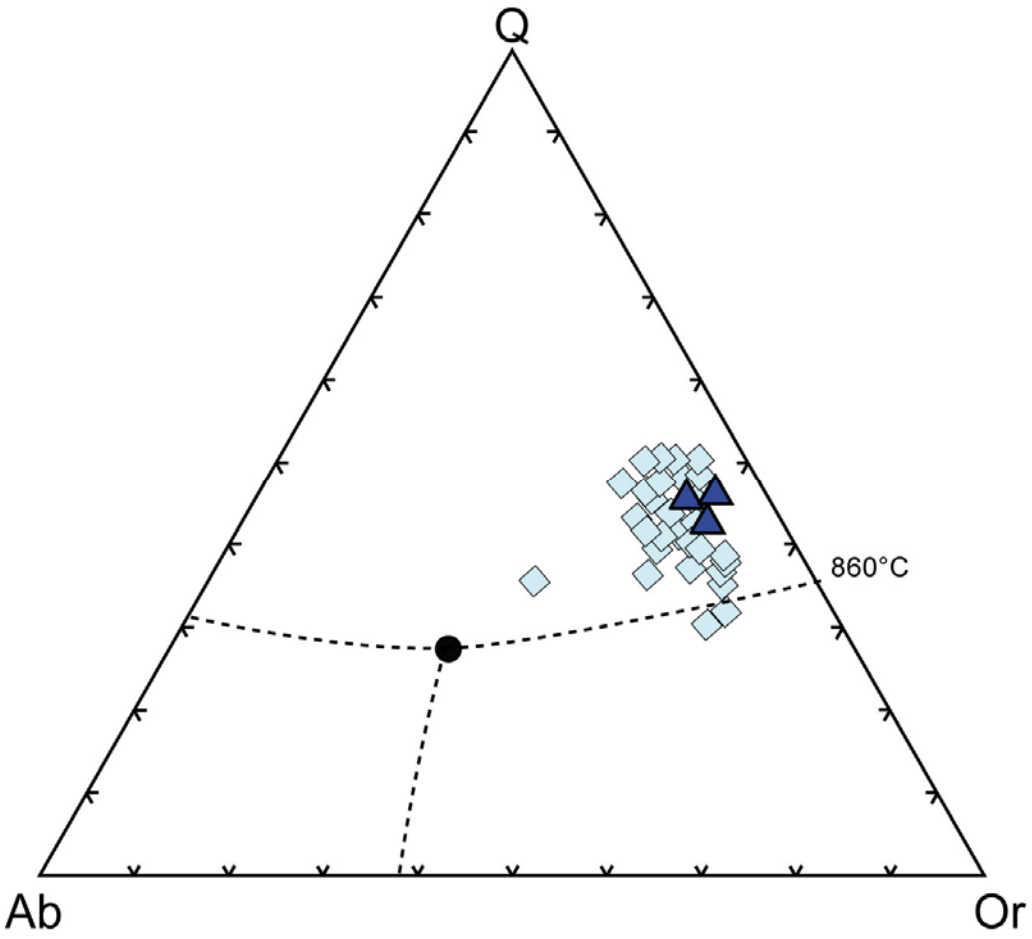

Figure 22: *compositions of homogenized inclusions (light-blue squares) and preserved glassy inclusions (blue triangles) in the CIPW Q-Ab-Or diagram. Cotectic curves for the subaluminous haplogranitic system at 5 kbar and a_{H2O}=0.5 (dashed black lines) and "minimum melt" composition (black dot) for the same conditions are reported for comparison, although in the peraluminous system, cotectic curves move toward Q-richer compositions (Johannes and Holtz, 1996). 860°C: temperature of beginning of melting at the cotectic compositions on the Q-Or join.*

With respect to the SiO_2 content, FeO commonly shows a negative correlation (Fig.21a), roughly defining a trend that does not point toward the garnet composition nor toward aluminous orthopyroxene, also reported in figure. FeO and Al_2O_3 contents, plotted in Fig.21b, define an almost flat trend, with a slightly positive correlation, although less clear, and form a less grouped cluster of points. Also in this case the linear trend does not point toward garnet or orthopyroxene compositions. In these diagrams the composition of preserved glassy inclusions acquired with the same probe diameter (analyses (1),(6) in table 8), are reported for comparison and plot away from the cluster of analyses, according to their lower FeO content. This absence of correlation among plotted data and garnet composition therefore rules out the hypothesis that a portion of the host garnet melted

during the high T experiments, but does not exclude that an elemental exchange occurred on heating (see discussion in section 2.8).

Table 9 also reports CIPW normative parameters for the homogenized MI. Glass is corundum-normative (1-5), and if plotted on the Q-Ab-Or diagram, it defines a cluster close to the Q-Or side (diamonds in Fig.22), according to the reported small amounts of Na with respect to SiO_2 and K_2O. Q/(Q+Or) values are scattered in the range 0.35-0.55. Preserved glassy inclusion compositions (triangles in Fig. 22) plot within the cluster, on its right, i.e. closer to the Q-Or side, in agreement with the amount of Na lower than in the homogenized inclusions. One single analysis plots away from the cluster and close to the center of the diagram.

2.7) Fluid inclusions in sillimanite

The khondalites from Kolliakode also contain fluid inclusions. In fact, in the matrix of Bt-rich melanosomes, large crystals of sillimanite locally contain abundant primary and pseudosecondary FI (Fig.23), whose microstructures suggest entrapment during host growth. In these samples coarse grained sillimanite appears in equilibrium with garnet, in which it may also occur as inclusion close to the rim. This suggests that sillimanite crystallized before and/or during partial melting, and continued to coarsen after garnet growth. A microthermometric study on primary FI was therefore undertaken to allow a better characterization of the pressure conditions at which anatexis took place.

FI occur in the inner part of crystals, forming clusters, ≤500 μm across (white arrows, Fig.23a), in which they may be arranged in linear arrays perpendicular to the Z axis (black arrow, Fig.23a,b), probably marking subsequent stages of growth. FI also occur in few pseudosecondary arrays that cross several linear arrays but never touch crystal boundaries. In places FI may be isolated and occurring in the space among different arrays. FI occurrence is spatially correlated with the abundance of mineral inclusions, and FI clusters often develop in the surrounding of round crystals of graphite and biotite (Fig.23a,b), ≤200μm across, in places enclosing them.

FI are one phase, ≤25 μm in size, with shape variable from negative crystal to oval, and elongation commonly parallel to the sillimanite Z axis (Fig.23c,d). Often graphite occurs as trapped phase in FI (white arrows, fig.23c,d), along with small crystals of sillimanite, presumably grown on the walls of the inclusion. In inclusion-rich zones the host crystals

present several microcracks that, however, leave unaffected the most part of FI that generally do not present any evidence of post-entrapment textural modifications.

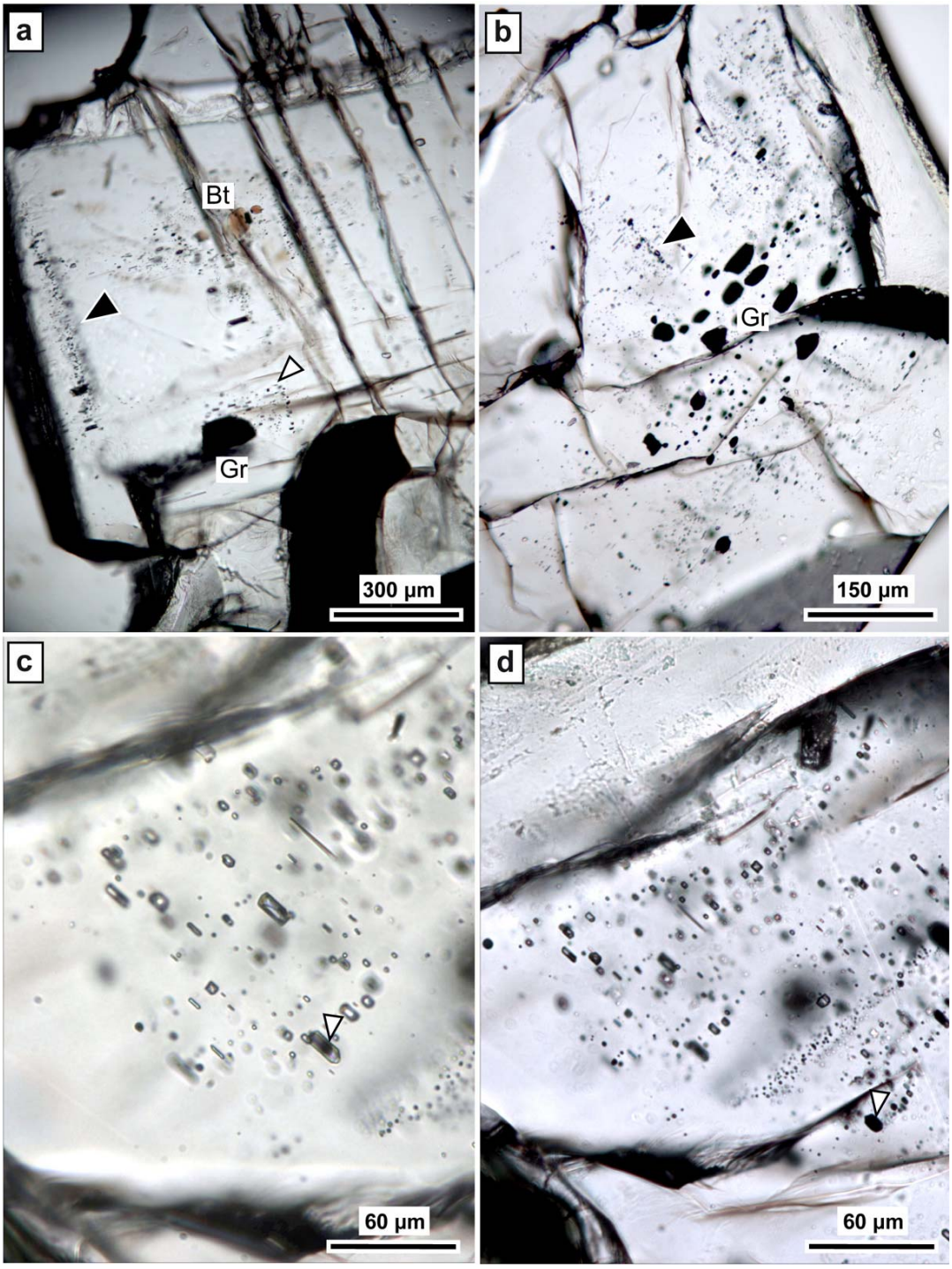

Figure 23: *a) and b) FI occurrence in sillimanite, plane polarized light. White arrow: FI cluster; black arrow: linear array; c) and d) cluster detail: FI elongated parallel to Z axis of the host, plane-polarized light. White arrow: graphite.*

During the microthermometric runs, the melting of solid CO_2 ($T_m^{CO_2}$) and the homogenization of CO_2 ($T_h^{CO_2}$) have been observed on heating from -180°C. The fluid has a $T_m^{CO_2}$ in the range -59.5 / -57.3°C and $T_h^{CO_2}$ in the range -5.3 / 12.6°C. The CO_2 homogenization occurs to liquid via bubble contraction and disappearance (L+V→L). Total microthemometric data from about 40 FI are plotted in the histograms of Fig.24. The measured $T_m^{CO_2}$ values are slightly lower than -56.6°C and suggest that FI contain a CO_2-rich fluid with low amounts of other chemical species. $T_h^{CO_2}$ are relatively well grouped, with average around T=0°C, and the occurrence of homogenization to liquid indicates that trapped fluid has high density.

Raman analyses have been carried out to detect and quantify the gas species present in the FI, investigating the spectral region between 1000 and 4200 cm^{-1}, where the vibrational modes of the most important geological fluids occur. Analyzed FI mainly contain CO_2 and N_2, with negligible traces of CH_4. Collected Raman spectra (Fig.25) always show the two peaks of CO_2 ($2\nu_2$ and ν_1) at 1388 cm^{-1} and 1285 cm^{-1},respectively and the N_2 peak at 2336 cm^{-1}. The CH_4 peak occurs at 2911 cm^{-1} (observed in 1/10 of studied FI). Molar ratios of the gaseous phases, χ_a, were calculated using the relation

$$\chi_a = [A_a/(\sigma_a \zeta_a)]/\sum_i [A_i/(\sigma_i \zeta_i)] \qquad (1)$$

where A_a is the area of the characteristic Raman peak (or band), σ_a the Raman scattering cross section (Burke, 2001) and ζ_a is the Raman instrument correction factor for the component *a*. For our purposes, the considered correction factors are IF_{CO2} = 0.9, IF_{N2} = 1.1, IF_{CH4} = 2.2, previously determined for the Raman instrument in the Fluids Research Laboratory at Virginia Tech using a standard gas mixture (R. J. Bodnar, pers. comm.). compositions estimated by this approach are reported in table 10. The average composition of FI is 92 mol% CO_2, 8 mol% N_2, with CH_4 ≤2 mol%, with CO2 content variable in the range 83-97 mol%.

Based on the estimated composition and MT data, FI density was calculated by means of Loner H, from Software Package FLUIDS, v.2 (Bakker, 2009). Density value has a range 0.81-0.88 gcm^{-3}, with the highest density corresponding to $T_h^{CO_2}$ = -3.6°C. The occurrence of a density range rather than one single value suggests that FI probably underwent slight post entrapment modifications.

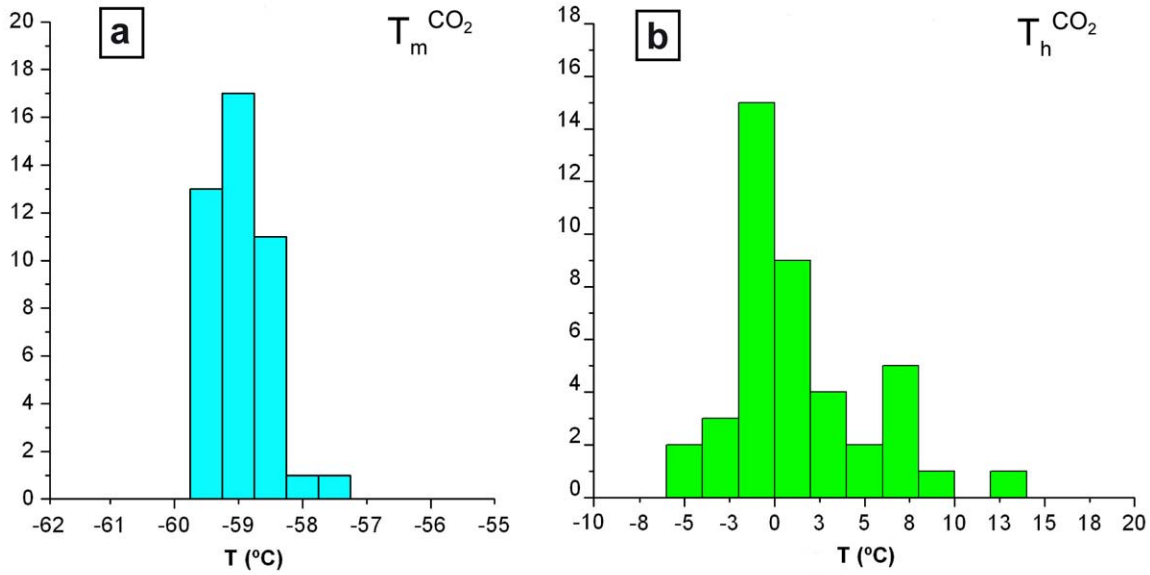

Figure 24: *microthermometric data on FI in sillimanite. a) CO_2 melting T; b) CO_2 homogenization T.*

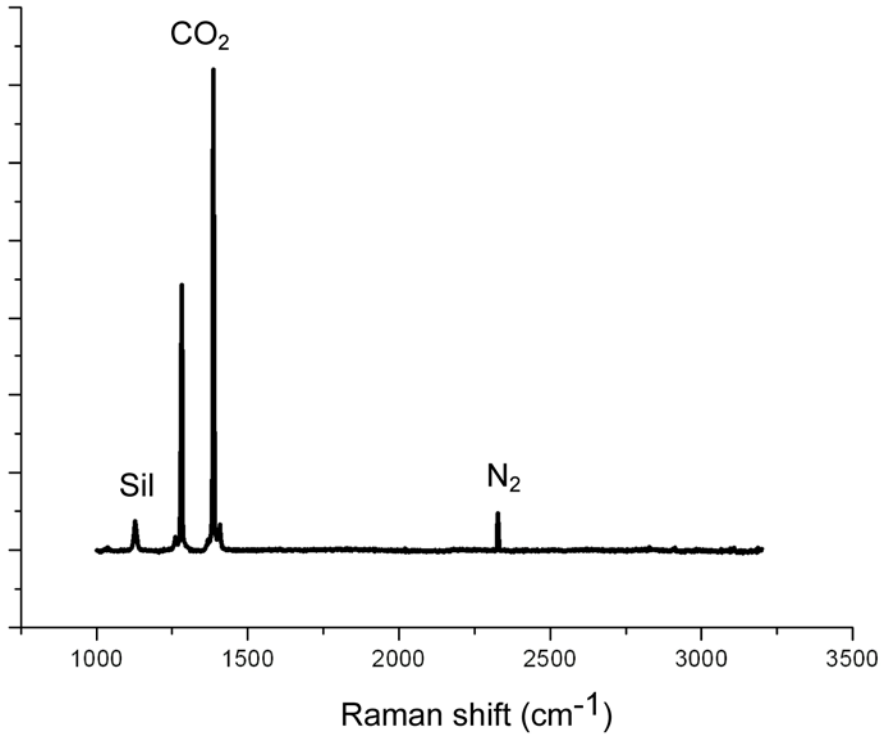

Figure 25: *representative FI Raman spectra. Sil: characteristic sillimanite peak in the investigated spectral region.*

	CO_2	N_2	CH_4	T_h^{CO2}
A	0.93	0.07	0.00	-0.8
B	0.97	0.03	0.00	2.5
C	0.91	0.09	0.00	-0.4
D	0.88	0.12	0.00	-0.4
E	0.89	0.11	0.00	-0.4
F	0.92	0.08	0.00	0.4
G	0.93	0.07	0.00	3.6
H	0.94	0.06	0.00	n.d.
I	0.96	0.04	0.00	n.d.
L	0.93	0.07	0.00	0.8
M	0.92	0.07	0.00	6.2
N	0.92	0.07	0.01	5.5
O	0.91	0.08	0.01	6.2
P	0.92	0.08	0.00	7.4
V	0.93	0.07	0.01	1.3
Z	0.92	0.08	0.00	-1.5
X	0.92	0.08	0.00	-2.1
Y	0.92	0.08	0.00	-3.6
XX	0.83	0.15	0.02	0
YY	0.93	0.06	0.01	-2.8
Average	0.92	0.08	0.00	
Std. dev.	0.03	0.03	0.01	

Table 10: *gas composition (mol %) of the analyzed fluid inclusions (n=22) in sillimanite, calculated from Raman spectroscopy; n.d: not determined on the reported FI.*

Isochores were determined by means of the software package FLUIDS, Program 2: ISOC, version 01/03 (Bakker 2003), applying the EOS developed by Holloway (1977) and Flowers (1979) for CO_2-N_2 mixtures. Calculated isochores, reported in Fig.26, define a pressure range of about 2 kbar in the inferred T interval of trapping (800-900°C), as a result of the measured range of density of FI. In metamorphic rocks changes in FI density commonly occur if the post-entrapment cooling trajectory of the host rocks do not follow a path similar to the isochore defined by the FI density value (e.g. Touret, 2009). Proposed post peak path for Khondalites in this area involves a limited cooling until ~800°C (Nandakumar and Harley, 2000), followed by a isothermal decompression (Santosh, 1987) which define therefore a retrograde path mainly characterized by depressurization. In this case the internal fluid pressure remains almost constant, whereas that in the surrounding host is progressively lowered, so that the conditions of microfracturing of the host may be attained, with FI partial decrepitation and subsequent density decrease due to volume expansion and leakage. Based on this consideration, the highest density FI is considered also the less re-equilibrated, and therefore the related calculated pressure value is likely to be the closer one to the entrapment conditions. The highest density isochore is very close

(within error) to the proposed conditions for equilibration of the Grt-Crd-Bt-Sil-Spl assemblage in the Bt-rich melanosome, 820°C and 5 kbar (L. Tajcmanova, pers.comm), suggesting that FI-bearing, coarse-grained sillimanite may have crystallized or re-crystallized at these conditions. If compared with P conditions proposed for the central part of the KKB, P values retrieved by MT means are slightly (6-8 kbar, Cenki et al., 2002) to notably lower (10 kbar, Tadokoro et al., 2008). However it must be noted that values reported in literature may not apply to the present situation, that does not represent the stage of maximum P recorded by the rock. In fact the occurrence of rutile inclusions in some garnets suggests that the early crystallization of garnet took place at higher pressures than those at which the rock is now chemically reequilibrated.

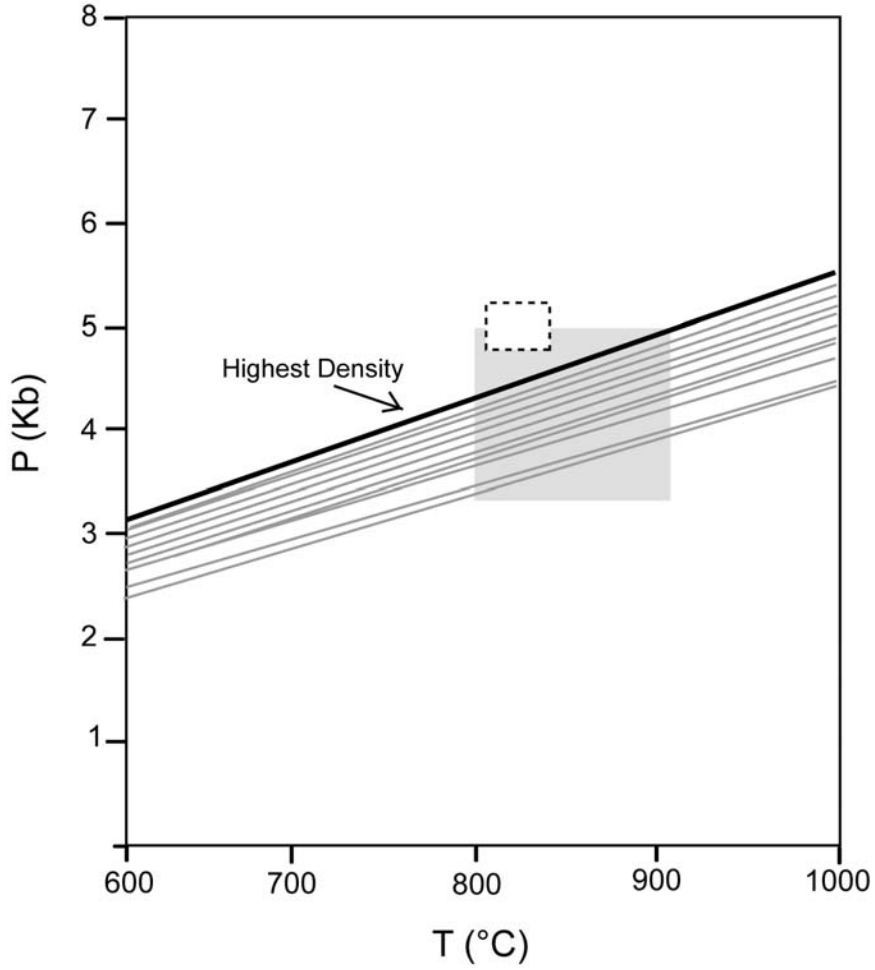

Figure 26: *PT diagram with calculated isochores. Bold line: maximum density isochore. Light gray box: inferred T interval of trapping. Dashed box: equilibration conditions of the Grt-Crd-Bt-Sil-Spl assemblage in FI-bearing samples (L. Tajcmanova, pers.comm.).*

2-8) Discussion

Melt inclusions occur in garnet from khondalites collected in the Koliakkode quarry, in the Kerala Khondalite Belt, India. Their microstructural occurrence suggests that MI entrapment occurred during garnet growth during partial melting, and therefore that MI represent small portions of the melt produced by anatexis of metapelitic migmatites. MI-bearing samples are rare and garnet is the only phase that seems to contain MI. Garnet may crystallize in two different melanosome types, Bt-rich and Bt-poor, intimately connected since they coexist also at the thin section scale. Although modal abundance of garnet is high in both melanosome types, only few porphyroblasts host MI and these are more abundant in the Bt-poor melanosome. Garnet composition is always rich in almandine component, and no systematic differences in composition were found between MI-bearing and MI-free garnets, except in Bt-rich melanosome where the first type is slightly more enriched in pyrope component than the latter.

Two main type of inclusions were identified, nanogranites and glassy inclusions. The first type is slightly larger in size and contain a polycrystalline aggregate with variable grain size, the second type is smaller and contains glass coexistent with solid inclusions. A smaller portion of clusters is formed by a third MI type, intermediate between the two main types, formed in variable proportions by a polycrystalline aggregate and preserved glass. Nanogranites contain quartz, biotite, K-feldspar and plagioclase, and according to the phase assemblage and the collected X-ray maps, these inclusions have a granitic composition, with K higher than Na and Ca, and Mg higher than Fe, as showed by the occurrence of Mg-rich biotite. Similar composition is shown by partially crystallized inclusions: in fact although no plagioclase has been detected, Na is present along with Ca in the residual melt. Glassy inclusions show a peraluminous, ultrapotassic rhyolitic composition, consistent with the phase assemblage recognized in nanogranites, and characterized by ASI values typical of granitic melts in equilibrium with peraluminous minerals (Acosta-Vigil, 2003). Based on these considerations, all the studied inclusions are likely to have contained (nanogranites) or contain (glassy inclusions) the same anatectic melt. The widespread occurrence of Zn-bearing spinel, present as solid inclusion in about 50% of the studied MI, is consistent with the presence of round crystals of spinel, with slightly larger size, in the host garnet.

Plotting close to the Q-Or join in a Q-Ab-Or ternary diagram (Fig.22), glass composition is far from the “minimum melt” compositions (Johannes and Holtz, 1996) commonly

considered as representative of an anatectic melt (see for example Sawyer, 2008). This ultrapotassic composition, not common in nature, is however similar to that of lavas from the Malani Group (India), interpreted as products of high-temperature crustal anatexis (Maheshwari et al., 1996) and to that of experimental glasses produced by the water-absent partial melting of Na-poor natural pelites (Patiño-Douce and Johnston, 1991). The very low Na content is in agreement with the scarcity or absence of plagioclase in the melanosome of studied samples, and suggests that the melting reaction was close to the (Ti)KFMASH end member Bt + Sil + Qtz ± Ilm = melt + Grt ± Rut (Patiño Douce and Johnston, 1991). The low amount of water in analyzed glass, estimated by difference on the EMP total (Acosta-Vigil et al; 2007, 2003) as 2-4 wt%, suggests a low water activity for the formation of melt, consistent with the occurrence of rare carbonic FI without detectable acqueous phase. Considering these H_2O contents, the glass compositional data indicate melts produced at temperature ≥850°C, in agreement with petrological studies showing that garnet growth by the dehydration melting of biotite took place in these rocks at 6-8 kbar and T> 900°C (Nandakumar and Harley, 2000).

The occurrence of glassy inclusions is a striking finding, because melt is normally expected to crystallize completely in regional, slowly cooled migmatite terrains, as it occurred for melt in nanogranites. Since geochronological data indicate that, after anatexis, the rocks of the KKB took at least 60 m.y. to cool from 850 °C to c. 350 °C (Cenki et al., 2004), the delay in nucleation by supercooling of melt in inclusions (Donaldson, 1979) should be minimal and negligible for the present case study, and we can rule out very rapid cooling as the possible cause of glass preservation. Another cause could be the chemical composition of glass, for example a high viscosity or low volatile content slowing down diffusion of elements toward growing nuclei. However, glassy inclusions coexist with totally crystallized ones in the same clusters, and it is unlikely that chemical inhomogeneities in granitic melts can occur at length scales <100 μm. This conclusion will be reinforced in the next section, where the bulk composition of rehomogenized nanogranite inclusions will be discussed. One measurable parameter differing among glassy and nanogranite inclusions is size. Although there is a significant overlap, the two populations are statistically different (as visible in Fig.18) and it is likely that this difference in size was influential in the crystallization of melt droplets, so that (most of) the smaller inclusions remained amorphous (glassy) because of inhibited nucleation. The control of

pore size on nucleation is a well-known phenomenon in acqueous solutions (Putnis et al., 1995), where the finer pores maintain a higher threshold supersaturation. However, the critical physicochemical parameters of this process are still obscure, especially in silicate melts from which it is also reported (Holness and Sawyer, 2008): aspects such as diffusion gradients in the confined fluid and/or the critical dimension of crystal nuclei are qualitatively important (Putnis et al., 1995; Muncill and Lasaga, 1988). To this respect, it is interesting to note that: i) reported critical nucleus dimensions are 100–500 nm for olivine, and ii) plagioclase has much slower nucleation kinetics possibly due to a considerably larger critical nucleus size (Donaldson, 1979; Muncill and Lasaga, 1988). Therefore, crystallization was probably inhibited because the small inclusion volume did not allow the establishment of concentration gradients high enough to form the “large” critical nuclei of feldspar.

As already shown by the presence of glassy inclusions, MI have different behaviour on cooling also within the same cluster, markedly in crystallization sequence and in crystallization degrees. Different behaviour on cooling may be expected in melts with different compositions: as stated above, chemical inhomogenities at the investigated scale are not expected, and moreover crystallized inclusions show a constant phase assemblage. The differences in crystallization degrees observed between nanogranites and partially crystallized inclusions is difficult to explain, in fact in this case there is no statistic correlation among MI size and degree of crystallization, and therefore the size influence proposed to explain the glassy inclusions occurrence does not apply to this context.

In places largest nanogranites and few partially crystallized inclusions show microfractures. No external components seems to have entered the inclusions, since no differences in assemblage are visible between MI with microfractures and the intact ones, and microfractures are limited to the MI surrounding. Biotite crystallizes in microfractures, suggesting that their formation predates the start of melt crystallization. Since no important differential pressure is expected in a low-H_2O melt on cooling, observed microfractures are likely to be due to local defects of garnet lattice, whose crystalline structure is weakened by the occurrence of the MI and therefore more subject to be cracked along the post entrapment path.

Reheating experiments led to the re-melting of the nanogranites in garnet. This is confirmed by the increased amount of glassy inclusions in the clusters, recognizable under microscope observation, and by the finding of glass in many of the studied MI under BSE investigation. The degree of melting obtained in the studied MI is variable, and generally lower in larger inclusions. Retrieved compositional data on homogenized inclusions are consistent with both the compositions of the preserved glassy inclusions and the phase assemblage of nanogranites previously discussed. This strongly support the hypothesis that a homogeneous peraluminous rhyolitic melt was trapped during garnet growth, and that this melt represents the anatectic melt produced by partial melting in the khondalites. Glass analyses from both re-heated and natural samples plot in a relatively small area on the right hand side of the Q-Ab-Or diagram (fig.22). The new compositional data confirm the Na-poor nature of the trapped melt, already observed in preserved glassy inclusions, with a composition very far from the minimum melt composition (Johannes and Holtz, 1996).

Major element variations are visible in the analyses of homogenized inclusions. These may be related to incomplete melting or analytical uncertainties, despite of the careful microstructural study performed to select homogeneous volumes of glass. In fact the volume of sample excited by the electron-beam may comprise also garnet in very shallow inclusions, with resultant contribution of the host to the analytical results. However this effect is likely to be very limited because 1) the analytical parameters are expected to produce a small excitation volume in the sample, with maximum diameter estimated as 2-2.5 μm, as visible in fig.20, and 2) very shallow inclusions were recognized by BSE investigation and excluded from the set of workable inclusions.

One of the most variable parameters of analyzed glasses is the FeO content, both among the collected analyses on homogenized inclusions and between these and the preserved glassy inclusions in not-reheated samples. FeO variations could be produced by melting of small portions of garnet during the heating runs. The melting of the host crystals is commonly expected during re-homogenization experiments on MI in magmatic rocks, because of the parental character of the trapped melt with respect to the host crystal. In the present case, however, host garnet and trapped melt are products of the same metamorphic reaction, in equilibrium with each other at the T values at which the melt is present, and therefore host melting on re-homogenization is (almost) not expected, unless

the trapping T is largely exceeded. The absence -or the limited amount- of garnet melting is confirmed by the lack of correlation among FeO variations both respect to SiO_2 and Al_2O_3, and by the collected BSE images of homogenized inclusions, where negative crystal shapes are quite common and embayments in MI walls, that suggest a reaction among garnet and melt during the re-melting, are extremely limited. Moreover the occurrence of Fe-oxides along with the embayments suggest that these took all the FeO made available by garnet reaction. Based on these considerations, the FeO content of homogenized inclusions may have been influenced by an elemental exchange on heating.

However, the discrepancy in FeO content between preserved glassy and homogenized inclusions is difficult to explain also if an elemental exchange with host garnet is taken in account. In fact, if the composition of the latter inclusion type is considered as representative of the original composition of the trapped anatectic melt, this would mean that melt of glassy inclusions lost about 1-2 wt% of the original FeO content toward garnet during the post-entrapment history. This should have caused a corresponding increase in Fe-vicariant elements, Mg and Ca. However, this hypothesis appears untenable because FeO, MgO and CaO contents are lower in glassy inclusions with respect to homogenized inclusions.

The presence of bubbles is reported in almost all the studied inclusions, with the exception of the smaller ones, in which they could be so small to be optically invisible. Their occurrence may be due to (1) the contraction of the melt on cooling, and therefore they would represent shrinkage bubbles, (2) the presence of a fluid phase coexistent with the melt at high T during the heating runs, or to (3) bubble nucleation by decrepitation and decompression during heating.

In the case (1), bubble should have nucleated in the few seconds needed to open the heating stage and put the sample in liquid nitrogen. This hypothesis may be ruled out, because shrinkage bubbles formation in such a short span of time has been observed exclusively in melts with water content higher than the maximum estimated in this study, 4% (R.J. Bodnar, pers.comm.). The occurrence of a fluid phase (case 2) already at high T during heating experiments is impossible to verify both because of the poor quality of the field view during the experimental runs and because of the bubble sizes below the detection limit of the Micro Raman spectroscopy. The lack of data on the hosted fluid phase prevent any further consideration on this hypothesis. A bubble nucleation by partial decrepitation of the inclusion (case 3) appears the most likely explanation. In fact, MI

depressurization during the heating runs is suggested by the commonly observed opening of microfractures on the MI walls at T>850°C, and, as outlined by Lowenstern (1995), "*rapid decompression and resultant overpressures within the* (silicate melt) *inclusion (…) can result in fracturing of a phenocryst, depressurization and vesiculation*". A further evidence of partial decrepitation, according to Lowenstern (1995) is the occurrence of variable melt-bubbles ratios in different MI of the same cluster, likely to be caused by the different extents of microfracturing suffered by the inclusions, with consequently different extents of depressurization.

In MI study on magmatic rocks, the homogenization T determined through microthermometric studies gives information on the trapping temperature of the MI (Frezzotti, 2001), and therefore on the conditions of growth of the host crystal. In this samples, the retrieved homogenization T, ~1050°C is not consistent with the proposed partial melting conditions for the Khondalites in this area, 850-900°C (Braun et al., 1996; Shabeer, 2004, Nandakumar and Harley, 2000, Cesare et al., 2008) and with the lack of any UHT mineral compatible with the melting T in the host rock assemblage. The homogenization of MI at temperatures higher than the real trapping T is a problem commonly encountered in MI studies of volcanic and plutonic rocks (Bodnar and Student, 2006) if not appropriate heating rates are applied during the heating runs, and for this reason the correct rate is commonly defined by performing several experiments with different techniques to find the most suitable setting to obtain the real entrapment T (Danyushevsky et al., 2002). In the present study, however, the obtained homogenization T values are not expected to be representative of the MI trapping conditions, since the relative scarcity of MI-bearing garnets in khondalites did not allow us to follow the procedure described above, and the proposed heating ramp represents therefore the best compromise between that limitation and our main purpose i.e. the homogenization of the nanogranites.

Chapter 3
"Primary" Fluid Inclusions in Peritectic Garnet from Metapelitic Enclaves, El Hoyazo, Spain

3.1) Introduction

The present chapter discusses the results of a fluid inclusions study performed on peritectic garnet from partially melted metapelitic enclaves, abundant in dacitic lavas from the Neogene Volcanic Province (NVP) in southern Spain. Enclaves contain anatectic melt (Acosta-Vigil et al., 2007, 2010; Cesare et al., 2007; see also chapter 1), preserved as an amorphous phase (glass), in intergranular layers, in microfractures and in melt inclusions. Besides the occurrence of quenched anatectic melt, a peculiar aspect of the El Hoyazo enclaves is the occurrence of fluid-melt immiscibility: anatectic melt was trapped along with a COH fluid phase in different minerals, including cordierite and plagioclase (Cesare et al., 2007) and garnet (Alvarez-Valero et al., 2005a; this study). Fluid-melt immiscibility is a well known phenomenon that has been extensively studied using FI (Roedder, 1992 and references therein), and has been recognized in mafic melts (Andersen and Neumann, 2001), silicic melts (De Vivo and Frezzotti, 1994), as a secondary feature accompanying the crystallization and/or outgassing of magma during cooling (Roedder, 1992), in ore-forming magmatic systems (Student and Bodnar, 2004), and has been reproduced experimentally using synthetic silicate melt and fluid inclusions (Student and Bodnar, 1999). In high grade, partially melted rocks, COH fluids are commonly reported (Touret, 2009), and the coexistence of a CO_2-rich phase and a melt is expected because experimental studies (Holloway, 1976; Tamic et al., 2001) demonstrate the low solubility of CO_2 in silicate melts. However, fluid-melt immiscibility is only seldom reported for granulites and migmatites (Touret, 1971, 1981), probably because MI and FI in HT peak minerals are likely to be destroyed during deformation and re-crystallization during the retrograde PT evolution. The enclaves from El Hoyazo have not experienced a long retrograde history, and therefore they preserve exceptional evidence of primary fluid-melt immiscibility that was developed during peritectic garnet growth and syngenetic origin of anatectic magma.

The PT conditions of the anatectic process at El Hoyazo are still a matter of much debate. Previous studies based on classical geothermobarometers determined that the peak metamorphic partial melting event occurred at 850±50°C and 5-7 kbar (Cesare et al., 1997), followed by biotite dehydration melting at 900°C and 5 kbar. Recently, based

on a pseudosection calculation for sample HO50 that is also used in this study, Tajcmanova et al. (2009) proposed that enclaves equilibrated in the cordierite field at 790-825°C and 5 kbar. However, these conditions do not correspond to those at which garnet formed: both textural and microchemical data (Acosta-Vigil et al. 2007; 2010) indicate that initial garnet growth began early in the melting history of the enclaves, and at temperatures lower than peak values. The pressure at which this event took place is not well constrained, and with this purpose Cesare et al. (2007) estimated pressures based on primary FI coexisting with melt in cordierite and plagioclase. However, their microthermometric study and isochore calculations resulted in pressures of FI and MI entrapment that were very low and inconsistent with their primary nature and the PT estimation based on sample petrology.

A goal of the present study is to refine pressure estimates for the initial stages of partial melting of these rocks. Our research is focused on primary FI in the peritectic garnet, selected for study because it is well known that "harder" minerals are less likely to re-equilibrate, both in nature and in the laboratory (Bodnar, 2003), and more likely to preserve original formation conditions: in fact, garnet is known to act as a shelter for trapped fluid inclusions, preserving them from post entrapment modifications (Pretorius and Barton, 2003; Torok et al., 2005, Santosh et al., 1991, 2003).

Data reported in this chapter represent a further contribution to our understanding of conditions of partial melting in the lower crust beneath the NVP. In particular, our results add new constraints to the composition of the fluid phase coexisting with anatectic melt during partial melting of a metapelitic protolith.

3.2) Geological setting

The NVP is located in the Betic Cordillera, which forms the western termination of the Alpine orogen in the Mediterranean region, along with the Moroccan Rif (Fig.1). The area is characterized by a thinned ithosphere, a consequence of the opening of the Alboran Domain in the late Tertiary (Comas et al., 1999). The upwelling of asthenospheric mantle caused an anomalous heat flow, still present in the area, with partial melting of the lower crust and subsequent eruption or emplacement of large volumes of magmas of variable composition, ranging from basaltic andesites to rhyolites, between 15 and 2 Ma (Comas et al., 1999; Zeck and Williams, 2002; Duggen et al., 2004; Cesare et al., 2003, 2009c). Enclaves included in the present study are hosted in high-K calc-alkaline to shoshonitic lavas of upper Miocene age, and represent partially melted metapelites of the lower crust that were brought to the

surface by uprising magmas and emplaced in a shallow submarine environment (Zeck, 1970; Cesare et al., 1997).

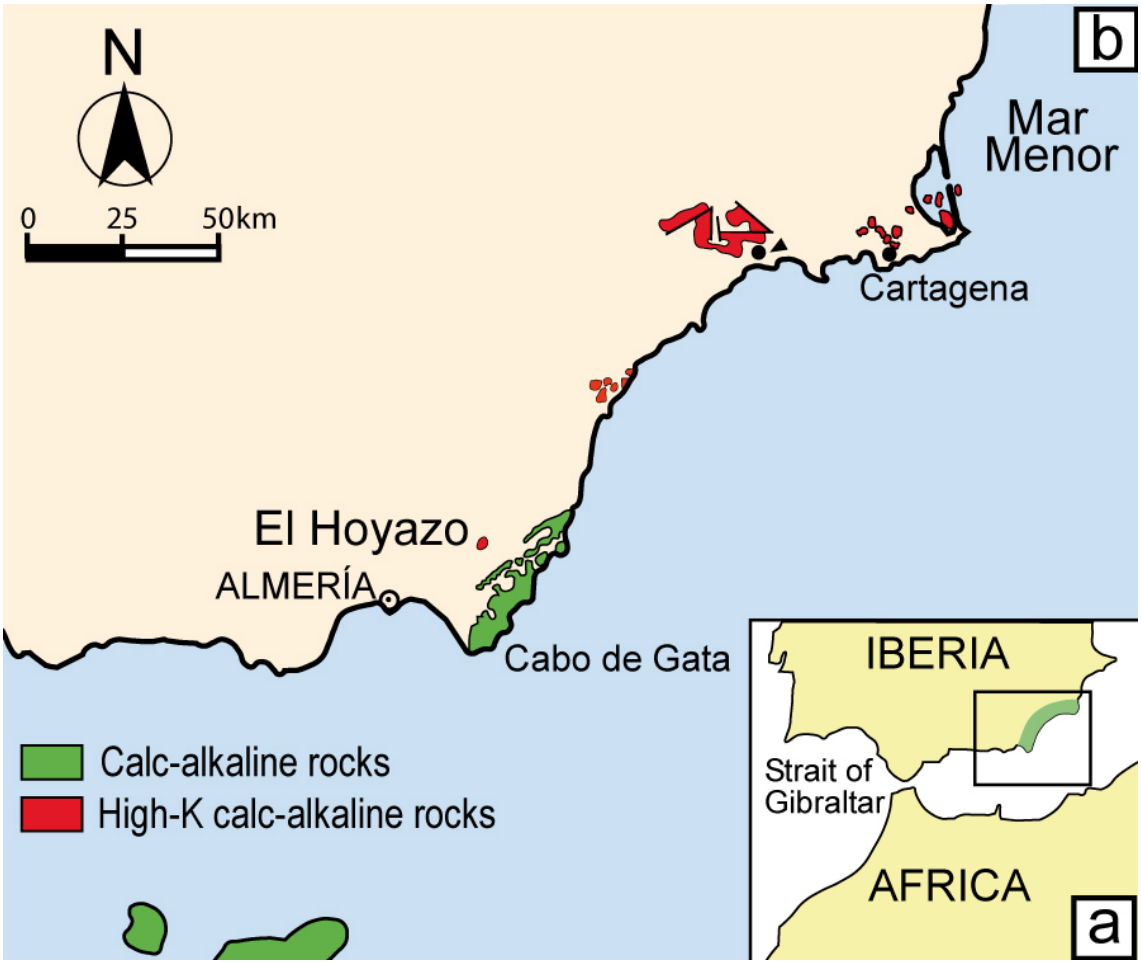

***Figure 1**: the Neogene Volcanic Province, SE Spain. a) geographic scheme of the western Mediterranean, with NVP province in green (box); b) Enlarged box of fig.1a, with location of the main outcrops. Studied samples are from El Hoyazo, in SW part of the NVP, close to Almeria (redrawn after Lopez Ruiz and Rodriguez Badiola, 1980).*

The host lavas are considered largely syngenetic with the enclaves themselves, based on petrographic and isotopic evidence (Zeck, 1970; Munskgaard, 1984, 1985, Perini et al, 2009), although the extent of contamination by mantle-derived magmas is still under debate (Benito et al., 1999; Turner et al., 1999; Duggen et al., 2005; Acosta-Vigil et al.; 2010). The studied enclaves come from El Hoyazo, a small dome of peraluminous dacite in the SW of the NVP. This site is characterized by abundant crustal material (10-15 vol%; Zeck, 1992) that mainly consists of Bt-Grt-Sil and Spl-Crd crustal enclaves. Petrological features of both enclave types have been characterized by several past studies (Zeck, 1970; Cesare, 2000; Cesare et al., 1997, 2000, 2005;

Alvarez-Valero, 2004; Acosta-Vigil et al., 2007; 2010). Despite differences in their microstructures and mineral assemblage, probably reflecting compositionally different protoliths, both enclave types show 1) residual bulk composition, with quartz only present as mineral inclusions, due to extensive melt-extraction (30-60 wt%, Cesare et al., 1997); 2) abundance of graphite (≥1 wt%, Cesare and Maineri, 1999) both as mineral inclusions and as large flakes parallel to foliation, accounting for a graphite-rich protolith, and 3) abundance of glass, interpreted as anatectic melt (Cesare et al., 1997), in thin layers, pockets and MI in minerals.

The occurrence of primary MI in almost every mineral of the assemblage suggests coexistence among melt and growing crystal phases such as garnet, ilmenite, biotite, spinel and plagioclase. While garnet and ilmenite commonly occur as peritectic phases from biotite melting, and therefore are expected to trap inclusions of anatectic melt, other minerals such as plagioclase and biotite are commonly reactants in melting reactions, and should not enclose melt. Cesare and Maineri (1999) explained this apparent paradox by suggesting that rapid heating induced disequilibrium melt production in Bt-Grt-Sil enclaves, according to a reaction such as:

Chl+Ms+Qtz+Ilm+COH fluid phase=Grt+Pl+Sil+Bt+Melt+Gr (1)

that involved a low-grade, graphite-rich protolith, similar to phyllites and schists outcropping in the Alpurrjade Complex of the Betic Cordillera. In the proposed process, the rocks quickly evolved from a low-temperature mineral assemblage to a melt-bearing one, bypassing several intermediate mineral equilibria reactions of the upper amphibolite facies. The products of the proposed reaction (in particular garnet, plagioclase and biotite) are consistent with the observed MI-bearing minerals in the studied samples. The petrological model for the anatexis of Bt-Grt-Sil enclaves has been recently refined by Acosta-Vigil et al. (2010) who proposed that MI trapped in garnet and plagioclase represent the melt produced during the prograde heating of the sample, at 690-750°C, before metamorphic peak was reached at 850°C (Cesare et al., 1997). The age of anatexis beneath El Hoyazo (9.3-9.9 Ma) was determined by Cesare et al., (2003, 2009c) via U-Pb dating on MI-bearing zircons and monazites, while the host dacite extrusion occurred at 6.3 Ma (Zeck and Williams, 2002). This means that these rocks resided in the lower crust for 3 m.y. at partial melting conditions (Cesare et al. 2003).

The presence of a free fluid phase during partial melting of El Hoyazo enclaves, suggested by Cesare and Maineri (1999), is attested by the coeval entrapment of FI and MI, indicating melt-fluid immiscibility. Primary FI and MI in plagioclase and cordierite from Bt-Grt-Sil enclaves were studied by Cesare et al. (2007) to characterize their composition and to better constrain the depth at which anatexis took place. They showed that the trapped fluid is a CO_2-N_2-CH_4 mixture, with >85 mol% CO_2, and traces of CO and H_2S. Calculated isochores for most of the studied FI predict pressures ≤0.5 kbar at the inferred temperature of trapping (800-900°C), much lower than the pressure of 5-7 kbar estimated for the partial melting event. Cesare et al. (2007) back-calculated the compositions of the original fluid phase coexisting with anatectic melt and concluded that leakage of components had occurred, with a loss of about 25 mol% of H_2O, and that, despite their primary appearance, FI inclusions underwent extensive re-equilibration. Therefore, the pressures derived from calculated isochores are not representative of entrapment conditions. Cordierite from the same enclaves is almost H_2O-free and not in chemical equilibrium at the estimated P-T conditions of formation (Della Ventura et al., 2009). In this case, it was proposed that H_2O loss from cordierite was due to the rapid decompression accompanying lava ascent.

3.3) Petrography of the samples

Samples from the two main types of enclaves occurring at el Hoyazo - Bt-Grt-Sil and spl-Crd enclaves - were utilized for this study.

Bt-Grt-Sil enclaves are the most abundant and occur as fragments ≤60 cm (Fig.2a). Their phase assemblage consists of variable proportions of garnet, plagioclase, biotite, sillimanite and glass (Zeck, 1970; Acosta-Vigil et al., 2007). Generally a medium to coarse-grained matrix surrounds large garnet porphyroblasts (≤1cm in diameter) wrapped by Bt-rich folia (Fig.2b). The matrix mainly consists of plagioclase and a fine-grained, sponge-like aggregate of fibrolitic sillimanite and glass (named "mix" by Cesare et al., 1997), forming irregular to elongated domains. Samples also contain graphite, apatite, zircon and monazite, with ilmenite, cordierite, hercynitic spinel, or quartz irregularly distributed.

Garnet porphyroblasts are euhedral to subhedral, and commonly show an inclusion-rich dark core containing biotite, graphite, MI and FI, surrounded by an inclusion-free rim of variable thickness (up to 2 mm). Several generations of biotite, with widely varying size (tens of μm to 4 mm), are present as subhedral to euhedral porphyroblasts. Partially resorbed biotite occurs as inclusions in garnet, plagioclase and cordierite, or in skeletal crystals surrounded by fibrolitic sillimanite and glass mix.

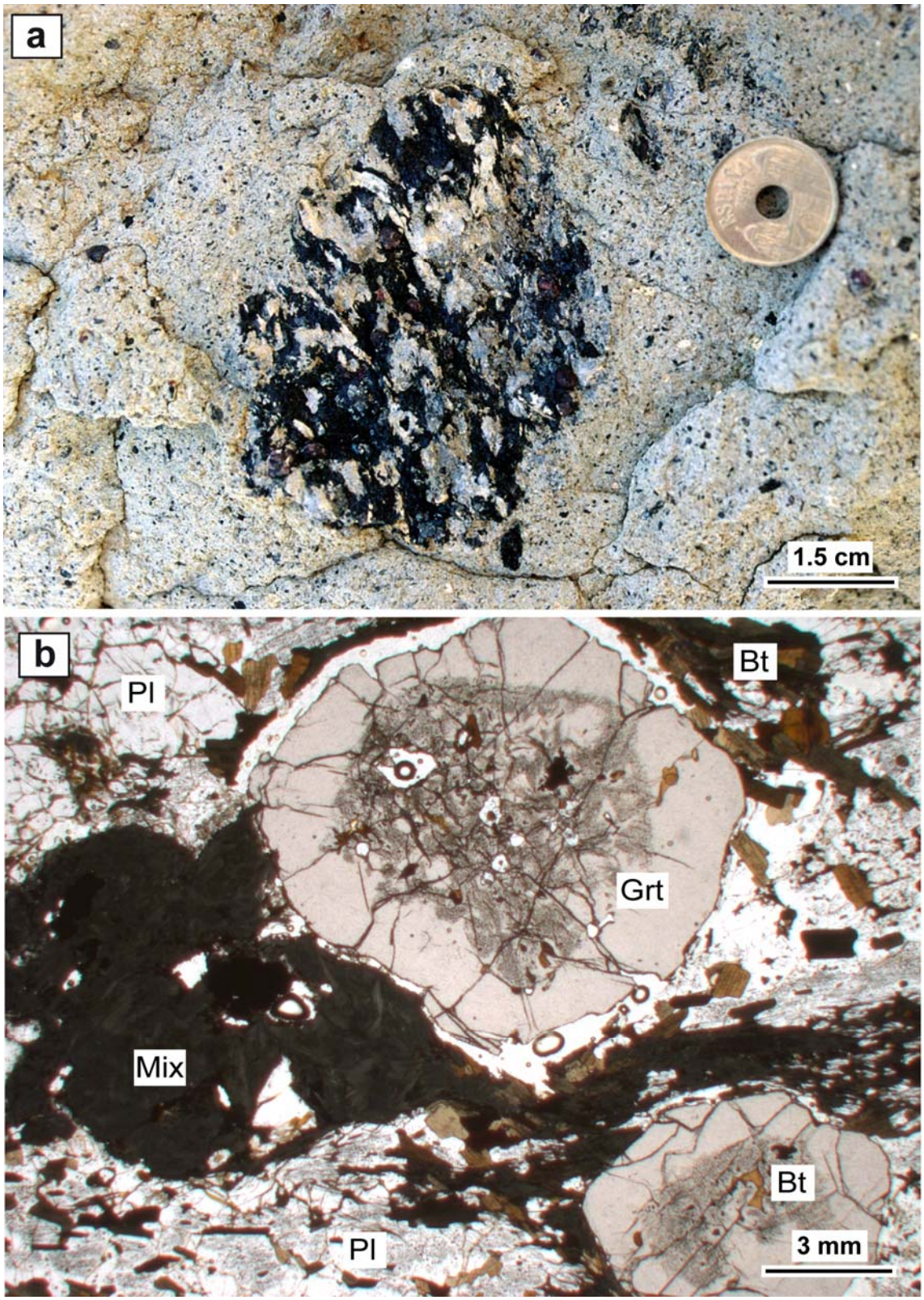

***Figure 2**: Bt-Grt-Sil enclaves. a) outcrop of dacitic lavas with enclosed a Bt-Grt-Sil enclave; b) common occurrence of garnet in these enclaves. Large (≤ 1 cm across) garnet porphyroblasts, with inclusion-rich core, in a matrix formed by biotite, fibrolite and sillimanite in a fine sponge-like aggregate, large plagioclase porphyroblasts with a typical dusty aspect, due to the high amount of inclusions. White arrow: empty space left by devitrified melt, ripped off by polishing. Often glass surrounds large garnet porphyroblasts.*

Largest biotite porphyroblasts define the foliation, forming Bt-rich layers that anastomose around garnet. Plagioclase forms anhedral poikiloblastic crystals with extremely dusty appearance owing to the abundance of inclusions of graphite, glass, fibrolite, and biotite. When present, cordierite also forms dusty, anhedral poikiloblastic crystals. They contain graphite, MI, and FI along with fibrolitic sillimanite and large crystals of partially resorbed biotite, oriented parallel to the foliation. Fibrolitic sillimanite is abundant both as a component of the "mix" and as inclusions in garnet, while in plagioclase and cordierite it is locally oriented, along with graphite, along the main foliation of the samples. In pockets around garnet, fibrolitic sillimanite and glass mix may define folded patterns, testifying for a syn-anatectic deformation.

In the field, Spl-Crd enclaves are smaller than Bt-Grt-Sil enclaves, with fragments ≤10cm. Spl-Crd enclaves are fine-grained and show a closely spaced foliation (Fig.3a), defined by oriented biotite and fibrolite, overprinted by porphyroblasts of hercynitic spinel (≤2mm) (Cesare et al., 1997). Foliation often anastomoses around granoblastic domains formed by euhedral garnet, cordierite and plagioclase. Fibrolitic sillimanite and glass mix are present but not as abundant as in the Bt-Grt-Sil enclaves. Ilmenite, glass, ±garnet, ±plagioclase, ±quartz, ±K-feldspar may also be present. Spinel porphyroblasts range from subhedral to euhedral in shape and are often surrounded by small coronas of cordierite or K-feldspar. Locally, cordierite overgrows the fibrolitic sillimanite and glass mix, occurring interstitially among garnet crystals, forming large anhedral porphyroblasts. Plagioclase is often associated with cordierite and grows in elongated grains parallel to foliation at the borders of the unfoliated domains. As in Bt-Grt-Sil enclaves, both cordierite and plagioclase are very dusty, and contain mainly FI, MI and graphite; in places biotite and oriented fibrolite also occur. Biotite forms oriented subhedral to euhedral porphyroblasts of variable size, ≤100 μm, in Bt-rich folia, and may crystallize in pressure shadows around garnet, locally overgrowing it (see also Alvarez-Valero et al., 2005). In statically re-crystallized domains biotite occurs both in large porphyroblasts and partially resorbed crystals, especially where enclosed in cordierite or plagioclase. Sillimanite occurs as sub-oriented to oriented fibrolite, mainly fine-grained, but locally passing to coarse-grained prisms.

Garnet in Spl-Crd enclaves is less abundant, and smaller in size (≤2 mm) (Fig.3b), than in Bt-Grt-Sil enclaves. It crystallizes in euhedral or elongated crystals, depending on its microstructural environment. Garnet is euhedral and inclusion-free in statically re-crystallized domains, while it is subhedral and inclusion-rich in strongly foliated

domains, where it displays a variable aspect ratio of up to 10:1 (Alvarez-Valero et al., 2005) and is characterized by a dark, dusty, sometimes circular core (Fig.4a-b).

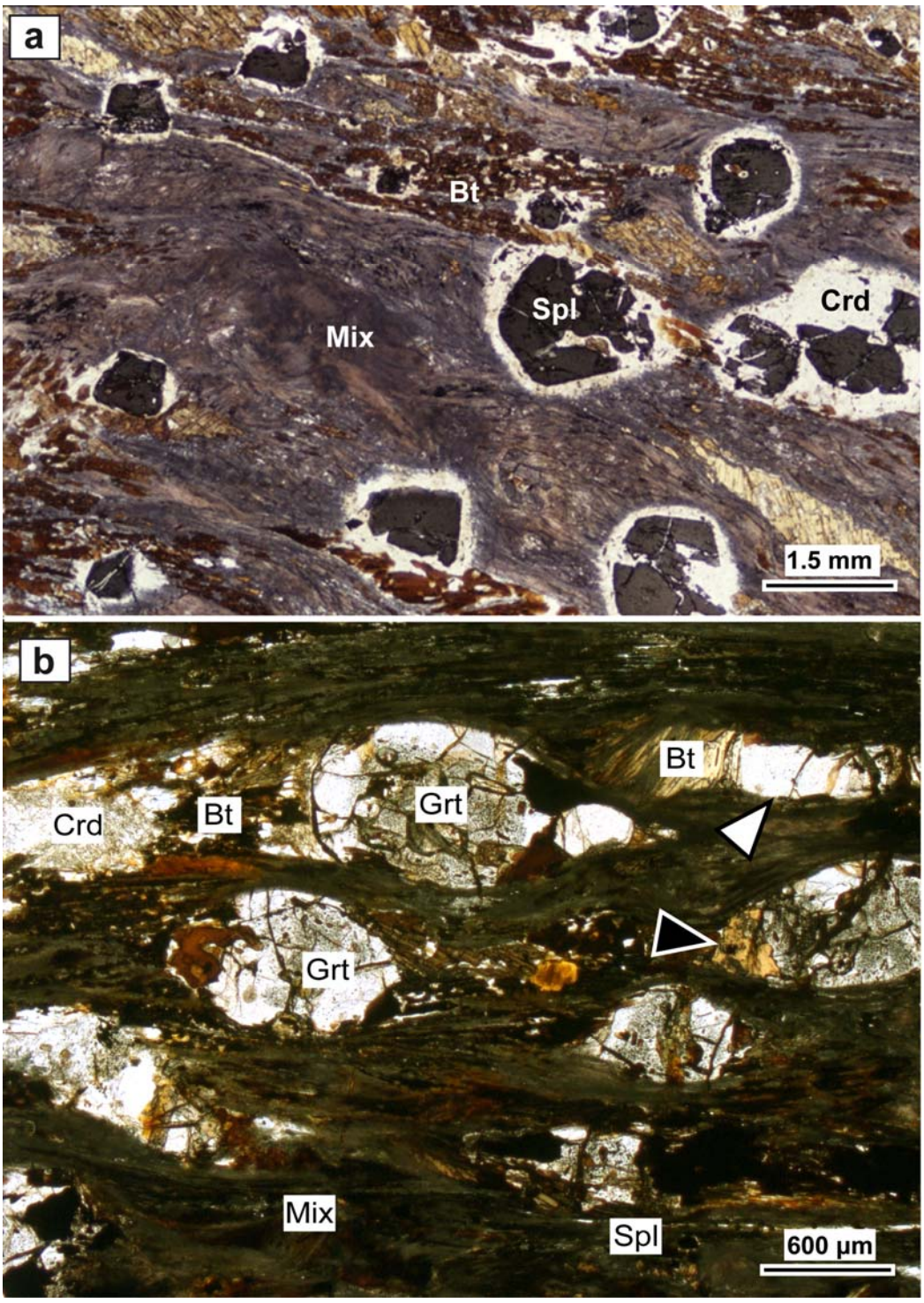

Figure 3: *Spl-Crd enclaves. a) common aspect of Spl-Crd enclaves at thin section scale, characterized by abundant spinel porphyroblasts in a fine-grained foliated matrix formed by mix and oriented biotite; b) elliptical garnets, with inclusion-rich core, in Spl-Crd enclaves. In figure is visible the well-developed foliation, defined by biotite and fibrolite+melt domains. Biotite also grows in garnet pressure shadows, locally overgrowing it (black arrow). Cordierite forms poikiloblastic crystals in less deformed domains. White arrow: well-developed elliptical garnet.*

Dark domains are surrounded by an asymmetrical inclusion-free external area up to 150 μm thick, which is better developed parallel to foliation. Inclusion-rich cores contain MI, FI, partially resorbed crystals of biotite, abundant graphite, fibrolite and rare plagioclase. Where garnet cores host large (≤50 μm across) biotite flakes, inclusions define a circular pattern around the core, with inclusion-free zones surrounding biotite (Alvarez-Valero et al., 2005). The process of elliptical garnet formation has been studied by Alvarez-Valero et al. (2005), and is summarized as follows. The original euhedral garnet porphyroblasts crystallized in the presence of melt (evidenced by primary MI and FI in the core), then underwent localized dissolution at strain caps and re-precipitation in the strain shadows, resulting in garnet growth along foliation and the truncation of inclusion circular patterns at garnet core. Static growth of new skeletal garnet followed the strain-solution process.

Glass, representing former anatectic melt, is abundant in both Bt-Grt-Sil and Spl-Crd enclaves. Glass may occur as layers (≤100 μm), parallel to foliation, as thin films coating garnet and spinel porphyroblasts and as inclusions (≤50 μm) in almost all minerals, the most important being garnet, cordierite, biotite, spinel and plagioclase. Melt inclusions often occur in the interior of the host minerals, in a microstructural position that suggest primary trapping (Roedder, 1984) during host growth. MI are not present in sillimanite, however this phase is genetically associated with melt represented by the glass in the fibrolitic sillimanite and glass mix, and probably only the small crystal size prevented sillimanite from trapping MI. Acosta-Vigil et al. (2007; 2010) studied in detail the microstructural features and compositions of MI in different minerals and matrix from Bt-Grt-Sil enclaves. The glasses have a leucogranitic and peraluminous composition, with systematic differences among melts trapped in different minerals, possibly related to melt evolution during partial melting process of metapelites. Chemical compositions of interstitial melt layers (Alvarez-Valero et al., 2005) in Spl-Crd enclaves confirm a peraluminous rhyolitic composition, similar to glasses from Bt-Grt-Sil enclaves.

3.4) Samples and methods

Approximately 20 normal thin sections and doubly polished thick sections from two Spl-Crd enclaves (samples HO19 and AVHZ13) and from one Bt-Grt-Sil enclave (sample HO50) were examined to characterize fluid inclusions, melt inclusions and garnet host. Sample preparation and petrographic examination were conducted at the Department of Geosciences, University of Padua – Italy. The microthermometric (MT)

study and Raman analyses were performed at the Department of Geosciences, Virginia Tech - USA. About 40 FI, recognized as primary and belonging to the same FIA (Goldstein and Reynolds, 2003), were analyzed using a USGS-type gas-flow heating and cooling stage (Werre et al., 1979), mounted on an Olympus BX51 microscope, and a Linkam THMSG 600°C programmable heating/cooling stage, mounted on Olympus BX60 microscope. The accuracy of measurements is ±0.1°C in the range -100/+31°C and ±1°C in the range 250/340°C. Stage calibration was done using synthetic CO_2-H_2O synthetic FI standards (Sterner and Bodnar, 1984).

Raman analyses were performed at the Vibrational Spectroscopy Laboratory, using the same analytical conditions described in section 2.3. Qualitative Raman analyses were conducted on ≈200 FI. The gas (vapor-bubble) portion of 68 FI was also quantitatively analyzed, and the gas density was estimated for 21 of the 68 analyzed FI, using the densimeter developed by Kawakami et al, (2003) and improved by Fall (2009). The densimeter is based on the relative position of the CO_2 Fermi diad Raman peaks, whose separation distance is density-dependent (Wright and Wang, 1973; 1975). Different analytical conditions were used for these analyses, to obtain a higher accuracy in the estimation of the relative positions of the CO_2 peaks, by using an 80X objective, spectral window between 1150 and 1450 cm^{-1}, integrating 5 cycles of 20-30 sec for each determination, and using a grating of 2400 gmm^{-1}. The spectral resolution using these analytical conditions is ~0.3 cm^{-1}.

EMP analyses of MI in garnet from Spl-Crd samples were performed at I.N.G.V., Rome (see section 2.31 for details). Analyses were conducted with a 1.5 μm beam, 10 kV accelerating voltage and 3 nA current. Na, K, Al and Si were analyzed first to eliminate the influence of alkali loss on the counting statistics on the two most abundant elements (Si, Al).

Transmission electron microscopy (TEM) was carried out in the Earth Science Department, University of Siena - Italy using a JEOL 2010 microscope, operating at 200 kV, with LaB_6 source, ultra-high resolution pole pieces and 0.19 nm point-to-point resolution. The microscope is equipped with an ultra-thin window energy dispersive spectrometer (EDS – ISIS Oxford). TEM grids were extracted from polished thin sections of two garnets and thinned by Ar^+ ion-milling (Gatan Dual Ion Mill), at 20°- 5 kV and at 12°- 1.5 kV. In TEM samples, electron-transparent portions are typically thinner than ~100 nm, thus micrometer-sized inclusions would have lost their fluid content during ion-milling procedures.

3.5) Results

3.5.1) Inclusions microstructures

In Spl-Crd enclaves HO19 and AVHZ13, most FI are <5 μm (Fig.4c-d), and only a very few are up to 25 μm (Fig.4d-e) and suitable for microthermometry.

The analyzed FI are two phase (L+V), and vapor-rich (c. 60-80 vol%) at room temperature. Their shape ranges from spherical to tubular (Fig.4d). Toward the garnet rim the abundance of FI can decrease both abruptly or gradually and sometimes the boundary between the fluid inclusion-present zone and the fluid inclusion-absent zone defines a surface resembling the crystallographic face of the garnet. Very often the outer part of the host garnet is FI-free (Fig.4a). The largest FI are often entrapped close to the cluster boundary. Locally the FI-rich core touches the grain boundary, probably due to a strain-solution process (Alvarez-Valero et al., 2005). In few cases FI form pseudosecondary arrays that do not cross the cluster boundaries. Almost all the garnets display some cracks crossing the entire crystal: studied FI have been selected for domains free of microfractures (Fig.4b).

The presence of melt inclusions (Fig.4c,f) in Spl-Crd enclaves was reported by Alvarez-Valero et al. (2005), and here we expand on their description and analyses. MI are ≤8 μm in size, ovoidal to tubular in shape, and contain a clear, homogeneous glass with a one phase shrinkage bubble (Fig.5). A third type of inclusion contains both melt and fluid in proportions ranging from ≈100% fluid (end-member FI) to almost 100% melt (end-member MI with shrinkage bubble). These inclusions are referred to as mixed inclusions (Lowenstern, 2003, Frezzotti et al., 2004, Cesare et al. 2007), and occur locally in the Spl-Crd enclaves (Fig.4f,6). Mixed inclusions are usually larger (≤40 μm) than both MI and FI, and may contain graphite as a trapped mineral phase (Fig.4e). Locally, the fluid portion of the mixed inclusions is two phase (Fig.6). Both MI and mixed inclusions are less abundant in this type of enclave compared to Bt-Grt-Sil enclaves (HO50 sample).

The occurrence of FI, MI and mixed inclusions in clusters in the garnet core suggests a primary origin for the inclusions and that they all belong to the same fluid inclusion assemblage. The three inclusion types would have been trapped during a single event, under conditions of immiscibility between anatectic melt and fluid (Roedder, 1992, Cesare et al., 2007). Many garnets show partially healed fractures that contain secondary FIAs comprised of very small, strongly irregular one phase FI (Fig. 4e). Preliminary Raman data from these FI show a CO_2-rich vapor at room T and minor amounts of CH_4. No further studies have been carried out on these secondary FI.

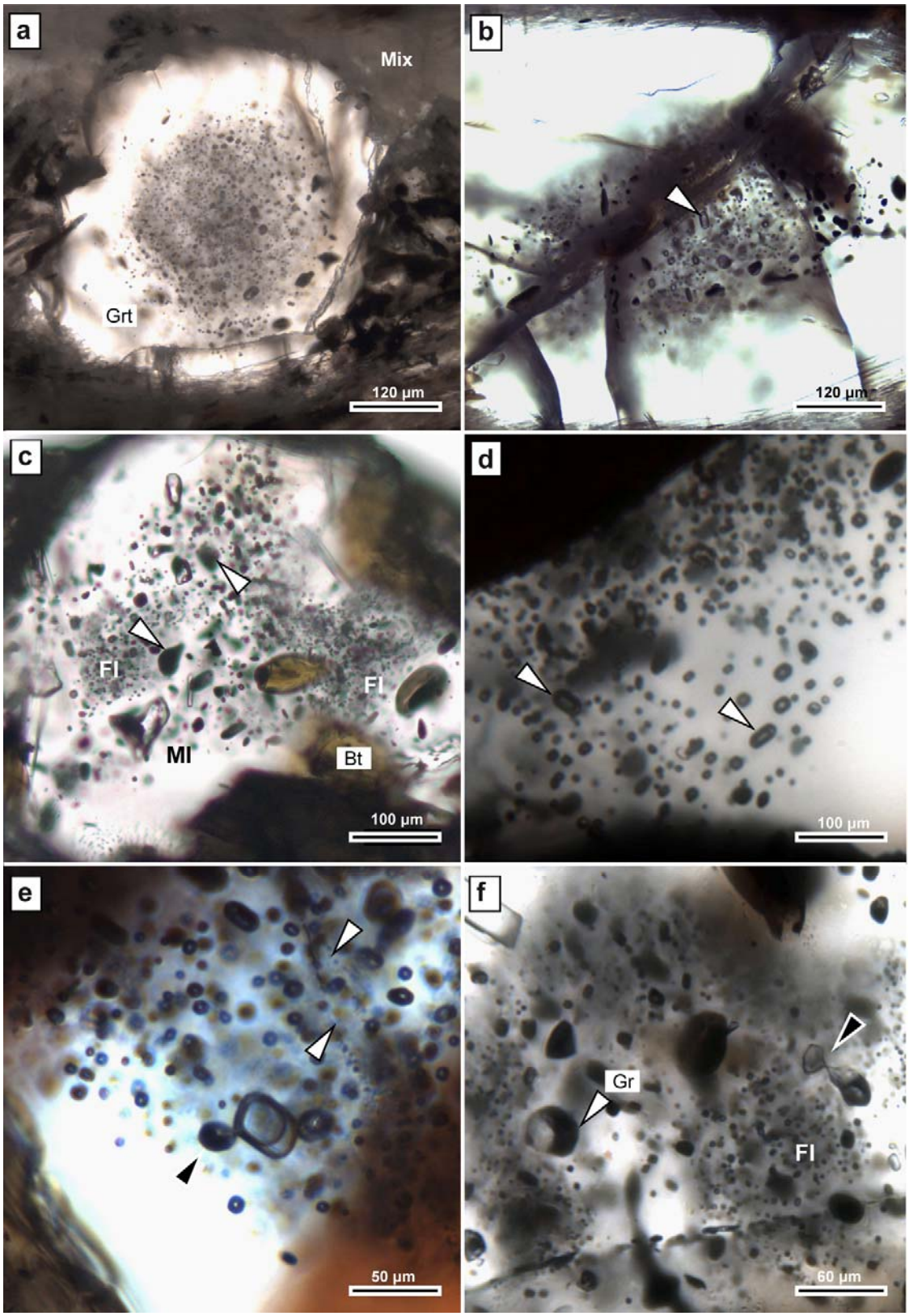

Figure 4: *microstructures of FI and MI in garnet from Spl-Crd enclaves. a) Characteristic round garnets in sample AVHZ13. The garnet core is dark because of the high spatial density of small FI and other mineral inclusions. The rim of the garnet is usually clear and inclusion-free; b) detail of the core of an elongated garnet. Often the core presents multiple unhealed cracks, but their spacing (≥100 µm) leaves the major part of the core apparently undisturbed; c) inclusions in the dark core. Biotite), fibrolite, FI and MI, along with graphite (white arrows) can be recognized; d) Cluster periphery (continues)*

The variety in shape and size of the studied FI can be appreciated in the picture. FI range from ≤1μm in the upper part to ~16 μm in the center lower part, while their shape varies from spherical to tubular. White arrows: two-phase inclusions. e) Two phase, vapor-rich inclusions. Black arrow: graphite trapped in a FI. White arrows: two small FI secondary arrays; f) MI and mixed inclusions occurrence in same cluster along with FI. White arrow: large inclusion containing melt, a small shrinkage bubble in the upper part and graphite as trapped phase. Black arrow: partially necked-down mixed inclusion.

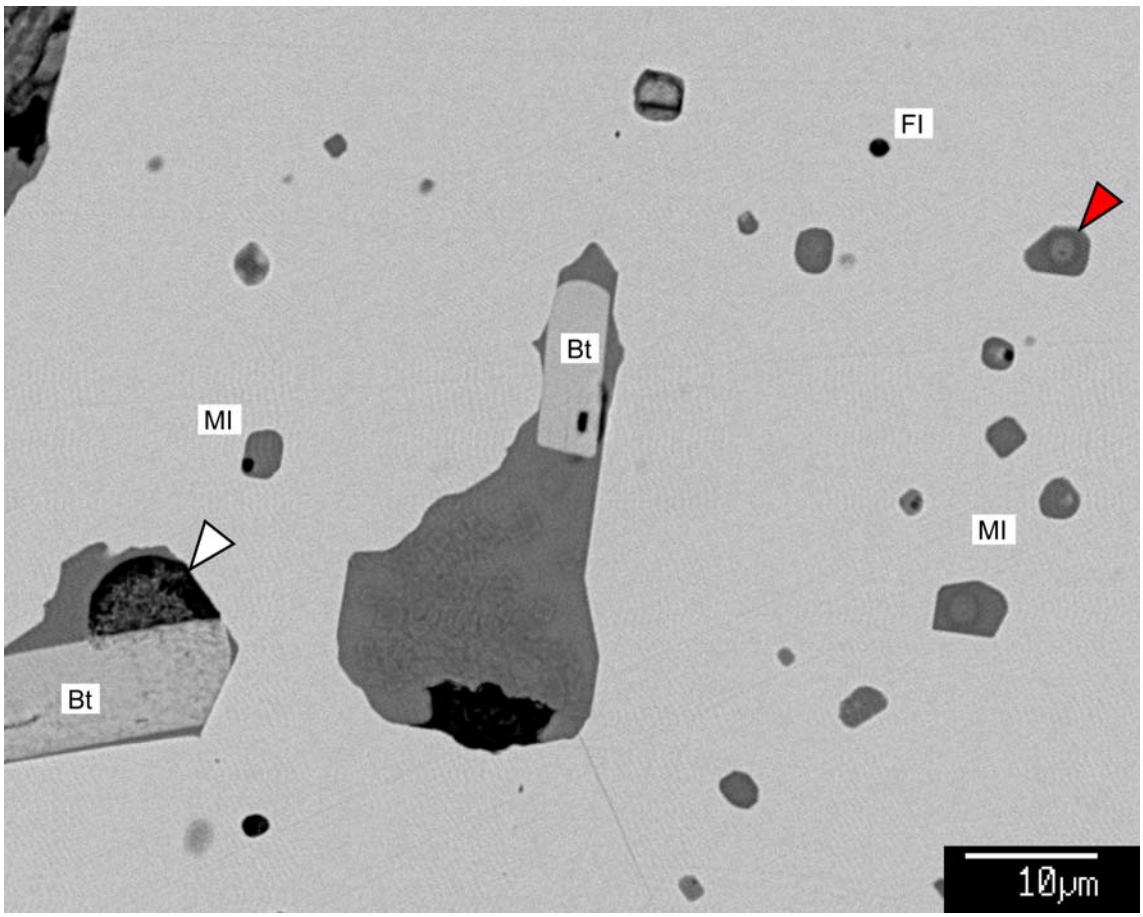

Figure 5: *aspect of MI in the core of the garnet in Spl-Crd enclaves, BSE image. The large MI in the center of the picture is a large partially devitrified MI. White arrow: mixed inclusion trapped along with biotite; red arrow: pit left on the sample by the EMP beam.*

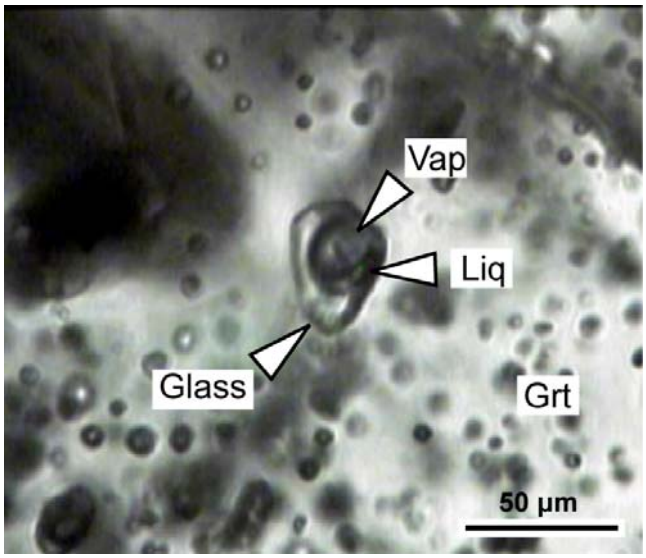

Figure 6: *mixed inclusion with a two phase fluid portion. Raman analyses confirmed the presence of a H_2O-rich liquid portion, wetting the lower part of the bubble in the image, along with CO_2-rich, vapor portion. The clearest portion is glass.*

In the garnet, graphite is the most abundant mineral inclusion, forming round to elongated 10 to 200 μm crystals. Biotite occurs in garnet core (Fig.4c) both as large subhedral to euhedral crystals, ≤ 200 μm, and as small subhedral grains, ~ 20 μm, in FI+MI clusters and, in places, enclosed in MI as solid inclusion (Fig.7). Needles of fibrolite, with diameter ≤1μm, are often present in the garnet. The presence of large grains of biotite and sillimanite often appears to inhibit the formation of FI and MI in their immediate vicinity inside the cluster (see also Acosta-Vigil et al., 2007). Conversely, graphite appears to favor the entrapment of FI and MI during crystal growth. In places, FI may contain a few crystalline phases, the most common is graphite which occurs as round crystals. Because of its size, which is always too large to be reasonably considered to be a daughter mineral, and of its variable location with respect to the fluid or melt inclusion boundaries, graphite is considered a trapped mineral (Fig. 4c, see also Cesare and Maineri, 1999). Rare carbonates have been identified via Raman analyses and FESEM imaging in a few FI (<5% of total observed inclusions). Rare zircon and xenotime are also present and are likely to be phases trapped during FI formation. Except for graphite, present in 5 of the 40 studied inclusions, no accessory minerals were found in FI analyzed in the microthermometric study.

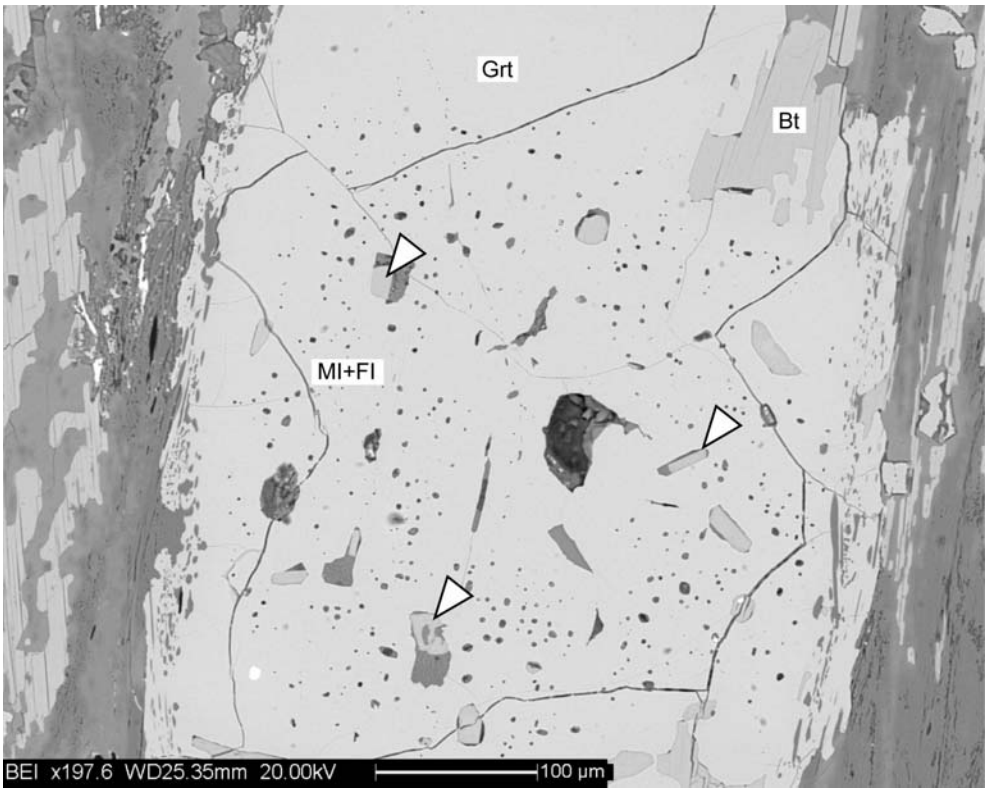

Figure 7: *biotite occurrence at garnet core in Spl-Crd enclaves, BSE image. White arrows: biotite enclosed in MI.*

In Bt-Grt-Sil enclaves (sample HO50), garnet porphyroblasts display an inclusion-rich core (Fig.8a), with the outer limits of the inclusion-rich zone often resembling crystal faces (Fig.8a,b). As with the Spl-Crd enclaves, FI, MI, mixed inclusions and mineral inclusions (mainly graphite and biotite) occur in the same cluster. Several secondary assemblages of FI are visible, often crossing the cluster borders (Fig.8b). Many cracks are visible in the garnet, both in the core and in the rim, often intersecting both mineral and fluid/melt inclusions. Nonetheless, several crack-free domains have been identified, hosting FI suitable for microthermometric study. Generally, FI in Bt-Grt-Sil enclaves are smaller, ≤15μm, and less abundant than in the Spl-Crd enclaves. All of the fluid inclusions are one phase at room temperature, with shape varying from spherical to negative-crystal (Fig.8c).

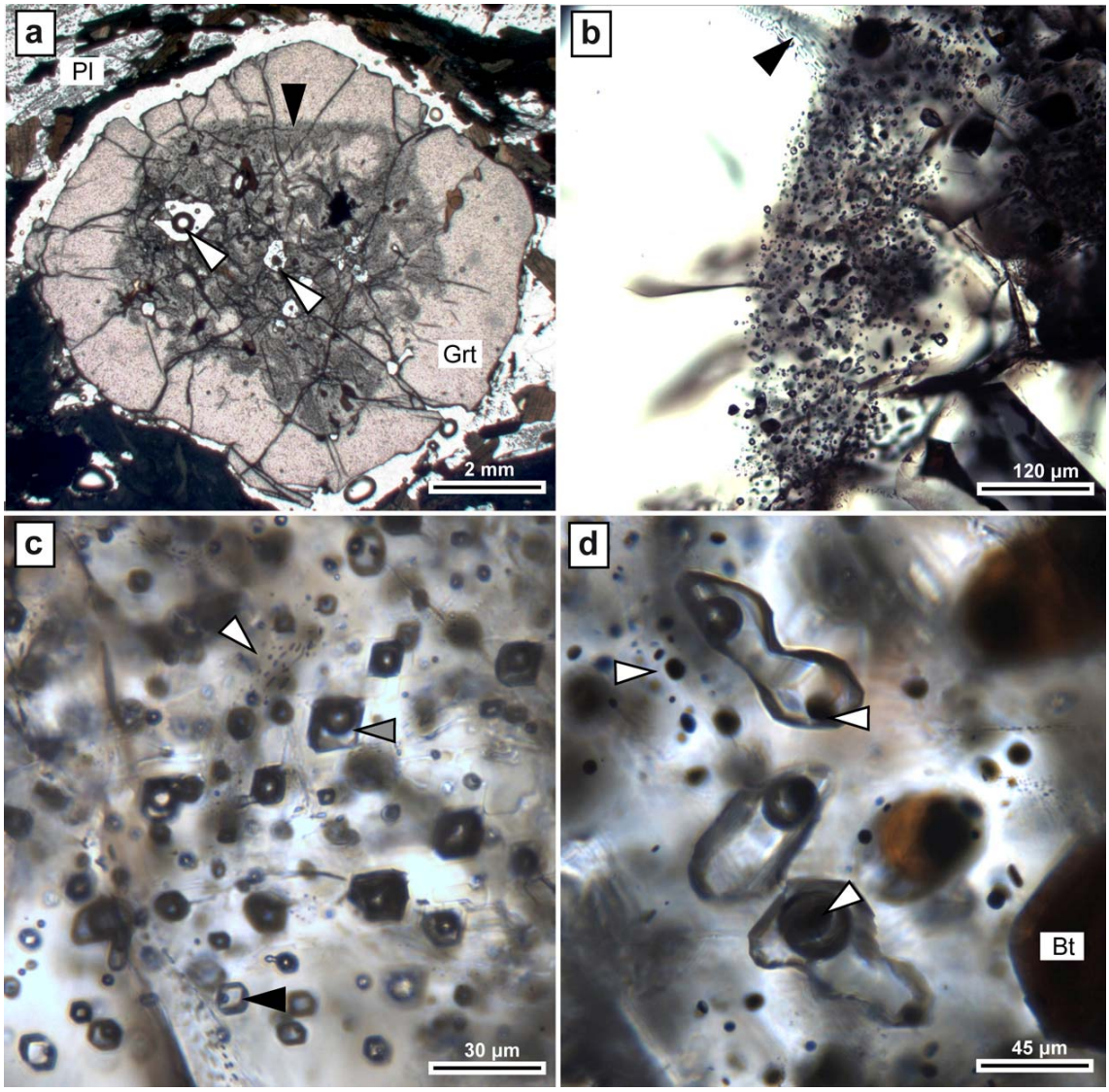

Figure 8 (previous page): *microstructures of FI and MI in garnet from Bt-Grt-Sil enclaves. a) subhedral garnet, surrounded by a foliation defined by biotite and sillimanite. Inclusions of various natures (MI, FI, mixed inclusions, and mineral inclusions) present a clear zonal arrangement, often with straight boundaries (black arrow), and characterize the garnet core. White arrows: holes; b) limits of the cluster. Often in this sample cluster borders strongly resemble the crystallographic face of the garnet. Black arrow: secondary FI array; c) detail of a cluster, showing the occurrence in conditions of immiscibility of FI (white arrow), MI (black arrow) and mixed inclusions (gray arrow) with different volume percentages of fluid portions; d) irregularly-shaped mixed inclusions with different amounts of trapped fluid. White arrows: Graphite is visible as trapped phase inside both the melt and the fluid portion of the mixed inclusions and as mineral inclusion in the surroundings. Euhedral biotite is visible on the right side of the picture.*

Most inclusion assemblages in garnet consist of MI and mixed inclusions. As in the Spl-Crd enclaves, this occurrence confirms the primary origin of the inclusions (Roedder, 1984) and the presence of melt-fluid immiscibility during garnet growth. Melt inclusions are ≤150 μm, with irregular (Fig.8d and 9) to negative-crystal shape (Fig.8c and 9). Acosta-Vigil et al. (2007) provide a detailed description of microstructures and composition of melt inclusions from enclave HO50, the same sample studied here. Anhedral graphite, both fine-grained (~5 μm) and coarser, and subhedral biotite (≤ 200 μm) are present (Fig. 8d), but are less abundant compared to the Spl-Crd enclaves.

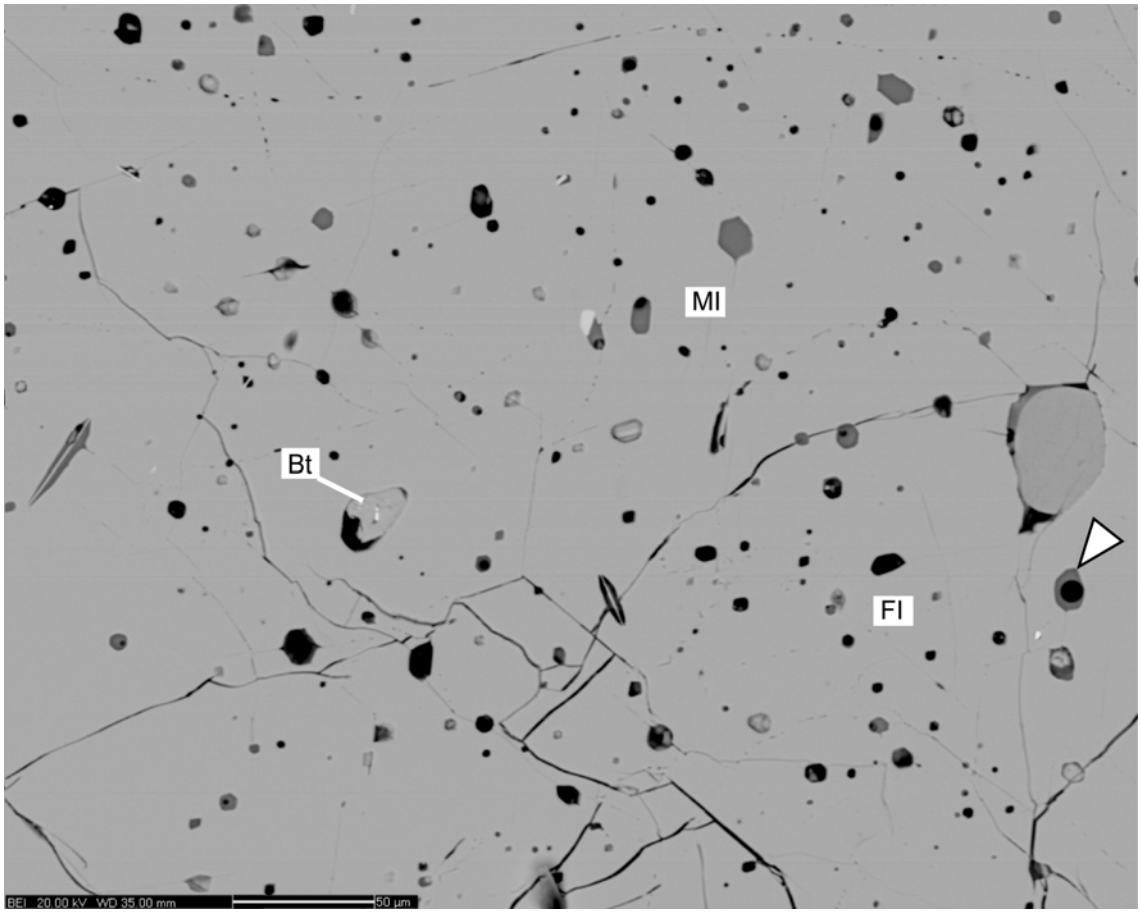

Figure 9: *MI occurrence in garnet from Bt-Grt-Sil enclaves, BSE image. White arrow: mixed inclusion.*

3.5.2) Microthermometry

FI from the Spl-Crd enclaves showed phase transitions during heating/cooling runs, while no phase transitions were detected within FI from Bt-Grt-Sil enclaves. All microthermometric data are reported in Table 1.

In Spl–Crd samples, on heating from -180°C, the melting of solid CO_2 ($T_m^{CO_2}$) and the total homogenization (T_h) were observed, while homogenization of the CO_2-rich portion ($T_h^{CO_2}$) was never detected. The MT study shows slight differences among fluid inclusions from sample HO19 and those from sample AVHZ13 (Table 1). FI in garnet from sample HO19 show a $T_m^{CO_2}$ = -60 to -56.8°C and the total T_h = 332-339°C; they homogenize via critical behavior with fading of the meniscus between vapor and liquid. In a few fluid inclusions, the formation of clathrates was also recognized, with T_m^{cla} = +9.2 to +9.8°C.

Enclave Type	Sample	Hom mode	T_m CO_2(ºC)	T_h (ºC)
Spl - Crd	HO19	Crit. Behavior	- 60 / - 56.8	332 - 339
	AV-HZ 13	Vapor	- 64.7 / - 58.3	335 - 339

Table 1: *summary of microthermometric data from FI (n= 36) on Spl-Crd enclaves. Hom. Mode = homogenization mode. Crit. Behavior= the homogenization occurs via fading of the meniscus.*

FI in garnet from sample AVHZ13 have $T_m^{CO_2}$ in the range -64.7 to -58.3°C, and total T_h = 335-339°C to vapor. Microthermometric data are plotted in histograms on Fig.10a and b. Measured $T_m^{CO_2}$ values in both samples are generally lower than -56.6°C, with AVHZ13 $T_m^{CO_2}$ values extending to lower temperature than those from HO19, suggesting for both samples the presence of volatiles other than CO_2 in the vapor portion of the inclusion, with slightly higher amounts in AVHZ13 (see Fig.10a). Clathrate melting observed in a few inclusions indicates a low-salinity for the aqueous phase. The high T_h values are consistent with a high X_{H2O} in the inclusion, probably ≥ 0.80 mol% (Takenouchi and Kennedy, 1984; Bodnar et al., 2009), with a density equal to (HO19) or lower than (AVHZ13) the critical density. The CO_2-rich fluid portion of the inclusions appears to contain a single phase, even at the melting point of the CO_2-solid. However, we cannot exclude the possibility that a thin film liquid CO_2 may be present around the outer portion of the CO_2 bubble walls and be optically unresolvable. In any case, the microthermometric data are consistent with a low density CO_2-rich mixture in the vapor phase of the inclusions.

The total density and bulk composition of the inclusions could not be estimated from microthermometric data, owing to the lack of $T_h^{CO_2}$ data. For this reason total densities and bulk compositions were estimated using a mass balance calculation, based on available MT and Raman data (detailed in Supplementary Material 4).

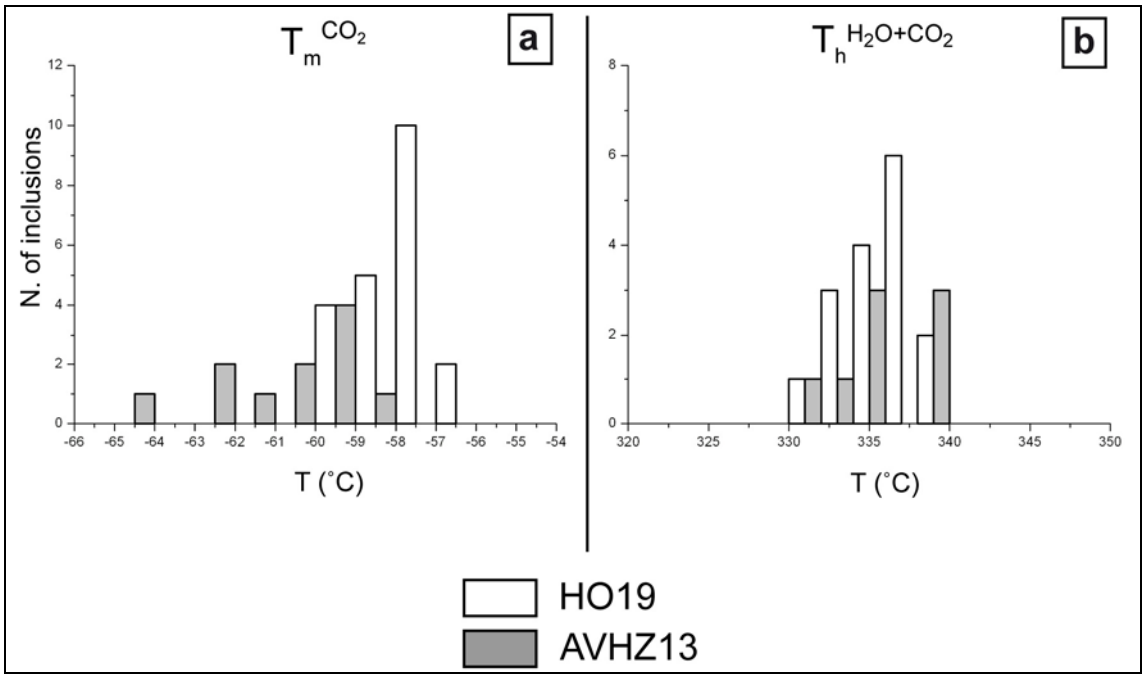

Figure 10: *microthermometric data for the two studied samples of Spl-Crd enclaves. a) Solid CO_2 melting temperature histogram; b) Total homogenization temperatures histogram. According to the legend, different colors indicate different studied samples of Spl-Crd enclaves.*

3.5.3) Raman spectroscopy

Raman analyses were conducted to characterize the trapped fluid and quantify the amounts of gas species present. In Spl-Crd enclaves, the gas portion of two-phase FI consists mainly of CO_2 and N_2, while the liquid portion contains H_2O (Fig.11). All analyzed FI show CO_2 peaks ($2v_2$ and v_1) at 1388 cm^{-1} and 1285 cm^{-1}, respectively, an N_2 peak at 2336 cm^{-1}, and a broad band for H_2O between 3100 and 3600 cm^{-1}. Sample HO19 may also contain H_2S, both in the gas phase (2611 cm^{-1}) and in the liquid H_2O phase (2579 cm^{-1}), and also CH_4 (2916 cm^{-1}) in a few cases. One-phase FI from Bt-Grt-Sil enclaves contain CO_2 and N_2, and H_2O was not detected. Molar ratios of the gaseous phases, χ_a, were calculated using the equation (1) from section 2.7, and the considered correction factors are IF_{CO2} = 0.9, IF_{N2} = 1.1, IF_{H2S} = 1, determined as reported in the same section.

In sample HO19, the average composition of the vapor phase is 84 mol% CO_2, 15 mol% N_2 and 1 mol% H_2S (Table 2). Methane (CH_4) has been detected in about 5% of

the analyzed inclusions, with an average content of 3 mol%. The vapor portion of FI from sample AVHZ13 has a similar average composition, 80 mol% CO_2 and 20 mol% N_2, with higher compositional variation towards higher amounts of N_2 (up to 60 mol% N_2 in one FI), compared to HO19 sample.

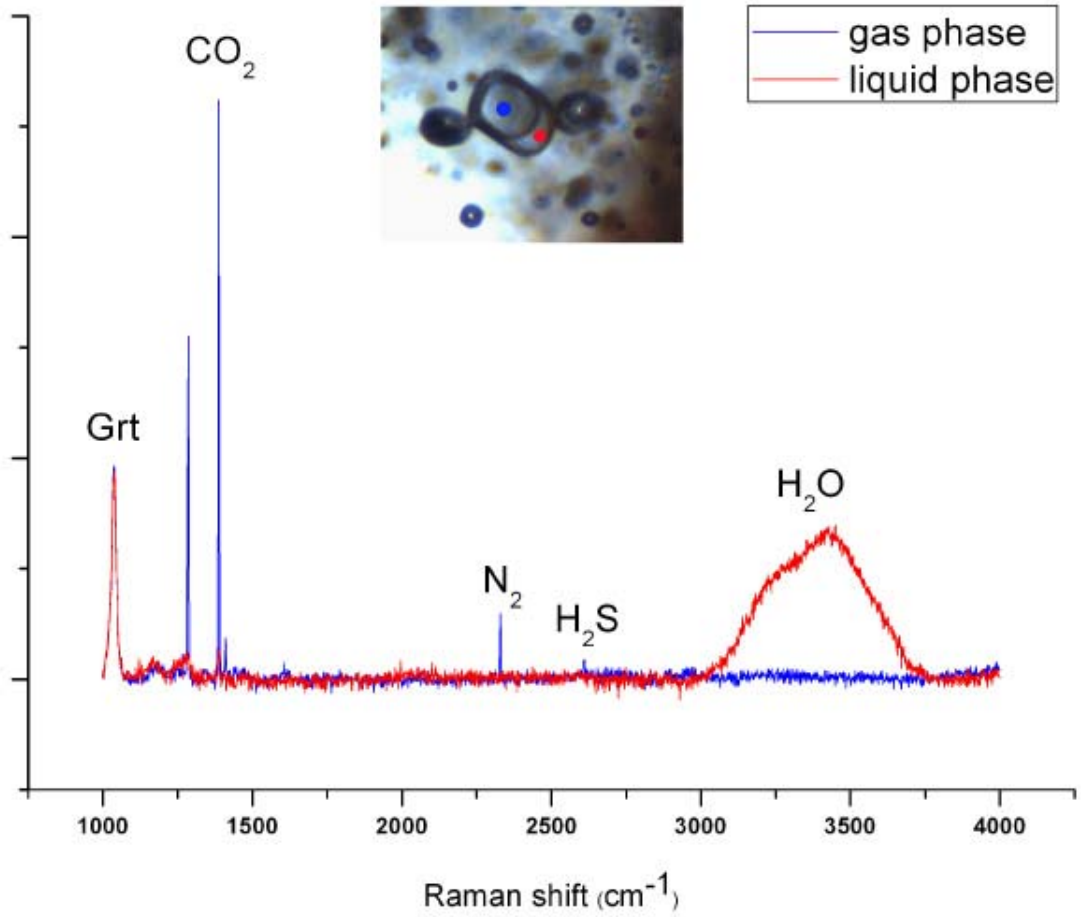

Figure 11: *example of Raman spectra on FI in garnet from Spl-Crd enclave. The blue spectrum has been collected in the gas, CO_2-rich portion (blue dot) of the FI in the picture, red spectrum was collected in the liquid, H_2O rich portion (red dot).*

FI in Bt-Grt-Sil in enclave HO50 are single-phase at room temperature, and their total composition can be estimated directly using equation (1). The trapped fluid in these inclusions is a mixture of CO_2 and N_2 in variable proportions (CO_2= 41-81 mol%), with an average composition of 55 mol% CO_2 and 45 mol% N_2. Results for Bt-Grt-Sil enclaves are summarized in table 2 and reported in detail in table 4.

Enclave Type	Sample	CO_2	N_2	H_2S	CH_4	accessories
Spl-Crd	HO19A	75-100 (av. 84)	24-0 (av. 15)	≤3	≤7 (av. <0.1)	± Gr ± Cal
	AVHZ13	40-97 (av. 80)	60-30 (av. 20)	0	0	± Gr ± Cal ± Zrn ± Xtm
Grt-Bt-Sil	HO50	35-90 (av. 82)	65-10 (av. 18)	0	0	± Gr

Table 2: *vapour composition (mol %) of representative fluid inclusions (n=68), calculated from Raman spectroscopy.*

3.5.4) Total composition and density

Composition and density of FI from Spl-Crd enclaves

As previously stated, failure to recognize a homogenization transition for the carbonic portion of FI in Spl-Crd enclaves prevented us from estimating total composition and density by using microthermometric data alone (see Diamond, 2001, Fig.10). Bulk compositions and total densities of FI in Spl-Crd enclaves were thus determined using data from petrographic observation and Raman analysis, employing the CO_2 densimeter of Fall (2009) and the mass balance calculation method described in Sup.Mat. 4. Calculated densities, ρ_{tot}, and bulk compositions (mol%) of trapped fluid obtained by this approach are reported in table 3.

Fluid inclusions trapped in HO19 contain 78-91 mol% H_2O, 7-18 mol% CO_2 and 0-4 mol% N_2, while fluid composition in AVHZ13 shows a wider range in H_2O (44-84 mol%) and N_2 content (2-21 mol%). Knowing the molar fractions of the components, total densities (ρ_{tot}) of fluid inclusions were calculated using the same mass balance method as before (table 3). Calculated densities range from 0.53 $g \cdot cm^{-3}$ to 0.27 $g \cdot cm^{-3}$, and the highest density value corresponds to a composition of 90 mol% H_2O, 8 mol% CO_2 and 2 mol% N_2.

Densities of FI from Bt-Grt-Sil enclaves

Because no phase transition was detected during microthermometry, FI densities were estimated in a manner similar to that used for Spl-Crd enclave FI and described in Sup.Mat. 4. Total density, ρ_{tot}, was estimated using LonerW, from Software Package FLUIDS, v.2 (Bakker, 2008), assuming T = 22°C (ambient temperature during Raman analysis) and FI internal pressure derived for each FI using the NIST database (Lemmon et al., 2009). Resultant FI densities (table 4) range from 0.05 to 0.10 $g \cdot cm^{-3}$ and are notably lower than densities of FI from Spl-Crd enclaves.

Spl-Crd enclaves		Raman data on vapour portion				Values from NIST Database		Mass balance calculation results			
Sample	**FI name**	**CO_2 mol%**	**N_2 mol%**	**ρ_{CO_2}**	**% vap**	**P NIST (bar)**	**ρ NIST N_2**	**CO_2 mol%**	**N_2 mol%**	**H_2O mol%**	**ρ_{tot} (g/cm^3)**
HO19	flincAgrt11	80	20	0,10	0,72	45	0,049	7	2	91	0,35
	flincBgrt11	78	21	0,10	0,77	45	0,049	9	2	89	0,30
	flincCgrt11	80	20	0,24	0,67	73	0,079	12	3	86	0,46
	flincDgrt11	81	18	0,23	0,77	71	0,077	18	4	78	0,37
	flinc6	100	0	0,23	0,69	71	0,077	17	0	83	0,47
	flincEgrt11	83	16	0,23	0,70	71	0,077	13	3	84	0,43
	1	80	18	0,23	0,57	71	0,077	8	2	90	0,53
	2	82	16	0,23	0,64	71	0,077	11	2	87	0,48
	3	81	19	0,23	0,71	71	0,077	13	3	84	0,42
	flinc4grt1	82	17	0,19	0,75	66	0,072	14	3	83	0,37
	flinc3grt1	81	18	0,23	0,66	71	0,077	11	2	86	0,46
	flinc9	90	8	0,10	0,81	65	0,072	14	1	85	0,27
	flinc10	84	15	0,23	0,70	77	0,080	14	2	83	0,43
AVHZ 13	A	82	18	0,23	0,78	71	0,077	18	4	78	0,37
	E	74	26	0,36	0,87	80	0,087	30	11	60	0,33
	M	83	17	0,23	0,71	71	0,077	14	3	84	0,43
	E*	82	18	0,23	0,80	71	0,077	20	4	76	0,35
	P	86	14	0,23	0,75	71	0,077	17	3	80	0,40
	F	40	60	0,23	0,90	71	0,077	14	21	65	0,21
	G	97	3	0,36	0,90	80	0,087	54	2	44	0,40
	H	97	3	0,36	0,90	80	0,087	54	2	44	0,40

Table 3. *Summary of compositional data (Raman and mass balance calculation) on FI from Spl-Crd enclaves.* ***%vap*** *= volume proportions of the CO2-rich vapor phase at room temperature;* ***ρ CO2****= density estimated from Raman-based CO_2 densimeter (Fall, 2009). CH_4 and H_2S are not reported: the first only occur in a low percentage of measured FI (5%), the latter is not as rare as CH_4, but it occurs in negligible amounts (≤ 3 mol%). For explanations on the calculation method see Sup. Mat. 4.*

Grt-Bt-Sil enclaves		Raman Calculation			Values NIST Database	
Sample	**FI name**	**CO_2 mol%**	**N_2 mol%**	**ρ_{CO_2}**	**P NIST (bar)**	**ρ_{tot} (g/cm^3)**
HO50	1a	60	40	0.09	38	0.06
	2a	47	53	0.09	38	0.06
	3a	81	19	0.10	43	0.09
	4a	58	42	0.06	28	0.05
	5a	65	35	0.10	40	0.07
	4b	41	59	0.22	60	0.10
	6b	42	58	0.10	41	0.06
	7b	42	58	0.10	41	0.06

Table 4. *Summary of compositional data (Raman and mass balance calculation) on FI from Bt-Grt-Sil enclaves.* ***ρ CO_2****= density estimated from Raman-based CO_2 densimeter (Fall, 2009). For explanations on the calculation method see sup. Mat. 4.*

3.5.5) Isochores determination

The fluid trapped in Spl-Crd enclaves can be approximated by the CO_2-H_2O binary, and this is especially appropriate for the highest density FI from sample HO19. The calculated bulk compositions and densities were used as input data in the software NEWTWO (Bodnar et al, 2009), to determine the isochores for every measured fluid inclusion. This software uses a modified Redlich-Kwong equation of state (Bodnar et al., 2009), developed to calculate the volumetric properties in the CO_2-H_2O system. The required input parameters are X_{H2O}, T_h and P_h (pressure at homogenization). P_h is grossly derived at first by available thermophysical data (Lemmon et al., 2009). Then the value is refined and more precisely estimated by performing several iterations and comparing the total density and CO_2 density predicted by the algorithm with the same parameters obtained via mass balance calculation and Raman analyses, until the output parameters match the mass balance calculation parameters. Isochores calculated according to this methodology are reported in Fig.12.

The highest calculated density for Spl-Crd enclaves, 0.53 g·cm^{-3} (thick black line in Fig.12), defines a trapping pressure of 3.0-3.5 kbar, assuming a trapping temperature of 800-900°C, while the lowest calculated density predicts a trapping pressure of 1.5 kbar. The maximum pressure obtained from FI in garnet is about 2 kbar lower than the minimum P of formation predicted by the GASP barometer applied to HO19 (Field A in figure 12; Cesare et al., 1997). In conclusion, as shown in Fig.12, isochores do not intersect the peak P-T conditions estimated for enclaves. The discrepancy is even larger if entrapment of FI and MI in garnet took place early in the history of partial melting of the enclaves, at 700-750°C (field B in Fig.12), as proposed by Acosta-Vigil et al. (2010).

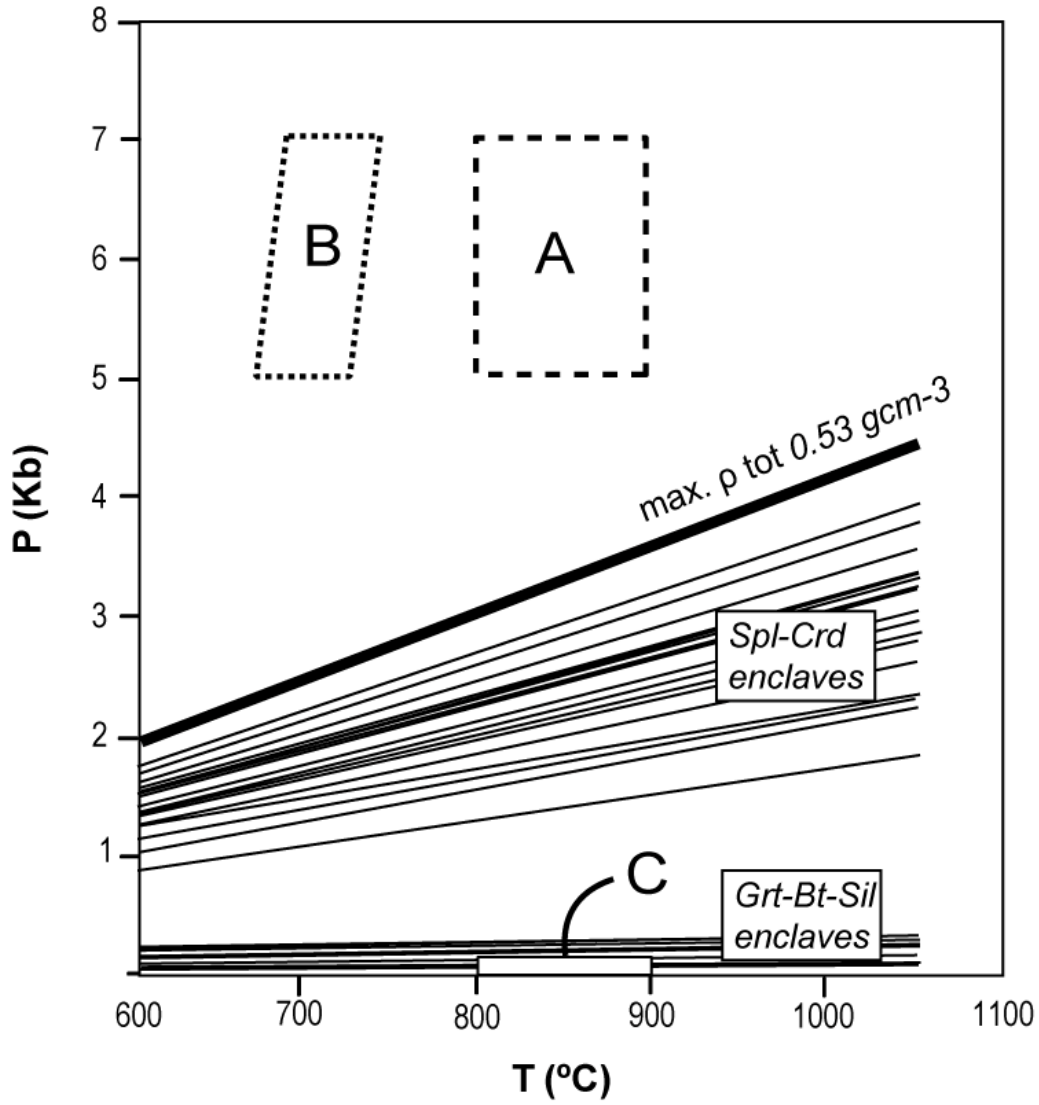

Figure 12: *PT diagram with calculated isochors based on microthermometric and Raman data about FI in garnet from Spl-Crd and Bt-Grt-Sil enclaves. Every isochore represents a single measured fluid inclusion. Field C: emplacement conditions of enclaves on the sea floor.*

Isochores for FI in Bt-Grt-Sil enclaves were determined using the software package FLUIDS, Program 2: ISOC, version 01/03 (Bakker 2003), applying the EOS developed by Holloway (1977) and Flowers (1979) for CO_2-N_2 mixtures. The isochores determined for the lowest density FI of sample HO50 are almost flat (Fig.12) and provide hypothetical entrapment pressures of <500 bar (in the 700-900°C range), far-removed from the inferred P-T trapping conditions.

3.5.6) TEM study of host garnet from Bt-Grt-Sil enclave

Calculated densities show that, if FI in Bt-Grt-Sil enclaves were trapped at the peak P-T conditions, they have experienced a larger density decrease compared to FI in Spl-Crd enclaves (see below). For this reason, sample HO50 was characterized by TEM, to search for cracks, dislocations or other structural discontinuities at the nanometer scale that could have been pathways for fluid loss from the FI during reequilibration. Dark cores (containing abundant FI) from two different garnet crystals were selected for this investigation.

Low magnification TEM images show several subspherical FI (Fig.13a), larger than 1.5 μm and representing approximately the smallest FI detectable using the optical microscope. As a consequence of thinning procedures, these "large" inclusions are always empty in the TEM sample, and the surrounding garnet is poorly transparent to electrons. Fig.13a shows a "large", 2.5 μm, subspherical to negative-crystal-shaped inclusion. The surrounding garnet structure appears to be free of dislocations or other defect structures. Low magnification TEM images also revealed the occurrence of other "large" pockets and cracks containing a poorly-crystalline to amorphous material, very likely representing glass in microfractures such as those shown in Fig.8b,c.

In addition to the "large" micrometer-sized inclusions, the dark garnet cores also host trails of nanometer-sized (up to 300 nm) FI (Fig.13b,c). These FI are often aligned along dark contrast features, indicative of crystal structural strain, and reasonably corresponding to structural discontinuities such as nanofractures or dislocations. These structural discontinuities connect all inclusions in the trail and are similar to features observed by Vityk et al. (2000) associated with FI in quartz that had been experimentally reequilibrated to cause fluid leakage. The shape of nanometer-sized inclusions ranges from rounded, “drop-like” to negative crystal (Fig.13d,e respectively). Figure 13d shows the details of the connection between an inclusion and structural defects (i.e., the linear feature on the right side of image).

Microstructures associated with partially decrepitated FI include linear crystal defects or trails of secondary fluid inclusions if the cracks are partially annealed, often with a radial arrangement around decrepitated FI (Vityk et al., 2000; Viti and Frezzotti, 2001). Unfortunately, due to the small field of view on electron-transparent areas, the geometric relationships between isolated micrometer-sized inclusions and trails of nanometer-sized inclusions are not clear, and direct emanation of trails from large inclusions could not be observed. However, it seems realistic to consider these nanometrer-sized trails as the path for fluid transport out of inclusions during reequilibration.

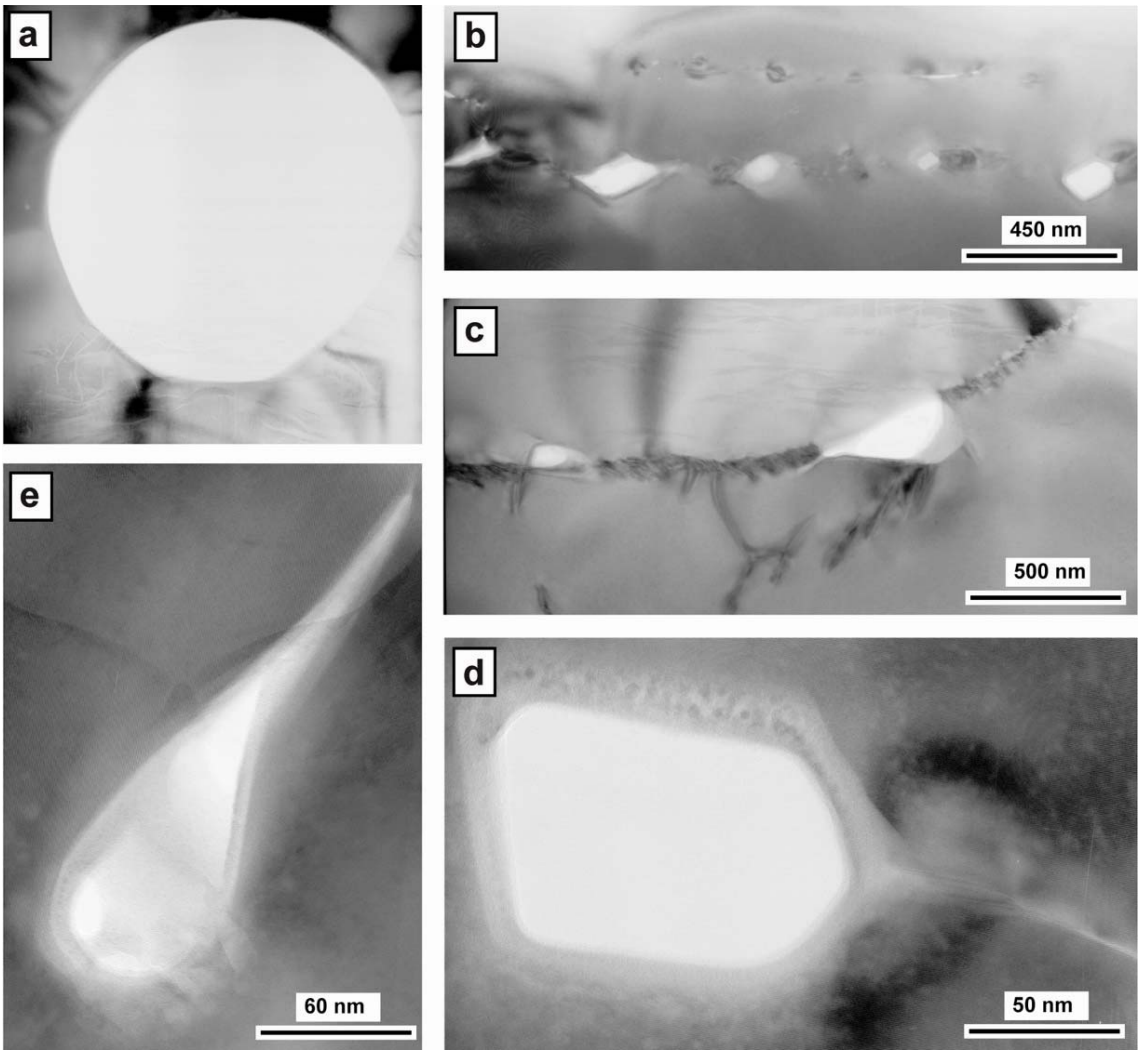

Figure 13: *TEM images of FI in garnet from Bt-Grt-Sil enclaves (sample HO50). a) subspherical to negative-crystal FI, surrounding host shows no dislocations or other defective structures. Field view: 3 µm; b) and c) trails of nanometer-sized FI, ≤300 nm across, with dark contrast features, most likely structural discontinuities (i.e. nanofractures, dislocations), that connect all inclusions in the trail. d) negative crystal FI visible in detected trails. e) drop-like shaped FI with visible the connection between inclusion and structural defects (right side of the image).*

3.5.7) Composition of MI and biotite in garnet from Spl-Crd enclaves

The glass in MI from Bt-Grt-Sil enclave HO50 was thoroughly characterized by Acosta-Vigil et al. (2007, 2010). In the present study we analyzed by EMP the glasses hosted in MI and mixed inclusions from Spl-Crd enclaves. Sodium loss during EMP analysis is on average 57% relative, estimated using a rhyolitic standard analyzed at the same operating conditions. Therefore, melt analyses have been corrected by increasing Na_2O by 57% relative, and decreasing SiO_2 and Al_2O_3, in a manner similar to that discussed in Cesare et al. (2009). Results (table 5) indicate a peraluminous, rhyolitic and felsic melt composition, with average SiO_2 = 69 wt%, K_2O>Na_2O (average

values 4.5 and 2.2 wt% respectively), low CaO (0.6 wt%) and ($FeO+MgO+TiO_2$)<1.5 wt%.

Sample	HO19	
No. Analyses	15	(std dev)
SiO_2	68.95	(1.60)
TiO_2	0.10	(0.11)
Al_2O_3	12.82	(1.10)
FeO	1.32	(0.40)
MnO	0.16	(0.16)
MgO	0.02	(0.03)
CaO	0.68	(0.16)
Na_2O	2.25	(0.33)
K_2O	4.56	(0.80)
P_2O_5	0.16	(0.07)
F	0.01	(0.03)
H_2O by diff.	8.97	(1.57)
#Mg	0.03	(0.03)
ASI	1.30	
Norm Qtz	36.19	
Norm Ab	19.06	
Norm Or	26.93	
Norm An	2.34	
Norm Crn	3.32	

Table 5: *EMP analyses of melt inclusions in Spl-Crd enclaves (sample HO19).*

The magnesium number is low (X_{Mg} = 0.03). The H_2O content, assumed to be the difference between the EMP total and 100%, is variable but generally high and compatible to that of a melt saturated in a H_2O-rich fluid at the inferred PT conditions of garnet growth, as also suggested by the average ASI value (1.30). Except for the markedly higher average H_2O content (8.9 wt% vs. 2.7 wt%) these melts from the Spl-Crd enclave are similar to those occurring in MI from Bt-Grt-Sil enclaves (Acosta-Vigil et al., 2007).

Biotites enclosed at garnet core have different composition depending on their size, as reported in table 6. Small subhedral biotites (Bt1) have an average TiO_2 = 3.4 wt%, lower than the average TiO_2 content found in the larger crystals (Bt2), 5.40 wt%. Conversely X Fe values are generally higher in the first type, 0.68 – 0.75, than in the latter, 0.66 - 0.68.

	Bt1	Bt1	Bt1	Bt1	Bt1	Bt1	Bt2	Bt2
Na_2O	0.21	0.22	0.21	0.17	0.34	0.25	0.23	0.30
MgO	4.70	4.83	4.67	4.62	6.01	4.73	6.11	6.03
Al_2O_3	18.85	19.70	18.61	18.59	17.98	18.25	18.60	17.11
SiO_2	34.40	34.57	35.11	35.06	34.83	34.56	33.68	34.77
K_2O	10.10	9.93	10.01	10.00	10.01	10.06	9.84	9.75
CaO	0.03	0.03	0.06	0.07	0.00	0.05	0.08	0.05
TiO_2	3.38	2.97	2.81	2.66	4.95	3.61	5.53	6.10
MnO	0.65	0.54	0.62	0.60	0.41	0.55	0.27	0.14
FeO	25.08	25.04	24.93	25.18	22.80	25.32	21.22	22.58
Total	97.52	97.91	97.33	97.02	97.72	97.55	95.91	97.14
Si	5.307	5.291	5.409	5.425	5.299	5.335	5.189	5.312
Ti	0.392	0.342	0.326	0.310	0.566	0.419	0.641	0.700
Al	3.427	3.553	3.379	3.391	3.224	3.321	3.377	3.080
Fe^{2+}	3.236	3.205	3.212	3.258	2.901	3.269	2.734	2.884
Mn	0.085	0.070	0.081	0.078	0.053	0.071	0.035	0.018
Mg	1.080	1.101	1.072	1.066	1.363	1.089	1.403	1.373
Ca	0.005	0.005	0.010	0.011	0.000	0.008	0.012	0.009
Na	0.064	0.065	0.063	0.050	0.100	0.075	0.069	0.089
K	1.988	1.938	1.968	1.974	1.943	1.980	1.934	1.901
Total	15.598	15.614	15.663	15.602	15.639	15.659	15.572	15.519
A site	2.057	2.008	2.041	2.035	2.043	2.064	2.015	1.999
X_{Fe}	0.75	0.74	0.75	0.75	0.68	0.75	0.66	0.68

Table 6: *EMP analyses of biotite in garnet from Spl-Crd enclaves (sample HO19). All Fe considered as* Fe^{2+}.

3.6) Discussion

El Hoyazo enclaves were removed from the medium-deep crust during anatexis and rapidly transported and emplaced to the surface by upwelling magmas. In this setting, crystals hosting FI are subject to a sudden change in confining pressure: this can lead to a partial (leakage) to total (decrepitation) FI reequiibration, with formation of microfractures on the FI walls or decrepitation haloes surrounding the original FI. In garnet from Spl-Crd and Bt-Grt-Sill enclaves, FI lack optical evidence of decrepitation, and their microstructural features suggest that they were trapped during garnet growth and in a condition of fluid-melt immiscibility conditions. Although few partially healed cracks are visible in the garnet core in the studied samples, portions of the FI+MI clusters seem completely unaffected by this brittle deformation event (Fig. 4b, 6c).

Assuming that these inclusions are primary, their low calculated densities are incompatible with those expected both for the inferred garnet growth conditions, 690-750°C and 5-7 kbar (Acosta-Vigil et al. 2010), and for metamorphic peak conditions, 850±50°C and 5-7 kbar (Cesare et al.,1997) (boxes "A" and "B" respectively, Fig.12). This discrepancy suggests that the FI density decreased after entrapment, and this may have occurred in a closed system (with no loss of material), or by more extensive

leakage of components and their removal from the vicinity of the FI. Both hypotheses are considered below.

3.6.1) Density decrease: causes and conditions

Two different closed-system processes may have caused the observed decrease in density of the FI: stretching and step-daughter precipitation.

Fluid inclusion stretching (Bodnar, 2003) involves a FI volume change with little or no loss of fluid from the inclusion. This process may occur when the host mineral PT path results in a pressure inside the FI that is different (higher or lower) than the confining pressure. If the confining pressure is less than the internal pressure in the FI by more than some threshold value (that is a function of FI size, shape and host mineral, see Bodnar, 2003), the higher FI internal pressure may produce plastic deformation in the surrounding host. The result is an inclusion volume increase with concomitant FI density decrease, without mass loss. In the present case study, it would have been necessary for the observed inclusions to have expanded to account for their lower densities compared to those expected at peak P-T conditions. The highest calculated density FI (H_2O = 90 mol%, 0.53 g·cm^{-3}, fluid inclusion "1" in table 3) would require a volume reduction of about 25% from its present-day value to reach a density of 0.73 g·cm^{-3}, the minimum density required for an isochore to intersect the proposed PT conditions of entrapment (box "A" in Fig.12). The volume reduction required is even higher if referred to PT conditions of garnet growth proposed by Acosta-Vigil et al. (2010) (box "B" in Fig.12). Such a very large volume change is unlikely to be accommodated by plastic deformation for any mineral phase. Therefore, re-equilibration by stretching does not appear to be a reasonable interpretation of the FI from El Hoyazo.

Step-daughter precipitation occurs when trapped fluid interacts with the host mineral, with production of new crystalline phases in a closed system (Kleinefeld and Bakker, 2002; Heinrich and Gottschalk, 1995). In this reaction, fluid is partially consumed, and because of the higher density of solid phases, the remaining fluid density decreases. In the studied FI, carbonates locally occur as accessory phases: however, even assuming an original CO_2-rich composition (X_{CO2} = 0.7) for a fluid inclusion, with ρ_{tot} = 0.87 g·cm^{-3} (minimum density required to reach 5.5 kbar at 850°C, using isochores estimated by NEWTWO software), mass balance calculations show that re-equilibrated FI should contain a carbonate crystal occupying at least 25% of the FI volume. Obviously, such a phase should be easily recognizable during petrographic examination and during Raman analyses: conversely, only <5% of the analyzed inclusions contain visible

carbonates, and the carbonates are much smaller than 25% of the inclusion volume. It follows that this type of re-equilibration process cannot explain the discrepancy between inferred peak PT conditions and FI isochores. Similarly, closed-system re-equilibration of a COH fluid along a decreasing temperature path (Cesare, 1995) would have produced easily detectable amounts of graphite within inclusions, and can be also ruled out.

A decrease in the density of a FI may also occur by (partial) decrepitation (Bodnar, 2003). This re-equilibration process should be expected in the El Hoyazo enclaves as they were emplaced along a decreasing PT path, but as already stated we could not identify microstructural evidence of such reequilibration by optical investigation. TEM imaging of garnet from Bt-Grt-Sil enclaves revealed the presence of trails of sub-micron (≤200 nm) FI. Although no trails were observed that originated from larger FI, we propose that they may represent escape pathways for fluid in FI. No TEM images were collected on Spl-Crd enclaves, but the presence of similar cracks may be inferred based on the recorded densities, suggesting that FI opened and resealed during uplift of the enclaves to the surface.

If leakage occurs when H_2O and CO_2 are unmixed, water is more likely than CO_2 to infiltrate any microcracks opened on the FI walls, because of its higher wetting angle (Watson and Brenan, 1987). In this study, enclaves were brought to the surface in magma with a temperature of ~800°C. Therefore, trapped fluid is likely to have remained in a supercritical, homogeneous state until final cooling (after the enclaves were emplaced on the seafloor), because the two-phase (liquid+vapor) field does not extend to such high temperatures for low salinity H_2O-CO_2 mixtures (Schmidt and Bodnar, 2000). Preferential water removal from quartz-hosted FI with homogeneous H_2O-CO_2 fluids is discussed by Hollister (1990), who proposes that water may be selectively removed from the inclusions if the host mineral undergoes ductile strain, even if the fluid is in the one-phase (supercritical) state. Preferential water loss occurs because H_2O is known to create Si-OH bonds, favoring host quartz deformation, while CO_2 is not known to interact with the quartz structure, and therefore remains in the inclusion. However, a ductile strain environment is unlikely for the El Hoyazo enclaves, because the enclaves were rapidly transported to the surface in a fluid medium (magma), and observed nanocracks likely developed because of the sudden decompression during eruption. If leakage of a homogeneous fluid occurred, only the density of the FI would change and the original composition would be preserved. Conversely, if H_2O is preferentially removed, both the density and the composition

would change. Estimated compositions for Spl-Crd enclaves show a range of H_2O/CO_2 from 13 to 1 that is consistent with H_2O preferential leakage. However, the extremely low densities found in Bt-Grt-Sil enclave HO50 suggest the leakage involves all fluid components.

Trapped fluids in the two different enclave types appear to have leaked to different extents. In Spl-Crd enclaves, the highest density FI would have lost 50 wt% of the original water, assuming only H_2O removal and an original density of 0.73 $g \cdot cm^{-3}$ (an isochore drawn for this density would intersect the PT field defined by box "A" in Fig.12). The required loss would be even greater for the other measured inclusions in the Spl-Crd enclaves. In Bt-Grt-Sil enclaves the loss of components from FI was almost complete, given the low density of the FI (0.1 $g \cdot cm^{-3}$). FI are most likely to have been H_2O-bearing at entrapment, but water is no longer detectable, suggesting total H_2O removal, unlike FI in Spl-Crd enclaves. Relative amounts of CO_2 and N_2 in FI in Bt-Grt-Sil enclaves are more variable than in Spl-Crd enclaves. This fact, combined with the extremely low densities, suggests that, in addition to water, some CO_2 may have also been lost from the inclusions during re-equilibration.

Isochores for the FI clearly define two groups, depending on the enclave type, and represent different degrees of re-equilibration: isochores are steeper and more scattered for Spl-Crd enclaves, while isochores are almost flat and are more tightly grouped for the Bt-Grt-Sil enclaves. Given the assumption that both samples followed the same PT path, such a difference in isochores must reflect different FI behavior during decompression.

FI may leak if the internal pressure (P_i) exceeds the external pressure (P_e) and reaches a critical overpressure ($\Delta_P = P_i - P_e$) at which point re-equilibration begins. Several experimental studies (see Bodnar, 2003 and references therein) on minerals with Mohs hardness (H_M) ≤7 characterized the critical Δ_P as mainly dependent on FI size and host mineral features (i.e. hardness, presence of cleavage). In the present study, estimated densities suggest that FI in garnet in Spl-Crd enclaves partially decrepitated at Δ_P ≥3 kbar, while Bt-Grt-Sil enclaves FI at Δ_P ≈5.5 kbar. Such high pressure differentials for garnet are consistent with those expected for a mineral with Mohs hardness (garnet: H_M = 7.5-8) slightly higher than quartz (H_M = 7), although tensile strength is not a linear function of H_M and no experimental data on FI reequilibration are available for garnet (Bodnar, 2003).

Hard minerals such as quartz and garnet are expected to re-equilibrate by brittle deformation of the FI walls, with creation of micro-(nano-) cracks, as observed in the present work at TEM observation scale (Bodnar, 2003). These cracks may or may not

connect the inclusions to the exterior of the garnet host: 1) in the first case fluid loss and the resultant P_i (and then density) would be controlled by P_e at the moment of FI resealing, or 2) in the second case, microcracking would decrease density by increasing FI volume (through cracks opening) and by fluid leakage, but with no influence from the P_e, and then FI resealing would have been instantaneous. In the latter case, however, garnet is expected to have increased the volume to accommodate the space needed for the fluid expansion in the host.

Isochores for Spl-Crd enclaves span a range of 3 kbar at 850°C. If hypothesis (1) above is assumed, at El Hoyazo FI re-equilibration occurred as a *diachronous* process, in which the FI re-equilibrated at different depth during uplift, each one independent from the others. Assuming that enclaves remained at T~800°C until the eruption, then the highest density FI would have been the first one to open (and reseal) at ≈3 kbar; conversely, the lowest density FI would have been the last one to reseal at ≈1 kbar. Such a spread in the FI re-equilibration P within the same host mineral (even within the same grain) may reflect the effect of FI size. Generally, smaller FI (average size = 15 μm) tend to re-equilibrate at higher Δ_P values, compared to larger ones (Bodnar, 2003). In the case of El Hoyazo, Δ_P increases as the enclave is brought toward the surface, and the last re-equilibrated FI should be the smaller ones. However, the lack of a size-density correlation for the El Hoyazo FI eliminates this possibility. It also seems unlikely that several primary FI, belonging to the same FIA and in the same host, would have behaved so differently by re-equilibrating at different depths. If hypothesis (2) is considered, then FI re-equilibration at El Hoyazo was a *synchronous* process. As stated before, there is no density-size correlation among measured FI, so it is likely that every inclusion underwent decrepitation at the same depth of ≈3 kbar (re-equilibration depth for the less re-equilibrated FI). The resulting densities would depend only by the ability of garnet to develop a more or less extended system of micro-(nano-) cracks around each FI, with variable volume increase/density decrease. Based on these considerations, synchronous partial decrepitation seems the most likely process to have occurred in Spl-Crd enclaves. Conversely, in Bt-Grt-Sil enclaves, the abundance of cracks of different scales, ranging from mm to nm, (Fig. 8b,c and 13b,c) may have allowed P_i to be controlled by P_e. Therefore, tightly grouped isochores suggests that FI resealed at a shallow depth, most likely at a pressure of about 500 bar, very close to the time of eruption of the enclaves onto the seafloor.

Although both enclave types followed the same PT path, their FI underwent different extents of fluid loss. One factor that may have influenced host garnet behavior during decompression is the amount of inclusions, especially MI, in the garnet core. MI (and

FI) are much more abundant in Bt-Grt-Sil enclaves than in Spl-Crd enclaves. Inclusions act as defects in the crystal lattice, likely weakening its structure and making the large garnets in the Bt-Grt-Sil enclaves most likely to fracture. In this case, FI may have opened at depth, during uplift, and resealed later, when enclaves reached shallower crustal levels, allowing a more extensive fluid loss.

The occurrence of re-equilibrated FI in garnet is consistent with re-equilibration of inclusions found in cordierite and plagioclase in similar samples (Cesare et al., 2007), and demonstrates that enclaves lost part of their fluid component during their uplift to the surface. Loss of channel H_2O from cordierite during decompression from 5 kbar and equilibration at shallow levels has also been reported by Della Ventura et al. (2009) for El Hoyazo enclaves.

3.6.2) Composition of fluids and implications for anatexis

In Spl-Crd enclaves the highest density FI contains a fluid with ≤ 90 mol% H_2O, which increases to 95 mol% if the original composition is back-calculated assuming that only H_2O-removal occurred during re-equilibration. This aqueous fluid was trapped along with a peraluminous leucogranitic melt that is now enclosed in garnet as MI, under conditions of fluid-melt immiscibility. The estimated fluid composition is consistent with those reported for a COH fluid in equilibrium with a saturated melt (Eggler and Kadik, 1979; Tamic et al., 2001) in the range 700-800°C. The water content of the melt, estimated by difference from EMP totals, is ≈9 wt%, close to saturation values of 10-12 wt% in H_2O (Johannes and Holtz, 1996; Holtz et al., 2001) proposed for a rhyolitic melt at 700±20°C and 6 Kbar (Acosta-Vigil et al., 2010) in presence of a pure H_2O fluid. The water content is also in agreement with the average ASI value (1.30), that is close to those predicted for H_2O-saturated melting at 700-800°C (1.31-1.37, Acosta-Vigil et al., 2003).

The composition of biotite at the garnet core, along with MI, may suggest that the smallest biotite grains formed at temperatures slightly in excess of 750°C (Ti-in-Biotite thermometer, Henry et al., 2005; see also Cesare et al., 2008, Fig.10), before assemblage equilibration at the metamorphic peak conditions. This value is coherent with the hypothesis of an early garnet crystallization with respect to the peak assemblage, as proposed by Acosta-Vigil et al. (2010).

Fluid was also trapped in garnet in Bt-Grt-Sil enclaves under conditions of fluid-melt immiscibility. As in Spl-Crd enclaves, glass in MI in Bt-Grt-Sil enclaves is peraluminous and leucogranitic and similar in major element composition to MI in Spl-Crd enclaves, but with lower H_2O contents of 2.74 wt% (Acosta-Vigil et al., 2007), and lower average

ASI value (1.17). The fluid coexisting with such a melt is expected to contain H_2O, according to Johannes and Holtz (1996): however, since the fluid now contained in the FI is totally H_2O free, H_2O loss must have been complete.

In conclusion, originally trapped fluids in the two enclave types were different, according to the constraints defined by the coexisting melts: 1) garnets in Spl-Crd enclaves trapped an almost pure aqueous phase, with minor amounts of CO_2 and N_2, and the coexisting leucogranitic melt, high in water content, while 2) garnets in Bt-Grt-Sil enclaves enclosed a CO_2+H_2O+N_2 mixture, with a lower H_2O content than in the Spl-Crd enclaves, coexisting with a water-poor leucogranitic melt, both suggesting that the availability of water was limited during anatexis of the protolith.

Chapter 4
Summary and conclusions

4.1) Constraints on the PT conditions of partial melting

The data obtained in this work give constraints on the partial melting conditions of both khondalites and granulitic enclaves.

Regarding the partial melting of khondalites, the melt trapped is likely to have formed at temperature > 850°C, based on its ultrapotassic composition (see Fig.22, chapter 2) and on its average H_2O content (~2 wt%), estimated by EMP analyses on preserved glassy inclusions (Fig.1). These conditions agree with thermometry reported in literature for the khondalites in central KKB (e.g. Shabeer et al., 2002). The study of FI in sillimanite from the matrix of Bt-rich melanosome showed that this phase most probably crystallized (or re-crystallized) during the isothermal decompression, at conditions consistent with those proposed for the equilibration of the Grt-Crd-Bt-Sil-Spl assemblage, 820°C and 5 kbar (box "T", in Fig.1; L. Tajcmanova, pers.comm). However, as suggested by the occurrence of rutile inclusions in some garnets, an early garnet crystallization may have occurred at pressures higher than those at which the rock is now chemically reequilibrated. This hypothesis is consistent with the P value of 6-8 kbar, accepted as the most likely for partial melting in the central region of KKB (Cenki et al., 2002), that are therefore assumed as the probable conditions of MI entrapment. As a consequence, it can be conclude that MI were trapped in a different moment of the rock history with respect to the studied FI.

At El Hoyazo, the conditions of partial melting in the metapelitic enclaves were recently refined by Acosta-Vigil et al., (2010) after a careful study of trace elements in the MI trapped in different peritectic phases in Bt-Grt-Sil enclaves (Fig.2). The reported compositions of both fluid and melt in Spl-Crd enclaves are consistent with the proposed conditions of early melting during garnet growth at c. 700°C ("MI entrapment" in Fig.1), garnet being the first peritectic product of the beginning of the disequilibrium melting in the low-grade protolith (Cesare and Maineri, 1999; Acosta-Vigil et al., 2010). Partial melting proceeds during the prograde path of the enclaves, until the metamorphic peak is reached at 800-910°C (conventional geothermobarometry; Cesare et al., 1997). The retrograde path is characterized by a coronitic reaction with partial replacement of garnet (box "AV"; Alvarez et al., 2007) at ~820°C and 4.5 kbar, followed by the rapid uprise of the enclaves due to the magma ascent (dashed line in

Fig.2). Such a rapid transport toward the surface led to reequilibration of the FI at pressures estimated to be equal or lower than 3.3 kbar in Spl-Crd enclaves.

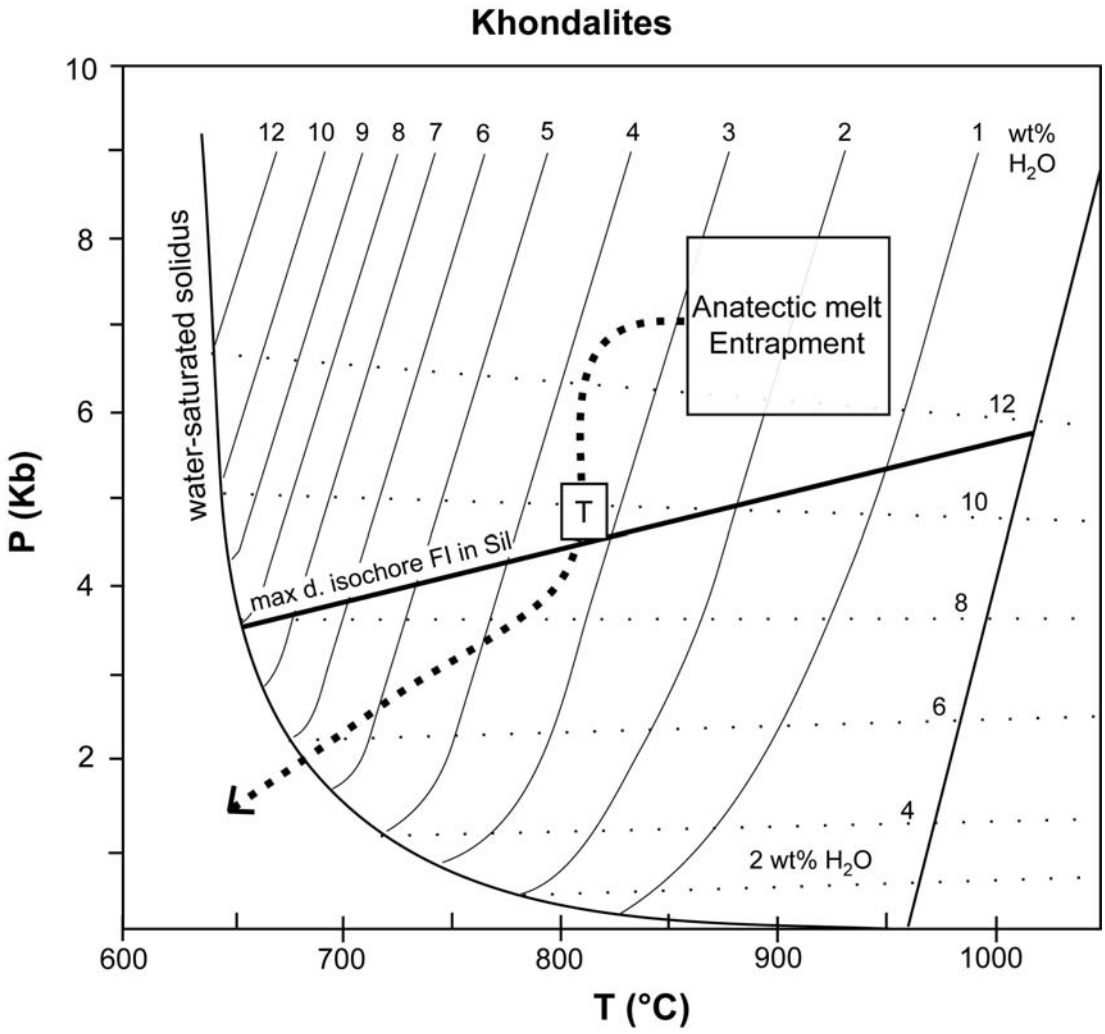

Figure 1: *proposed fluid-melt evolution in garnet from studied khondalites. Dashed bold line: exhumation path according to Nandakumar and Harley (2000) for the first, almost isobaric cooling path and to Santosh (1986) and Chacko et al. (1987) for the following isothermal decompression until 4.5-5 kbar. Box "T": proposed PT conditions for the equilibration of the Grt-Crd-Bt-Sil-Spl assemblage (L. Tajcmanova, pers.comm.); thin lines: liquidus curves of the system Q-Ab-Or for minimum melt compositions and specified H_2O contents; dotted lines: H_2O solubility isopleths for minimum and eutectic compositions in the system Q-Ab-Or (redrawn after Johannes and Holtz, 1996).*

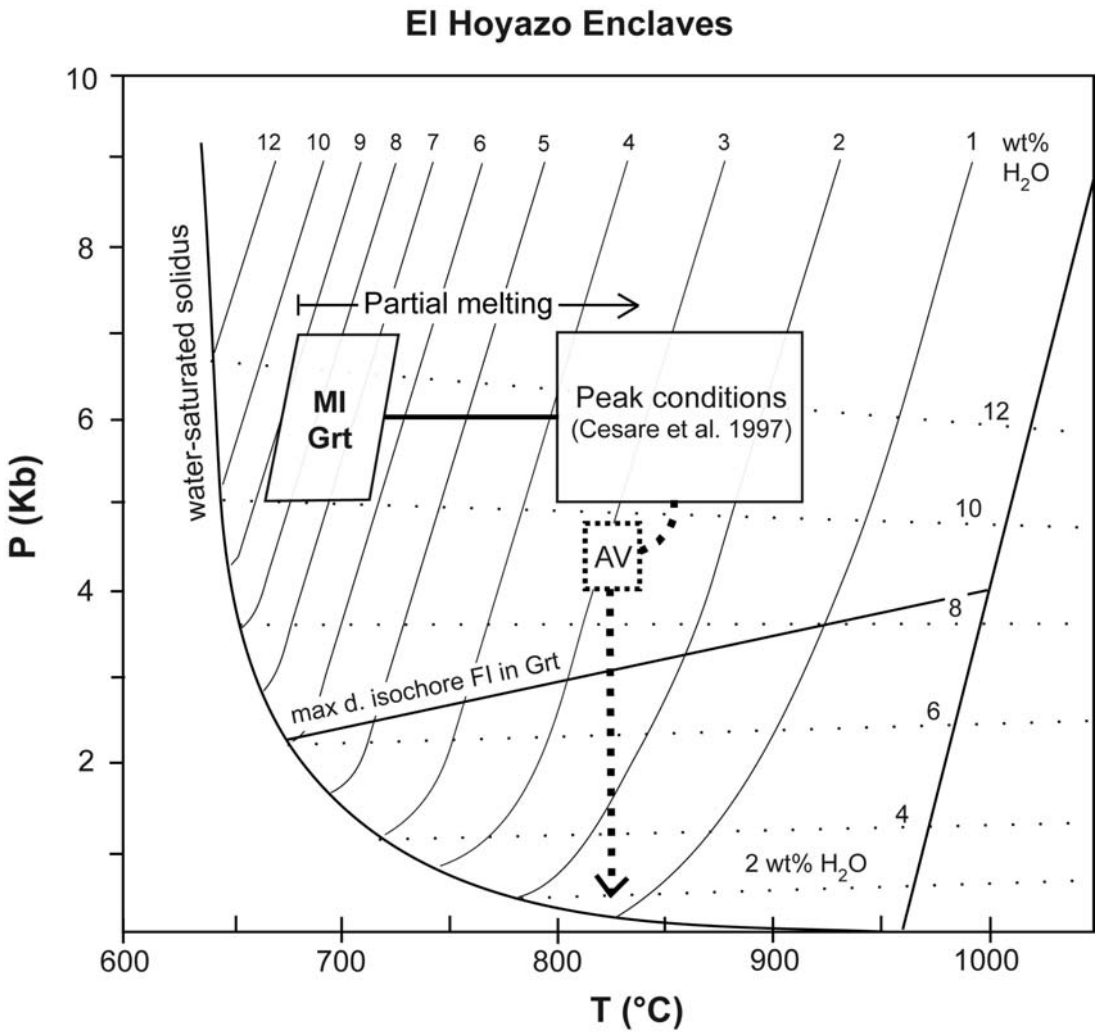

Figure 2: *proposed fluid-melt evolution in garnet of the El Hoyazo enclaves. Thin and dotted lines: see caption of Fig.1 (redrawn after Johannes and Holtz, 1996).*

4.2) Anatectic MI in khondalites: comments, reply and concluding remarks

The reported occurrence of MI in khondalites represents the first finding of MI in common slowly cooled metamorphic rocks, and makes of the present work the first detailed *in situ* study of anatectic melt in natural migmatites. The nature of the trapped phase, the retrieved compositions, the chosen approach and whether or not inclusions are representative of the original melt were largely questioned by Clemens (2009). In the present section these criticisms are taken in account and discussed.

EMP analyses on preserved glassy inclusions and homogenized nanogranites form the first dataset of melt compositions collected from MI in natural anatectic rocks. These data therefore represents one of the most important achievement of this project and expand the knowledge on leucosome compositions in metapelitic migmatites.

Special care was paid to the quality of the obtained microchemical data, especially regarding the problem of Na migration during analyses. Despite the observations of Clemens (2009), who highlights that even after Na correction the analyses probably still contain significant errors, the approach detailed in section 2.3 appears as a valid method to simulate the behavior of natural melts under the electron beam, with the aim of verifying the occurrence and the extent of Na loss at the selected analytical conditions, and therefore of calculating a correction factor. Based on these consideration, we believe that the use of a cooled stage for EMP analyses, although welcome, is not a necessary technical requirement, and that the collected compositions are indeed representative, also in their Na values, of the phase contained in MI.

Microchemical data confirmed that both homogenized nanogranites and preserved glassy inclusions contain the same ultrapotassic and Na-poor granitic melt. This phase plots very close to the Q-Or side of the CIPW Q-Ab-Or diagram (Fig.22, chapter 2), far from the “minimum melt” compositions (Johannes and Holtz, 1996) commonly considered as representative of an anatectic melt (see for example Sawyer, 2008). Clemens (2009) observed “this unusual composition suggests caution in their interpretation”, also because it appears in contrast with the detected occurrence of plagioclase in nanogranites assemblage. Although we agree that this composition is unusual, it should not be considered incorrect simply because dissimilar to the products commonly generated in partial melting experiments. In fact, ultrapotassic melt compositions do exist and are reported both in natural rhyolites (Maheshwari et al., 1996) and even in melts obtained by experimental melting of both on Na-poor natural metapelites (Patiño-Douce and Johnston, 1991) and haplogranitic synthetic systems at high temperature (T~900°C; Johannes and Holtz, 1996). Regarding the presence of plagioclase within nanogranites, this phase seems to be present only in small amounts not sufficient to be in contrast with the ultrapotassic character of the trapped melt, although a reliable visual estimate of phases modal abundance in nanogranites is not possible based on image analysis. In addition, the a Na-poor composition is largely confirmed as a common feature in all the analyzed remelted inclusions. This consistency of the compositional data also accounts for a substantial homogeneity of the melt phase trapped in different samples, ruling therefore out the influence of transient and local conditions, e.g. local disequilibrium melt-crystal phases, often observed in melt produced by partial melting experiments (Clemens, 2009 and references therein). The compositional homogeneity of glasses in MI from natural anatectic metapelites is also supported by the major and trace elements data obtained

by Acosta-Vigil et al. (2007,2010) from garnet and other mineral hosts in different samples of enclaves from El Hoyazo.

MI trapped in high-grade rocks should undergo crystallization because of the slow cooling rate experienced in regional metamorphic settings, estimated in <10 °C/m.y. for the studied khondalites (Cenki et al., 2004). In this context, the trapped melt should nucleate and grow crystal phases as commonly observed in MI from plutonic rocks (Frezzotti et al., 1992). This is observed also in the nanogranites of this study, the most abundant inclusion type in the MI clusters, that contain a polycrystalline aggregate of K-feldspar, quartz, biotite, and plagioclase. However, the presence of glassy inclusions and partially crystallized inclusions in the same clusters along with fully crystallized nanogranites demonstrates that inclusions containing the same melt may undergo variable degrees of crystallization. The occurrence of glassy inclusions is a striking finding in this setting and led Clemens (2009) to argue that this different behavior on cooling may indicate that nanogranites and glassy inclusions contain two different phases, e.g. a silicate melt and a ultrapotassic siliceous fluid respectively, likely to have been trapped in the garnet in different moments. Siliceous fluids similar to the proposed ones have been experimentally produced in the system KMASH between 300 and 600°C at P> 15 kbar (Massonne, 1992), while siliceous fluids with granitic compositions quite similar (8 wt% K_2O and 3 wt% Na_2O) to those of the studied inclusions are reported in experimental studies only at 30 kbar (sample quenched at 750°C, Burchard and Schreyer, 1995). Since khondalites from this area of the KKB underwent partial melting at medium pressures (6-8 kbar, e.g. Nandakumar and Harley, 2000), this hypothesis is untenable, as also confirmed by the water content estimated in studied MI (~2 wt%), while siliceous FI are generally much higher in H_2O (e.g. 25-50 wt%, Frezzotti et al., 2007). Moreover, both nanogranites and preserved glassy inclusions were trapped at the same time during garnet growth, i.e. they are primary (Roedder, 1982), and the lack of arrays of MI, typical microstructural occurrence of inclusions formed after the host growth, excludes the infiltration of external fluids. The explanation for the occurrence of preserved glass may be due to the size of glassy inclusions and nanogranites, demonstrated as statistically different (Fig.18, chapter 2). As discussed in detail in section 2.8, this suggest that most of the smaller inclusions remained amorphous (glassy) because the small inclusion volume did not allow the establishment of concentration gradients high enough to form the “large” critical nuclei, and crystallization was therefore probably inhibited (Putnis et al., 1995; Muncill and Lasaga, 1988). The impossibility for some crystal phases of reaching a critical nucleus size appears also supported by the lack of plagioclase observed in partially crystallized

inclusions, consistent with the much slower nucleation kinetics of this phase, possibly due to a considerably larger critical nucleus size (Donaldson, 1979; Muncill and Lasaga, 1988).

The problem of Fe, Mg and Ca loss toward the encasing garnet by diffusion on cooling has been also evaluated. Homogenized inclusions show a variable increase in these three elements, more (Fe) or less (Mg, Ca) pronounced, with respect to the preserved glassy inclusions, and suggests that MI lost or acquired part of these elements during cooling. Nonetheless an effective elemental exchange cannot be invoked, since all the three considered elements are lower in the glassy inclusions with respect to homogenized MI (section 2.6.3). It must be noted that, even if diffusion out of the MI took place during the retrograde history of the rock, since the total amount of FeO, MgO and CaO accounts for the <5 wt% of the total composition in the homogenized MI, the diffusion of these three elements would have not influenced the ultrapotassic and granitic character of the melt. However, this post-entrapment modification needs to be taken in account and evaluated to estimate more precisely the original composition of the trapped melt. A possible effect of Fe and Mg diffusion seems to be the magnesian composition of biotite in nanogranites, not consistent with a igneous mica in felsic rocks. This problem could be evaluated by modeling the diffusion between garnet and biotite, or by reheating the samples to reproduce the compositions of the two phases at the conditions of equilibrium attained at high temperature.

In conclusions, a careful microstructural investigation of the samples, coupled with the use of the correct techniques of MI homogenization, microchemical analyses (e.g. analytical instruments with the appropriate spatial resolution and control of electron beam diameter) and data correction, in our opinion should have overcome the proposed objections. The reported dataset supports therefore the interpretation of MI in garnet from khondalites as containing droplets of anatectic melt, and represents a valid contribution to the knowledge of anatectic melt in natural rocks.

4.3) El Hoyazo enclaves: concluding remarks

Results from El Hoyazo enclaves expand the dataset on fluid inclusions formed during anatexis in the lower crust of the Alboran Domain, by characterizing the garnet-hosted fluid phase and the coexisting anatectic melt, as previously done on melt and fluid inclusions in cordierite and plagioclase (Cesare et al., 2007).

Despite their primary-looking features, FI in garnet in El Hoyazo enclaves re-equilibrated following entrapment, as has been observed in other host phases from the

same rocks (Cesare et al., 2007). Re-equilibration probably occurred via partial decrepitation, without leaving detectable evidence at the optical scale, although the FI are supposed to have lost at least 30% of their total original content. High resolution studies (TEM) showed the occurrence of rare, partially healed cracks at sub-μm scale, containing small cavities, which may have been the escape pathways for fluids that leaked from inclusions.

The occurrence of FI and MI in the same cluster in peritectic garnet accounts for their entrapment at fluid-melt immiscibility condition, confirming that the fluid was coexistent with anatectic melt. In Spl-Crd enclaves a water-rich leucogranitic melt was trapped along with a H_2O-rich (≤95 mol%), consistently with the presence of a free COH fluid phase. The occurrence of such a phase has been previously inferred by Cesare and Maineri (1999), based on the study of the crystallinity of the different generations of graphite. Melt and fluid compositional parameters (H_2O content, ASI value) suggest garnet growth at around 700°C, in agreement with a model proposed by Acosta-Vigil et al. (2010). Concerning the Bt-Grt-Sil enclaves, the almost complete decrepitation and fluid leakage undergone by the studied FI did not allow to estimate the original composition of fluids hosted in garnet. Based on the H_2O content of coexisting melt inclusions (Acosta-Vigil et al., 2007), we have inferred that this fluid was more CO_2-rich than the fluid in the Spl-Crd enclaves. Although final results clearly show that enclaves lost part of the original fluids, this work adds further compositional constrains to the characterization of anatexis of metapelites in the lower crust.

4.4) General conclusions

Research on melt and fluid inclusions in peritectic minerals represents a new approach to the problem of partial melting in natural rocks, and the present study demonstrated that reliable petrological and geochemical information on anatexis can be collected from nano- to micron-scale objects. Moreover, the finding of MI in well-characterized migmatites such as the khondalites from KKB suggests that a careful reinvestigation of other granulite-migmatite terrains could lead to further findings of anatectic melt, trapped also in other peritectic phases such as orthopyroxene, spinel, cordierite and ilmenite, until now overlooked. The preservation of these inclusions will essentially depend on the extent of chemical interaction with the host mineral, and on the mechanical behavior of the host during the post-entrapment history, since microfracturing would allow access of fluids and alteration of the original composition of the inclusions. Based on these considerations, melt inclusions should be targeted in strong minerals from the least deformed rock domains. The possibility of finding further

case studies of MI in migmatites has been confirmed by the recent reports from migmatitic terrains that underwent partial melting at variable conditions, from low (i.e., Ronda migmatites; Cesare et al., 2009b), high (i.e. Himalyan Belt, C. Groppo, pers.comm.) and ultrahigh pressures (i.e., Ulten Zone; Braga and Massonne, 2008).

The dataset reported in this study widens the horizons in crustal petrology, because for the first time the crustal melt composition has been analyzed rather than assumed. This fact represents a very important step forward in the understanding of partial melting in the crust, as it will allow both a direct comparison between natural and experimental melts, and to better constrain the petrogenetic models that involve partially melted rocks.

The presence of fluids during partial melting is inferred in many studies on migmatites and suggested by experimental studies. Since high grade rocks commonly recrystallize along their post-peak trajectory, fluid inclusions trapped during partial melting are likely to change their original composition, or, very often, to be destroyed. Re-crystallization is also responsible for the lack of microstructures that may relate fluid inclusions entrapment and partial melting. In the case of El Hoyazo enclaves, primary melt and fluid inclusions, trapped in conditions of fluid-melt immiscibility, have been both preserved by the rapid exhumation. This exceptional occurrence allowed the identification and characterization of a H_2O-rich fluid present during the anatexis, whose composition, despite the suffered reequilibration via leakage, must be very close to the original, and is consistent with the composition of the coexisting melt.

Acknowledgements

The biggest “thanks!” goes to Bernardo Cesare, my boss and mentor, because he gave me the “keys” to enter the fascinating world of melt and fluid inclusions in high grade rocks. He showed me -and is showing me day by day- how a high-quality scientific research must be conducted, and the fundamental importance of being able to evaluate objectively any hypothesis and then to support the chosen one in the most proper way. All Bernardo’s suggestions and critics, always straight to the crucial point of the problems, along with the discussions helped me to grow as scientist, and showed me the fundamental importance of the debate. Besides that, I`m indebted with him for the chance he gave me to learn several different work methodologies by sending me all over the world (literally!), and especially for the patience demonstrated in the last, crazy months of work. *Hail to the chief!*

Thanks to Emma Salvioli-Mariani for having introduced me to the magic world of the microthermometric study on FI and MI, for the infinite patience showed in answering my questions and during the many discussions, in which the metamorphic and magmatic approaches were often clashing together, really fruitful and fundamental to me to go forward in the understanding of these tiny bubbles,.

I wish to express my gratitude to Robert J. Bodnar, from Virginia Tech, for welcomed me in his lab and having shared with me his outstanding knowledge on nature and behavior of fluids on Earths. He showed me a new (for me) and comprehensive way of thinking for the study of earth sciences, and I hope to be able to apply it in the following years of research activity.

Maria Luce Frezzotti, Robert J. Tracy and Danilo Pedron are also acknowledged for their help and the profitable discussions.

The accomplishment of the present project raised several problems related to sample preparation and analytical limits of the instruments, and for these reasons a special thanks goes to all the research technicians that have been involved in this study, particularly Raul Carampin (CNR-Padova), Andrea Cavallo (INGV, Rome), Steve McCartney (ICTAS,Virginia Tech), Charles Farley (Raman Lab, Virginia Tech) and Luca Peruzzo (CNR-Padova) because the fulfillment of this project really would have had hard times without their help and deep interest. I wish also to thank Leonardo Tauro and Elena Masiero for their impressive ability and speed in preparing perfect samples.

A special thanks to Alessandra, far-away PhD colleague and close friend, the best one I ever had, for the exhausting discussions on petrology&fluids&life, and for her friendship.

I wish to express my gratitude also to my colleagues from the Geoscience Department of Padova, Ilaria, Fabrizio, Marta, Daria, Daniele, Filo, Tiberio, Fabio, Raffaella, Lucje, Luca, Ivana, Lisa and Lara for their support along these years, and their tolerance in the last months. I`m deeply grateful to the “crew” of the Fluid inclusions Lab at Virginia Tech (Matt “The Cod”, Pilar, Rosario, Daniel, Andras, Max and John) for their friendship, the fun (PK’S!) and the continuous brainstorming, that contributed to make my experience at VT one of the best ones in my life.

I`d like to say thanks also some of the people I met in Padova since my arrival here, for whom I study “bubbles in the rocks”: Alfio, Alessandro, Alice, Dario, Marta, Giorgia (nice to have you back in Padova, crazy girl!), il Sauro, Mattia and Mirko. Their friendship made great my life here.

At last, the most important thanks go to my parents, for their support and love, and to my sister Sonia, who also chose to study geology..... I hope you`ll enjoy this stuff like I did, and still do.

References

Acosta-Vigil, A., Buick, I., Hermann, J., Cesare, B., Rubatto, D., London, D., Morgan VI, G., 2010. Mechanisms of crustal anatexis: a geochemical study of partially melted metapelitic enclaves and host dacite, SE Spain. Journal of Petrology, in press.

Acosta-Vigil, A., Cesare, B., London, D., Morgan VI, G.B., 2007. Microstructures and composition of melt inclusions in a crustal anatectic environment, represented by metapelitic enclaves within El Hoyazo dacites, SE Spain. Chemical Geology 235, 450–465.

Acosta-Vigil, A., London, D., Morgan VI, G.B., Dewers, T.A., 2003. Solubility of excess alumina in hydrous granitic melts in equilibrium with peraluminous minerals at 700–800ºC and 200 MPa, and applications of the aluminum saturation index. Contributions to Mineralogy and Petrology 146, 100–119.

Alvarez-Valero, A., Cesare, B., Kriegsman, L.M., 2005. Formation of elliptical garnet in a metapelitic enclave by melt-assisted dissolution and reprecipitation. Journal of Metamorphic Geology 23, 65–74.

Alvarez-Valero, A., Cesare, B., Kriegsman, L.M., 2007. Formation of spinel-cordierite-feldspar-glass coronas after garnet in metapelitic xenoliths: reaction modeling and geodynamic implications. Journal of Metamorphic Geology 25, 305– 320.

Alvarez-Valero, A.M., 2004. Petrographic and thermodynamic study of the partial melting of restitic xenoliths from the Neogene Volcanic Province of SE Spain. Unpublished Ph.D. Thesis, 223 pp., Padova, Italy.

Andersen, T., Neumann, E.R., 2001. Fluid inclusions in mantle xenoliths. Lithos 55, 301–320.

Anderson, A.J., Bodnar, R.J., 1993. An adaptation of the spindle stage for geometric analysis of fluid inclusions. American Mineralogist, 78, 657-664.

Bakker, R.J., 2003. Package FLUIDS 1. Computer programs for analysis of fluid inclusion data and for modelling bulk fluid properties. Chemical Geology 194, 3–23.

Bakker, R.J., 2009. Package FLUIDS. Part 3. Correlations between equations of state, thermodynamics and fluid inclusions. Geofluids 9 (1), 63-74.

Benito, R., López-Ruiz, J., Cebriá, J.M., Hertogen, J., Doblas, M., Oyarzun, R., Demaiffe, D., 1999. Sr and O isotope constraints on source and crustal contamination in the high-K calc-alkaline and shoshonitic neogene volcanic rocks of SE Spain. Lithos 46, 773–802.

Berkesi, M., Hidas, K., Guzmics, T., Dubessy, J., Bodnar, R.J., Szabó, C., Vajna, B., Tsunogae, T., 2009. Detection of small amounts of H_2O in CO_2-rich fluid inclusions using Raman spectroscopy. Journal of Raman Spectroscopy 40, 1461 – 1463.

Bindu, R.s., 1997. Granulite Facies Spinel-Cordierite Assemblages from the Kerala Khondalite Belt, Southern India. Gondwana Research 1, 121-128.

Bodnar, R.,J., Student, J.J., 2006. Melt inclusions in plutonic rocks: petrography and microthermometry. In: Webster, J.D. (ed.) Melt inclusions in plutonic rocks. Mineralogical Association of Canada, Short Course 36, 1-26.

Bodnar, R.J., 2003. Re-equilibration of fluid inclusions. In: Samson, I., Anderson, A.,, Marshall, D. (eds.) Fluid Inclusions: Analysis and Interpretation. Mineralogical Association of Canada, Short Course 32, 213-230.

Bodnar, R.J., Connolly, J.A.D., Steele-MacInnis, M.J. 2009. A modified Redlich-Kwong equation of state for H2O-CO2 mixtures: application to fluid inclusion studies. XX ECROFI meeting, Granada (abstract).

Bodnar, R.J., Reynolds, T.J., Kuehn C.A., 1985. Fluid inclusion systematics in epithermal systems. In: Berger, B.R. and Bethke P.M. (eds.) Geology and Geochemistry of Epithermal Systems. Society of Economic Geologists, Reviews in Economic Geology 2, 73-98.

Braga, R., Massonne, H.J., 2008. Mineralogy of inclusions in zircon from high-pressure crustal rocks from the Ulten Zone, Italian Alps. Periodico di Mineralogia 77, p. 43–64.

Braun, I., Raith, M. and Ravindra Kumar, G. R., 1996, Dehydration-melting phenomena in leptynitic gneisses and the generation of leucogranites: a case study from the Kerala Khondalite Belt, southern India: Journal of Petrology 37,1285–1305.

Brown, M. 2001. Orogeny, migmatites and leucogranites: a review. Proceedings of the Indian Academy of Science (Earth and Planetary Science) 110, 313-336.

Brown, M., 2007, Crustal melting and melt extraction, ascent and emplacement in orogens: mechanisms and consequences: Journal of the Geological Society 164, 709–730.

Brown, M., Rushmer, T., 2006, Evolution and Differentiation of the Continental Crust: Cambridge, Cambridge University Press, 553p.

Burchard, M., Schreyer, W. 1995. Melting experiments on the granitic country rocks of the Dora Maira pyrope quartzites. Bochumer Geologische und Geotechnische Arbeiten 44, 23-27.

Burke, E.A.J., 2001. Raman microspectrometry of fluid inclusions. Lithos 55, 139–158.

Carrington, D.P., Harley, S.L., 1995. Partial melting and phase relations in high-grade metapelites: an experimental petrogenetic grid in the KFMASH system. Contribution to Mineralogy and Petrology 120, 270–291.

Cenki, B., Braun, I., and Bröcker, M., 2004, Evolution of the continental crust in the Kerala Khondalite Belt, southernmost India: Evidence from Nd isotope mapping combined with U-Pb and Rb-Sr geochronology: Precambrian Research 134, 275–292.

Cenki, B., Kriegsman, L. M., Braun, I., 2002, Melt-producing and melt-consuming reactions in anatectic granulites: P-T evolution of the Achankovil cordierite gneisses, South India: Journal of Metamorphic Geology 20, 543-561.

Cesare, B., 1995. Graphite precipitation within C-O-H fluid inclusions: closed-system chemical and density changes, and thermobarometric implications. Contributions to Mineralogy and Petrology 122, 25-33.

Cesare, B., 2008a. Crustal melting: working with enclaves. In: Sawyer, E.W., Brown, M. (eds.) Working with Migmatites. Mineralogical Association of Canada, Short Course 38, 37–55.

Cesare, B., Ferrero, S., Bartoli, O., Braga, R., Salvioli-Mariani, E., AcostaVigil,A., Meli, S., 2009b. ”Nanogranite” inclusions in peritectic minerals: finding the anatectic melt in migmatites and granulites. GSA Annual Meeting, Portland, (abstract).

Cesare, B., Ferrero, S., Salvioli-Mariani, E., Pedron, D., Cavallo, A., 2009a. Nanogranite and glassy inclusions: the anatectic melt in migmatites and granulites. Geology 37, 627-630.

Cesare, B., Gomez-Pugnaire, M.T., 2001. Crustal melting in the Alborán domain: constraints from the xenoliths of the Neogene Volcanic Province. Physycs and Chemistry of the Earth 26 (4–5), 255–260.

Cesare, B., Gomez-Pugnaire, M.T., Rubatto, D., 2003. Residence time of S-type anatectic magmas beneath the Neogene Volcanic Province of SE Spain: a zircon and monazite SHRIMP study. Contributions to Mineralogy and Petrology 146, 28–43.

Cesare, B., Maineri, C., 1999. Fluid-present anatexis of metapelites at El Joyazo (SE Spain): constraints from Raman spectroscopy of graphite. Contributions to Mineralogy and Petrology 135, 41–52.

Cesare, B., Maineri, C., Baron Toaldo, A., Pedron, D., Acosta-Vigil, A., 2007. Immiscibility between carbonic fluids and granitic melts during crustal anatexis: a fluid and melt inclusion study in the enclaves of the Neogene Volcanic Province of SE Spain. Chemical Geology, 237, 433-449.

Cesare, B., Meli, S., Nodari, L., Russo, U., 2005. Fe3+ reduction during biotite melting in graphitic metapelites: another origin of CO_2 in granulites. Contributions to Mineralogy and Petrology 149, 129–140.

Cesare, B., Rubatto, D., Gómez-Pugnaire, M.T., 2009c. Do extrusion ages reflect magma generation processes at depth? An example from SE Spain. Contributions to Mineralogy and Petrology 157, 267-279.

Cesare, B., Salvioli Mariani, E., Venturelli, G., 1997. Crustal anatexis and melt extraction during deformation in the restitic xenoliths at El Joyazo (SE Spain). Mineralogical Magazine 61, 15–27.

Cesare, B., Satish-Kumar, M., Cruciani, G., Shabeer, P., Nodari, L., 2008. Mineral chemistry of Ti-rich biotite from pegmatite and metapelitic granulites of the Kerala Khondalite Belt (southeast India): Petrology and further insight into titanium substitutions. American Mineralogist 93, 327–338.

Chacko, T., Lamb, M., Farquhar, J., 1996, in The Archean and Proterozoic terrains in southern

India within East Gondwana. In: Santosh, M. and Yoshida, M. (eds.) Gondwana Research Group Memoir 3. Field Science, 157–165, Osaka.

Chacko, T., Ravindra-Kumar, G. R., Newton, R. C., 1987, Metamorphic P-T conditions of the Kerala (S. India) Khondalite belt, a granulite facies supracrustal terrain: Journal of Geology 95, 343–358.

Chacko, T., Ravindra-Kumar, G. R., Meen, J. K., Rogers, J. J. W., 1992, Geochemistry of high-grade supracrustal rocks from the Kerala Khondalite Belt and adjacent massif charnockites: Precambrian Research 55, 469–489.

Clemens, J.D, Vielzeuf, D., 1987. Constraints on melting and magma production in the crust. Earth and Planetary Science Letters 86, 287–306.

Clemens, J.D., 1990. The granulite - granite connexion, in Vielzeuf, D. and Vidal, P., eds., Granulites and Crustal Differentiation: Dordrecht, Kluwer Academic Publishers, 25–36.

Clemens, J.D., 2006. Melting of the continental crust: fluid regimes, melting reactions, and source-rock fertility, in Brown, M. and Rushmer, T., eds., Evolution and Differentiation of the Continental Crust: Cambridge, Cambridge University Press, 296–331.

Clemens, J.D., 2009. The message in the bottle: “Melt” inclusions in migmatitic garnets. Geology 37, 671-672.

Clemens, J.D., Holness, M.B., 2000.Textural evolution and partial melting of arkose in a contact aureole: a case study and implications. Electronic Geosciences 5, 4.

Collins, A.S., Windley, B.F., 2002. The tectonic evolution of central and northern Madagscar and its place in the final assembly of Gondwana. Journal of geology 110, 325–339.

Comas, M.C., Platt, J.P., Soto, J.I., Watts, A.B., 1999. The origin and tectonic history of the Alboran Basin: Insights from Leg 161. In: Zahn, R., Comas, M.C., Klaus, A. (eds) Proceedings ODP, Scientific Results 161, 555–579.

Connolly, J.A.D., Cesare, B., 1993. C-O-H-S fluid composition and oxygen fugacity in graphitic metapelites. Journal of Metamorphic Geology 11, 379-388

Danyushevsky, L.V., MCNeill, A.W., Sobolev, A.V., 2002.: Experimental and petrological studies of melt inclusions in phenocrysts from mantle-derived magmas: an overview of techniques, advantages and complications. Chemical Geology 183, 5–24.

De Vivo, B., Frezzotti, M.L., 1994. Evidence for magmatic immiscibility in Italian subvolcanic systems. In: De Vivo, B., Frezzotti, M.L. (Eds.), Fluid Inclusions in Minerals: Methods and Application. IMA Short Course, Virginia Polytechnic Institute and State University. Press, Blacksburg, VA, pp. 209–215.

Della Ventura, G., Bellatreccia, F., Cesare, B., Harley, S. and Piccinini, M. 2009. FTIR microspectroscopy and SIMS study of water-poor cordierite from El Hoyazo, Spain: Application to mineral and melt devolatilization. Lithos 113, 498-506.

Diamond, L.W., 2001: Review of the systematics of H_2O-CO_2 fluid inclusions. Lithos 55, 69-99.

Donaldson, C.H., 1979, An experimental investigation of the delay in nucleation of olivine in Mafic Magmas: Contributions to Mineralogy and Petrology 69, 21–32.

Drury, S.A., Harris, N.B.W., Holt, R.W., Reeves-Smith, G.W., Wightman, R.T., 1984. Precambrian tectonics and crustal evolution in South India. Joyurnal of Geology 92, 1–20.

Duggen, S., Hoernle, K., van den Bogaard, P., Garbe-Schonberg, D., 2005. Post-collisional transition from subduction- to intraplate-type magmatism in the westernmost Mediterranean: evidence for continental-edge delamination of subcontinental lithosphere. Journal of Petrology 46, 1155–1201.

Duggen, S., Hoernle, K., van den Bogaard, P., Harris, C., 2004. Magmatic evolution of the Alboran region: the role of subduction in forming the western Mediterranean and causing the Messinian Salinity Crisis. Earth Planetary Science Letters 218, 91–108.

Eggler, D.H, Kadik, A., 1979. The system $NaAlSi_3O_8$ -H_2O-CO_2 to 20 kbar pressure; I, Compositional and thermodynamic relations of liquids and vapors coexisting with albite. American Mineralogist 64, 1036-1048.

Elkins, L. T., Grove, T., 1990. Ternary feldspar experiments and thermodynamic models. American Mineralogist 75, 544–559.

Fall, A., 2009. Application of fluid inclusions in geological thermometry. PhD thesis, Virginia Polytechnic Institute and State University.

Ferrero S., Cesare B., Salvioli-Mariani, E., Bodnar, R.J, 2009a. Textural and compositional study of melt inclusions (nanogranites) in anatectic metapelites. GSA Annual Meeting, Portland (abstract).

Ferrero S., Cesare B., Salvioli-Mariani, E., Bodnar, R.J, 2009b. Textural and compositional study of melt inclusions (nanogranites) in anatectic metapelites. Granulites & Granulites, Praga (abstract).

Flowers, G C., 1979. Correction of Holloway's (1977) adaptation of the modified Redlich-Kwong equation of state for calculation of the fugacities of molecular species in supercritical fluids of geologic interest. Contributions to Mineralogy and Petrology 69, 315-318.

Frezzotti, M.L., 1992. Magmatic immiscibility and fluid phase evolution in the M. Genis granite (SE Sardinia, Italy). Geochimica and Cosmochimica Acta 56, 21-33.

Frezzotti, M.L., 2001. Silicate melt inclusions in magmatic rocks: applications to petrology. Lithos 55, 273–299.

Frezzotti, M.L., Ferrando, S., Dallai, L., Compagnoni, R. 2007. Intermediate Alkali^Alumino-silicate Aqueous Solutions Released by Deeply Subducted Continental Crust: Fluid Evolution in UHP OH-richTopaz^Kyanite Quartzites from Donghai (Sulu, China). Journal of Petrology 48, 1219-1241.

Frezzotti, M.L., Touret, J.L.R., Lustenhouwer, W., Neumann, E.R., 1994. Melt and fluid inclusions in dunite xenoliths from La Gomera, Canary Islands: tracking the mantle metasomatic fluids. European Journal of Mineralogy 6, 805–817.

Fuhrman, M., Lindsley, D.H., 1988. Ternary-feldspar modeling and thermometer. American Mineralogist 73, 201–215.

Fyfe, W.S., 1973. The granulite facies, partial melting and the Archean crust. Philosophical Transactions of the Royal Society of London 273, 457-461.

Gardien, V., Thompson, A.B., Grujic, D., Ulmer, P., 1995. Experimental melting of biotite + plagioclase + quartz ± muscovite assemblages and implications for crustal melting. Journal of Geophysical Research 100, 15581–15591

Geologic Survey of India, 1995. 1.500,000 Geological and mineralogical map of Kerala, Tamil Nadu and Pondicheri. Geologycal survey of India, Calcutta.

Goldstein, R.H., Reynolds, T.J., 1994. Systematics of fluid inclusions in diagenetic minerals. S.E.P.M. Short Course 31, 199 pp.

Guidotti, C.V.,1984. Micas in metamorphic rocks. In S.W. Bailey (Ed.), Micas, 13. Reviews in Mineralogy Mineralogical Society of America, Chantilly, Virginia, pp. 357–468.

Hansen, E. C., Newton, R. C., Prame, W. K. B. N., Ravindra Kumar, G. R., 1987. Charnockite in the making in southern India and Sri Lanka. Contributions to Mineralogy and Petrology 96, 225–244.

Harley, S.L. and Santosh, M., 1995. Wollastonite at Nuliyam, Kerala, southern India: a reassessment of CO_2 infiltration and charnockite formation at a classic locality. Contributions to Mineralogy and Petrology 120, 83-94

Harris, N.B.W., Santosh, M., Taylor, P.N., 1994. Crustal evolution in South India: constraints from Nd isotopes. Journal of Geology 102, 139–150.

Hartel, T. H. D., Pattison D. R. M., Helmers, H., Maaskant,P., 1990. Primary granitoid-composition inclusions in garnet from granulite facies metapelite: Direct evidence for the presence of a melt? Geological Association of Canada 15, 54 (abstract).

Heinrich, W., Gottschalk, M., 1995. Metamorphic reactions between fluid inclusions and mineral host: I. Progress of the reaction calcite + quartz = wollastonite + CO_2 in natural wollastonite-hosted fluid inclusions. Contributions to Mineralogy and Petrology 122, 51–61.

Holland, T.J.B., Powell, R., 1998. An internally consistent thermodynamic data set for phases of petrological interest. Journal of Metamorphic Geology 16, 309–343.

Hollister, L. S., 1990. Enrichment of CO2 in fluid inclusions in quartz by removal of H_2O during crystal plastic deformation. Journal Structural Geology 12, 895-901.

Holloway, J.R., 1976. Fluids in the evolution of granitic magmas:consequences of finite CO_2 solubility. GSA Bulletin 87, 1513–1518.

Holloway, J.R., 1977. Fugacity and activity of molecular species in supercritical fluids. In: Fraser, D. (Ed.), Thermodynamics in Geology. Reidel, Boston, MA, 161–181.

Holness, M.B., Sawyer, E.W., 2008, On the pseudomorphing of melt-filled pores during the crystallization of migmatites: Journal of Petrology 49, 1343–1363.

Holness, M.B., Clemens, J.D., 1999. Partial melting of the Appin Quartzite driven by fracture-controlled H_2O infiltration in the aureole of the Ballachulish Igneous Complex, Scottish Highlands. Contributions to Mineralogy and Petrology 136, 154-168.

Holtz, F., Johannes, W., Tamic, N., Behrens, H., 2001. Maximum and minimum water contents of granitic melts generated in the crust: a reevaluation and implications. Lithos 56, 1–14.

Hopkins, M., Harrison, M.T., Manning, C.E., 2008. Low heat flow inferred from >4 Gyr zircons suggests Hadean plate boundary interactions. Nature 456, 493–496, doi: 10.1038/nature07465.

Johannes, W., Holtz, F., 1996, Petrogenesis and experimental petrology of granitic rocks: Berlin, Springer, 335p.

Kawakami, Y., Yamamoto, J., Kagi, H., 2003: Micro-Raman densimeter for CO_2 inclusions in mantle-derived minerals. Applied Spectroscopy 57, 1333-1339.

Kleinefeld, B., Bakker, R.J., 2002. Fluid inclusions as micro-chemical systems: evidence and modelling of fluid–host interactions in plagioclase. Journal of Metamorphic Geology 20, 845–858.

Kretz, R., 1983, Symbols for rock-forming minerals. American Mineralogist 68, 277-279.

Lemmon, E.W.; McLinden, M.O.; Friend, D.G., 2009. Thermophysical Properties of Fluid Systems. In: Linstrom and Mallard (eds.) NIST Chemistry WebBook, 69, Gaithersburg MD - http://webbook.nist.gov

Lopez-Ruiz, J., Rodriguez-Badiola, E., 1980. La region volcanica Neogena del sureste de Espana. Estudios Geologicos 36, 5–63.

Lowenstern, J., 1995. Applications of silicate-melt inclusions to the study of magmatic volatiles. In: Thompson, J.F.H. (ed.). Magmas, Fluids and Ore Deposits. Mineralogical Association of Canada Short Course Volume 23, 71-99.

Lowenstern, J.B., 2003. Melt inclusions come of age: volatiles, volcanoes, and Sorby's legacy. In: De Vivo, B., Bodnar, R.J. (Eds.), Melt Inclusions in Volcanic Systems: Methods, Applications and Problems. Developments in Volcanology, vol. 5. Elsevier Press, Amsterdam, pp. 1–22.

Maheshwari, A., Coltorti, M., Sial, A.N., Mariano, G., 1996, Crustal influences in the petrogenesis of the Malani rhyolite, southwestern Rajasthan: Combined trace element and oxygen isotope constraints: Journal of the Geological Society of India 47, 611–619.

Marchildon, N., Brown, M., 2001. Melt segregation in late syn-tectonic anatectic migmatites: An example from the Onawa contact aureole, Maine, USA. Physics and Chemistry of the Earth, Part A: Solid Earth and Geodesy 26, 225–229.

Marchildon, N., Brown, M., 2002. Grain-scale melt distribution in two contact aureole rocks: implications for controls on melt localization and deformation. Journal of Metamorphic Geology 20, 381-396.

Massonne, H.J., 1992. Evidence for low-temperature ultrapotassic siliceous fl uids in subduction zone environments from experiments in the system K_2O-MgO-Al_2O_3-SiO_2-H_2O (KMASH). Lithos 28, 421–434.

Morgan, G.B., IV, London, D., 2005, Effect of current density on the electron microprobe analysis of alkali aluminosilicate glasses: The American Mineralogist 90, 1131–1138.

Muncill, G.E., Lasaga, A.C., 1988, Crystal-growth kinetics of plagioclase in igneous systems; isothermal H2O-saturated experiments and extension of a growth model to complex silicate melts: The American Mineralogist, 73, 982–992.

Munksgaard, N.C., 1985. A non-magmatic origin for compositionally zoned euhedral garnets in silicic Neogene volcanics from SE Spain. Neues Jahrbuch für Mineralogie Abhandlungen 2, 73–82.

Munskgaard, N., 1984. High δ^{18} and possible pre-eruptional Rb-Sr isochrons in cordierite-bearing Neogene volcanics from SE Spain. Contributions to Mineralogy and Petrology 87, 351-358.

Nandakumar, V., Harley, S.L., 2000, A reappraisal of the pressure-temperature path of granulites from the Kerala Khondalite Belt, Southern India: Journal of Geology 108, 687–703.

Patiño Douce, A.E., 1996, Effects of pressure and H_2O content on the compositions of primary crustal melts: Transactions of the Royal Society of Edinburgh. Earth Sciences 87, 11–21.

Patiño Douce, A.E., 1999, What do experiments tell us about the relative contributions of crust and mantle to the origin of granitic magmas?: Geological Society of London: Special Publications, 168, 55–75.

Patiño Douce, A.E., Harris, N., 1998. Experimental Constraints on Himalayan Anatexis. Journal of Petrology 39, 689-710.

Patiño Douce, A.E., Johnston, A.D., 1991, Phase equilibria and melt productivity in the pelitic system: implications for the origin of peraluminous granitoids: Contributions to Mineralogy and Petrology 107, 202–218.

Pattison, D.R.M., 2006. The fate of graphite in prograde metamorphism of pelites: An example from the Ballachulish aureole, Scotland. Lithos 88, 85-99.

Perini G., Cesare B., Gómez-Pugnaire M.T., Ghezzi, S., Tommasini S., 2009. Armouring effect in decoupling Sr-Nd isotopes during disequilibrium crustal melting: the case study of frozen migmatites from El Hoyazo and Mazarrón, SE Spain. European Journal of Mineralogy 21, 117-131, in press.

Petford, N., Cruden, A.R., McCaffrey, K.J.W., Vigneresse, J.-L., 2000, Granite magma formation, transport and emplacement in the Earth's crust: Nature 408, 669–673.

Peucat, J. J., Vidal, P., Bernard-Griffiths, J., Condie, K. C.,1989. Sr, Nd, and Pb isotopic systematics in the Archean low- to high grade transition zone of southern India: syn-accretion vs post accretion granulites. Journal of Geology 97, 537–550.

Pitcher, W.S., 1993, The nature and origin of granite: London, Blackie Academic & Professional, 321 p.

Pretorius, W., Barton Jr, J.M., 2003. Petrology and geochemistry of crustal and upper mantle xenoliths from the Venetia Diamond Mine – evidence for Archean crustal growth and subduction. South African Journal of Geology 106, 213-230.

Putnis, A., Prieto, M., Fernandez-Diaz, L., 1995, Fluid supersaturation and crystallization in porous media: Geological Magazine 132, 1–13.

Roedder, E., 1984, Fluid inclusions: Mineralogical Society of America, Reviews in Mineralogy, v. 12, 644p.

Roedder, E., 1992. Fluid inclusion evidence for immiscibility in magmatic differentiation. Geochimica et Cosmochimica Acta 56, 5–20.

Santosh, M., 1986, Cordierite gneisses of southern Kerala, India: petrology, fluid inclusions and implications for crustal uplift history: Contributions to Mineralogy and Petrology 96,343–356.

Santosh, M., 1996. The Trivandrum and Nagercoil granulite blocks. In: Santosh, M., Yoshida, M. (Eds.), The Archaean and Proterozoic terrains in southern India within East Gondwana, 3. Gondwana Research Group Memoires 243–277.

Santosh, M., Jackson, D.H, Harris, N.B.W., Mattey, D.P., 1991. Carbonic fluid inclusions in South Indian granulites: evidence for entrapment during charnockite formation. Contributions to Mineralogy and Petrology 110, 318-330.

Santosh, M., Tsunogae, T., 2003. Extremely high density pure CO_2 fluid inclusions in a garnet granulite from Southern India. The Journal of Geology 111, 1–16.

Satish-Kumar, M.; Santosh, M.; Harley, S. L.; Yoshida, M., 1996. Calc-silicate assemblages from the Kerala Khondalite Belt, southern India: implications for pressure-temperature-fluid histories. Journal of Southeast Asian Earth Sciences 14, 245–263.

Sawyer, E.W., 1996, Melt-segregation and magma flow in migmatites: implications for the generation of granite magmas: Transactions of the Royal Society of Edinburgh. Earth Sciences 87, 85–94.

Sawyer, E.W., 2008, Atlas of Migmatites: Quebec, Mineralogical Association of Canada, The Canadian Mineralogist Special Publication 9, 386p.

Sawyer, E.W.,, Brown, M., 2008. Working with migmatites. Quebec, Mineralogical Association of Canada, Short Course Series 38, 158 p.

Shabeer, K. P., 2004, Petrology and geochronology of granulite facies metamorphic rocks from Kerala Khondalite Belt, southern India: implications to partial melting and heat source: Ph.D. thesis, Osaka City University, Osaka.

Shabeer, K. P., Satish-Kumar, M., Armstrong, R., Buick, I. S., 2005, Constraints on the timing of Pan-African granulite-facies metamorphism in the Kerala Khondalite Belt of southern India: SHRIMP mineral ages and Nd isotopic systematics: Journal of Geology 113, 95-106.

Sorby, H.C., 1858: On the microscopical structure of crystals, indicating origin of minerals and rocks. Quarterly Journal of the Geological Society of London 14, 453–500.

Srikantappa, C., Raith, M., Spiering, B., 1985. Progressive charnockitization of a leptynite-khondalite suite in southernKerala, India - evidence for formation of charnockites through decrease in fluid pressure? Journal of the Geologycal Society of India 26, 849–872.

Sterner, S.M., Bodnar, R.J., 1984. Synthetic fluid inclusions in natural quartz. I. Compositional types synthesized and applications to experimental geochemistry. Geochimica et Cosmochimica Acta 48, 2659-2668.

Sterner, S.M., Bodnar, R.J., 1989. Synthetic fluid inclusions –VII. Re-equilibration of fluid inclusions in quartz during laboratory-simulated metamorphic burial and uplift. Journal of Metamorphic Geology 7, 243–260.

Stevens, G., Clemens, J.D., Droop, T.R., 1997. Melt production during granulite-facies anatexis: experimental data from “primitive” metasedimentary protoliths. Contributions to Mineralogy and Petrology 128, 352–370.

Stockhert, B., Trepmann, C.A., Massonne H.J., 2009. Decrepitated UHP fluid inclusions: about diverse phase assemblages and extreme decompression rates (Erzgebirge, Germany). Journal of metamorphic geology 27, 673–684.

Student, J.J., Bodnar, R.J., 1999. Synthetic fluid inclusions XIV: Microthermometric and compositional analysis of coexisting silicate melt and aqueous fluid inclusions trapped in the haplogranite-H_2O-NaCl-KCl system at 800°C and 2000 bars. Journal of Petrology 40, 1509-1525.

Student, J.J., Bodnar, R.J., 2004 Silicate melt inclusions in porphyry copper deposits: Identification and homogenization behavior. Canadian Mineralogist 42,1563-1600.

Tadokoro, H., Tsunogae, T., Santosh, M., 2008, Metamorphic P-T path of the eastern Trivandrum Granulite Block, southern India: implications for regional correlation of lower crustal fragments: Journal of Mineralogical and Petrological Sciences 103, 279-284.

Tajčmanová, L., Connolly, J.A.D, Cesare, B., 2009. A thermodynamic model for titanium and ferric iron solution in biotite. Journal of Metamorphic Geology 27, 153-165.

Tamic, N., Behrens, H., Holtz, F. 2001. The solubility of H_2O and CO_2 in rhyolitic melts in equilibrium with a mixed CO_2–H_2O fluid phase. Chemical Geology 174, 333–347.

Thomas, J.B., Bodnar, R.J., Shimizu, N., Sinha, A.K., 2002, Determination of zircon/melt trace element partition coefficients from SIMS analysis of melt inclusions in zircon: Geochimica et Cosmochimica Acta 66, 2887–2901.

Thompson, A.B., 1982. Dehydration melting of pelitic rocks and the generation of H_2O-undersaturated granitic liquids. American Journal Sciences 282, 1567-1595

Thompson, A.B., 2001. Clockwise *P–T* paths for crustal melting and H_2O recycling in granite source regions and migmatite terrains. Lithos 56, 33-45.

Tomilenko, A.A.,Chupin V.P., 1983. Studying Inclusions in Minerals from Metamorphic Complexes (Nauka), Novosibirsk, 524

Torok, K., Degi, J., Szep, A., Marosi, G., 2005. Reduced carbonic fluids in mafic granulite xenoliths from the Bakony-Balaton Highland Volcanic Field, W-Hungary. Chemical geology 223, 93-108.

Touret, J., Olsen, S.N., 1985. Fluid inclusions in migmatites. In: Ashworth, J.R. (ed.), Migmatites, Blackie, Chapman and Hall, New York, 265-288.

Touret, J.L.R., 1971. Le faciès granulite en Norvège méridionale. Les inclusions fluides. Lithos 4, 423–436.

Touret, J.L.R., 1981. Fluid inclusions in high grade metamorphic rocks. In: Hollister, L.S., Crawford, M.L. (Eds.), Short Course in Fluid Inclusions: Applications to Petrology. Mineralogical Association of Canada, Calgary, 182–208.

Touret, J.L.R., 2009. Mantle to lower-crust fluid/melt transfer through granulite metamorphism. Russian Geology and Geophysics 50, 1052–1062.

Turner, S.P., Platt, J.P., George, R.M.M., Kelley, S.P., Pearson, D.G., Nowell, G.M., 1999 Magmatism associated with orogenic collapse of the Betic-Alboran Domain, SE Spain. Journal of Petrology 40, 1011–1036.

Tuttle, O.F., Bowen, N.L., 1958. Origin of granite in the light of experimental studies in the system $NaAlSi_3O_8$-$KAlSi_3O_8$-SiO_2-H_2O. Geological Society of America Memories 74, 153 p

Vanderhaeghe, O., 2001, Melt segregation, pervasive melt migration and magma mobility in the continental crust: the structural record from pores to orogens: Physics and Chemistry of the Earth. Part A: Solid Earth and Geodesy 26, 213–223.

Vernon, R. H., 2004. A Practical Guide to Rock Microstructure. Cambridge: Cambridge University Press, 594 pp

Vernon, R.H., 2007. Problems in identifying restite in S-type granites of southeastern Australia, with speculations on sources of magma and enclaves. Canadian Mineralogist 45, 147-178.

Vielzeuf, D., Clemens, J.C., Pin, C., Moinet, E., 1990, Granites, granulites and crustal differentiation, in Vielzeuf, D. and Vidal, P. (eds), Granulites and Crustal Differentiation: Dordrecht, Kluwer Academic Publishers, 59–85.

Vielzeuf, D., Holloway, J.R., 1988. Experimental determination of the fluid-absent melting relations in the pelitic system. Contribution to Mineralogy and Petrology 98, 257-276.

Vityk, M.O., Bodnar, R.J., Doukhan, J.C., 2000. Synthetic fluid inclusions: XV. TEM investigationof plastic flow associated with re-equilibration of synthetic fluid inclusions in natural quartz. Contributions to Mineralogy and Petrology 139, n. 3, 285-297.

Walte, N.P., Bons, P.D., Passchier, C.W., 2005. Deformation of melt-bearing systems-insight from in situ grain-scale analogue experiments. Journal of Structural Geology 27, 1666-1679.

Wang, C.H., Wright, R.B., 1973. Raman studies of the effect of density of the Fermi resonance in CO_2. Chemical Physycs Letters 23, 241-246.

Watson, E.B., Brenan, J.M. 1987. Fluids in the lithosphere 1. Experimentally determined wetting characteristics of CO_2-H_2O fluids and their implication for fluid transport, host-rock physical properties and fluid inclusion formation. Earth and Planetary Science. Letters 85, 497–515.

Werre, R.W., Bodnar, R.J., Bethke, P.M., Barton, P.B. Jr., 1979. A novel gas-flow fluid inclusions heating/freezing stage. Geological Society of America 11, 539 (abstract).

White, A.J.R., Chapell, B.W., 1983. Granitoid types and their distribution in the Lachlan fold belt, southeastern Australia. In Roddick, A.J. (ed.), Circum-Pacific Plutonic Terranes. Geological Society of America Memories 159, 21-34.

White, R.W., (2008): Insights gained from the petrological modeling of migmatites: Particular reference to mineral assemblages and common replacement textures. In: Sawyer, E.W., Brown, M. (eds.), Working with Migmatites. Mineralogical Association of Canada, Short Course 38, 77–96.

Zeck H.P., 1992. Restite-melt and mafic-felsic magma mixing and mingling in an S-type dacite, Cerro del Hoyazo, southeastern Spain. Transactions of the Royal Society of Edinburgh 83, 139-144.

Zeck, H.P., Williams, I., 2002. Inherited and magmatic zircon from Neogene Hoyazo cordierite dacite, SE Spain-Anatectic source rock provenance and magmatic evolution. Journal of Petrology 43,1089–1104.

Zeck. H.P., 1970. An erupted migmatite from Cerro de Hoyazo, SE Spain. Contributions to Mineralogy and Petrology 26, 225–246.

SUPPLEMENTARY

MATERIALS

(1)_Atlas of nanogranites

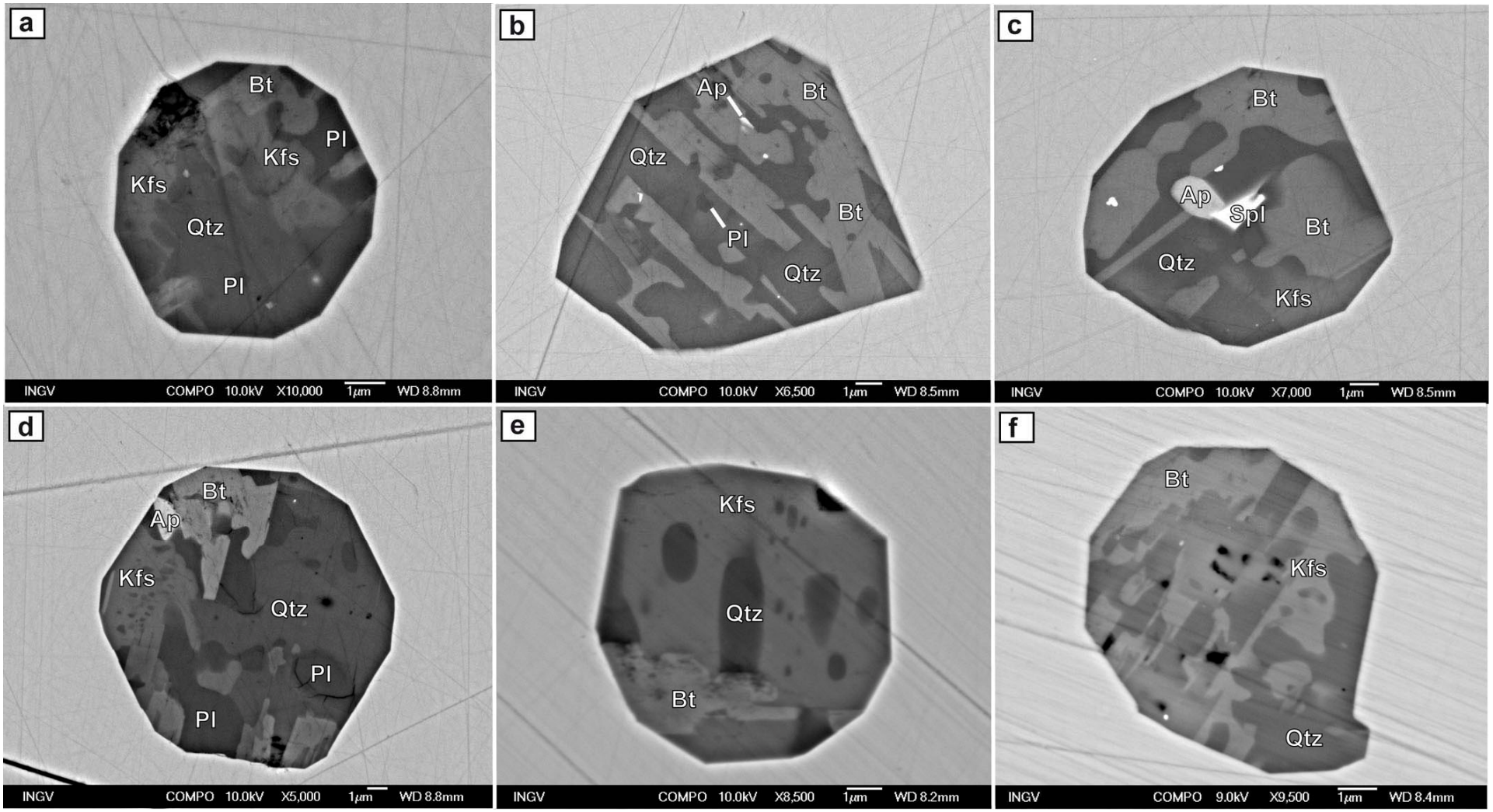

Figure 1: *Nanogranites, BSE images. Mineral abbreviations after Kretz, 1983.*

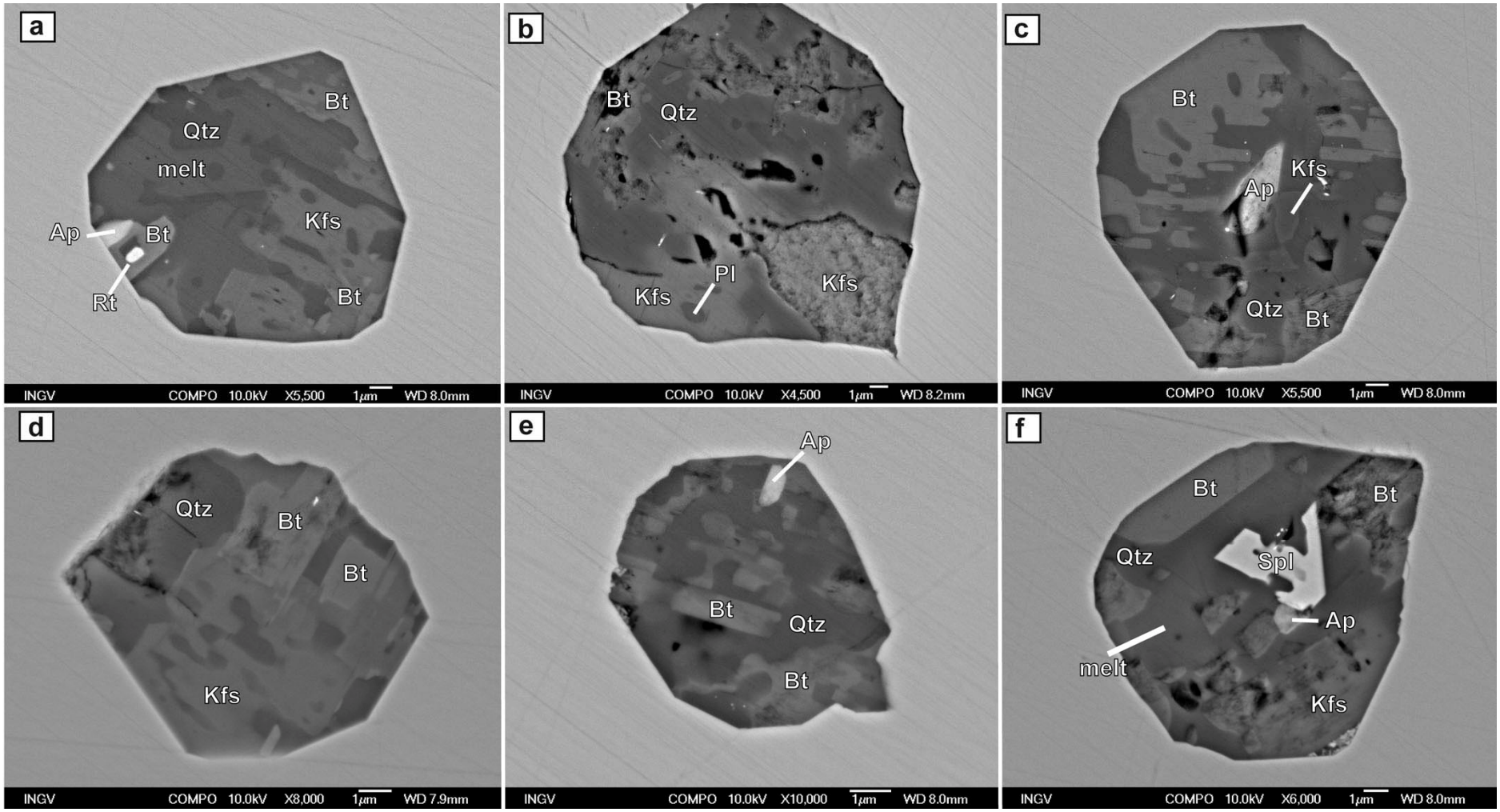

Figure 2: *Nanogranites, BSE images. Melt: Residual melt in partially crystallized inclusions.*

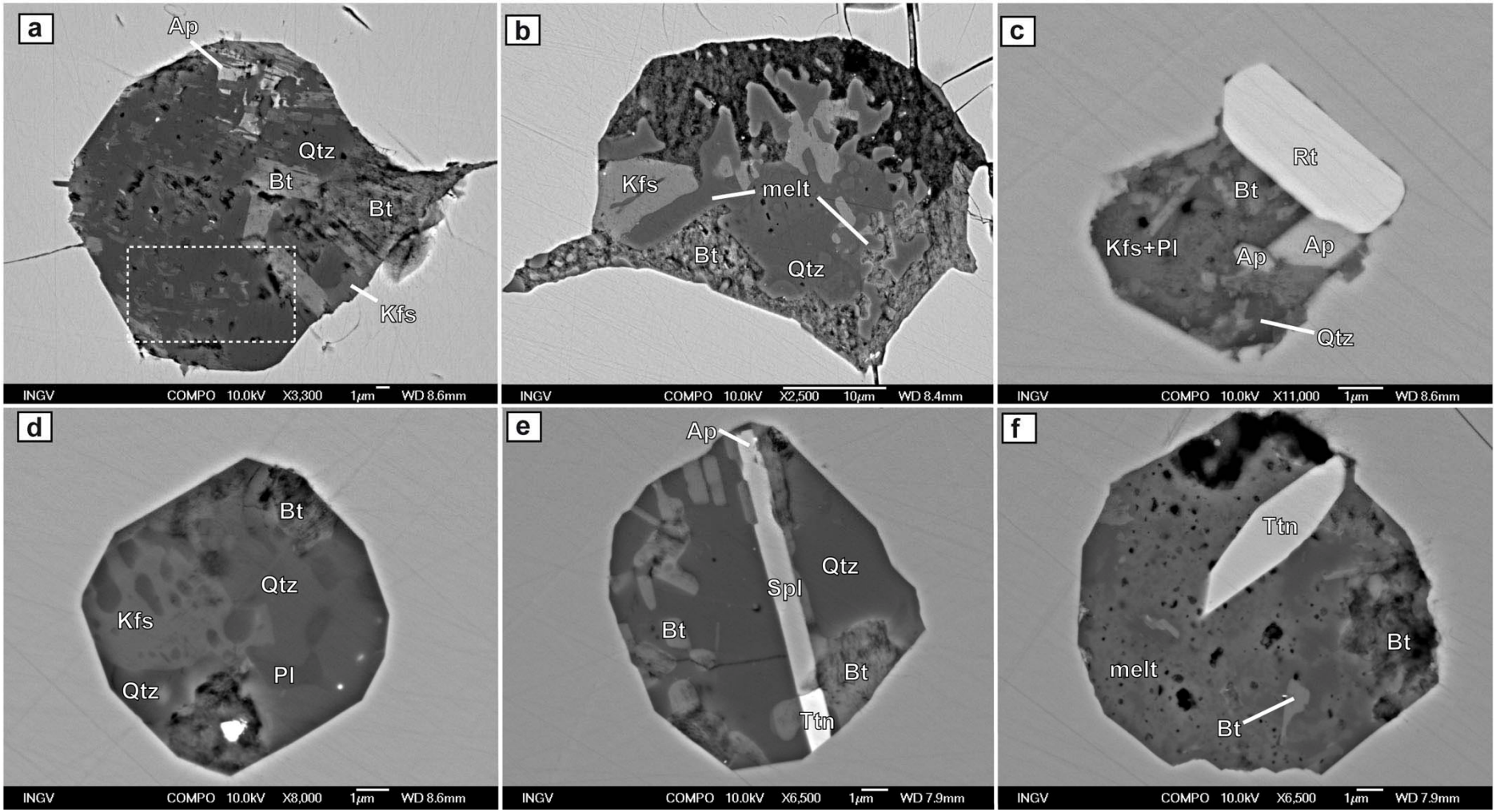

Figure 3: *Nanogranites, BSE images. Dashed white box: graphic intergrowths of K-feldspar in quartz.*

(3)_ X-ray maps
of nanogranites and partially crystallized inclusions

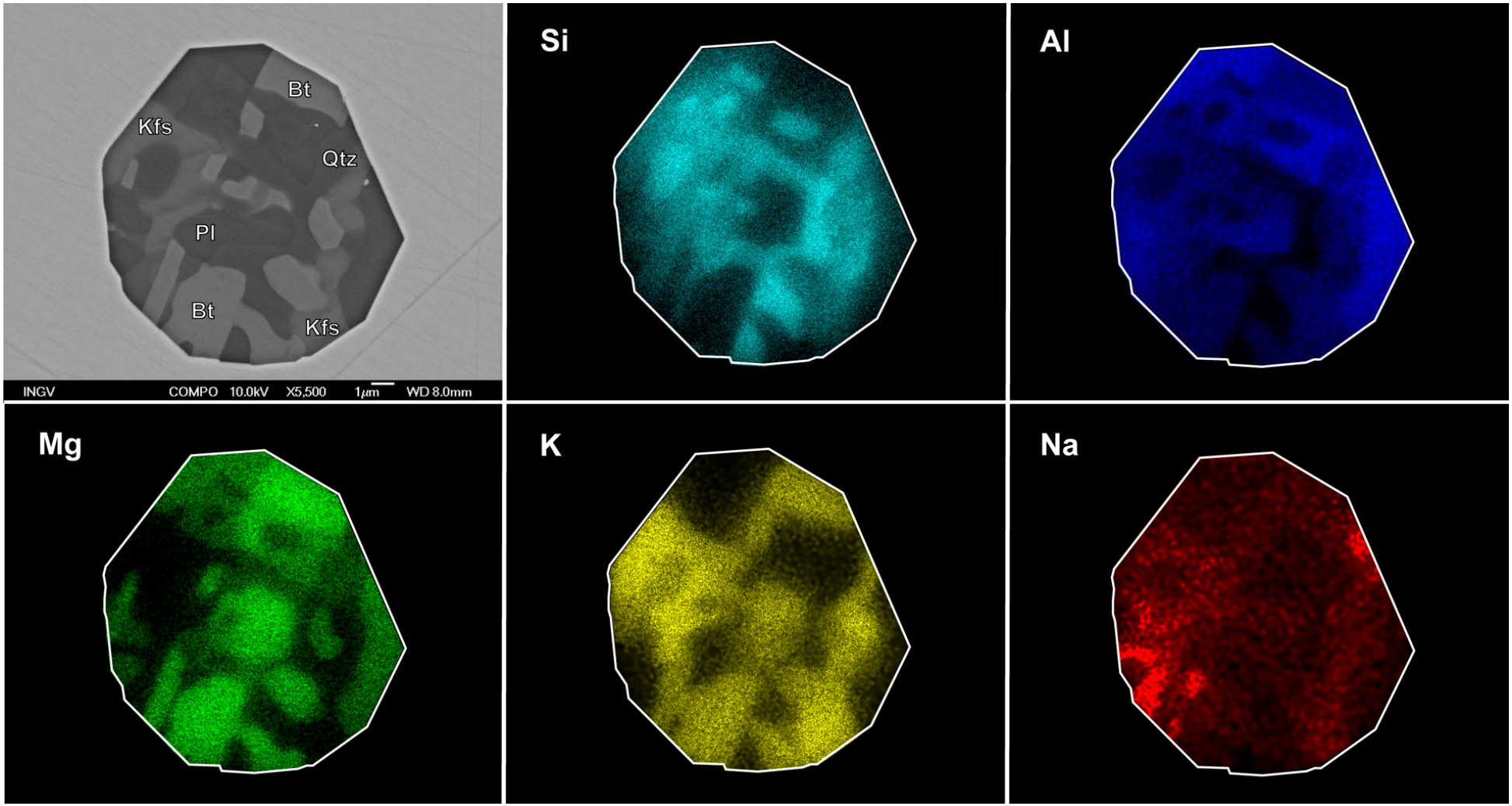

Figure 1: *X-ray maps of the elements of interest of a nanogranite (same of Fig.12c, chapter 2). Accelerating voltage: 20 kV, resolution: 500X375 pixel.*

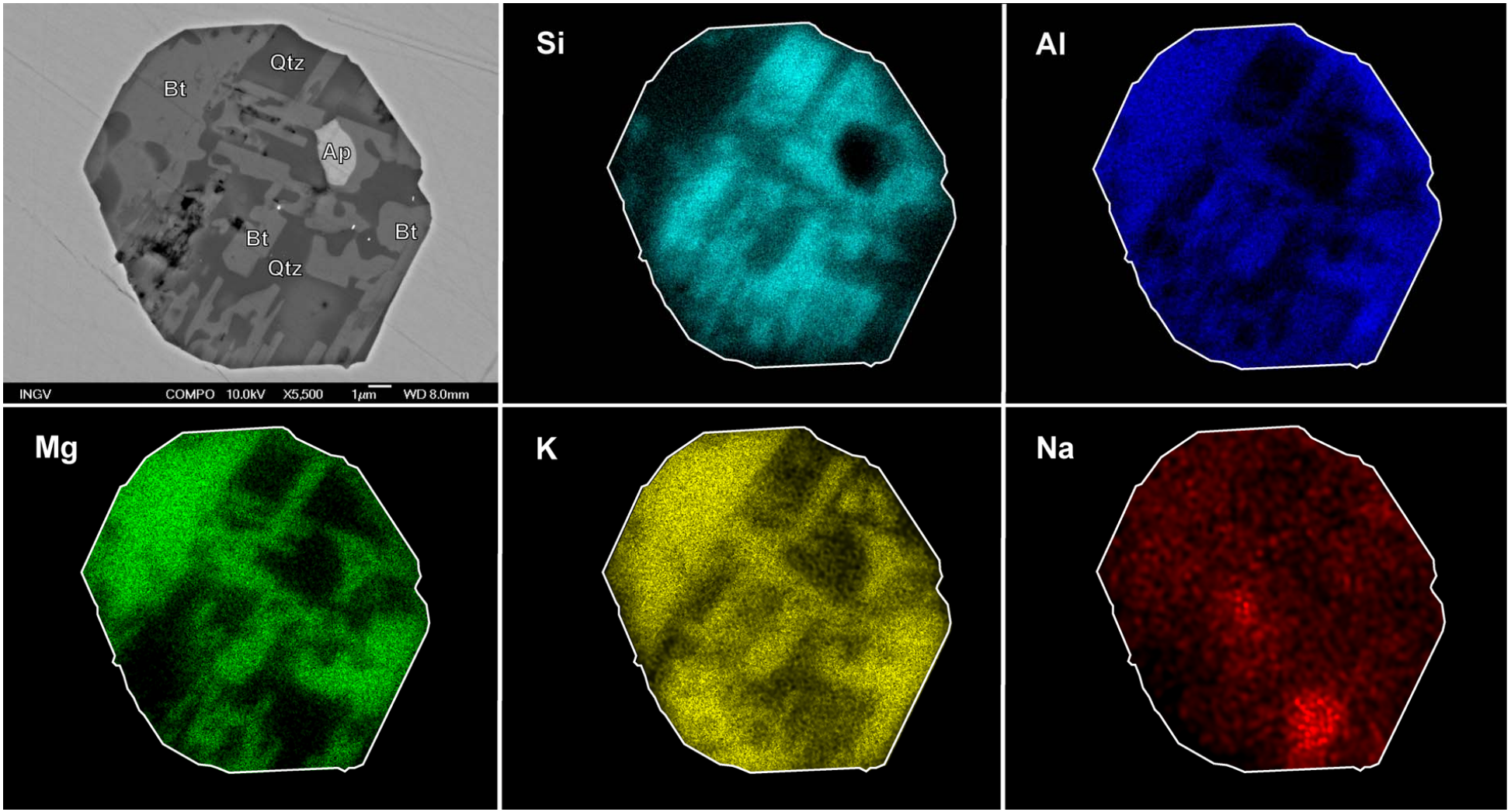

Figure 2: *X-ray maps of the elements of interest of a nanogranite (same of Fig.12e, chapter 2). Accelerating voltage: 20 kV, resolution: 500X375 pixel.*

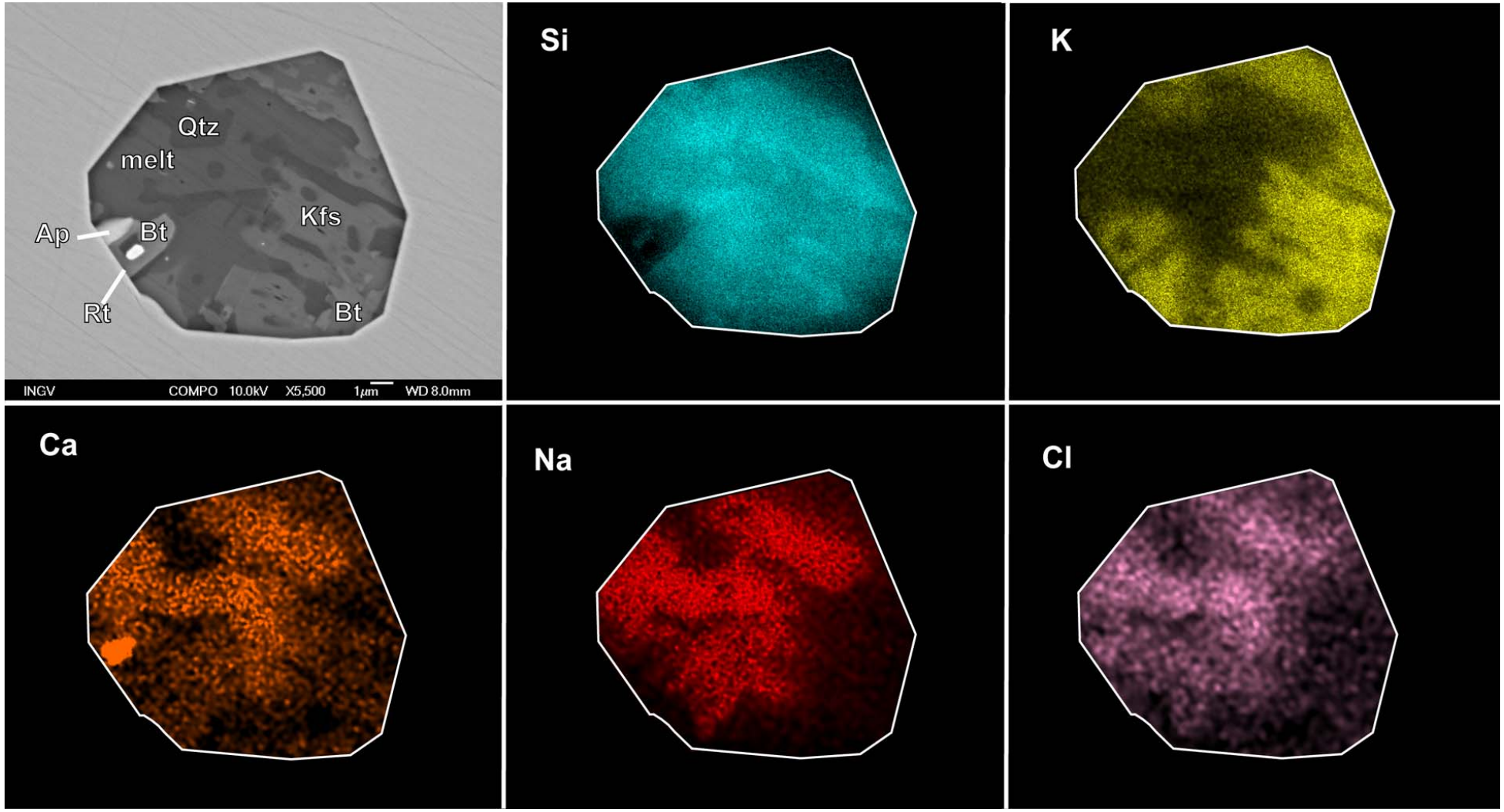

Figure 3: *X-ray maps of the elements of interest of a partially crystallized inclusion (same of Sup.Mat.1, Fig.2a,). Accelerating voltage: 20 kV, resolution: 500X375 pixel.*

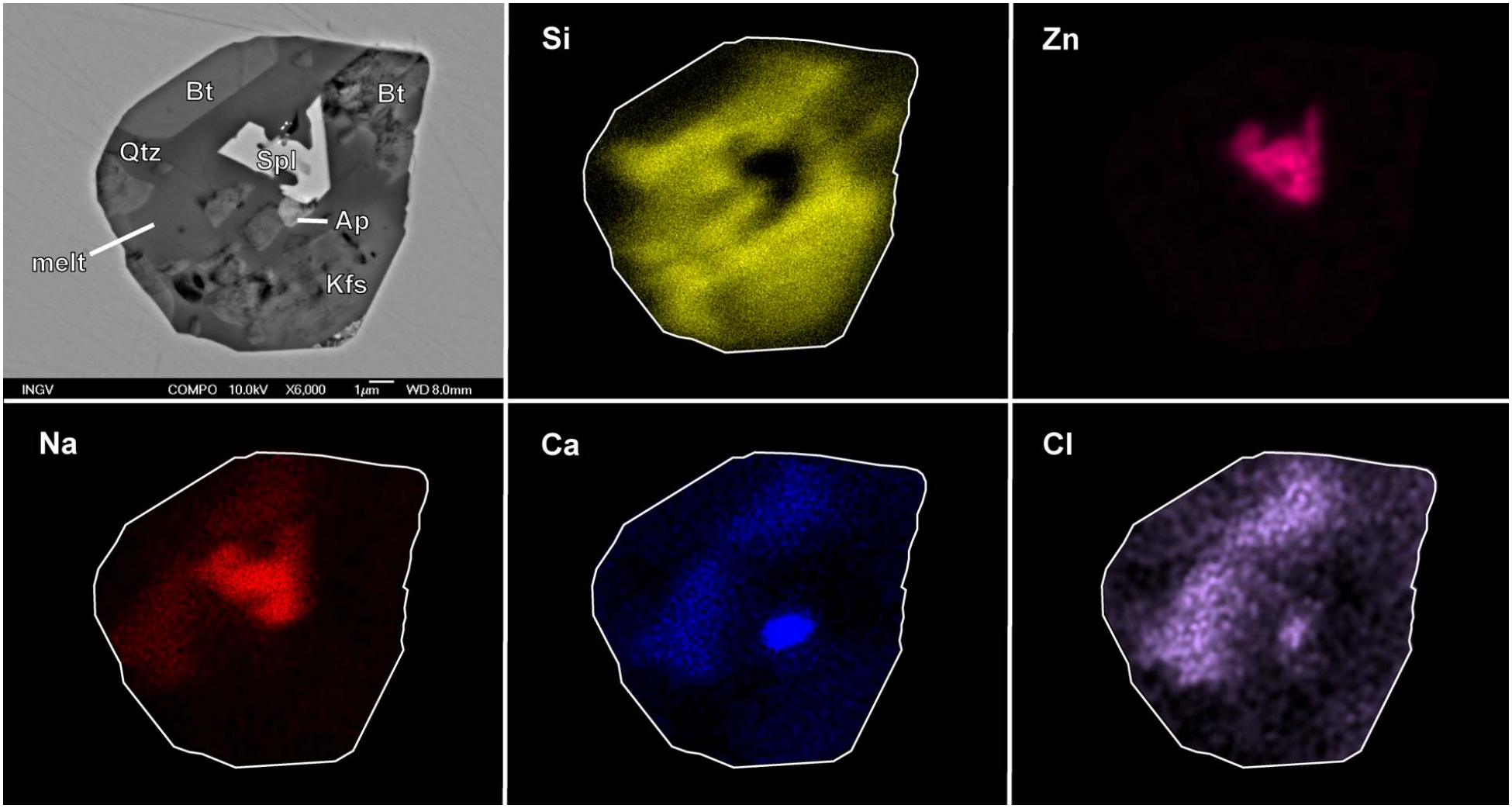

Figure 4: *X-ray maps of the elements of interest of a partially crystallized inclusion (same of Sup.Mat.1, Fig.2f,). Accelerating voltage: 20 kV, resolution: 500X375 pixel*

(2)_Total EMP analyses of homogenized inclusions

	12_1	12_3	12_8	10_7	9_1	9_2	7_5	7_6	6_1	6_3	4_5	4_11	4_12
SiO_2	70.87	68.18	74.11	69.24	77.02	76.28	75.84	76.81	75.92	72.93	72.08	72.42	71.00
TiO_2	0.00	0.03	0.27	0.18	0.00	0.10	0.02	0.11	0.20	0.11	0.18	0.00	0.02
Al_2O_3	14.45	15.25	13.86	14.90	12.62	11.11	11.93	11.32	11.71	14.12	12.99	13.41	16.29
FeO	3.18	4.00	2.94	4.13	2.73	3.12	2.70	2.16	2.38	2.47	3.14	4.39	3.60
MnO	0.06	0.00	0.07	0.07	0.01	0.08	0.00	0.06	0.00	0.00	0.00	0.06	0.00
MgO	0.72	1.52	0.42	0.90	0.67	0.40	0.43	0.62	0.99	0.91	0.66	0.45	0.56
CaO	0.48	1.01	0.70	0.88	0.55	0.54	0.11	0.33	0.57	0.54	0.51	0.63	0.68
Na_2O	1.41	0.88	1.02	1.24	0.51	0.70	0.80	1.30	1.07	1.24	1.48	1.38	2.97
K_2O	8.19	7.34	7.04	6.24	6.66	6.36	7.14	6.24	5.83	7.60	6.23	6.43	5.01
P_2O_5	0.04	1.06	0.10	0.00	0.02	0.02	0.17	0.00	0.00	0.00	0.02	0.02	0.26
Cl	0.36	0.19	0.21	0.34	0.08	0.14	0.09	0.18	0.20	0.37	0.44	0.33	0.38
total	99.76	99.46	100.74	98.12	100.86	98.85	99.23	99.12	98.88	100.29	97.73	99.53	100.77
H2O by diff.	0.24	0.54	-0.74	1.88	-0.86	1.16	0.77	0.88	1.12	-0.29	2.27	0.47	-0.77
ASI	1.20	1.36	1.31	1.43	1.39	1.23	1.29	1.19	1.29	1.26	1.29	1.29	1.41
Norm Cor	2	6	4	4	4	2	3	2	3	3	3	3	5
Norm Qz	31	37	42	40	50	50	46	47	50	37	42	41	35
Norm Ab	14	9	10	13	5	7	7	12	11	12	15	14	30
Norm Or	56	54	48	47	45	43	47	41	40	51	44	45	35
Norm An	2	0	3	4	3	3	0	2	3	3	2	3	2
Q/(Q+Or)	0.35	0.40	0.47	0.46	0.53	0.54	0.49	0.53	0.55	0.42	0.49	0.47	0.50
Q/(Q+Ab)	0.69	0.80	0.81	0.75	0.91	0.88	0.86	0.79	0.83	0.75	0.74	0.74	0.54

Table 1a: *for details of the analytical conditions see section 2.3.2.*

	4_13	4_14	15_3	12_2	12_5	12_7	10_3	10_4	10_5	10_6	10_8	9_4	9_5
SiO_2	72.44	72.70	73.44	69.48	72.65	67.34	73.28	74.91	74.40	70.38	70.25	75.81	69.35
TiO_2	0.14	0.00	0.11	0.10	0.19	0.10	0.07	0.02	0.10	0.00	0.14	0.00	0.10
Al_2O_3	14.28	13.60	13.71	14.40	13.41	13.65	13.35	12.95	13.48	14.73	13.78	11.67	14.66
FeO	2.92	4.00	4.00	2.80	2.94	3.76	3.65	2.67	2.57	3.70	3.31	2.93	5.72
MnO	0.08	0.08	0.00	0.01	0.01	0.03	0.02	0.00	0.05	0.00	0.04	0.00	0.05
MgO	0.84	0.86	1.05	0.75	0.77	0.92	1.00	0.66	0.76	0.85	0.72	0.40	1.20
CaO	0.73	0.65	0.81	0.67	0.50	0.68	0.54	0.49	0.76	0.99	0.66	0.46	1.63
Na_2O	1.81	1.41	1.07	1.00	1.08	1.03	1.15	1.47	0.97	1.03	1.48	0.82	0.57
K_2O	6.83	5.26	6.38	7.77	8.12	7.97	6.80	6.86	7.07	6.15	5.69	6.58	5.21
P_2O_5	0.14	0.02	0.15	0.05	0.05	0.23	0.25	0.00	0.01	0.08	0.02	0.01	0.19
Cl	0.41	0.33	0.22	0.21	0.17	0.60	0.25	0.22	0.21	0.18	0.23	0.15	0.29
total	100.61	98.90	100.94	97.24	99.89	96.32	100.34	100.24	100.38	98.09	96.31	98.85	98.96
H2O by diff.	-0.61	1.10	-0.94	2.76	0.11	3.68	-0.34	-0.24	-0.38	1.91	3.69	1.15	1.04
ASI	1.22	1.48	1.35	1.28	1.17	1.18	1.30	1.21	1.27	1.45	1.41	1.25	1.54
Norm Cor	3	4	4	3	2	3	4	2	3	5	4	2	6
Norm Qz	36	47	44	35	35	31	42	40	42	43	43	48	51
Norm Ab	18	15	11	10	10	11	11	14	9	11	15	8	7
Norm Or	47	38	45	55	55	58	47	46	48	46	42	44	43
Norm An	3	3	3	3	2	2	1	2	4	4	3	2	7
Q/(Q+Or)	0.43	0.55	0.49	0.39	0.39	0.35	0.47	0.47	0.47	0.49	0.51	0.52	0.54
Q/(Q+Ab)	0.67	0.76	0.80	0.78	0.77	0.75	0.78	0.74	0.82	0.80	0.74	0.86	0.88

Table 1b: *for details of the analytical conditions see section 2.3.2.*

	7_4	7_7	6_4	6_6	6_8	15_4	3_1	3_2	8_2	9_3	15_5	**average**	**std dev**
SiO_2	71.48	73.24	74.91	69.61	74.51	72.87	78.50	75.62	75.10	73.01	74.19	73.08	2.72
TiO_2	0.02	0.00	0.15	0.25	0.07	0.13	0.00	0.00	0.10	0.00	0.00	0.08	0.08
Al_2O_3	13.89	12.67	12.52	14.60	13.21	13.10	10.10	13.06	12.21	13.24	13.08	13.31	1.28
FeO	2.30	2.47	2.43	3.03	2.53	3.49	2.05	2.22	1.00	3.10	2.75	3.03	0.83
MnO	0.01	0.00	0.00	0.05	0.03	0.02	0.03	0.07	0.10	0.00	0.00	0.03	0.03
MgO	0.72	0.40	1.00	1.17	0.78	1.42	0.48	0.49	0.01	0.76	0.89	0.76	0.31
CaO	0.54	0.10	0.61	0.78	0.42	0.66	0.40	0.60	0.00	0.51	0.66	0.60	0.27
Na_2O	1.05	1.51	1.00	0.81	1.16	1.13	0.88	1.31	0.97	1.02	1.18	1.14	0.41
K_2O	7.30	6.97	6.26	7.40	7.02	5.94	6.38	7.17	8.68	6.64	7.18	6.76	0.81
P_2O_5	0.00	0.14	0.15	0.15	0.00	0.03	0.09	0.09	0.07	0.00	0.02	0.09	0.18
Cl	0.12	0.19	0.27	0.34	0.25	0.18	0.18	0.21	0.52	0.08	0.22	0.25	0.12
total	97.43	97.69	99.30	98.20	99.98	98.97	99.09	100.84	98.75	98.36	100.17	99.13	1.22
H2O by diff.	2.57	2.31	0.70	1.80	0.02	1.03	0.91	-0.84	1.25	1.64	-0.17	0.87	1.22
ASI	1.31	1.24	1.32	1.36	1.29	1.38	1.11	1.19	1.11	1.35	1.20	1.30	0.10
Norm Cor	3	3	3	4	3	4	1	2	1	3	2	3	1
Norm Qz	39	39	47	38	42	46	50	41	37	43	40	42	5
Norm Ab	10	14	10	8	11	12	8	12	9	10	11	11	4
Norm Or	51	46	43	53	47	43	41	47	54	46	49	47	5
Norm An	3	0	2	3	2	3	1	2	0	3	3	2	1
Q/(Q+Or)	0.44	0.46	0.52	0.42	0.47	0.52	0.55	0.47	0.41	0.48	0.45	0.47	0.05
Q/(Q+Ab)	0.79	0.73	0.83	0.82	0.79	0.80	0.86	0.77	0.81	0.81	0.78	0.79	0.07

Table 1c: *for details of the analytical conditions see section 2.3.2. Bold lined box: average and standard deviation of the reported analyses.*

(3)_Mass balance calculation: method

The total composition of H_2O-bearing fluid inclusions has been determined trough a mass balance calculation. The first step to determine the composition and density of the two-phase FI in Crd-Spl xenoliths is to determine the volume proportions of the aqueous and gas phases at room temperature. This was accomplished by first collecting a digital image of each inclusion and determining the areas of the aqueous and vapor phases using image-analyses software, and then converting these values into volume percentages of the liquid and vapor phases assuming a tubular cylindrical shape (see Roedder, 1984, figures 9-12 to 9-15). This assumption may underestimate the volume of the carbonic vapor phase by about 10-20 percent relative. The mole percent CO_2 in the inclusion will be similarly slightly underestimated based on this volume error. However, a more accurate estimate of the volume percentages cannot be accomplished without complete knowledge of the exact shape of the inclusions.

The density of the CO_2 phase in the FI was estimated using the Fall (2009) densimeter, previously described. Peak positions were measured at 35°C, which is above the critical temperature of CO_2 (31.1°C), using a Linkam THMSG600 heating/cooling stage mounted on the Raman microprobe, to assure that the CO_2-rich phase was homogeneous during the analyses. For each inclusion, the pressure corresponding to the calculated CO_2 density was determined, and then the density of N_2 was estimated at this same pressure and 35°C using the available thermophysical data (Lemmon et al., 2009). The density of H_2O is assumed to be 1 g/cm^3 in all of the inclusions at the conditions of analyses (35°C).

Using the compositions, volume proportions and densities of individual phases estimated as described above, the total inclusion composition and density was calculated based on mass balance considerations. Assuming that the total mass of "vapor" (CO_2 + N_2) in the FI = $M_{gas,\ total}$, the masses of the individual gas species are given by

$$m_{species} = \text{wt. fraction}_{(species)} \times M_{gas,\ total} \quad (4)$$

Where wt. fraction$_{(species)}$ represents the weight fractions of the individual gas species (CO_2 or N_2) determined by Raman analyses, and $M_{gas,\ total}$ represents the sum of the masses of CO_2 and N_2 in the FI. For simplicity, we have assumed that the total mass of gas equals 1 gram (the actual mass does not matter, as the final calculation involves

only mass fractions and not total mass). The volume occupied by each gas species ($V_{species}$) in the FI is given by:

$$V_{species} = m_{species} / \rho_{species} \quad (5)$$

where $\rho_{species}$ represents the density of each component that has been determined previously from Raman analyses. The total volume of the gas phase, $V_{gas\ total}$, equals the sum of the volumes of the individual gas species according to:

$$V_{gas\ total} = V_{CO2} + V_{N2} \quad (6)$$

Then, the total volume of the FI ($V_{FI,\ total}$) is given by

$$V_{FI,\ total} = V_{gas\ total} / V_{gas\ fraction} \quad (7)$$

Where $V_{gas,\ fraction}$ is the volume fraction of the inclusion that is occupied by the gas phase that has been previously determined as described above.

The volume of H_2O in the FI is given by:

$$V_{H2O} = V_{FI,\ total} - V_{gas\ total} \quad (8)$$

and the mass of H_2O in the inclusion is given by:

$$m_{H2O} = V_{H2O} \times \rho_{H2O} \quad (10)$$

Where ρ_{H2O} = 1 g/cm^3. The total density of the FI is then given by:

$$\rho_{FI,\ total} = (m_{CO2} + m_{N2} + m_{H2O}) / V_{FI,\ total} \quad (11)$$